The Dissertation Committee for Siddharth Misra Certifies that this is the approved version of the following dissertation:

Wideband Directional Complex Electrical Conductivity of Geomaterials: a Mechanistic Description

Committee:

Carlos Torres-Verdín, Supervisor

Kamy Sepehrnoori

Dean M. Homan

David DiCarlo

Hugh Daigle

Nan Sun

Wideband Directional Complex Electrical Conductivity of Geomaterials: a Mechanistic Description

by

Siddharth Misra, B.Tech.; M.S.E.

Dissertation

Presented to the Faculty of the Graduate School of

The University of Texas at Austin

in Partial Fulfillment

of the Requirements

for the Degree of

Doctor of Philosophy

The University of Texas at Austin

August 2015

Dedication

This dissertation is dedicated

to my wife, Swati,

my parents, Surekha and Rabindra Nath Misra,

and my brother, Samarth,

whose love, support, encouragement, and companionship

gave beauty and meaning to my doctoral journey.

Acknowledgements

I would like to express my sincere gratitude to my doctoral advisor, Dr. Carlos Torres-Verdín, for his guidance and continuous support all these years. I feel blessed for being given the opportunity to pursue my doctoral studies with him. He helped me evolve as a researcher. His able guidance aided my holistic professional development. Special thanks to Dr. Dean Homan for helping me comprehend the physics of triaxial electromagnetic induction using the tools and apparatus that he helped design at Schlumberger Houston Formation Evaluation. His enthusiasm, foresight, and optimism helped overcome challenges and uncertainties during the early days of my doctoral research. I want to thank John Rasmus for introducing me to several petrophysically challenging topics mentioned in this dissertation. He helped establish and maintain a strong research collaboration between the University of Texas at Austin Research Consortium on Formation Evaluation and Schlumberger.

I want to express my gratitude to Joachim Strobel and Late Richard Woodhouse for giving me valuable petrophysical insights during my early days as a doctoral researcher. I would like to acknowledge the members of my dissertation committee, Dr. Kamy Sepehrnoori, Dr. David DiCarlo, Dr. Hugh Daigle, and Dr. Nan Sun, for the technical discussions and insights related to this dissertation. I want to sincerely thank Dr. Kamy Sepehrnoori for resolving many of my research-related dilemma. I was fortunate to spend several months as a visiting researcher at the Schlumberger Houston Formation Evaluation Center at Sugar Land, Texas. I am immensely grateful to Schlumberger for the technical contributions toward the developments documented in this dissertation. Special thanks to

Gerald Minerbo, Mark Frey, Aditya Gupta, Mark Andersen, and Alexander Nadeev from Schlumberger for their support during my visits.

I am grateful to my friends: Ankit Jain, Mike Lacy, Linda Lacy, Chinmoy Mohapatra, Abhishek Shrivastava, Sayantan Bhowmik, Vicky Jha, Himanshu Yadav, Harish Sangireddy, Paras Choudhary, Rudra Narayan, Sundaram Das, Kriti Nigam, Garima Gupta, Abhishek Bansal, Melvin Blackburn, Abhilash Chandran, Sunil Kundal, and Vivek Arya for adding multitude of joy and adventure to my experiences. A special note of thanks to Swati's parents, Swagatika and Ganesh Satpathy for being the source of strength, affection, and hope. I would also like to thank my cousin brothers and sisters in India who made me smile with their stories and jokes.

I would like to thank my former and current colleagues at the Research Consortium on Formation Evaluation: Rohollah Abdollah Pour, Olabode Ijasan, Shaina Kelly, Hamid Hadibeik, Edwin Ortega, Chicheng Xu, Antoine Montaut, Paul Sayar, Oyinkansola Ajayi, Amir Frooqnia, Haryanto Adiguna, Hyungjoo Lee, Vivek Ramachandran, Shan Huang, Elton Ferreria, Philippe Marouby, Kanay Jerath, Eva Vinegar, Elsa Maalouf, Juan D. Escobar, David Medellin, Wilberth Herrera, and Joshua Bautista. Special thanks to Rey Casanova for his administrative support at the formation evaluation research consortium.

The work reported in this dissertation was funded by The University of Texas at Austin's Research Consortium on Formation Evaluation, jointly sponsored by Anadarko, Aramco, Baker-Hughes, BG, BHP Billiton, BP, Chevron, China Oilfield Services LTD., ConocoPhillips, Det Norske, Deutsche Erdoel AG, ENI, ExxonMobil, Halliburton, Hess, Maersk, Paradigm, Petrobras, PTT Exploration and Production, Repsol, Schlumberger, Shell, Southwestern Energy, Statoil, TOTAL, Weatherford, Wintershall, and Woodside Petroleum Limited.

Wideband Directional Complex Electrical Conductivity of Geomaterials: a Mechanistic Description

Siddharth Misra, Ph.D.

The University of Texas at Austin, 2015

Supervisor: Carlos Torres-Verdín

Subsurface electromagnetic (EM) measurements in shaly sands, sand-shale laminations, and organic-rich mudrocks, to name a few examples, exhibit directional and frequency dispersive characteristics primarily due to the effects of electrical conductivity anisotropy, dielectric permittivity anisotropy, and interfacial polarization phenomena. Conventional resistivity interpretation techniques for laboratory and subsurface EM measurements do not account for the effects of dielectric permittivity, dielectric loss factor, dielectric dispersion, and dielectric permittivity anisotropy arising from interfacial polarization phenomena. Furthermore, laboratory measurements on 1.5-inch-diameter, 2.5-inch-long core plugs acquired at discrete depths in wells are generally utilized to improve the estimation of petrophysical properties based on conventional resistivity interpretation of subsurface EM measurements.

Electrical measurements performed on 4-inch-diameter, 2-feet-long whole core samples represent closer approximations to the electrical properties of subsurface formations compared to widely-used galvanic measurements of core plugs. The first objective of this dissertation is to develop a non-contact and non-invasive, laboratory-based

EM induction apparatus, referred to as the WCEMIT, to measure the complex-valued electrical conductivity tensor of whole core samples at high resolution and at multiple frequencies for improved core-well log correlation. The tensor functionality of the WCEMIT is sensitive to the directional nature of electrical conductivity, dielectric permittivity, and dielectric loss factor, while its multi-frequency functionality is sensitive to the frequency-dispersive electrical properties of the samples. Finite-element and semi-analytic EM forward models of the WCEMIT are used to calibrate WCEMIT measurements and to estimate various effective electrical properties. WCEMIT measurements are successfully applied to the estimation of directional conductivity, dielectric permittivity, formation resistivity factor, Archie's porosity exponent, relative dip, azimuth, and anisotropy ratio.

It is found that brine-saturated samples containing pyrite and graphite inclusions exhibit a negative X-signal response, large frequency dispersion in the R-signal response, large effective permittivity, and significant frequency dispersion of effective conductivity and permittivity in the frequency range of 10 kHz to 300 kHz. Further, graphite-bearing samples exhibit significantly different frequency dispersion properties compared to pyrite-bearing samples. Estimated values of effective relative permittivity of samples containing uniformly distributed 1.5-vol% of pyrite inclusions were in the range of 10^3 to 10^4, while those containing uniformly distributed 1.5-vol% of graphite inclusions were in the range of 10^5 to 10^6. At an operating frequency of 58.5 kHz, samples containing 1.5-vol% of graphite inclusions and those containing 1.5-vol% of pyrite inclusions exhibited effective conductivity values that were 200% and 95%, respectively, of the host conductivity.

True conductivity and permittivity of hydrocarbon-bearing host media can be determined by processing the estimated effective conductivity and permittivity of conductive-mineral-bearing samples. Accordingly, the second objective of this dissertation is to develop a mechanistic electrochemical model, referred to as the PPIP-SCAIP model, that quantifies the directional complex electrical conductivity of geomaterials containing electrically conductive mineral inclusions, such as pyrite and magnetite, that are uniformly distributed in a fluid-filled, porous matrix made of non-conductive grains possessing surface conductance, such as silica, clay-sized particles, and clay minerals. PPIP-SCAIP model predictions successfully reproduce several laboratory measurements of multi-frequency complex electrical conductivity, relaxation time, and chargeability of mixtures containing electrically conductive inclusions in the frequency range of 100 Hz to 10 MHz.

The mechanistic model predicts that the low-frequency effective electrical conductivity of geomaterials containing as low as 5% volume fraction of disseminated conductive inclusions will vary in the range of 70% to 200% of the host conductivity for operating frequencies between 100 Hz to 100 kHz, while its high-frequency effective relative permittivity will vary in the range of 190% to 90% of the host relative permittivity for operating frequencies between 100 kHz and 10 MHz. The model indicates high sensitivity of subsurface EM measurements to the electrical properties, shape, volumetric concentration, and size of the inclusion phase, and to the conductivity of pore-filling electrolyte.

Table of Contents

List of Tables

List of Figures

Figure 6.11: Comparison of the PPIP-SCAIP model predictions of the LF σ_{eff} and HF $\varepsilon_{r,eff}$ responses of mixtures S, SP1, SP2, SP3, and SCl containing no inclusions, 5% volume fraction of 200-μm diameter spherical grains, 5% volume fraction of 20-μm diameter long rods, 5% volume fraction of 1-mm thick sheets, and 5% volume fraction of 10-μm diameter surface-charge-bearing, non-conductive spherical grains exhibiting Σ_s of 10^{-8} S, respectively, uniformly distributed in a matrix made of 70% volume fraction of 1-mm diameter, non-conductive spherical grains that is completely saturated with electrolyte for various electrolyte conductivities. Pairs of Figures 11a and 11b, 11c and 11d, 11e and 11f, and 11g and 11h identify the computed LF σ_{eff} and HF $\varepsilon_{r,eff}$ of mixtures, respectively, fully saturated with 0.001-, 0.01-, 0.1-, and 1-S/m electrolyte, respectively. Conductive inclusion phase has a relative permittivity of 12, conductivity of 5000 S/m, and diffusion coefficient of charge carriers is 5×10^{-5} m^2/s. Relative permittivity of the electrolyte is 80 and the diffusion coefficient of ions in the electrolyte is 10^{-9} m^2/s. The assumed value of relative permittivity of non-conductive spherical grain possessing Σ_s of 10^{-9} S, identifying a sand grain, is 4 and that of non-conductive spherical grain possessing Σ_s of 10^{-8} S, identifying a clay-grain, is 8. All the plots share the same legend.....233

Chapter 1: Introduction

A detailed knowledge of reservoir rock properties is crucial for efficient hydrocarbon production. Geoscientists and petrophysicists have developed variety of reservoir characterization techniques, such as seismic surveys, well logging, and core analysis, to evaluate the hydrocarbon storage potential and producibility of hydrocarbon-bearing reservoirs. Currently, a vast majority of O&G exploration and production activities are in geologically complex reservoirs, such as shaly sands, sand-shale laminations, and organic-rich mudrocks. New reservoir characterization techniques are required to accurately estimate the hydrocarbon pore volume in such reservoirs.

Existing interpretation methods for subsurface EM measurements in formations containing dispersed and/or laminated clay minerals, clay-sized grains, and conductive minerals rely on empirical models and lack reliable mechanistic models. Electrical conductivity anisotropy, dielectric permittivity anisotropy, and interfacial polarization of these formations significantly influence the EM measurements. Hence, the accuracy of estimation of petrophysical properties based on conventional resistivity interpretation of the EM measurements is generally improved by correlating the subsurface measurements with laboratory measurements on core plugs. However, as-received and/or re-saturated whole core measurements of electrical properties better represent the subsurface formation compared to the widely used galvanic measurements on core plugs extracted from discrete depths. For purposes of improved core-well log correlation, a non-contact and non-invasive laboratory-based electrical apparatus needs to be developed to measure complex electrical conductivity tensor of whole core samples at multiple frequencies. Moreover, a wideband mechanistic model that can quantify the directional effective complex electrical

conductivity of geomaterials over a broad frequency range should be developed for purposes of improving resistivity interpretation in formations containing dispersed and/or laminated clay minerals, clay-sized grains, and conductive minerals.

1.1 PROBLEM STATEMENT

The relative proportions of hydrocarbon reserves contained in shaly sands, sand-shale laminations, and organic-rich mudrocks are constantly increasing with the steady decline of reserves in conventional reservoirs. Moreover, the high cost of deepwater exploration demands high-accuracy petrophysical wellbore and laboratory measurements. Conventional EM measurements are generally correlated with laboratory measurements on core plugs assuming that these small-volume core plugs extracted from discrete depths of the formation reliably represent the subsurface formation (Laswell, 2006). In certain cases, subsurface EM measurements are re-calibrated based on galvanic measurements of core plugs assuming negligible effects of electrode and core plug geometries, current flow path and cross contamination issues, uncertainty in degree and area of contact between electrodes and core plug, and poor electrical anisotropy characterization capabilities (Kickhofel et al., 2010; Ubani et al., 2012). Further, conventional interpretation methods neglect the effects of interfacial polarization and frequency-dispersive electrical properties of formations (Anderson et al., 2006). From a practical view point, the validity of the above-mentioned assumptions for geologically complex formations is being increasingly questioned.

Several laboratory and field studies show that geomaterials exhibit electrical conductivity anisotropy (Klein, 1996; Gianzero, 1999 ; Kennedy and Herrick, 2004), large values of dielectric permittivity (Jackson and Hagiwara, 1998; Anderson et al., 2006; Le et al., 2011), dielectric permittivity anisotropy (Wu et al., 1997; Lüling et al., 2005),

interfacial polarization (Vinegar and Waxman, 1984; Yan et al. 2014), and frequency dispersion of the EM response (Sen, 1980; Hizem et al., 2008; Revil, 2012; Wang and Poppitt, 2013). Conventional interpretations of electrical measurements neglect dielectric permittivity, dielectric permittivity anisotropy, dielectric loss factor, and interfacial polarization phenomena. In doing so, it is typically assumed that the electric field in the formation due to an EM source in the borehole is not affected by the interfacial polarization of clay minerals, clay-sized particles, and conductive minerals.

The effects of conductivity anisotropy on electrical measurements and the methods to correct for such effects during resistivity interpretation of the EM measurements have been extensively investigated in the last 20 years. Jiangqing et al. (1994) developed a laboratory-based galvanic technique to measure the conductivity anisotropy ratio of formations encountered in horizontal and deviated wells. They emphasized that the study of electrical anisotropy requires high resolution measurements on larger dimension cores. Kriegshäuser et al. (2000) developed the first logging tool capable of measuring an electrical conductivity tensor to describe the electrical anisotropy of the subsurface environment using three separate orthogonal coil-systems. Following that, Rosthal et al. (2003) field tested a logging tool capable of full electrical conductivity tensor measurement using three collocated, orthogonal coil-systems.

Electrical conductivity tensor logging tools have a vertical resolution of 2 feet. These measurements are adversely affected by environmental effects (Wu et al., 2007). Also, resistive cemented streaks (Yu et al., 2001), fractures (Wu et al., 2013), and bed boundaries (Wang et al., 2003; Zhdanov et al., 2003) below the tool resolution significantly alter the tool measurements and increase the uncertainty in subsequent interpretation. The presence of conductive minerals, clay minerals, and clay-particles also influences the

conductivity tensor measurements (Anderson et al, 2007; Altman et al., 2008). Of special significance is that in laminated reservoirs, the accuracy in the values of resistivity and electrical anisotropy ratio of a representative shale unit is crucial for accurately interpreting these measurements (Schoen et al., 1999). Some publications mention the substantial uncertainty in the assessment of electrical properties of the representative shale unit. The accuracy of resistivity interpretation of electrical logging tool measurements relies immensely on the robustness of the inversion algorithm. All the above-mentioned factors, warrant the development of a "standard" non-contact and non-invasive method to measure the conductivity tensor of whole core samples at a high resolution and at multiple frequencies to re-calibrate the log measurements, provide additional data to improve the accuracy of inversion algorithms, measure electrical properties of the representative shale unit for accurate laminated sand-shale analysis, and facilitate quantitative laboratory investigation of the effects of above-mentioned factors on the conductivity tensor measurements. Kickhofel et al. (2010) built a tool to measure the conductivity tensor of whole core samples at a single operating frequency. They presented the reliability and robustness of tensor EM induction measurements on whole core samples. However, the petrophysical applications of that tool and a method for developing multifrequency measurement capability were not studied in their work.

Interfacial polarization phenomena is the process of charge accumulation/depletion at phase boundaries on a mesoscopic scale under the influence of an external electric field. There are various types of interfacial polarization phenomena depending on the electrical properties of the phase interfaces, electrical properties of the phases, and frequency of the external electric field. Typically, for colloidal suspensions, four types of interfacial polarization phenomena are observed within the frequency range of 10 to 10^{10} Hz, namely

α-, β-, γ-, (Shilov and Borkovskaya, 2010) and δ-polarization. The low-frequency α-polarization is a consequence of selective conductivity of membrane structures, such as electric double layers. This polarization mechanism is relevant to clay particles and clay-sized grains possessing surface conductance. The mid-frequency β-polarization is governed by thin membranes that restrict conduction of current until the frequency of externally applied electric field increases so that the capacitive resistance of the membrane becomes smaller than the effective ohmic resistance of the discharging medium. This polarization mechanism is relevant to the conductive mineral inclusions and beds that give rise to charge accumulation on their surfaces under the influence of an external electric field. The high-frequency γ-polarization is due to Maxwell-Wagner polarization associated with the difference in bulk conductivity of phases in contact. This polarization mechanism is relevant to surfaces of pores and pore throats. At frequencies beyond 1 GHz, δ-polarization (orientation polarization) occurs due to the permanent dipole moment of materials such as water and hydrogen chloride in the mixture.

In geomaterials, different types of polarization phenomena occur. For instance, polarization arising due to the difference in mobility of charge carriers in electrolyte, also referred to as the concentration polarization (Khair and Squires, 2008), exchange of ions between electric double layer around clay-sized particles and electrolyte (Revil et al., 2012), surface conductance of clay minerals, also referred to as the membrane polarization (Shilov et al., 2001), different types of charge carriers in host and inclusion phase (Wong et al., 1979), oxidation-reduction reaction at the host-inclusion interfaces (Placencia-Gomez and Slater, 2014), accumulation of charges around pore throats and at pore surfaces, also referred to as the Maxwell-Wagner polarization (Volkmann and Kiltzsch, 2010), and orientation polarization of water, minerals, and hydrocarbon (Hizem et al., 2008).

Interfacial polarization alters electromigration and electrodiffusion processes (Schmuck and Bazant, 2012). Most interpretation methods for the electrical tools neglect the effects of interfacial polarization; thereby, they lead to inaccurate estimation of petrophysical properties in formations that are susceptible to significant interfacial polarization, such as pyrite-bearing sedimentary rocks (Altman et al., 2008), clay-mineral-bearing mudrocks (Josh and Clennell, 2015), and pyrite- and graphite-bearing organic source rocks (Anderson et al., 2008). Subsurface galvanic and EM induction measurements are typically interpreted at a single frequency using empirical equations ignoring the effects of interfacial polarization due to clay minerals, conductive minerals, and clay-sized particles (Anderson et al., 2007; Corley et al., 2010). Though, EM propagation logs are measured and interpreted at several frequencies, the empirical equations used for interpretation are based on mixing laws that neglect polarization due to conductive minerals and Maxwell-Wagner polarization due to pore throats and pore surfaces (e.g., Hizem et al., 2008; Han et al., 2012). Empirical equations like the Archie's equation and Waxman-Smits equation are valid only at very low frequencies, whereas the Cole-Cole-type dielectric dispersion models are suitable for computing frequency-dependent electrical properties but are unsuitable for estimating petrophysically-relevant properties of geomaterials (Toumelin, 2006).

Owing to the interfacial polarization phenomena, geomaterials exhibit large dielectric permittivity (Le et al., 2011), non-negligible dielectric permittivity anisotropy (Lüling et al., 2005), and large frequency dispersion of their EM response (Wang and Poppitt, 2013). As a first step toward improved resistivity interpretation in such formations, the resistivity model for interpreting the galvanic resistivity, EM induction, and EM propagation measurements needs to account for the effects of interfacial polarization due

to surface conductivity of clay minerals and clay-sized particles and that due to impermeable interfaces of conductive minerals with electrolyte/matrix. In doing so, these multi-tool, multi-frequency measurements can be jointly interpreted in shaly sand, sand-shale laminated, mudrocks, and conductive-mineral-bearing formations. Consequently, the estimation of water saturation and TOC can be improved in these formations. The Wong (1979) model assumes an infinitely-conducting and spherically shaped inclusion phase to quantify the complex conductivity of a suspension of conductive minerals in an electrolyte, whereas the Dukhin et al. (1974) model assumes a diffused double layer to quantify the complex conductivity of a suspension of non-conductive particles in an electrolyte. However, there is no mechanistic model that quantifies the directional complex electrical conductivity of mixtures containing electrically conductive mineral inclusions of various shapes uniformly distributed in a fluid-filled, porous matrix made of non-conductive grains possessing surface conductance. No numerical modeling work has been carried out on understanding the relative effects of interfacial polarization due to clay particles and conductive minerals on the subsurface galvanic resistivity, EM induction, and EM propagation logging measurements. No numerical modeling work has been carried out on understanding the relative effects of interfacial polarization due to conductive mineralization of varied shapes on the subsurface galvanic resistivity, EM induction, and EM propagation logging measurements. Moreover, conventional resistivity interpretation lacks a wideband mechanistic model that facilitates joint interpretation of multi-tool, multi-frequency EM measurements (Wang and Poppitt, 2013). Such a wideband model is critical to accurate estimation of TOC and water saturation in the presence of frequency-dependent electrical properties, dielectric permittivity, and interfacial polarization phenomena.

To further complicate the existing challenges, there is no commercial non-contact and non-invasive laboratory-based apparatus to measure the complex electrical conductivity tensor of whole core samples at multiple frequencies. A continuous, non-invasive EM measurement on a standard 2-ft-long, 4-inch-diameter whole core sample is a better representative of the subsurface formation compared to the widely used galvanic measurement on standard 2-inch-long, 1.5-inch-diameter core plugs. Existing special core analyses do not characterize the electrical conductivity, anisotropy, dielectric permittivity, and frequency dispersion characteristic of whole-core samples. There is no published work on improving resistivity characterization of reservoir rocks by measuring electrical properties of whole core samples in their as-received or re-saturated state. Few laboratory investigations have been carried out to test the validity and reliability of conductivity tensor measurements based on electromagnetic induction principles and the accuracy of its interpretation results. Also, no laboratory investigation has been carried out to measure the complex conductivity tensor of mixtures containing conductive mineral inclusions, such as pyrite and graphite, in the EM induction frequency range from 10 kHz to 300 kHz, to better understand the effects of interfacial polarization on subsurface triaxial EM induction measurements.

Therefore, it is time to develop a new non-invasive and non-contact electrical method to measure complex conductivity tensor of whole core samples, to comprehensively study the relative effects of pyrite and graphite on electromagnetic induction measurements, and to develop a wideband mechanistic model that quantifies the effects of interfacial polarization due to clay minerals, clay-sized grains, and conductive minerals on the EM response to facilitate joint interpretation of multi-tool, multi-frequency subsurface EM measurements.

1.2 RESEARCH OBJECTIVES

The main thrust of this dissertation is to develop a laboratory measurement technique and a quantitative interpretation method that explicitly account for the effects of interfacial polarization due to conductive minerals, clay-sized particles, and clay minerals uniformly distributed in a fluid-filled porous geological host. In doing so, the resistivity interpretation of subsurface EM measurements can be improved for applications in shaly sands, sand-shale laminations, mudrocks, and conductive-mineral-bearing formations. Specifically, the objectives of this dissertation are as follows:

- To develop a non-contact and non-invasive laboratory-based apparatus to measure the complex electrical conductivity tensor of whole core samples at multiple frequencies.
- To develop and validate a finite-element and/or a semi-analytic EM forward model of the developed tool.
- To verify the reliability of the developed tool for purposes of estimating the electrical properties of whole core samples. To achieve this objective, an inversion scheme in conjunction with one of the developed EM forward models needs to be implemented to process the multi-frequency complex conductivity measurements.
- To demonstrate the petrophysical applications of the developed tool for purposes of whole core analysis in various types of formations, such as isotropic, vuggy, layered, etc..
- To use the developed tool to estimate the directional complex conductivity of mixtures containing conductive mineral inclusions in the EM induction frequency range of 10 kHz to 300 kHz. This study is crucial for understanding the effects of interfacial polarization on the subsurface EM induction measurements.

- To develop a mechanistic model that quantifies the directional complex electrical conductivity of mixtures containing electrically conductive mineral inclusions of various shapes uniformly distributed in a fluid-filled, porous matrix made of non-conductive grains possessing surface conductance.
- To verify the reliability of the developed mechanistic model by quantitatively comparing the model predictions to laboratory measurements on mixtures containing uniformly distributed inclusions. Also, the model predictions will be compared with the predictions of widely used empirical models.
- To predict the effects of interfacial polarization due to clay particles and conductive minerals on subsurface galvanic resistivity, EM induction, and EM propagation logging measurements.

1.3 METHOD OVERVIEW

Results presented in this dissertation are based on the laboratory measurements, numerical modeling, and analytical modeling of directional complex conductivity of geomaterials. These methods allow researchers to calculate the effective electrical properties and electrical properties of individual components of geomaterials.

In the first part of this dissertation, I develop the apparatus to measure the complex conductivity tensor of whole core samples. The tool is designed based on the physics of tri-axial electromagnetic induction physics (Rosthal et al., 2003). The apparatus comprises three orthogonal (tri-axial) transmitter, bucking, and receiver coils built on the outer surface of a tubular conduit that holds whole core samples, which are 2 feet in length and 4 inches in diameter. A resonance circuit energizes one of the three orthogonal transmitter coils by injecting a current of known value at a specific frequency. The frequency of excitation is selected by selecting a particular capacitor bank built in the resonance circuit.

A LABVIEW code is implemented to automate the selection of the frequency of the transmitter current. When an alternating current flows through the transmitter coil, eddy currents are induced in surrounding volume. These eddy currents induce complex-valued voltage in the three orthogonal receiver coils. The LABVIEW-code automates the selection of the receiver coil for measurement of the complex-valued induced voltage. The magnitudes of the induced voltages due to whole core samples are typically on the order of microvolts and subsequently amplified using a Lock-in amplifier. One complete cycle of the tool measurement generates nine induced complex-valued voltage measurements, which are subsequently converted to the complex-conductivity tensor of the whole core sample (Kickhofel et al., 2010).

Next, I develop and validate a COMSOL-based finite element model and a MATLAB-based semi-analytic model of the developed tool response. The semi-analytic model is developed in MATLAB to quantify the tool response to an infinitely long, 4-inch-diameter cylindrical volume placed in the tool conduit as a function of its horizontal conductivity (σ_{hor}), horizontal relative permittivity ($\varepsilon_{r,hor}$), conductivity anisotropy ratio (λ_c), permittivity anisotropy ratio (λ_p), and the operating frequency (Misra et al, 2015a). On the other hand, the finite-element model is developed in COMSOL to quantify the tool response to a 4-inch-diameter, 24-inch-long cylindrical volume, placed coaxially inside the transmitter, receiver, and bucking coils, as a function of σ_{hor}, $\varepsilon_{r,hor}$, λ_c, λ_p, dip (θ), azimuth (β), and the operating frequency (Misra et al., 2015b). Both the models describe tool response in the induction (10-400 kHz) and propagation (0.4-2 MHz) frequency ranges. The MATLAB-based semi-analytic model is significantly faster than the COMSOL-based finite-element forward model.

The semi-analytic model is used to calibrate the nine transmitter-receiver coupling responses (Misra et al., 2015b). It is also extensively used to estimate the horizontal and vertical effective conductivity and relative permittivity values of samples containing uniformly distributed conductive minerals (Misra et al., 2015a). The finite-element model is used to estimate the geometric factor of each of the nine-transmitter receiver coupling that is used to convert the measured values of induced receiver voltages and the transmitter current to apparent complex conductivity measurements, which constitute the complex conductivity tensor of a whole core sample (Misra et al., 2015b). It is also extensively used to invert the complex conductivity tensor of layered whole core samples to obtain σ_{hor}, λ_c, θ, and β (Misra et al., 2015b). Several synthetic whole core samples are prepared and measured using the developed tool. Predictions of both the models are compared against the laboratory measurements to validate the tool responses (Misra et al., 2015b).

After validating the tool response, petrophysical applications of the developed tool are tested on isotropic, anisotropic, layered, vuggy, and conductive-mineral-bearing whole core samples (Misra et al., 2015b). All this required the use of various inversion schemes in conjunction with the developed EM forward models. First, I prepared glass-bead packs containing conductive mineral inclusions fully saturated with brine inside 4-inch outer diameter, 3.8-inch inner diameter, 2-ft long cylindrical glass vases. Two types of nearly spherical pyrite inclusions are used in this work, namely Pyrite Red (average diameter = 50 µm) and Pyrite Yellow (average diameter = 130 µm) manufactured by Washington Mills. Two types of flaky graphite inclusions are used in this work, namely #2 flake graphite (50×200 mesh size, average surface area = 0.02 mm^2) and #1 flake graphite (50×80 mesh size, average surface area = 0.06 mm^2) from Dixon Graphite. Glass beads used in this work are 1.15-mm-diameter Megalux beads from Swarco Company. The

directional complex conductivity of these conductive-mineral-bearing samples are estimated in the frequency range from 10 kHz to 300 kHz. The laboratory investigation shows that samples containing these conductive inclusions exhibit significant frequency dispersion of the EM response in the EM induction frequency range and large values of dielectric permittivity (Misra et al., 2015a).

In the penultimate part of the dissertation, I develop a mechanistic model of the directional complex conductivity of geomaterials containing conductive and clay minerals uniformly distributed in a fluid-filled, porous matrix made of non-conductive grains possessing surface conductance (Misra et al., 2015c). The mechanistic description of interfacial polarization phenomena used in this new model is constructed based on laboratory investigation performed by several researchers on mixtures containing non-conductive particles exhibiting surface conductance (e.g., Dukhin et al., 1974; Grosse and Foster, 1987) and on mixtures containing conductive mineral inclusions (e.g., Wong, 1979; Chu and Bazant, 2006). Concepts implemented in the mathematical formulation of the interfacial phenomena are attributed to Wong (1979) and to Grosse and Barchini (1992). Our model invokes a new formulation of the Poisson-Nernst-Plank's equation (Schmuck and Bazant, 2012) followed by a consistent effective medium approximation (Giordano, 2003) to compute the wideband directional complex conductivity of geomaterials. The developed model is implemented as an analytical expression in Cartesian, cylindrical, and spherical coordinates (Misra et al., 2015c). The model is validated by comparing the model predictions against the laboratory measurements of dispersive effective conductivity and relative permittivity of mixtures containing uniformly distributed inclusions (e.g., Abdel Aal et al., 2015; Revil et al., 2015a). Importantly, the developed tool responses to pyrite-

bearing samples are successfully quantified using the developed mechanistic model (Misra et al., 2015a).

Finally, I perform extensive mechanistic modeling in the operating frequency ranges of subsurface galvanic resistivity (1 Hz – 1 kHz), EM induction (10 kHz – 100 kHz), and EM propagation (400 kHz – 10 MHz) logging tools for various petrophysical properties of the inclusion phase and host medium. Consequently, I obtain a comparative description of the sensitivity of measurements of these tools to petrophysical properties of the geological mixture (Misra et al., 2015d). I find a strong dependence of these subsurface EM measurements on the volume content, conductivity, surface conductance, shape, and size of inclusion phase and on the conductivity of electrolyte in the host medium. Comparison of the computed complex conductivity of mixtures against that of uncontaminated sample indicates drastic frequency dispersion of the EM response and large alterations of EM measurements over a broad frequency range. This necessitates the implementation of such wideband mechanistic models to improve resistivity interpretation in shaly sands, sand-shale laminations, and organic-rich mudrocks.

1.4 OUTLINE OF THE DISSERTATION

This dissertation consists of six additional chapters following this introductory chapter. Chapter 2 introduces a new tool for measuring complex conductivity tensor of whole core samples. It first discusses the theory, design, and setup of the new apparatus. Next, I discuss and validate semi-analytic and finite-element EM forward models of the tool response. Tool responses are then calibrated using a tilted test loop.

Subsequently, Chapter 3 documents various petrophysical applications of the developed tool described in Chapter 2 for purposes of whole core analysis of isotropic, anisotropic, layered, vuggy, and conductive-mineral-bearing whole core samples. Prior to

that, the tool measurements are validated by comparing them against the EM forward model predictions of the tool response to synthetic samples. Numerical models of the tool response are implemented to estimate various petrophysical properties of whole core samples, notably host conductivity, σ_{hor}, λ_c, θ, and β.

Chapter 4 describes laboratory investigation of the directional complex conductivity of mixtures containing conductive mineral inclusions in the EM induction frequency range from 10 kHz to 300 kHz using the developed tool described in Chapter 2. It emphasizes the estimation of effective electrical properties of conductive-mineral-bearing mixtures as a function of the operating frequency of measurement, and shape, size, material, and volume content of the inclusion phase. Also, it compares the electrical properties of mixtures containing pyrite with those containing graphite.

Chapter 5 develops and validates a mechanistic model of directional complex conductivity of mixtures containing electrically conductive mineral inclusions of various shapes uniformly distributed in a fluid-filled, porous matrix made of non-conductive grains possessing surface conductance. The model is implemented in Cartesian, cylindrical, and spherical coordinates. I introduce a new effective medium formulation for mixtures exhibiting both surface-conductance-assisted (clay particles and clay-sized grains) and perfectly-polarized (conductive mineral inclusions) interfacial polarization phenomena. Also, various laboratory measurements of effective electrical properties and their frequency dispersion are reproduced using the new model.

Chapter 6 extends the new mechanistic model to describe the impact of interfacial polarization due to clay minerals, clay-sized particles, and conductive minerals on subsurface galvanic resistivity, EM induction, and EM propagation logging measurements.

Emphasis is also placed on the directional complex conductivity of mixtures containing rod-like and sheet-like inclusions.

Finally, Chapter 7 summarizes the research achievements and contributions of the dissertation. Conclusions are based on the laboratory investigation, mechanistic model predictions of the directional complex conductivity, and effective electrical properties estimated using the semi-analytic model. Also, I provide recommendations for future research.

Chapter 2: Laboratory Apparatus for Multi-Frequency Inductive-Complex Conductivity Tensor Measurements

This chapter introduces a new laboratory apparatus capable of high-resolution multi-frequency complex conductivity tensor measurements on whole core samples and continuous-feed cylindrical volumes in the EM induction (EMI) frequency range of 10 kHz to 300 kHz. This experimental EM laboratory apparatus is referred to as the Whole Core EM Induction Tool (WCEMIT). It is based on the physics of triaxial EM induction (Rosthal et al., 2003) for a three-coil sonde (Barber, 1987) design. It is primarily a non-invasive, non-contact measurement technique for examining whole core samples in their as-received and re-saturated state. Tensor functionality of this tool is sensitive to the directional electrical conductivity (σ) and dielectric relative permittivity (ε_r) of geomaterials, while its multi-frequency functionality is sensitive to the dispersive electrical properties of geomaterials.

I develop a COMSOL-based finite-element (FE) EM forward model and a MATLAB-based semi-analytic (SA) EM forward model of the developed tool response. The FE model is used to validate the SA model. The SA model predictions are used to calibrate the complex impedance values measured for the nine transmitter-receiver (TR) couplings of the WCEMIT.

2.1 INTRODUCTION

Conventional core and rotary sidewall-core samples provide petrophysicists, engineers, and geologists with rock-based data for improved reservoir characterization. Laboratory core measurements are used to estimate the electrical properties of reservoir rocks, such as the parameters of the Archie's equation or Waxman-Smits equation (Laswell, 2006). Currently, there are no standard methods of laboratory-based electrical

measurements on rock core samples to estimate the electrical conductivity anisotropy, low-frequency dielectric permittivity, and wideband frequency dispersion of electrical properties of a subsurface formation (Ubani et al., 2012). Moreover, the widely-used galvanic techniques for core plugs are adversely impacted by the dependence on electrode and core plug geometries, lack of rock fabric preservation, poor electrical anisotropy characterization capability, partial conductivity tensor measurement capability, current path and cross contamination issues, and uncertainty in degree and area of contact between the electrodes and core plug (Kickhofel et al., 2010). The newly developed WCEMIT performs non-invasive, non-contact, high-resolution, multifrequency complex conductivity tensor measurements on whole core samples. I claim that a continuous non-invasive EM measurement on a standard 2-ft-long, 4-inch-diameter whole core sample is a more accurate and efficient representation of a subsurface formation than the widely-used galvanic measurement on standard 2-inch-long, 1.5-inch-diameter core plugs extracted from discrete depths of the formation.

Induction-type conductivity sensors were first used in metal detectors in 19th century. Within the oilfield services industry, Doll (1949) introduced the theory of inductive resistivity measurements. The theory of conductivity tensor logging was fully developed in the 1970s. However, the practical oilfield measurement of conductivity tensor was introduced much later by Kriegshäuser et al. (2000) as a multicomponent induction tool and then by Rosthal et al. (2003) as a triaxial induction tool. Currently, the conductivity tensor tools are used worldwide to improve the interpretation of formation anisotropy, dip, cross-bedding, bed boundaries, and fractures.

Wakamatsu (1997) developed an EM technique for dielectric spectroscopy measurement using toroidal induction coils. This technique is free from electrode

polarization effects prevalent in galvanic techniques; therefore, it provides improved high-conductivity colloidal liquid evaluation in the frequency range of 75 kHz to 30 MHz. Wakamatsu (1997) shows that the analysis of measured dielectric relaxation response of a colloidal liquid based on an appropriate theory of interfacial polarization provides information on the structural and electrical properties of the colloidal particles. Asami et al. (1999) used the non-electrode EMI method developed by Wakamatsu (1997) for real-time monitoring of yeast cell growth. Biological cells in an external field give rise to interfacial polarization phenomena, thereby producing a time-varying dielectric relaxation response as a function of the yeast cell population. Won and Keiswetter (1998) investigated applications of spectral EMI measurements to detect and characterize the geometry and material composition of a metallic object in the frequency range of 30 Hz to 24 kHz using collocated coils and transmitter-bucked EMI sensor. They used pulsed-width modulation to create the desired transmitter waveform for a particular survey. They assumed a negligible displacement current resulting from the dielectric property of the surrounding upto a megahertz frequency. Scharfetter et al. (1999) developed an in-vivo inductive bioimepedance spectroscopy technique applicable in the frequency range of 50 kHz to 5 MHz and conductivity range of 0.66 to 10 S/m. Further, the EMI physics is utilized extensively for purposes of non-destructive testing in the metals industry to inspect the quality of materials at high speed without requiring direct physical contact between the sensor and material under inspection (Garcia-Martin et al., 2011).

With regard to laboratory analysis of rock cores, there is little published research work on measuring electrical properties of whole cores using the EMI principles (Kickhofel et al., 2010). Jackson et al. (2006) developed an apparatus for non-contact, non-invasive measurement of whole-core and split-core resistivity values as a continuous log

at a resolution of 10 mm. They implemented a four-coil arrangement, of two pairs of transmitter and receiver coils. The drawbacks of this apparatus were that it measures partial conductivity tensor and has a small depth of investigation. Homan et al. (2009) introduced the first laboratory, fully triaxial induction apparatus. It is capable of inductive-conductivity tensor measurements on flowline, standard whole cores, and continuous-feed cylindrical materials at a single operating frequency of 51.28 kHz. Kickhofel et al. (2010) validated the measurements of the apparatus developed by Homan et al. (2009), and applied it to estimate σ_{hor} and λ_{c} on a sand-shale laminated whole core at 51.28 kHz. In my work, I extend Kickhofel et al.'s (2010) tool design by adding multi-frequency measurement capability, applying multifrequency EM forward models of the developed tool response to estimate electrical properties of whole core samples, and developing a robust inversion algorithm to estimate σ_{hor}, λ_{c}, β, and θ of whole core samples. The developed apparatus is primarily utilized to estimate the directional and dispersive σ_{eff} and $\varepsilon_{\mathrm{eff}}$ of conductive-mineral-bearing samples.

2.2 THEORETICAL CONSIDERATIONS

2.2.1 Basic Theory of EM Induction Measurements

Moran and Kunz (1962) outlined the theory of the two-coil sonde from first principles. The two-coil sonde comprises a transmitter coil and a receiver coil, each of radius *a'*, positioned at a distance *x* apart. When an alternating current *I* energizes the transmitter coil, it creates a time-varying 3D magnetic field $\boldsymbol{b}$, which further induces eddy currents in the surrounding volume. A small secondary magnetic field emanating from the induced eddy currents induces a complex-valued voltage v_{R} in the receiver coil. EMI physics is completely described by Maxwell's four equations, and analytical solutions

beyond simplest geometry are rare due to their mathematical complexity. Nonetheless, for the limiting case of a point dipole transmitter and receiver in an isotropic homogeneous medium, Moran and Kunz (1962) derived an expression for the complex-valued induced voltage in the receiver as

$$v_{\mathrm{R}}^{*} = \mathrm{i}\frac{m_{\mathrm{R}} m_{\mathrm{T}} (\pi a'^{2})^{2}}{2\pi} I_{\mathrm{T}} \omega \mu (1 - \mathrm{i}kx) \frac{\mathrm{e}^{\mathrm{i}kx}}{x^{3}}, \tag{1}$$

where m_{R} and m_{T} are the number of turns in the receiver and transmitter, respectively, ω is the angular frequency of the current in transmitter coil, μ is magnetic permeability of the surrounding volume, I_{T} is the current in the transmitter coil, i is equal to $\sqrt{-1}$, and k is the wavenumber that is related to complex conductivity σ^{*} of the surrounding volume as $k = \sqrt{\mathrm{i}\omega\mu\sigma^{*}}$, where $\sigma^{*} = \sigma + \mathrm{i}\omega\varepsilon_0\varepsilon_{\mathrm{r}}$, in which σ is the conductivity of surrounding volume, ε_0 is absolute vacuum permittivity and ε_{r} is the relative permittivity of surrounding volume.

Equation 1 can be expanded as powers of kx assuming small values of permittivity of the material to obtain approximate expressions for the real part and imaginary part of the induced receiver voltage as

$$\mathrm{Re}(v_{\mathrm{R}}^{*}) = -G I_{\mathrm{T}} \sigma \left(1 - \frac{2x}{3\delta}\right), \tag{2}$$

and

$$\mathrm{Im}(v_{\mathrm{R}}^{*}) = G I_{\mathrm{T}} \sigma \frac{\delta^{2}}{x^{2}} \left(1 - \frac{2\delta^{3}}{3x^{3}}\right), \tag{3}$$

respectively, where $\delta = \sqrt{2/\omega\mu\sigma}$ is the skin depth of the medium and G is the geometrical factor of the TR coupling, which is expressed as

$$G = \frac{(\omega\mu)^{2} (A_{\mathrm{R}} A_{\mathrm{T}})(m_{\mathrm{R}} m_{\mathrm{T}})}{4\pi x}, \tag{4}$$

where A_{R} and A_{T} are the cross-sectional areas of the transmitter and receiver coils, respectively (Moran and Kunz, 1962). Equation 2 indicates that the real part of the induced

receiver voltage is linearly related to the conductivity of surrounding volume, while the imaginary part of the induced receiver voltage is independent of the conductivity of surrounding volume when the surrounding volume is of negligible permittivity. Consequently, the imaginary part of the induced receiver voltage identifies the direct mutual coupling between transmitter and receiver coils for a two-coil sonde.

Most of the oilfield induction tools use the three-coil sonde design (Barber, 1987) to remove the direct coupling of TR coupling from the complex-valued induced receiver voltage measurements. A secondary receiver coil, referred to as the bucking coil, is placed coaxially between the main receiver and transmitter coils with a magnetic moment orientation in opposite direction to that of the main receiver coil. The number of turns and the position of the bucking coil are such that the magnitude of the imaginary part of the voltage induced in the main receiver coil is equal to that in the bucking coil. When the complex-valued voltage induced in main receiver coil and that in the bucking coil are measured in series, the direct magnetic coupling between main receiver coil and transmitter coil is eliminated; thereby improving the sensitivity of the EMI sensor to the conductivity of surrounding volume. After eliminating the contribution due to the direct magnetic coupling, the σ_{app} (or Σ) response of the surrounding volume for the TR coupling is calculated as

$$\Sigma = \sigma_{\text{app}} = -\frac{v}{GI_{\text{T}}} \cong \sigma\left(1 - \frac{2x}{3\delta}\right), \tag{5}$$

where $v = v_{\text{R}}^{*} + v_{\text{B}}^{*}$ is the induced voltage measured in the three-coil sonde after eliminating the direct magnetic TR coupling and v_{B}^{*} is the complex-valued induced voltage in the bucking coil. I will refer the buck-corrected receiver voltage v simply as "receiver voltage" from here onward. The effect of skin depth is evident in equation 5. This above

theory is bound by the assumptions that the surrounding environment is isotropic, non-dispersive, and negligibly dielectric, and that the coils act as point dipoles.

2.2.2 Triaxial EM Induction Measurements

The WCEMIT (Figure 2.1) uses coaxial triaxial transmitter, receiver, and bucking coil systems for purposes of performing complex conductivity tensor measurements on whole core samples. Figure 2.2 shows a 24-inch-long Berea sandstone whole core sample placed coaxially inside the 20-inch-long WCEMIT conduit. A triaxial coil system comprises three collocated orthogonal coils, namely *x*-directed saddle coil, *y*-directed saddle coil, and *z*-directed helical coil. Figure 2.3a shows a COMSOL-generated model of a triaxial coil system containing one helical *z*-directed coil, one *x*-directed saddle coil, and one *y*-directed saddle coil. Figure 2.3b shows a COMSOL-generated model of a triaxial transmitter coil system (below) and a helical z-directed receiver coil (above), and Figure 2.3c shows a COMSOL-generated model of a whole core sample placed coaxially inside a triaxial transmitter coil system and a helical receiver coil. The *x*- and *y*-directed saddle coils, as shown in Figure 2.4, are created by wrapping a thin flexible circuit board around the fiberglass conduit that holds the whole core sample during tensor measurements. The *x*- and *y*-directed saddle coils have their magnetic moments directed along *x*- and *y*-axis, respectively, while the *z*-directed helical coil has its magnetic moment directed along the *z*-axis. Each saddle coil consists of m_x turns, such that the height of the *j*-th turn of the saddle coil is denoted as h_j, the coil arc radius is *a'*, and β_j' is the angle subtended by the arc of the *j*-th turn. Figure 2.5 is a sketch of single turns of each one of the pair of *x*-directed saddle coils.

The *x*- and *y*-directed saddle coils in the triaxial transmitter coil system generate transverse magnetic moments of equal magnitude, which are also equal to the magnitude

of longitudinal magnetic moment of the *z*-directed helical coil. The induced eddy currents in the surrounding volume due to an energized g-th transmitter coil subsequently induces complex-valued voltages $v^*_{\mathrm{R},k}$ and $v^*_{\mathrm{B},k}$ in the three orthogonal coils in the receiver and bucking coil systems, respectively, where subscripts g and k can be assigned as *x*-, *y*-, or *z*-directed coils. The design constraint on the saddle coils is to match the induced voltages in the saddle receiver coils to that in the helical receiver coil for a homogeneous isotropic surrounding volume.

Saddle bucking coils of magnetic moment opposite to that of saddle receiver coils are used to remove the direct coupling between saddle transmitter and receiver coils. Complex-valued induced voltages in saddle bucking coils are simultaneously measured in series with that in the corresponding saddle receiver coils. The direct coupling between helical transmitter and receiver coils is eliminated as described above for the three-coil sonde design. In the WCEMIT, the complex-valued voltages induced in one of the three collocated orthogonal coils in the receiver coil system and that induced in the corresponding coil of the bucking coil system are simultaneously measured through the input channel of the lock-in amplifier driven by an Agilent *E3630A* DC power supply.

2.2.3 Apparent Complex Conductivity Tensor

An EMI sensor based on three-coil sonde design measures the apparent complex conductivity of surrounding volume. An inversion algorithm is required to transform the apparent complex conductivity of the surrounding volume to the complex conductivity, which contains the information on effective conductivity and permittivity of the surrounding volume. Current $I_{\mathrm{T},g}$ in g-th transmitter coil induces a buck-corrected complex-valued voltage v^*_k in *k*-th receiver coil. Apparent complex conductivity measurement Σ_{gk} is the ratio of v^*_k to the mathematical product of geometrical factor of g-

th transmitter, *k*-th receiver coupling, denoted by G_{gk}, and $I_{\mathrm{T},g}$. Values of G_{gk} for *xx*, *yy*, and *zz* TR couplings are calculated using an EM forward model of the tool response, while the values of G_{gk} for rest of the 6 TR couplings, namely *xy*, *xz*, *yx*, *yz*, *zx*, and *zy*, are defined empirically (Kickhofel et al., 2010). The imaginary part of an apparent complex conductivity Σ_{gk} is referred as the X-signal X_{gk}, and the real part is referred as the R-signal R_{gk}. Therefore, R_{gk} identifies the resistive component, and X_{gk} identifies the reactive component of Σ_{gk}. The Σ_{gk} can also be expressed as the ratio of trans-impedance ($Z_{gk} = v_k^* / I_{\mathrm{T},g}$) and geometrical factor of the TR coupling G_{gk} as

$$\Sigma_{gk} = \mathrm{R}_{gk} + \mathrm{i}\mathrm{X}_{gk} = -\left(\frac{Z_{gk}}{G_{gk}}\right) = -\left(\frac{v_k^*}{G_{gk} I_{T,g}}\right). \quad (6)$$

Conventional rock formations typically are of low dielectric permittivity and non-dispersive electrical properties; therefore, they exhibit negligible phase and frequency dependence of Σ_{gk} and negligible X-signal values. Hence, conventional resistivity interpretation of the EMI sensor data generally ignores X-signal response (Anderson et al., 2006) or uses it only for skin effect correction (Mitchell, 1997). However, in my work, I measure samples exhibiting high dielectric permittivity and substantial frequency dispersion due to interfacial polarization phenomena associated with disseminated conductive minerals, clay minerals, and clay-sized particles. It is crucial for my work to account for the negative-values of X-signal response for purposes of inverting the measured complex electrical conductivity tensor, $\boldsymbol{\Sigma}$, to obtain the effective horizontal conductivity ($\sigma_{\mathrm{hor,eff}}$), horizontal permittivity ($\varepsilon_{\mathrm{hor,eff}}$), conductivity anisotropy ($\lambda_{\mathrm{c,eff}}$), and permittivity anisotropy ($\lambda_{\mathrm{p,eff}}$) of the sample placed in the tool conduit. The apparent complex conductivity tensor is a collection of apparent complex conductivity values measured for all nine TR couplings, and is expressed as

$$\boldsymbol{\Sigma} = \begin{pmatrix} \Sigma_{xx} & \Sigma_{xy} & \Sigma_{xz} \\ \Sigma_{yx} & \Sigma_{yy} & \Sigma_{yz} \\ \Sigma_{zx} & \Sigma_{zy} & \Sigma_{zz} \end{pmatrix}. \quad (7)$$

2.3 WHOLE CORE ELECTROMAGNETIC INDUCTION TOOL (WCEMIT)

The WCEMIT performs high-resolution, multi-frequency, complex conductivity tensor measurements on as-received or re-saturated whole core samples and continuous-feed cylindrical volumes at seven discrete frequencies in the EM induction frequency range of 10 kHz to 300 kHz.

2.3.1 Tool Design

The proposed apparatus comprises a 20-inch long cylindrical fiberglass sleeve (conduit) sized to fit a 4-inch-diameter, 24-inch-long geological whole core (Figure 2.2). The tubular shape of the WCEMIT conduit exhibits a strong proclivity toward flowline, continuous-feed cylindrical volume, and whole core measurements. Three orthogonal tri-axial transmitter (T or Tx), bucking (B), and receiver (R or Rx) coils are built on the outer surface of the tubular conduit (Figure 2.2). The sample to be investigated is always placed inside the apparatus conduit. A schematic of the apparatus is shown in Figure 2.6. The helical *z*-directed transmitter coil is wound with 27 AWG HML coated magnet wire. The center of this coil is designated as the apparatus origin (z=0). Similarly, the helical *z*-directed bucking and receiver coils are wrapped at z=3 inches and z=6 inches, respectively. On the other hand, the *x*- and *y*-directed saddle coil pairs are printed together on a thin flexible circuit board of length slightly longer than the circumference of one turn of the helical coil winding. Three such flexible circuit boards are wrapped at z=0, z=3, and z=6 electrically insulated about the helical coils, such that saddle coils and helical coil are collocated with and orthogonal to each other.

One complete WCEMIT measurement cycle includes nine induced voltage measurements, which are subsequently converted to apparent complex conductivity values and then to the complex conductivity tensor of the whole core sample. The tensor functionality of the tool, due to the triaxial coil systems, is sensitive to the directional nature of electrical conductivity and dielectric permittivity of rock samples similar to Schlumberger's RtScanner downhole tool. At the same time, the WCEMIT's multi-frequency functionality, owing to a selectable capacitor bank built in the transmitter (Tx) resonance circuit (Figure 2.1), is sensitive to the dielectric-dispersive characteristic of the whole cores similar to Schlumberger's DielectricScanner downhole tool. The transmitter coil system is energized at one of the 7 discrete frequencies, namely 19.6, 31.2, 41.5, 58.5, 87.6, 150, or 261 kHz, during each cycle of measurement.

2.3.2 Electronic Setup

Figure 2.1 shows the laboratory setup and Figure 2.7 shows a schematic of the laboratory setup of the WCEMIT apparatus and peripheral electronics, such as Tx resonance circuit, receiver (Rx) amplifier, switch unit, Tx pre-amplifier, and lock-in amplifier. The tri-axial transmitter coils are voltage driven by an Anfatec eLockIn204/2 lock-in amplifier at a single frequency. The tool operates at seven discrete drive frequencies. For frequencies below 10 kHz, the magnitude of induced receiver voltage drastically decreases and its phase becomes affected by environmental noise. At the other extreme, for frequencies above 300 kHz, the operating frequency approaches the resonant frequency of the transmitter coils; consequently, the coils exhibit capacitive properties that decrease the stability of the measurements. The highest frequency for exciting the transmitter coil is a factor of 2 less than the natural resonant frequency of the coil. Grounds

of various electronic equipment are brought to a common point at the lock-in amplifier BNC input to avoid ground loops in the circuitry.

The signal from the lock-in amplifier is fed to a high power audio amplifier CE1000A. Following that, the driven signal is sequentially commuted through one of the 21 resonance circuits in the Tx resonance box by an Agilent 34970A data acquisition/switch unit to energize one of the three orthogonal coils of the transmitter coil system at a specific frequency. Current flowing through the transmitter is measured via a pick-off transformer, a low drift resistor, and an AD8228 (low-gain drift precision instrumentation amplifier) within the transmitter resonance circuit by an external Agilent 34401A 6.5 digit multimeter. The energized transmitter induces complex voltages in all the three orthogonal receiver coils. The phase and amplitude of the induced receiver voltages are sequentially measured through the input channel of the lock-in amplifier by means of an amplifier powered by an Agilent E3630A dc power supply. The lock-in amplifier serves to digitally filter out all frequencies other than the specific driving frequency generated by the Tx resonance box.

For one energized transmitter coil, three apparent complex conductivity measurements are recorded using the electronic setup. The three orthogonal transmitter coils are sequentially energized by Agilent 34970A switch unit. Therefore, one WCEMIT measurement cycle generates nine apparent complex conductivity measurements that constitutes the complex conductivity tensor of a whole core sample. This complete experimental setup is automated in National Instruments LabVIEW^{TM} 8.0 script so that all of the three orthogonal receiver voltage and one transmitter current corresponding to the energized transmitter coil can be controlled, acquired, processed into impedances, and stored for post processing. A volume of approximately one cubic meter surrounding the

apparatus is cleared of conductive materials to minimize fluctuations in the background noise. Further, tightly twisted shielded cables are implemented for all connections between the apparatus and the electronics.

2.4 NUMERICAL MODEL OF THE WCEMIT RESPONSE

A numerical EM forward model of the WCEMIT response is crucial for estimating petrophysical properties and electrical properties of whole core samples from the measured complex conductivity tensor of the sample. A semi-analytical (SA) EM method was developed to perform the WCEMIT response modeling (Misra et al., 2015c) that is significantly faster than the WCEMIT simulation performed with COMSOL-based finite-element (FE) EM forward model. Both SA and FE forward models quantify the helical and saddle-type coil responses in the EM induction (1-200 kHz) and EM propagation (0.4-2 MHz) frequency ranges. For modeling purposes, a circular coil identifies a single turn of the helical coil, and each turn of the saddle-type coils is represented by a single-turn coil described by an azimuthal aperture angle β', height, and radius a' (Figure 2.5).

2.4.1 Finite-element EM Forward Model

The sequence of FE forward modeling of a physical problem is: (a) Identify the representative physics based on a set of partial differential equations (PDE) to represent the physics of the phenomena to be modeled, (b) define the geometry on which to solve the physical problem, (c) assign the material properties, which identify the constants that appear in the set of PDEs to be solved, (d) describe the boundary conditions and initial conditions of the problem, (e) choose an element type and mesh the geometry, (f) choose a solver and solve for the unknowns, and (g) post process the results.

The COMSOL AC/DC module is a powerful numerical modeling tool for finite-element EM calculations. Kennedy et al. (2011) used COMSOL 4.2a to examine the agreement between COMSOL 2D axial symmetric models, classical analytical solutions, and experimental data associated with EM induction in the frequency range of 50 Hz to 500 kHz. Santandrea and Le Bihan (2010) solved the TEAM (Testing Electromagnetic Analysis Methods) Workshop 15-1 and JSAEM (Japan Society of Applied Electromagnetic and Mechanics) 2-5 benchmark problems using COMSOL multiphysics 3D EM FE modeling formulation. I develop a COMSOL-based FE forward model to quantify the WCEMIT response to a 4-inch-diameter, 24-inch-long test volume as a function of its σ_{hor}, $\varepsilon_{\mathrm{r,hor}}$, λ_{c}, λ_{p}, θ, β, and the operating frequency. Moreover, an inversion scheme was coupled with the FE model to estimate σ_{hor}, λ_{c}, θ, and β of samples. I used COMOSL 3.5a to build this model. COMSOL was coupled with MATLAB to automate simulation of synthetic cases for various parameters. I built the entire model as a MATLAB code that interfaces with COMSOL. In comparison to the SA forward model, the FE forward model quantifies the WCEMIT response to 4-inch diameter samples of finite length of non-zero dip and azimuth. In this model, the sample is assumed to be coaxially centered inside the triaxial transmitter, bucking, and receiver coil systems, and the sample is surrounded by non-conductive air of ε_{r} of 1.

Since the energized transmitter coils are driven by sinusoidal current, a time harmonic approach is used. Moreover, in order to reduce the computational complexity of the FE model, the high number of turns of transmitter, bucking, and receiver coils are approximated as three turns distributed uniformly over the extent of the coils. The three turns of transmitter coils in the model produce an approximate magnetic field distribution in space and near the three turns of receiver and bucking coil systems. In doing so, the

physics of the tool design is honored by capturing the EM coupling of the closest and farthest turns of the transmitter coils with the closest and farthest turns of the bucking and receiver coils, respectively. Induced voltage is then simply corrected by a ratio of the number of turns in the WCEMIT to the number of turns assumed in the model.

In this model, first σ_{hor}, $\varepsilon_{\mathrm{r,hor}}$, λ_{c}, λ_{p}, θ, β and geometry of the sample is specified. A cylindrical cage of radius 0.75 inches larger than the radius of the sample is defined for purposes of grid control. The FE model generally requires a fine mesh around the coils or regions exhibiting large skin depth. Next, parameters of one transmitter and two receiver helical and saddle coils are assigned to the model, which includes number of turns, axial position, radius, and height of the coils. For saddle type coils, aperture angles need to be defined for each turn, where an aperture angle is the angle subtended by a turn of saddle type coil at the axis of the coil. Sensitivity and sonde error of direct TR coupling, namely *xx*, *yy*, and *zz*, at various frequencies are calculated based on initial model predictions for different values conductivity of the sample and operating frequencies. Sensitivity and sonde error of the rest of the TR coupling at various frequencies are estimated empirically (Kickhofel et al., 2010).

A simple non-reflection boundary condition was used in this model to avoid spurious reflections from the artificial boundary to confine the computation to a particular region around the coils. The artificial boundary surrounds the scattering region as a sphere. In published literature, various approximate boundary conditions have been implemented as non-reflecting boundary conditions. Most approximate non-reflecting boundary conditions degrade rapidly as grazing incidence is approached (Grote, 1998). The formulation used in my work requires that the ratios of the tangential components of the electric field $\boldsymbol{e}$ to that of the magnetic field $\boldsymbol{h}$ on a sphere, which identifies the artificial

boundary, surrounding the antenna are forced to have a value computed from formulas for a point magnetic dipole antenna at the center of spherical polar coordinates *r*, φ, and θ. The justification is that the fields produced by a magnetic source must approach point dipole fields at a sufficiently large distance away from the source.

It is known that the ratio $Z_s = -e_\varphi/h_\theta$, where $\boldsymbol{e}$ is electric field and $\boldsymbol{h}$ is the magnetic field, on a sphere of radius *R* is independent of magnetic moment of dipole, and independent of position on the sphere. The formula for the fields produced by a point magnetic dipole source can be found in several textbooks on electromagnetics (e.g., Stratton, 2007). The ratio Z_s can be expressed as

$$Z_s = \mathrm{i}\omega\mu R\frac{1+\mathrm{i}kR}{1+\mathrm{i}kR+(\mathrm{i}kR)^2}, \tag{8}$$

where ω is the angular frequency, μ is magnetic permeability of the medium, and *k* is the wavenumber. In COMSOL, I specify a set of electrical parameters ε_s, μ_s, and σ_s on the surface of the sphere. These parameters are internally used to compute the boundary impedance $\omega\mu_s/k_s$, where $k_s = \sqrt{-\mathrm{i}\omega\mu_s\sigma_s + \omega^2\mu_s\varepsilon_s}$. Now, I equate the boundary impedance to the computed Z_s, and assume $\mu_s = \mu$, without the loss of generality, to obtain

$$\frac{\omega\mu_s}{k_s} = \mathrm{i}\omega\mu R\frac{1+\mathrm{i}kR}{1+\mathrm{i}kR+(\mathrm{i}kR)^2}. \tag{9}$$

The condition then gives

$$\varepsilon_s = -\frac{\mathrm{real}(f^2)}{\omega^2\mu R^2}, \tag{10}$$

and

$$\sigma_s = -\frac{\mathrm{imag}(f^2)}{\omega\mu R^2}, \tag{11}$$

where

$$f = \frac{1+\mathrm{i}kR+(\mathrm{i}kR)^2}{1+\mathrm{i}kR}. \tag{12}$$

After that, the geometry is built in the model as a combination of the outer sphere, which identifies the artificial non-reflecting boundary, the cage cylinder, and the sample cylinder. Following that, all axial coils and saddle coils are built in the model. The mesh for the geometry is initialized using tetrahedral mesh elements. The quality of the meshing is crucial for a FE model simulation. Mesh size is decided to optimize the accuracy of numerical solutions within a reasonable computational time. I forced maximum mesh size of 0.4 inches on coils, 1.2 inches on the curved faces of cylindrical cage, and 2 inches on the end faces of the cylindrical cage. The meshed FE model is shown in Figure 2.8. Then, the code performs an edge analysis of the axial coil edges and horizontal and vertical edges of the saddle coil to define properties of the edges, namely edge identifier, edge type, and presence of current in the edge. Non-reflecting boundary condition is applied to the artificial boundary as a impedance boundary of ε_s and σ_s values as derived in equations 10 and 11. The remaining boundaries are defined as a continuous boundary. Finally, the permittivity and conductivity of the sample are described as tensors, and the surrounding air is assumed isotropic of ε_0 of 1 and σ of 10^{-5} S/m. Figures 2.9 and 2.10 show the modeling results of the ***b***-field and ***e***-field for an energized *z*-directed and *y*-directed transmitter coils, respectively.

2.4.2 Semi-analytic EM Forward Model

A semi-analytic (SA) forward model was applied to quantify the full-triaxial WCEMIT response to an infinitely-long, 4-inch-diameter cylindrical volume, placed in the WCEMIT conduit, as a function of its σ_{hor}, $\varepsilon_{\mathrm{r,hor}}$, λ_{c}, and λ_{p}. The SA model assumes the surrounding volume as two infinitely-long, anisotropic, axially-symmetrical, concentric cylindrical regions in electrical communication with each other. In addition, this model is used to quantify the WCEMIT response to a tilted test loop (TTL); this modeled response

is then used to calibrate the WCEMIT response. The SA model is applicable at induction frequencies as well as propagation frequencies.

In one formulation, for an infinite homogeneous medium with TI anisotropy containing a source, electric field $\boldsymbol{e}$ at any point $\boldsymbol{r_1}$ due to a source current density $\boldsymbol{j}$ at $\boldsymbol{r_2}$ can be computed analytically as

$$\boldsymbol{e}(\boldsymbol{r}_1) = -\mathrm{i}k_0 \int \bar{\bar{\Gamma}}\,(\boldsymbol{r}_1, \boldsymbol{r}_2).\boldsymbol{j}(\boldsymbol{r}_2)d^3r_2, \tag{13}$$

where $k_0 = \omega\sqrt{\varepsilon_0\mu_0}$ and $\bar{\bar{\Gamma}}$ is the Green's dyadic that can be constructed with two vector fields $\boldsymbol{m}^h$ and $\boldsymbol{n}^e$, which are derived from two scalar Hansen potentials φ^{h} and φ^{e}, respectively, expressed as

$$\boldsymbol{m}^h = \nabla \times \boldsymbol{u}_z\varphi^{\mathrm{h}}, \tag{14}$$

$$\boldsymbol{n}^e = \frac{1}{k_0}\nabla \times \bar{\bar{\mu}}^{-1}.(\nabla \times \boldsymbol{u}_z\varphi^{\mathrm{e}}), \tag{15}$$

where $\bar{\bar{\mu}}$ is magnetic permeability tensor of the medium and $\boldsymbol{u}_z$ is the z-directed unit vector in cylindrical coordinates. φ^{h} and φ^{e} can be expressed as the solutions of the scalar Helmholtz equation in cylindrical coordinates. In the second formulation, for each source-free homogeneous anisotropic cylindrical subregions, the electric field $\boldsymbol{e}$ and magnetic field $\boldsymbol{h}$ are expressed as linear combinations of vector fields $\boldsymbol{m}^h$ and $\boldsymbol{n}^e$. Such an expression has several unknown coefficients.

The two above-mentioned formulations are compared on the cylindrical surface containing the transmitter coils to obtain the discontinuity in the values of unknown coefficients of the linear combination, which was obtained in the second formulation, due to current density in the transmitter coils. Next, Maxwell's equations are solved to obtain the values for the unknown coefficients of the linear combination, which was obtained in the second formulation. The following boundary conditions are used to solve the system of Maxwell's equation: (a) continuity of tangential components of $\boldsymbol{e}$ and $\boldsymbol{h}$ at the outer

surface of the inner cylinder that identifies the whole core sample, (b) no incoming wave at the outermost surface of the outer cylinder, and (c) finite solution along the entire *z*-axis. After obtaining the values of unknown coefficients, the voltage induced in a receiver coil is obtained as a volume integral along the geometry of the receiver coil expressed as

$$v_{\mathrm{R}} = Z_0 \oint \boldsymbol{e}.d\boldsymbol{r} = Z_0 \int \chi_{\mathrm{R}} . \boldsymbol{e} d^3 r, \tag{16}$$

where $Z_0 = \sqrt{\mu_0/\varepsilon_0} = 376.7$ ohms is the impedance of free space. A MATLAB-based adaptive Lobatto Quadrature method (Gander and Gautschi, 1998) was implemented to solve the integral forms.

2.4.3 Model Validation

The accuracy of the FE model is confirmed by comparing model predictions and analytical solution for a circular loop of current in an infinite isotropic medium at several frequencies in the range of 10 to 300 kHz. Analytical solution to this physical problem is derived by Moran and Kunz (1962). For further validation of the FE model, I compute the real part of the induced voltage response of the three direct couplings, namely *xx*, *yy*, and *zz*, for various values of conductivity of a 24-inch-long, 4-inch-diameter cylindrical volume (sample) placed inside the coils. The log-log plot in Figure 2.11 depicts a linear relationship of the real part of the induced voltage response of *zz*-coupling to the conductivity of the sample for conductivity values of 0.1, 1, and 10 S/m, respectively. This observed linear relationship is analogous to the linearity of induced voltage and conductivity of surrounding medium for a two-coil sonde configuration assuming point dipole approximation, as derived by Moran and Kunz (1962). The induced voltage responses of *xx*- coupling and *yy*-coupling also display linear relationships with conductivity of the sample. Such linear relationships have been used as a benchmark for the validity of the predictions of numerical models of EMI coils. The slopes of the straight lines plotted in

Figure 2.11 are equal to the geometrical factor (Table 2.1) for the zz-coupling at the seven discrete frequencies, namely 19.6, 31.2, 41.5, 58.5, 87.6, 150.4, and 261 kHz. The computed values of geometrical factors for *zz*-coupling and *yy*-coupling of 1.5×10^{-4} and 3.6×10^{-5} m.Ω/s, respectively, at 58.5 kHz is close to the values of geometrical factors for *zz*-coupling and *yy*-coupling of 1.42×10^{-4} and 3.54×10^{-5} m.Ω/s, respectively, at 51.28 kHz obtained by Kickhofel et al. (2010).

For further validation of the FE model, I investigated the relationship of the geometrical factor of the *zz*-coupling with the operating frequency. Moran and Kunz (1962) showed analytically that the geometrical factor of the *zz*-coupling of a two-coil sonde in an isotropic homogeneous medium is directly proportional to the square of the operating frequency. Although the FE model is for a cylindrical sample placed inside a three-coil sonde, the log-log plot in Figure 2.12 illustrates that the geometrical factor of *zz*-coupling computed based on the FE model predictions of the WCEMIT response to 1-S/m conductivity cylindrical volume is directly proportional to the square of the operating frequency. Another important validation involves comparing FE model predictions against the Maxwell-Garnett effective medium (Giordano, 2003) predictions of the effective conductivity of a 1-S/m-conductivity 4-inch diameter cylindrical sample containing homogeneously distributed spheres for different values of conductivity and radius of the spherical inclusion phase. Figure 2.13 illustrates the COMSOL-generated meshed model of the 4-inch-diameter cylinder containing 0.35-inch-radius spheres. Figure 2.14 indicates a good agreement between the effective medium predictions and FE model predictions for conductivity values of spherical inclusions in the range of 0.1 S/m to 100 S/m and for radius of spherical inclusions in the range of 0.35 to 0.6 inches. The observed agreement however deteriorates for spherical inclusion phases of higher conductivity and larger radius due to

inherent discrepancies of the Maxwell-Garnett effective medium predictions arising from the EM interactions of the inclusions and due to the high contrast in electrical properties of the inclusion and host phase.

After validating the FE model predictions, I compare the SA model predictions against that of the FE model for purposes of validating the SA model predictions. First, the log-log plot in Figure 2.15 shows the good agreement between both the model predictions of the real part of the induced voltage response of *zz*-coupling to three cylindrical volumes of conductivity of 0.1, 1, and 10 S/m, respectively, for different values of the operating frequency. Further, the SA model predictions of R- and X-signal responses *yy*-coupling and *zz*-coupling to two cylindrical volumes of σ_{hor} of 1 S/m, ε_{r} of 10^5, and dielectric loss factor (δ) of 0 (Figure 2.16) and 0.1 (Figure 2.17), respectively are compared with that of the FE model. The SA model predictions for both of the cases match very well with the FE model predictions for both the *yy*-coupling and *zz*-coupling responses, as illustrated in Figures 2.16 and 2.17.

Figure 2.16 depict the FE and SA model predictions of R- and X-signal response to a sample of σ_{hor} of 1 S/m, ε_{r} of 10^5, and δ of 0. Both the models in Figure 2.16 predict large negative values of the X-signal response, varying from -0.01 S/m to -1.5 S/m with the variation in the operating frequency from 19.6 kHz to 261 kHz. Moreover, Figure 2.16 indicates that an order of magnitude increase in the operating frequency produces a two-order of magnitude increase in X-signal response. Such a substantial frequency dispersion in X-signal is a consequence of the large value of the relative permittivity of the sample. Nonetheless, in Figure 2.16, the frequency dispersion in R-signal response is negligible because the δ of the medium is assumed to be zero. In contrast, the FE and SA model predictions of R- and X-signal response to a sample of σ_{hor} of 1 S/m, ε_{r} of 10^5, and δ of

0.1, as presented in Figure 2.17, indicate a large frequency dispersion in R-signal response as a consequence of the non-zero δ of the sample. In addition, the magnitude of R-signal response increases with an increase in the operating frequency. On comparing X- and R-signal responses depicted in Figures 2.16 with that in Figure 2.17, I infer that variation in δ has negligible influence on the X-signal response, whereas variation in ε_r has negligible influence on the R-signal. Due to the absence of electrical and dielectric anisotropy in the samples, the computed *yy*-coupling response matches very well with the computed *zz*-coupling responses.

2.5 WCEMIT CALIBRATION

During the construction of coils, the bucking coil system is translated along the tool axis until the complex-valued voltage response on the *z*-directed receiver coil for an energized *z*-directed transmitter is at a minimum, which ensures that the direct magnetic field coupling between the two coils is minimized for purposes of an improved signal-to-noise ratio. The *z*-directed buck coil is then fixed at that position. Following that, the saddle coils of the bucking coil system are slightly rotated about the tool axis to balance the complex-valued voltage response of the *x*-directed and *y*-directed receiver coils for the energized *z*-directed transmitter coil. The nine TR coupling responses are then calibrated using the tilted test loop (TTL) method to find the gain amplitude and phase corrections (Kilic, 2014).

The WCEMIT response to a TTL provides reference measurements for calibrating the nine TR coupling responses. The TTL comprises a copper wire in series with a resistor of known impedance oriented at a 45°-dip on an 8-inch-diameter tube coaxial to the tool axis. Figure 2.18 shows the laboratory set-up of the WCEMIT placed coaxially inside the 8-inch-diameter tube that holds the TTL at 45°-dip. The impedance of the resistor changes

with operating frequency; therefore I measure the frequency-dependent impedance of the resistor at various frequencies (Table 2.2) using a calibrated HP4194A impedance/gain-phase analyzer. These measured impedance values for the resistor is used in the SA model to quantify the WCEMIT response to the TTL for various positons of the TTL at azimuthal orientations of the TTL of 0°, 45°, and 90°. Using the SA model predictions, I design the calibration process such that all the nine responses of the WCEMIT can be excited with the TTL at azimuths of 0°, 45°, and 90° by placing the TTL at specific distances away from the center of transmitter coil along the tool axis. The various azimuthal orientations and positions of the TTL for purposes of calibrating the nine TR coupling responses are shown in Table 2.3.

To obtain the gain correction for a specific TR coupling, the TTL is positioned and oriented as displayed in Table 2.3 for the corresponding TR coupling. Next, the impedance of TTL with respect to the corresponding TR coupling is measured using the WCEMIT. Figure 2.19 shows a schematic of the TTL translation and azimuthal orientation about the WCEMIT. The complex-valued gain required for calibrating a specific TR coupling is expressed as

$$g_{gk} = \frac{Z_{gk}^{mod}}{Z_{gk}^{meas} - Z_{gk}^{air}}, \tag{17}$$

where g denotes the energized g-directed transmitter, k denotes the k-directed receiver at which the induced voltage is measured, Z_{gk}^{mod} is the theoretical impedance response calculated using the SA model of the gk-coupling response, Z_{gk}^{meas} is the measured value of raw impedance of the TTL at a particular location and orientation with respect to the gk-coupling, and Z_{gk}^{air} is the measured value of raw impedance of the background with respect to the gk-coupling. This complex-valued gain is unique to the apparatus for a given TR coupling and operating frequency. Tables 2.4 and 2.5 contain the amplitude and phase of

gain correction derived for the nine TR couplings at seven discrete operating frequencies, namely 19.6, 31.2, 41.5, 58.5, 87.6, 150.4, and 261 kHz. Importantly, the amplitude of gain correction values obtained at operating frequencies of 31.2, 41.5, 58.5, and 87.6 kHz are close to 1, which indicates the reliability of this calibration process, wherein the measured impedance values are compared against the SA model predictions.

To calibrate both the amplitude and the phase of subsequent WCEMIT apparent complex conductivity measurements, the complex-valued gain correction is applied as

$$\Sigma_{gk} = g_{gk}\left(\frac{Z_{gk}^{meas} - Z_{gk}^{air}}{G_{gk}}\right), \tag{18}$$

where $\Sigma_{gk}$is the apparent complex conductivity of the sample with respect to the *gk*-coupling, G_{gk} is the geometrical factor of the *gk*-coupling, g_{gk} is the complex-valued gain correction for the *gk*-coupling, and Z_{gk}^{air} is the measured value of raw impedance of the background with respect to the *gk*-coupling.

2.6 CONCLUSIONS

I described the theory, tool design, and electronic setup of the WCEMIT capable of non-invasive, non-contact, high-resolution, multifrequency, complex conductivity tensor measurements on whole core samples. I developed and validated a COMSOL-based finite-element EM forward model and a MATLAB-based semi-analytic EM forward model of the WCEMIT response. Predictions of the finite-element forward model match those of the semi-analytic forward model. Finally, the nine TR coupling responses were calibrated using a tilted-test-loop method at seven discrete frequencies, namely 19.6, 31.2, 41.5, 58.5, 87.6, 150.4, and 261 kHz.

Improved resistivity interpretation in shaly, sand-shale laminated, source rock, and mudrock formations requires high-resolution non-invasive whole core measurement

techniques. The developments in this chapter encourage laboratory investigation of petrophysical applications of this new electromagnetic measurement method.

Table 2.1: The values geometrical factor *K* of yy-coupling and zz-coupling at various frequencies.

	Frequency (kHz)						
***K* (m.Ω/S)**	**19.6**	**31.2**	**41.5**	**58.5**	**87.6**	**150.4**	**261**
yy	4.0×10^{-6}	1.0×10^{-5}	1.8×10^{-5}	3.6×10^{-5}	8.0×10^{-5}	2.4×10^{-4}	7.1×10^{-4}
zz	1.6×10^{-5}	4.1×10^{-5}	7.4×10^{-5}	1.5×10^{-4}	3.3×10^{-4}	9.7×10^{-4}	2.9×10^{-4}

Table 2.2: TTL impedance at various frequencies.

Frequency (kHz)	**TTL impedance (Ω)**
11.094	10.0173 - 0.0655i
19.58	10.0098 - 0.0656i
31.267	10.0082 - 0.1746i
41.54	10.0116 - 0.0870i
58.5	10.0082 - 0.1746i
88.119	10.0085 - 0.3495i
150.424	10.01167 - 0.5175i
261.347	10.0141 - 1.5280i

Table 2.3: Azimuthal orientation and location of the TTL for purposes of calibrating specific TR coupling responses.

TR Coupling	**Azimuth (°)**	**TTL-location (in.)**
xx	0	3.10
xy	45	3.20
xz	0	2.42
yx	45	3.20
yy	90	3.10
yz	90	2.42
zx	0	3.82
zy	90	3.82
zz	0	3.11

Table 2.4: Amplitude and phase (°) of gain corrections for the nine TR couplings at operating frequencies of 19.6, 31.2, 41.5, and 58.5 kHz.

	Frequency (Hz)							
	19.6		**31.2**		**41.5**		**58.5**	
TR Coupling	**Gain amp.**	**Gain phase**	**Gain amp.**	**Gain phase**	**Gain amp.**	**Gain phase**	**Gain amp.**	**Gain phase**
xx	1.0	154.8	1.0	142.0	1.1	118.3	1.2	93.5
xy	3.2	179.2	1.0	142.2	1.2	93.5	1.2	93.5
xz	3.0	180.0	0.9	140.0	1.1	92.2	1.1	92.2
yx	3.3	180.0	0.2	104.0	1.2	93.9	1.2	93.9
yy	1.0	153.6	1.0	141.4	1.1	117.6	1.2	93.3
yz	3.0	179.1	0.9	139.7	1.1	92.6	1.1	92.6
zx	2.9	-20.3	0.9	-83.1	1.1	-119.5	1.1	-119.5
zy	2.9	-19.1	0.9	-82.6	1.1	-120.4	1.1	-120.4
zz	0.9	-25.9	0.9	-69.0	0.9	-86.7	1.0	-111.6

Table 2.5: Amplitude and phase (°) of gain corrections for the nine TR couplings at operating frequencies of 87.6, 150.4, and 261 kHz.

	Frequency (Hz)					
	87.6		**150.4**		**261.0**	
TR Coupling	**Gain amp.**	**Gain phase**	**Gain amp.**	**Gain phase**	**Gain amp.**	**Gain phase**
xx	1.4	100.9	2.2	4.7	3.8	-51.8
xy	1.4	101.1	0.4	-57.8	3.5	-52.1
xz	1.3	98.8	0.6	-62.2	5.3	-56.5
yx	1.4	100.6	0.4	-74.0	3.7	-68.2
yy	1.4	95.5	2.2	-2.7	3.6	-66.9
yz	1.3	101.9	0.5	-77.1	4.7	-71.4
zx	1.2	-99.5	0.3	148.0	3.1	153.7
zy	1.2	-98.4	0.4	-177.1	3.5	-171.4
zz	1.1	-95.4	1.8	174.1	2.8	147.6

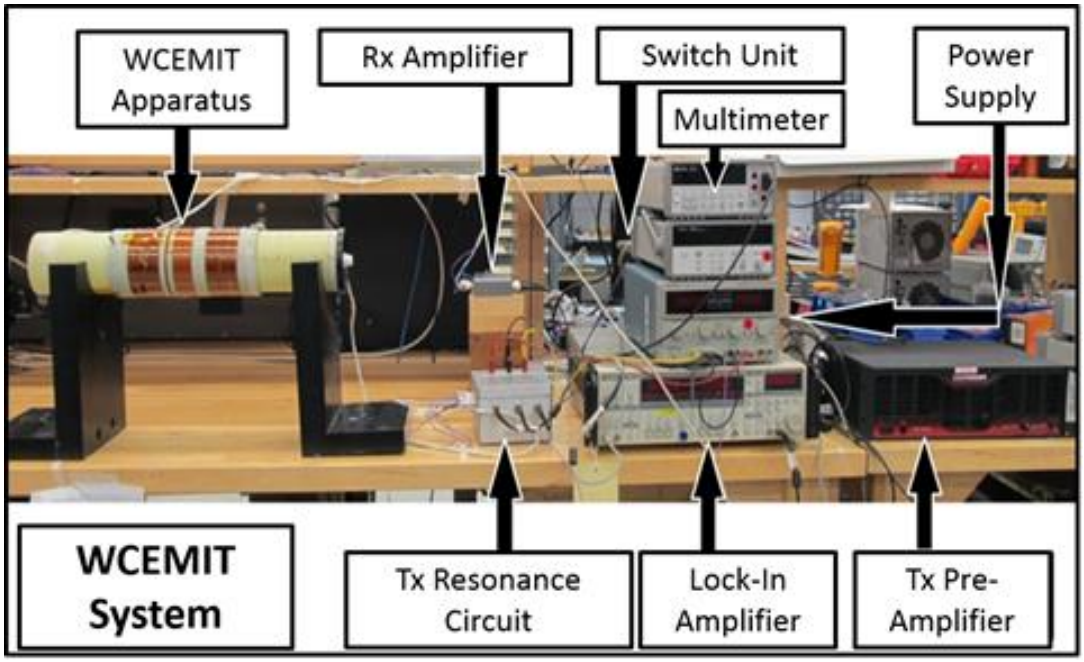

Figure 2.1: Photograph of the WCEMIT comprising a 20-inch-long WCEMIT conduit, coil systems, and peripheral electronics.

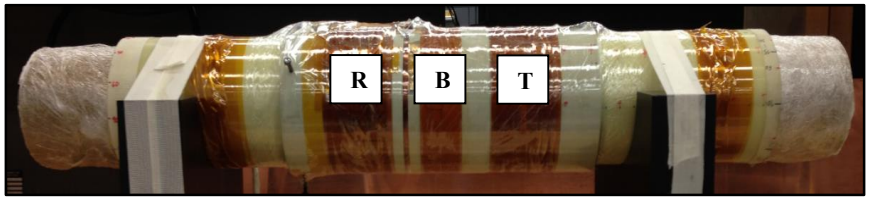

Figure 2.2: Photograph of a Berea sandstone whole core placed in the 4-inch-inner-diameter, 20-inch-long WCEMIT conduit. Letters R, B, and T identify orthogonal receiver, bucking, and transmitter coil systems, respectively.

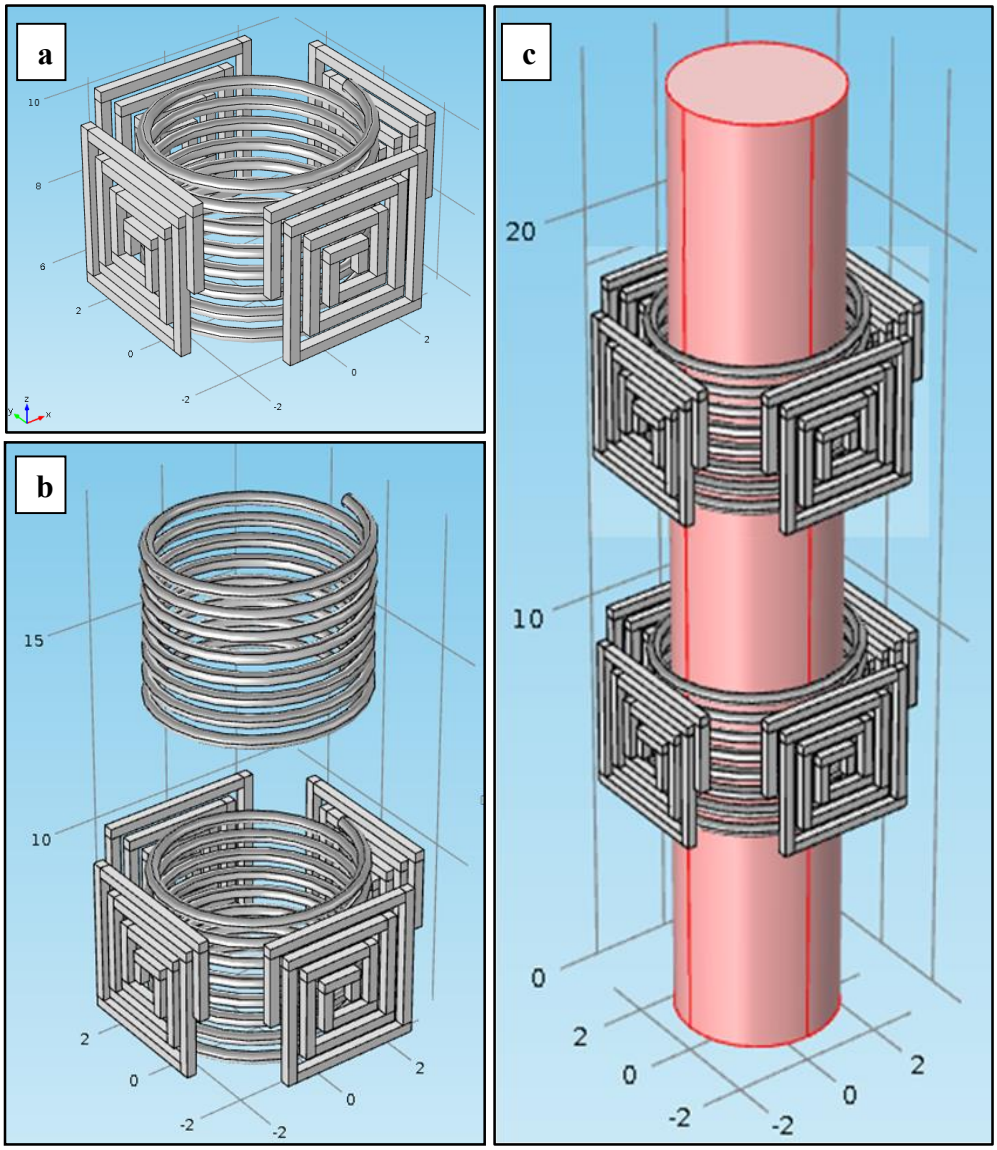

Figure 2.3: COMSOL-generated model of (a) a simplified triaxial coil system containing one helical *z*-directed coil, one *x*-directed saddle coil, and one *y*-directed saddle coil, (b) a simplified triaxial transmitter coil system (below) and a helical z-directed receiver coil (above), and (c) a whole core sample placed coaxially inside simplified triaxial transmitter (below) and receiver (above) coil systems.

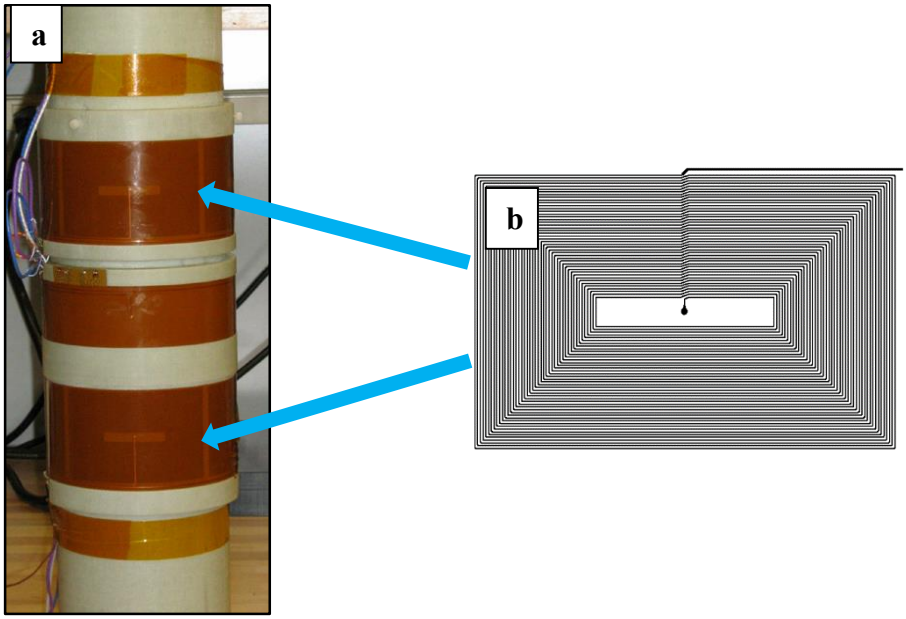

Figure 2.4: (a) Photograph of the WCEMIT shows one of the pair of *x*-directed transmitter saddle coils (below) and that of the *x*-directed receiver saddle coils (above), as indicated by blue arrows. (b) A zoomed-in schematic of a saddle coil.

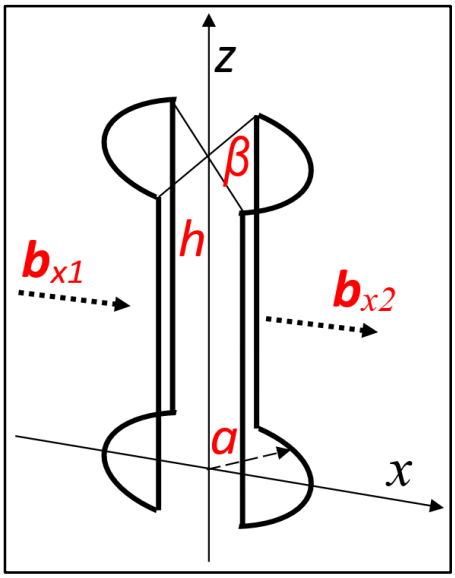

Figure 2.5: A sketch of single turns of each one of the pair of *x*-directed saddle coils, where the height of the single turns is *h*, the coil arc radius is *a*, β is the angle subtended by the arc of the single turns, and $\boldsymbol{b}_{x1}$ and $\boldsymbol{b}_{x2}$ are the magnetic moments of each one of the pair of x-directed saddle coils.

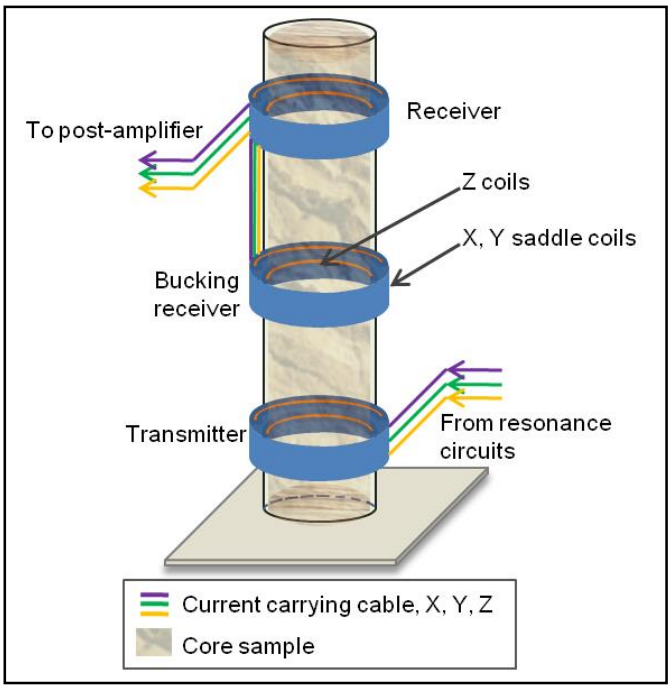

Figure 2.6: A schematic of the WCEMIT, where the fiberglass sleeve between the coils and the whole core sample is made transparent to show a 4-inch-diameter whole core sample.

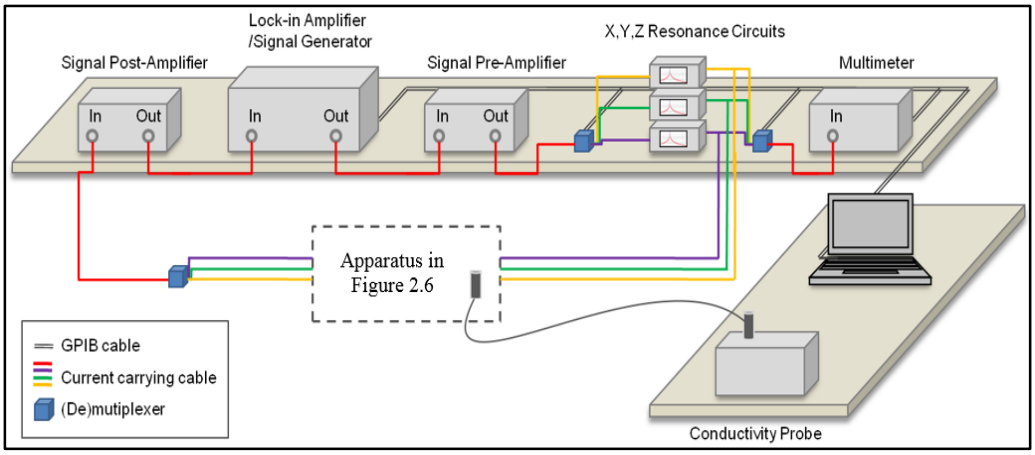

Figure 2.7: A schematic of the laboratory setup for measuring complex conductivity tensor using the WCEMIT.

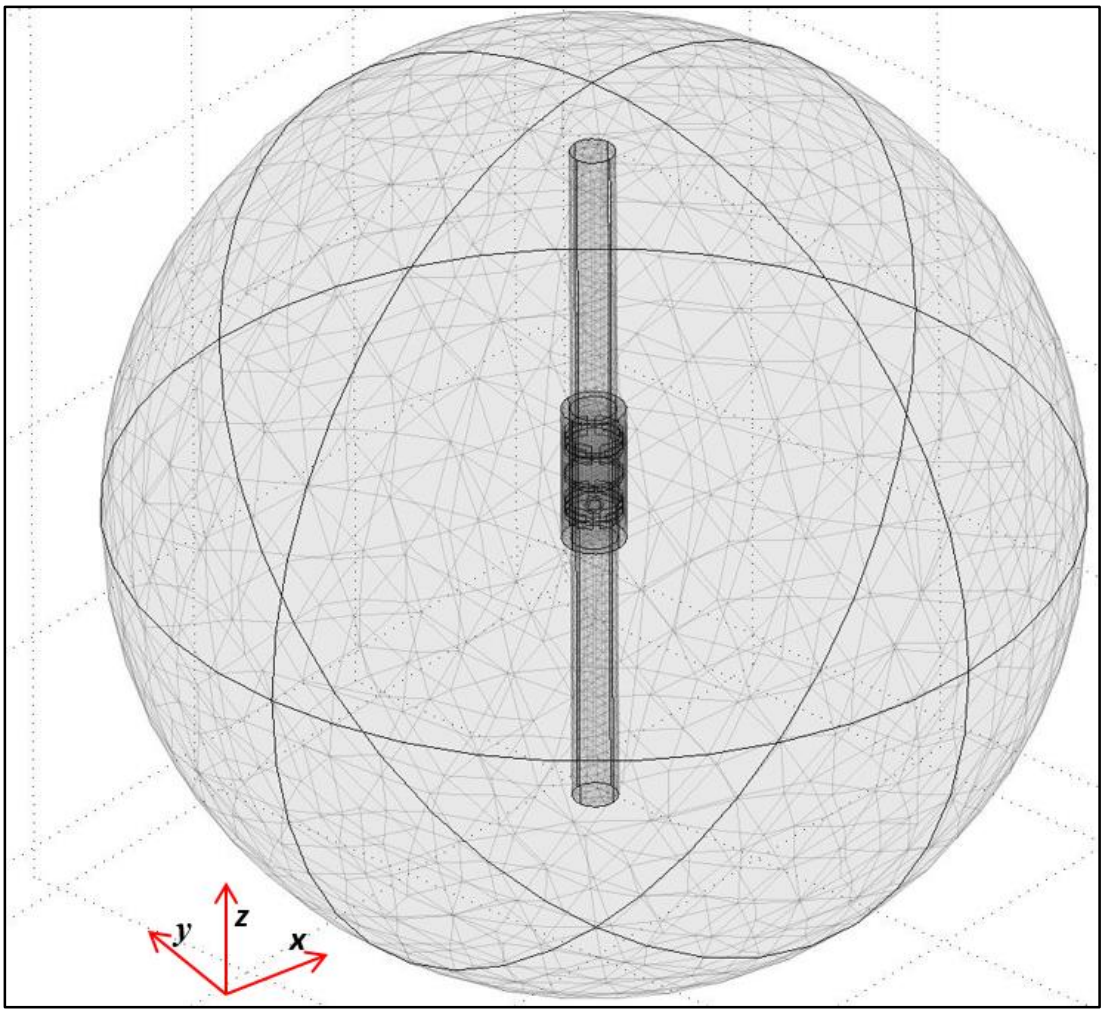

Figure 2.8: A COMSOL-generated meshed model of the WCEMIT. The figure depicts the outer artificial non-reflecting boundary, the triaxial transmitter, receiver, and bucking coil systems, and the 4-inch-diameter, 20-inch-long cylindrical volume identifying the whole core sample.

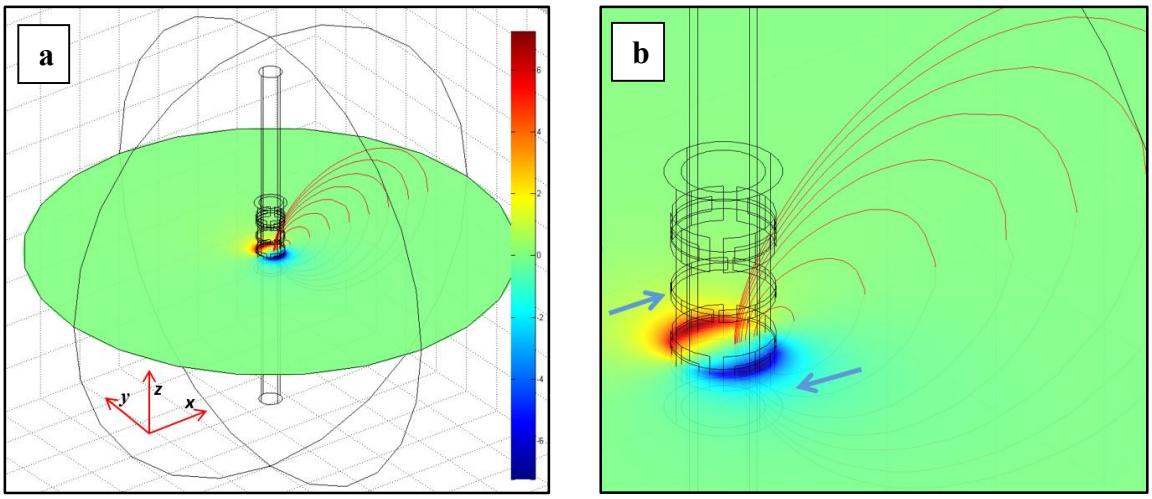

Figure 2.9: (a) FE model results for an energized *z*-directed transmitter coil, where the streamline track the ***b***-field in the *zx*-plane and the slice of *yx*-plane, in green, shows the magnitude of the imaginary part of *x*-component of the ***e***-field, shown by arrows, as color map. (b) A zoom-in around the coils of the FE model results.

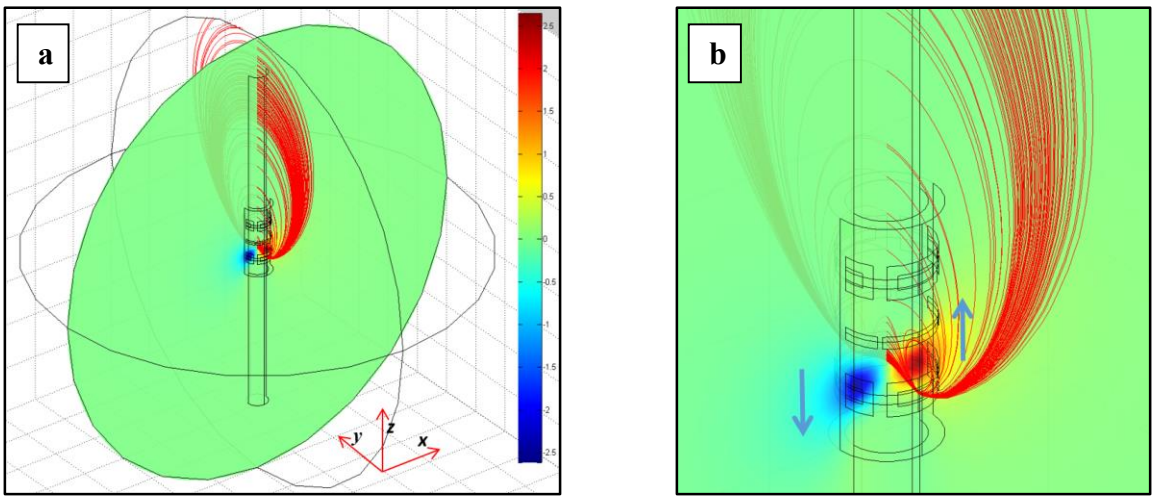

Figure 2.10: (a) FE model results for an energized *y*-directed transmitter coil, where the streamline track the ***b***-field in the *zy*-plane and the slice of *zx*-plane, in green, shows the magnitude of the imaginary part of *z*-component of the ***e***-field, shown by arrows, as color map. (b) A zoom-in around the coils of the FE model results.

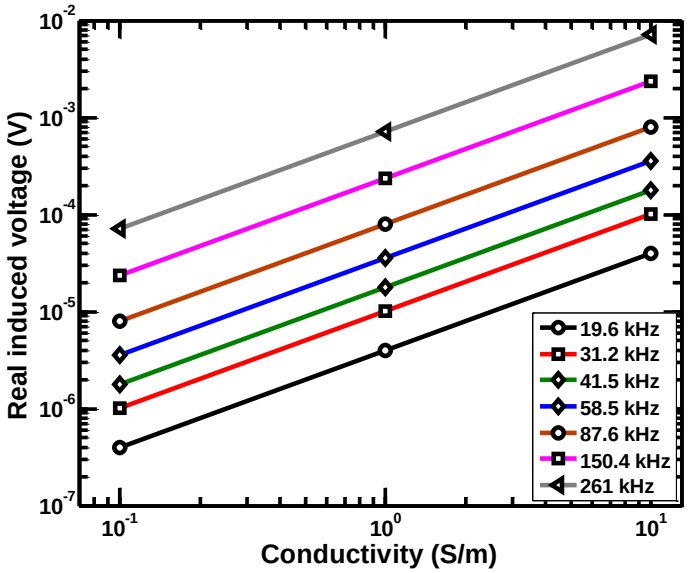

Figure 2.11: FE model predictions of the real part of the buck-corrected induced voltage response of *zz*-coupling to three isotropic cylindrical volumes of σ_{hor} of 0.1, 1, and 10 S/m, respectively, computed at 19.6, 31.2, 41.5, 58.5, 87.6, 150.4, and 261 kHz.

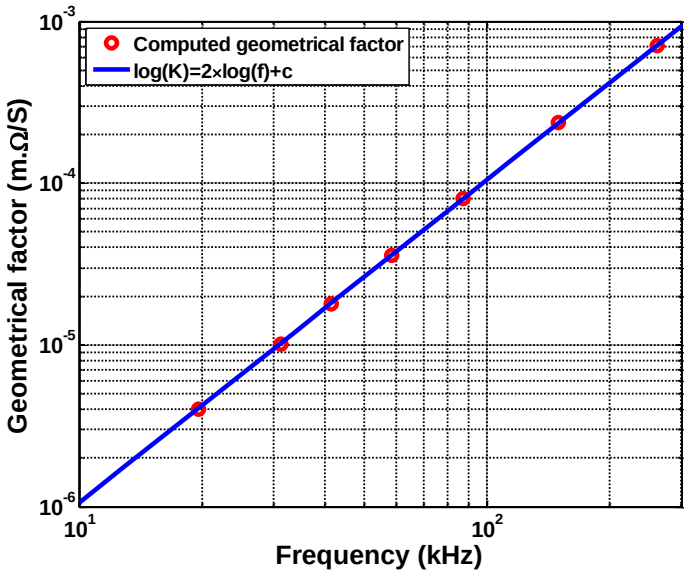

Figure 2.12: FE model predictions of the geometrical factor of the zz-coupling as a function of operating frequency.

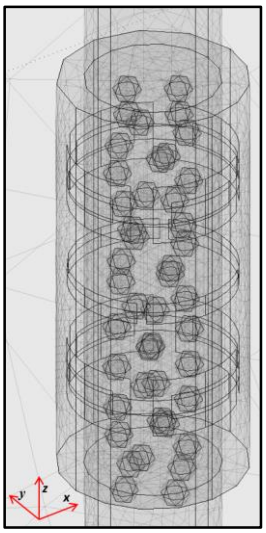

Figure 2.13: A COMSOL-generated meshed model of the 4-inch-diameter isotropic cylinder containing randomly distributed 0.35-inch-radius isotropic spheres placed inside the triaxial transmitter, receiver, and bucking coil systems.

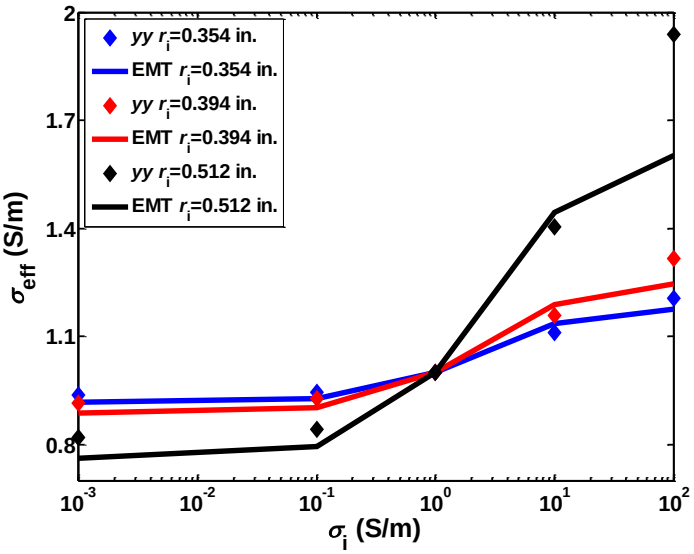

Figure 2.14: Comparison of the FE model predictions against the Maxwell-Garnett effective medium predictions of effective conductivity of a 1-S/m-conductivity cylindrical volume containing randomly distributed spheres at 58.5 kHz for spheres of 0.001, 0.1-, 1-, 10-, or 100-S/m-conductivity. Both the cylindrical volume and the spheres have relative permittivity of 1. The FE model predictions are for the *yy*-coupling response.

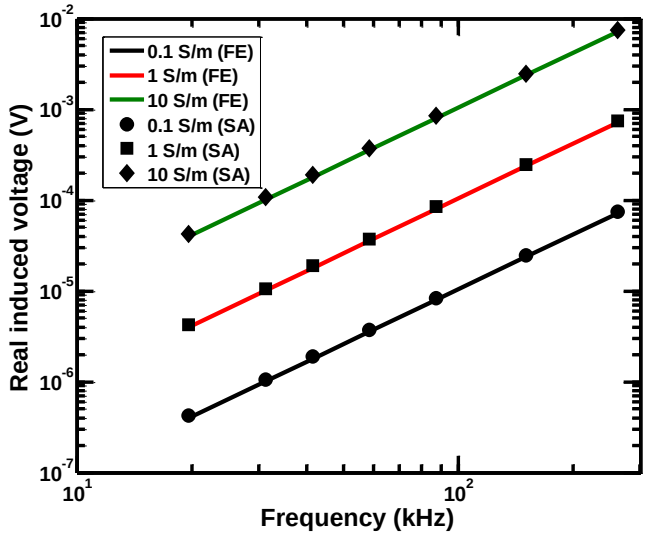

Figure 2.15: Comparison of the SA model predictions against the FE model predictions of the real part of the induced voltage response of *zz*-coupling to three isotropic cylindrical volumes of σ_{hor} of 0.1, 1, and 10 S/m, respectively, computed at 19.6, 31.2, 41.5, 58.5, 87.6, 150.4, and 261 kHz.

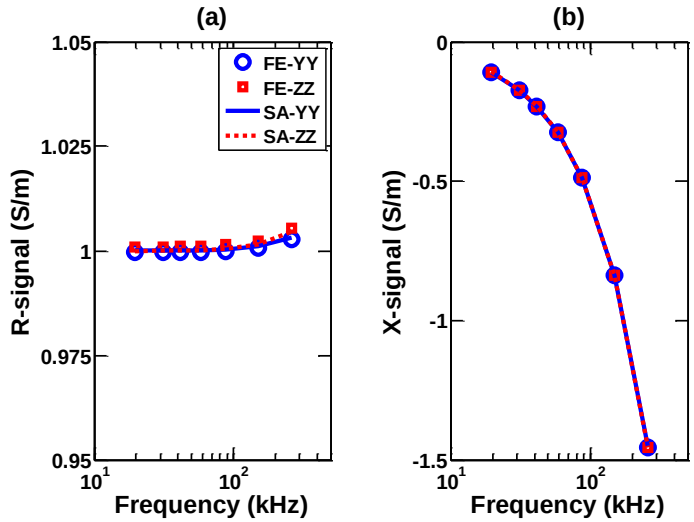

Figure 2.16: Comparison of the SA model predictions against the FE model predictions of (a) R-signal and (b) X-signal responses of *yy*-coupling and *zz*-coupling to isotropic cylindrical volume of σ_{hor} of 1 S/m, ε_{r} of 10^5, and δ of 0 computed at 19.6, 31.2, 41.5, 58.5, 87.6, 150.4, and 261 kHz.

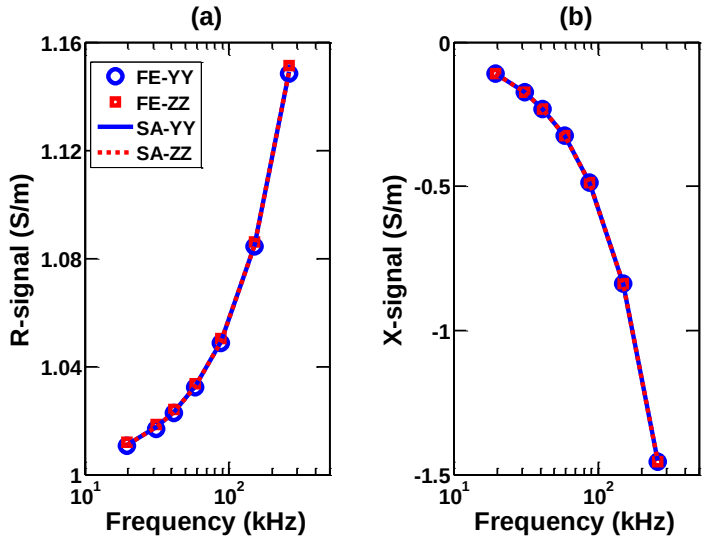

Figure 2.17: Comparison of the SA model predictions against the FE model predictions of (a) R-signal and (b) X-signal responses of *yy*-coupling and *zz*-coupling to isotropic cylindrical volume of σ_{hor} of 1 S/m, ε_{r} of 10^5, and δ of 0.1 computed at 19.6, 31.2, 41.5, 58.5, 87.6, 150.4, and 261 kHz.

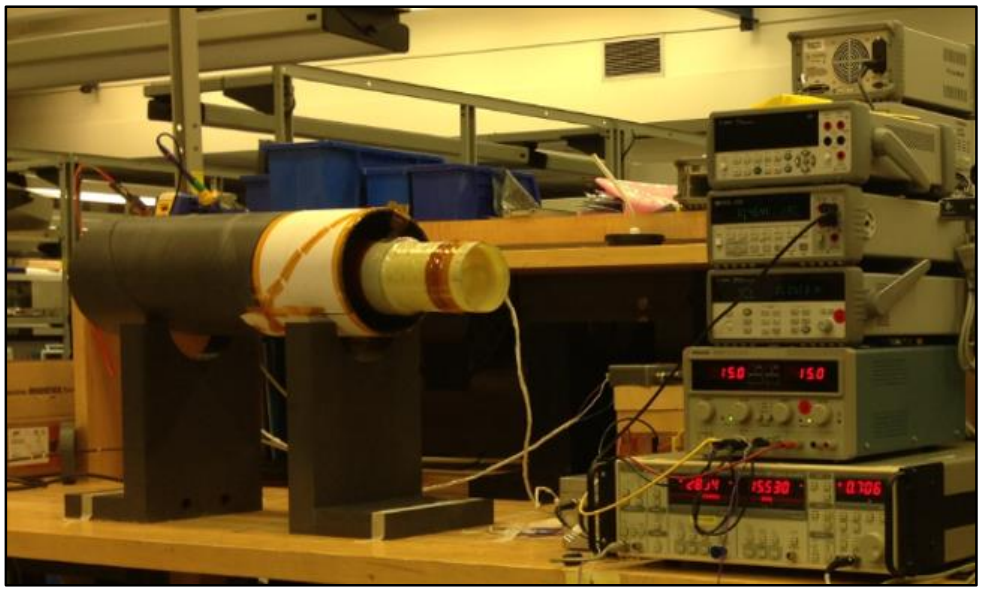

Figure 2.18: Laboratory set-up of the WCEMIT placed coaxially inside an 8-inch-diameter tube that holds the tilted test loop (TTL) at a 45°-dip.

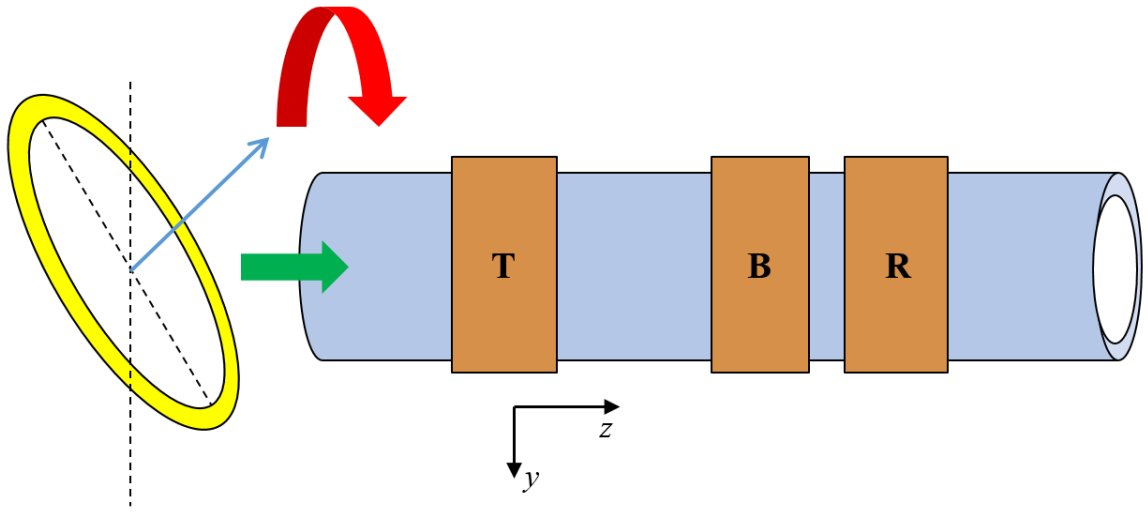

Figure 2.19: The TTL (yellow) is placed coaxially around the WCEMIT such that the dip of the TTL, which is the angle between the direction of magnetic moment of the TTL (blue arrow) and the *z*-axis, is 45°, and the azimuthal orientation (red arrow) of the TTL, which is the angle between the direction of magnetic moment of the TTL (blue arrow) and the *x*-axis, is either 0°, 45°, or 90°. The TTL translates along the tool axis (*z*-axis, green arrow).

Chapter 3: Petrophysical Applications of Multi-Frequency Inductive-Complex Electrical Conductivity Tensor Measurements on Whole Core Samples

Until now, electrical measurement methods on whole core samples so far have not been used for purposes of laboratory-based petrophysical characterization. In this chapter, I use the laboratory apparatus WCEMIT, described in Chapter 2, to measure the multi-frequency inductive-complex electrical conductivity tensor of whole core samples of various rock facies. First, the WCEMIT measurements are validated by comparing the WCEMIT responses to various synthetic samples against the numerical predictions of the semi-analytic (SA) EM forward model, introduced in Chapter 2. I then invoke an inversion scheme that processes WCEMIT measurements to estimate the electrical properties of natural and synthetic whole core samples in the EM induction frequency range of 10 kHz to 300 kHz. Finally, the Archie's equation, laminated sand-shale model, tensor resistivity model, and Maxwell-Garnett effective medium model are implemented for estimating petrophysical properties of the whole core samples of various rock facies. I also apply the SA forward model to investigate petrophysical applications of the WCEMIT measurements on whole core samples exhibiting large dielectric permittivity, permittivity anisotropy, dielectric loss factor, and frequency dispersive dielectric properties. Further, I invoke the finite-element (FE) EM forward model, introduced in Chapter 2, to investigate a whole core logging method that will improve the resistivity characterization of turbiditic and multi-layered formations.

3.1 INTRODUCTION

The primary objective of this chapter is to present the petrophysical applications of the WCEMIT through laboratory and numerical modeling investigations. I claim that

electrical measurements of as-received or cleaned whole core samples using the non-contact and non-invasive electromagnetic induction technique of the WCEMIT will substantially improve the subsurface resistivity interpretation. Existing laboratory measurements of electrical properties rely on galvanic measurements on core plugs. In complex lithologies, core plugs do not preserve the bulk electrical properties of the formation, such as anisotropy, Archie's porosity and water saturation exponent, and dielectric dispersion parameters. As described in Chapter 2, galvanic methods also suffer from other issues that adversely affect the accuracy of estimation of electrical properties.

The API recommended practice for core analysis procedure (RP40, 1960) states that whole cores are essential in vuggy carbonates, fractured reservoirs, and conglomerates, where significant large scale heterogeneity exists. Keelan (1982) listed a comparative data to highlight the need for whole core measurements in quantifying fracture effects. He summarized that the sample size should be such that the total pore space is small compared to the bulk volume, and that any estimations of directional properties, such as resistivity and permeability, are better represented by measuring whole cores instead of core plugs. Bergosh et al. (1985) mentioned that core plug measurements rarely capture fracture effects and are unrepresentative of fractured formations due to the limited sample size of core plugs. Additionally, the permeability anisotropy and variation in fluid distribution reduce the accuracy of core plug measurements. Honarpour et al. (2003) emphasized that whole core analysis is critical to characterizing porosity and directional permeability in heterogeneous, fractured, and anisotropic rocks because small-scale heterogeneity is not appropriately represented in plug measurements. They demonstrated that the whole core permeability measurements are better representative of heterogeneous carbonate formations compared to core plug measurements because they correctly average the high

and low permeability zones into overall volume. The greatest advantage of electrical measurements on whole cores is obtaining a representative porosity exponent in heterogeneous rocks (Honarpour et al., 2003).

Commercial labs have limited capabilities to clean and prepare resaturated whole core samples. They perform only selected conventional core analyses on whole core samples, such as Computer Tomography (CT) and X-ray fluoroscopy. Special core analysis capabilities for analyzing whole core samples are rare (Honarpour et al., 2003). Jackson et al. (2006) developed the first electromagnetic induction device that is capable of non-invasive, non-contact whole core resistivity measurement, thereby generating continuous resistivity logs of whole cores. Ehrenberg (2007) found that, for carbonates, the estimated values of porosity of whole cores were systematically lower than those of core plugs, whereas estimated permeability values of whole cores were generally higher than those of core plugs. More recently, Mohamed et al. (2010) stated that whole core samples are as appropriate as 1.5”×3” core plugs for use in laboratory measurements of porosity, permeability, electrical properties, capillary pressure, and relative permeability. They observed that core plug measurements were highly variable in carbonate formations. They estimated whole core formation resistivity factors for selected whole cores at ambient and overburden stress, and they reported that local heterogeneity was better represented and averaged on the whole core measurements than on core plug measurements. Thus, whole core measurements of electrical properties leads to improved confidence in volumetric and reserve estimates (Mohamed et al., 2010). Finally, core plugs do not capture the effects of dip and azimuth. WCEMIT measurements enable the estimation of dip and azimuth that can improve the description of depositional environment and mapping overall structural features of a formation.

Limitations of using the WCEMIT for whole core analysis includes issues with cleaning the whole cores; nonetheless, gas-driven solvent extraction is the most common method used for whole core cleaning. Issues with whole core cleaning are severe for vuggy whole cores, where the mud system can penetrate deeply into rock and adversely impact the porosity and permeability. Extensive quality control must be enforced to ensure accurate data from a whole core analysis. Also, the WCEMIT measurements on as-received whole core samples require implementation of a forward model and an inversion scheme (e.g., Misra et al., 2013) to correct for the effects of invasion, core cutting, and core surfacing on the fluid distribution in the whole core samples.

In this chapter, I first validate the WCEMIT measurements by comparing the measured values against the model predictions. Several types of synthetic whole cores are prepared and used for purposes of validating all the nine transmitter-receiver (TR) coupling responses of the WCEMIT. Following that, I conduct laboratory investigation of the petrophysical applications of the WCEMIT. Isotropic, polar anisotropic, vuggy, and layered whole cores are measured using the WCEMIT. An inversion scheme coupled with FE model predictions is used to estimate electrical properties such as Archie's porosity exponent, formation resistivity factor, host conductivity, layer conductivity, anisotropy ratio (λ), dip (θ), and azimuth (β). Additionally, numerical modeling investigation of the petrophysical applications of the WCEMIT is conducted for purposes of resistivity characterization of whole cores from multi-layered formations and from formations exhibiting dielectric and frequency dispersive properties.

3.2 MEASUREMENT VALIDATION

3.2.1 Tilted test loop

In Chapter 2, the tilted test loop (TTL) method was introduced for calibrating the nine TR coupling responses of the WCEMIT at seven discrete frequencies, namely 19.6, 31.2, 41.5, 58.5, 87.6, 150.4, and 261 kHz. Magnetic moment of the TTL is fixed at 45°-dip and its azimuthal orientation (β) and location along the tool axis is changed for purposes of calibration.

The first validation of the calibrated WCEMIT response involves comparing the measured values against the modeled values of the WCEMIT impedance response to the TTL at 58.5 kHz as the TTL is translated coaxially along the tool axis from a distance of -6 inches to +8 inches away from the center of z-transmitter coil. I perform two such comparison for the azimuthal orientation of the TTL of 0° and 45°, respectively. All model predictions in this section are computed using the SA model. The calibrated WCEMIT impedance response is calculated as expressed in equation 18 of Chapter 2. Figures 3.1 and 3.2 depict the good agreement between the modeled and measured values of the WCEMIT impedance response to the TTL at an azimuthal orientation of 0° and 45°, respectively, for various locations of the TTL. Note that the end effects for all the nine TR coupling responses are negligible at a distance more than +8 or less than -4 inches away from the center of transmitter coil system.

At an azimuthal orientation of 0°, the magnetic moment of the TTL is in the xz plane; therefore, negligible voltage is induced in the y-directed receiver coil. Moreover, an energized y-directed transmitter coil is not able to induce any eddy current in the TTL that is oriented at 0°-azimuth. Consequently, all the TR coupling responses to the TTL oriented at 0°-azimuth that are associated with the y-directed transmitter coil or y-directed

receiver coil, namely *xy*, *yx*, *yy*, *yz*, and *zy* couplings, exhibit negligible impedance responses, as shown in Figure 3.1. When the TTL is oriented at 45°-azimuth, all the nine TR coupling responses exhibit non-negligible impedance responses because the magnetic moment of the TTL has equal components in *xz*- and *yz*-planes. Importantly, the *xx*, *yy*, *xy* and *yx* coupling responses to the TTL oriented at 45°-azimuth are equal in magnitude for all the locations of the TTL. Also, *zx* and *zy* coupling responses and *xz* and *yz* coupling responses to the TTL oriented at 45°-azimuth are equal in magnitude, respectively, for all the locations of the TTL. I obtain similar agreement between the modeled and measured responses for other frequencies. This method allows validation of each of the nine coupling responses for all the operating frequencies.

3.2.2 Isotropic cylinder of brine

When measuring an isotropic homogeneous sample, the apparent conductivity values measured by the calibrated direct couplings, namely *xx*, *yy*, and *zz* couplings, should be equal to the true conductivity of the sample, while the rest of the coupling responses should be close to zero for all the operating frequencies. This behavior arises from the physics of tensor conductivity measurements using triaxial coils, as explained by Anderson et al. (2002). I test the validity of the WCEMIT measurements by comparing the apparent conductivity response of the calibrated WCEMIT at 58.5 kHz against the measured values of conductivity response of a calibrated Orion^{TM} conductivity meter to 4-inch-diameter, 20-inch-long isotropic cylindrical volume of brine for varying values of conductivity of the brine. The cylindrical volume of brine is prepared by filling the space inside the WCEMIT conduit with brine when the WCEMIT is in a vertical position.

First, the Orion conductivity meter was calibrated using three Orion conductivity standard solutions of 1.413-, 111.9- and 12.9-mS/cm-conductivity. The probe of the

Orion^{TM} conductivity meter is then dipped into the cylindrical volume of brine inside the WCEMIT conduit to measure the true conductivity of the brine. Following that, the three direct coupling responses are measured at a specific frequency with the tool in a vertical position and the conduit completely filled with the brine of known conductivity. In agreement with theory, Figure 3.3 indicates a 1:1 correlation between the Orion conductivity measurements and the WCEMIT apparent conductivity measurements for the *xx*, *yy*, and *zz* couplings at an operating frequency of 58.5 kHz. Orion and WCEMIT measurements are in good agreement in the conductivity range of 5 mS/m to 5 S/m.

3.2.3 Bi-laminar synthetic whole core

Two 20-inch-long, 4-inch-diameter synthetic bilaminar whole core samples of 0°-dip and 45°-dip, respectively, were prepared for purposes of validating the WCEMIT measurements. These 0°-dip and 45°-dip synthetic cores comprise frameworks made of 0.25-inch-thick TIVAR^{TM} circular and elliptical discs, respectively, separated by 0.75 inches (Figure 3.4). The TIVAR layers are composed of conductive carbon powder and exhibit conductivity of 50 mS/m at an operating frequency of 58.5 kHz, as measured by HP4194A impedance/gain-phase analyzer. To measure these bilaminar TIVAR-brine synthetic cores with WCEMIT for validation purposes, the corresponding framework is placed coaxially inside the WCEMIT conduit and then the empty spaces around the framework are completely filled with brine. Conductivity of brine is selected such that the bilaminar TIVAR-brine core exhibits a specific conductivity anisotropy ratio (λ_c). I define $\lambda_c = \sigma_{hor}/\sigma_{vert}$, where σ_{hor} and σ_{vert} are the horizontal and vertical conductivity of the sample, respectively. Table 3.1 shows the required conductivity of the brine, filling the spaces between the TIVAR layers, to get the desired values of λ_c for both 0°-dip and 45°-dip bilaminar cores. The validity of the WCEMIT measurements was confirmed by

comparing the modeled and measured values of specific TR coupling responses to 0°-dip and 45°-dip bilaminar synthetic cores for different values of λ_c of the cores. All model predictions in this section are computed using the FE forward model.

First, I measure the direct coupling responses, namely the *xx*, *yy*, and *zz* responses, to four 0°-dip bilaminar synthetic cores of λ_c of 1, 2, 5, and 10, respectively. Figure 3.5 shows that the measured values were well reproduced by the FE model predictions. For the synthetic core of λ_c of 1, the measured direct TR coupling responses are close to 50 mS/m in that figure. Also, the *xx* and *yy* coupling responses to the synthetic core of λ_c of 2 exhibit apparent conductivity (Σ) of 170 mS/m, while the *zz* response for the same core exhibits Σ of 370 mS/m. Therefore, the ratio of Σ_{zz} to Σ_{yy} or Σ_{xx} is close to 2, which honors the λ_c of the synthetic core. The Σ_{yy} and Σ_{xx} decrease, while Σ_{zz} increases with an increase in the λ_c of the synthetic core.

Next, I validate all the diagonal coupling responses, namely *xx*, *yy*, *zz*, *xz*, and *zx* coupling responses, by comparing the measured responses against the modeled responses to four 45°-dip, 0°-azimuth bilaminar synthetic cores of λ_c of 1, 2, 5, and 10, respectively, at 58.5 kHz as described in Figure 3.6. These cores were oriented at 0°-azimuth by ensuring that the magnetic moments of the titled elliptical TIVAR discs lie entirely in the *xz*-plane. For the synthetic core of λ_c of 1, the measured direct TR coupling responses are close to 50 mS/m. Unlike the previous measurements on the non-dipping bilaminar synthetic cores, the *xx* and *yy* coupling responses to the 45°-dip bilaminar synthetic cores of λ_c more than 1 exhibit different values of Σ due to the effect of dipping beds. Also, unlike the previous case, the Σ_{yy}, Σ_{xx}, and Σ_{zz} increase with an increase in the λ_c of the synthetic core.

In order to validate all the nine TR coupling responses, I compare the modeled and measured WCEMIT responses to four 45°-dip, 60°-azimuth bilaminar synthetic cores of

λ_c of 1, 2, 5, and 10, respectively, at 58.5 kHz. These bilaminar cores were oriented inside the WCEMIT conduit such that the cores were at an azimuth of 60°, which means that the magnetic moments of the dipping elliptical TIVAR discs are at an angle of 60° from the *x* axis away from the *xz*-plane. Figure 3.7 illustrates a good agreement between the modeled and measured responses to these bilaminar TIVAR-brine cores for all the nine TR couplings at 58.5 kHz. Also, for the 45°-dip, 60°-azimuth synthetic core of λ_c of 1, the measured direct TR coupling responses are around 50 mS/m and those for the rest of the couplings are close to zero, which is in agreement with the theory of tensor conductivity. For a 45°-dip, 60°-azimuth synthetic core of λ_c of 2, the Figure 3.7 indicates non-negligible responses for the indirect couplings due to the effect of dip and azimuth. Further, according to the theory of tensor conductivity, *yx* and *xy* coupling responses are always equal irrespective of the λ_c, β, and θ of the bilaminar synthetic core. Also, it can be seen in Figure 3.7 that, at λ_c of 10, all the indirect coupling responses exhibit large Σ values ranging from 10 to 100 mS/m that are indicative of the effects of dip and azimuth.

3.3 LABORATORY INVESTIGATION OF PETROPHYSICAL APPLICATIONS

The WCEMIT performs high-resolution, multi-frequency, complex electrical conductivity tensor measurements on as-received or cleaned whole core samples and continuous-feed cylindrical volumes at seven discrete frequencies in the EM induction frequency range of 10 kHz to 300 kHz. There are very few published studies on the electrical measurements on whole core samples and their applications for purposes petrophysical characterization. The limited laboratory investigation on such measurements is primarily attributed to lack of suitable measurement and interpretation methods. In this section, I propose several new laboratory methods and interpretation techniques that use

the WCEMIT measurements on whole core samples to estimate their electrical properties, and further, estimate some of their petrophysical properties.

3.3.1 Archie's porosity exponent of Berea and Boise sandstone whole core samples

A 4-inch-diameter, 24-inch-long Berea sandstone (Figures 3.8a and 3.8b) and Boise sandstone whole core samples were fully saturated with 7.64-S/m-conductivity brine. A whole core sample was placed inside the WCEMIT conduit such that its top and bottom end were beyond +8 inches and -4 inches, respectively, from the center of the *z*-directed transmitter coil to minimize the end effects (Figure 3.8d) during the WCEMIT measurements. Full conductivity tensor $\boldsymbol{\Sigma}$ of the whole core samples were recorded at 58.5 kHz. $\boldsymbol{\Sigma}$ tensor contains nine apparent conductivity values measured by each of the nine WCEMIT TR couplings.

The full conductivity tensor of Berea sandstone whole core sample as measured with the WCEMIT was

$$\boldsymbol{\Sigma}_{\text{Berea}} = \begin{bmatrix} 713.64 & -26.05 & -12.13 \\ -14.66 & 737.17 & 17.13 \\ 12.08 & 1.34 & 759.35 \end{bmatrix} m\text{S/m}.$$

The terms in the leading diagonal of $\boldsymbol{\Sigma}_{\text{Berea}}$ represents the direct coupling responses. The *zz* coupling response is slightly higher than *xx* and *yy* coupling response. This indicates that the λ_c of this Berea sandstone whole core is close to 1. $\boldsymbol{\Sigma}_{\text{Berea}}$ is first rotated to minimize the square root of the sum of squares of the four off-diagonal terms, namely Σ_{xy}, Σ_{yx}, Σ_{yz}, and Σ_{zy}. The angle of rotation required for the minimization is an estimate of the azimuth (Wang et al., 2003). In doing so, the β of the Berea sandstone whole core is estimated to be 14°. Following that, a simple inversion scheme is implemented to obtain σ_{hor} of 0.756 S/m, λ_c of 1.01, and θ of 2.86°. Figure 3.9 illustrates the convergence of the inversion results to the estimated values of σ_{hor}, λ_c, and θ. A simple mass-balance performed on the

Berea whole core sample before and after saturation indicates that the brine-filled total porosity (ϕ_{tot}) of the Berea whole core sample is 26.5%. Now, the Archie's porosity exponent (m) of the Berea whole core can be calculated as

$$m = \frac{\log\left(\frac{\sigma_{\mathrm{t}}}{\sigma_{\mathrm{w}}}\right)}{\log(\phi_{\mathrm{tot}})}, \tag{1}$$

where σ_{t} is the effective conductivity of the 100%-brine-saturated Berea whole core that is equal to the estimated σ_{hor} of 0.75 S/m, σ_{w} is the conductivity of the Brine that is equal to 7.64 S/m, and ϕ_{tot} is the brine-filled total porosity of the whole core sample of 0.265. Using equation 1, the estimated value of m of the Berea whole core is 1.74, which is in good agreement with values of m of Berea sandstone samples reported in several peer-reviewed publications (e.g., Sprunt et al., 1990; Lesmes and Morgan, 2001; Revil, 2013).

Similarly, the full conductivity tensor of Boise sandstone whole core sample as measured with the WCEMIT was

$$\boldsymbol{\Sigma}_{\mathrm{Boise}} = \begin{bmatrix} 733.29 & 19.31 & 4.89 \\ 13.26 & 738.07 & 14.88 \\ -15.86 & -3.71 & 821.85 \end{bmatrix} m\mathrm{S/m}.$$

On rotating the $\boldsymbol{\Sigma}_{\mathrm{Boise}}$ to minimize the square root of the sum of squares of the four off-diagonal terms, I obtain the β of Boise sandstone whole core of 12°. Following that, the inversion scheme is applied to estimate σ_{hor} of 0.87 S/m, λ_{c} of 1.15, and θ of 2.86° (Figure 3.10). Mass-balance performed on the Boise whole core before and after saturation indicates that the ϕ_{tot} of the Boise whole core is 28%. Now, using the equation 1, the estimated value of m of the Boise whole core is 1.71.

3.3.2 Archie's porosity exponent of glass-bead packs

To ascertain further the petrophysical application of the WCEMIT to evaluate Archie's porosity exponent of whole core samples, I prepared three glass-bead packs, as

shown in Figure 3.11, by filling 3.8-inch-inner-diameter cylindrical glass vases with Swarco's Megalux glass beads of 6-, 1.15-, and 0.25-mm-diameter, respectively. These three glass-beads are referred to as Pack-1, Pack-2, and Pack-3, respectively. The packs studied in this section were fully saturated with brine of known conductivity, 2 feet in length, and 4 inches in outer diameter. To prepare these packs, first glass beads of desired size were poured into the glass vase to make a 2-inch-thick layer. Then, the brine of known conductivity was poured into the glass vase to fully saturate the 2-inch-thick layer. The vase was then vibrated using a mechanical hand-held shaker to consolidate the mixture, remove trapped air bubbles, and uniformly distribute the pore-filling brine. The three above-mentioned steps were repeated until the entire glass vase was tightly filled with glass beads and brine. In doing so, I consistently prepared 2-ft-long packs inside the glass vase with a brine-filled porosity of approximately 38% irrespective of the size of glass beads. A glass-bead pack is placed in the WCEMIT conduit such that its top and bottom end were beyond +8 inch and -4 inch, respectively, from the center of the *z*-directed transmitter coil. The $\boldsymbol{\Sigma}$ of the pack was the measured with WCEMIT at 58.5 kHz. The true conductivity (σ_t) of the pack was estimated by inverting the $\boldsymbol{\Sigma}$, as discussed in the previous section.

Archie's equation states that the σ_t of brine-saturated porous mixture is linearly related to the brine conductivity (σ_w). Also, based on the Archie's equation, the value of m of a mixture is equal to the slope of the log-log relationship between σ_t and σ_w, assuming tortuosity factor (a) equal to 1. σ_t of the pack is estimated by applying an inversion scheme on the measured $\boldsymbol{\Sigma}$ of the pack, and the brine conductivity (σ_w) is known a priori, as measured by Orion conductivity meter. In order to derive the relationship of σ_t and σ_w, the pack was sequentially fully-saturated with brine of 1104-, 1330-, 1784-, and 2620-mS/m conductivity. Figure 3.12 corroborates the linear relationship of the estimated σ_t values of

the brine-saturated glass-bead pack containing 6-mm diameter and the σ_w of the pore-filling brine. The estimated value of *m* of these glass-bead packs were close to 1.33, irrespective of the brine conductivity and size of the glass beads. The estimated values of *m* close to 1.33 honor the values of *m* estimated for similar brine-filled consolidated packs made of spherical grains by Jackson et al. (2008) and Revil and Skold (2011).

3.3.3 Formation resistivity factor of glass-bead packs

Based on the Archie's equation, the formation resistivity factor (*F*) of whole cores belonging to similar rock types can be expressed as a function of brine-filled porosity as

$$F = \frac{a}{\phi_{\mathrm{tot}}{}^{m}} = \frac{\sigma_{\mathrm{w}}}{\sigma_{\mathrm{o}}}, \quad (2)$$

where, *a* is the tortuosity factor assumed to be 1, ϕ_{tot} is total brine-filled porosity of the pack, σ_{w} is the pore-filling brine conductivity, *m* is the porosity exponent, which was found to be 1.33 as described in the previous section, and σ_{o} is the conductivity of 100%-brine saturated sample. σ_{o} in equation 2 can be replaced with σ_{t} because in our work σ_{t} is measured on 100%-brine-saturated glass bead packs.

I prepared homogeneous isotropic glass-bead packs of different values of porosity by mixing glass-beads of different sizes. I then fully saturated the packs with 2.62-S/m-conductivity brine. It is known that a consolidated mixture of uniform size of spheres exhibits hexagonal close packing; therefore, a pack made of uniform size of glass beads will have equal porosity irrespective of the sizes of the grains in the packs. However, when smaller-sized spherical grains are mixed with larger-sized grains, the smaller grains occupy the voids in the hexagonal packing of the larger spherical grains; thereby, lowering the porosity of the glass-bead pack. For purposes of this investigation, I was able to reduce the ϕ_{tot} of a glass-bead pack made of 1.15-mm diameter glass beads from 38% to 27% by uniformly mixing 0.25-mm-diameter glass beads with 1.15-mm diameter glass beads.

Also, I reduced the ϕ_{tot} of the glass-bead pack made of 6-mm-diameter beads from 38% to 18.9% by uniformly mixing 0.25-mm-diameter glass beads with 6-mm-diameter beads. The pack made by mixing 1.15-mm and 0.25-mm diameter beads and that made by mixing 6-mm and 0.25-mm diameter beads are referred to as Pack-4 and Pack-5, respectively. Figure 3.13 illustrates that the computed values of *F* of the five glass-bead packs, namely Pack-1, Pack-2, Pack-3, Pack-4, and Pack-5, honor the log-log relationship of the *F* with total porosity (ϕ_{tot}) as expressed in equation 2. Table 3.2 shows the estimated values of σ_{t} and *m* of each of the five packs. Estimated values of Archie's porosity exponents of all packs are close to 1.33.

3.3.4 Bed conductivity of bilaminar glass-bead packs

Bilaminar formations are common in turbidite formations, thinly bedded deltaic formations, and laminated shale-sand formations. In such formations, low-resistivity petrophysical layers, typically those bearing hydrocarbon, are bypassed due to the limited vertical resolution of subsurface electrical measurements. I investigate the application of the WCEMIT to quantify the conductivity of individual beds in bilaminar whole core using series-parallel resistivity model, as described in Klein et al. (1997). To that end, I prepare bilaminar glass-bead packs of approximately 2-inch-thick alternating beds made of mixtures of glass beads of varying sizes (Figure 3.14). As described in previous section, the porosity of a layer can be reduced by mixing two different size glass beads, such that smaller-sized bead occupies the voids in between larger-sized beads. In doing so, I prepare the bilaminar glass-bead packs with alternating beds of different porosity values; hence, these bilaminar packs had alternating beds of different conductivity that gave rise to the electrical anisotropy of these packs.

As mentioned in Table 3.2, Pack-4 made of mixture of 1.15-mm- and 0.25-mm-diameter beads, referred as mixture-1, exhibits ϕ_{tot} of 27% and σ_{t} of 0.455 S/m, while the glass-bead pack made of mixture of 6-mm and 0.25-mm diameter beads, referred as mixture-2, exhibits ϕ_{tot} of 18.9% and σ_{t} of 0.28 S/m. I prepared following three bilaminar glass-bead packs (Figure 3.14) having alternating 2-inch thick beds: (a) Pack-6 contained bed made of mixture-1 alternating with bed made of only 0.25-mm-diameter beads, Pack-7 contained bed made of mixture-2 alternating with bed made of only 0.25-mm-diameter beads, and Pack-8 contained bed made of mixture-1 alternating with bed made of mixture-2. Conductivity tensor measurements on Pack-6, Pack-7, and Pack-8 were inverted to estimate the σ_{hor} and λ_{c}, as described in Table 3.3. Pack-7 exhibits highest anisotropy due to largest difference of porosity values of the alternating beds. Series-parallel resistivity model was then implemented to estimate the conductivity of the two alternating beds in the bilaminar glass-bead packs. Importantly, the estimated values of the bed conductivity of bilaminar glass-bead packs, as shown in sixth and seventh column of the Table 3.3, match well with conductivity values of corresponding homogeneous glass-bead packs measured in the previous section, as shown in fourth column in the Table 3.2.

3.3.5 Host conductivity of vuggy glass-bead packs

Dissolution and crystallization create vuggy porosity in reservoir rocks. Carbonate formations typically have extensive vuggy porosity due to the dissolution process. Resistivity interpretation of subsurface measurements in vuggy formations is a challenging problem. Various electromagnetic mixing laws have been implemented for analyzing conductivity measurements in carbonate formations (Kuijper and Waal, 2007), vuggy fractured formation (Perez-Rosales et al., 2002), oomoldic rocks (Rasmus and Kenyon, 1985; Gray and Rasmus, 1988), and fractured reservoirs (Olusola et al., 2013). API

recommended practice for core analysis procedure (RP40, 1960) states that whole core measurements are essential in vuggy carbonates.

In this section, I propose a petrophysical application of the WCEMIT for analyzing whole core samples from vuggy formations. I compare conductivity estimates based on the WCEMIT measurements on glass-bead packs containing uniformly distributed non-conductive vugs against the Maxwell-Garnett model predictions (Giordano, 2003) by using a concept of modified formation factor (F_{mod}), similar to Rasmus and Kenyon (1985). I prepared brine-saturated vuggy glass-bead packs containing various volume fractions of uniformly distributed non-conductive vugs. In these cores, 1.15-mm-diameter glass beads formed the porous host matrix, while 6-mm-diameter glass-beads identify the non-conductive vugs. In these packs, the host porosity (ϕ_h) is approximately constant at 38%, while the vuggy porosity (ϕ_i) depends on the volume concentration of the 6-mm-diameter glass beads. Hence, the total porosity ϕ_{tot} of these cores is sum of ϕ_h and ϕ_i. Figure 3.15 shows the top-view of a 2-feet-long, 4-inch-diameter vuggy glass-bead pack of ϕ_i of 23%, ϕ_h of 38%, and ϕ_t of 51% completely saturated with brine of 2.62-S/m conductivity.

Figure 3.16 describes the relationship of the modified formation factor (F_{mod}) to the ϕ_t for samples that contain no vugs, isolated non-conductive spherical vugs, or conductive spherical vugs. The formation resistivity factor (F) of 100%-brine-saturated pack without vugs, shown as dashed line in Figure 3.16, is computed using the Archie's formation factor relation as expressed in equation 2. However, a combination of the Maxwell-Garnett's effective medium model and Archie's formation factor relation is used to compute the modified formation factor (F_{mod}) of vuggy samples (e.g., Gray and Rasmus, 1988), depicted as green and blue curves in Figure 3.16. At low frequencies, the Maxwell-

Garnett's model of effective conductivity of a mixture containing spherical inclusions is expressed as

$$\frac{\sigma_{\mathrm{t}} - \sigma_{\mathrm{h}}}{\sigma_{\mathrm{t}} + 2\sigma_{\mathrm{h}}} = \phi_{\mathrm{i}} \frac{\sigma_{\mathrm{i}} - \sigma_{\mathrm{h}}}{\sigma_{\mathrm{i}} + 2\sigma_{\mathrm{h}}}, \tag{3}$$

where σ_{t} is true (effective) conductivity of the vuggy sample, σ_{h} is conductivity of the host medium (in our case, host is the brine-saturated glass-bead pack comprising 1.15-mm-diameter glass beads), σ_{i} is conductivity of the inclusion phase (in our case, inclusion phase is the uniformly distributed non-conductive spherical vugs), and ϕ_{i} is the volume fraction of the inclusion phase. Equation 3 is modified to compute the true conductivity of vuggy glass-bead packs containing only isolated non-conductive spherical vugs as

$$\sigma_{\mathrm{t}} = \sigma_{\mathrm{h}} \left(\frac{1 - \phi_i}{1 + \phi_i/2} \right). \tag{4}$$

Therefore, the modified formation factor (F_{mod}) of these 100%-brine-saturated vuggy glass-bead packs can be expressed as

$$F_{\mathrm{mod}} = \frac{\sigma_{\mathrm{w}}}{\sigma_{\mathrm{o}}} = \frac{\sigma_{\mathrm{w}}}{\sigma_{\mathrm{t}}} = \frac{\sigma_{\mathrm{w}}}{\sigma_{\mathrm{h}}} \left(\frac{1 + \phi_i/2}{1 - \phi_i} \right) = F \left(\frac{1 + \phi_i/2}{1 - \phi_i} \right). \tag{5}$$

I measure the Σ response of the direct couplings to six synthetic cores of uniformly distributed non-conductive vuggy porosity values of 0, 6.6, 13, 18, 23, and 28%, respectively. The Σ response of the direct couplings to an isotropic sample is approximately equal to the σ_{t} of the vuggy glass-bead packs, as explained in previous sections. Using equation 4, I estimate the σ_{h} of each of the six vuggy glass-bead packs. The estimated values of σ_{h} of vuggy glass-bead packs, as shown in column three of Table 3.4, are nearly equal to the estimated values of σ_{t} of the homogeneous isotropic glass-bead packs made of uniformly sized glass beads, as shown in column four of Table 3.2.

3.3.6 Conductivity, anisotropy ratio, dip, and azimuth of bilaminar TIVAR-brine whole cores

In this section, I utilize the tensor functionality of the WCEMIT to quantify directional conductivities, θ, and β of a polar anisotropic synthetic whole core. The WCEMIT generates the $\boldsymbol{\Sigma}$ tensor of the polar anisotropic whole core. Then, the $\boldsymbol{\Sigma}$ tensor is rotated to obtain an estimate of the azimuthal orientation (β) of the bilaminar core, as explained in previous section. Following that, I use a simple inversion algorithm that couples a data table of the FE forward model predictions to estimate σ_{hor}, λ_{c}, and θ of the polar anisotropic whole core.

I prepared a synthetic bilaminar TIVAR-brine core of σ_{hor}, λ_{c}, β, and θ of 0.88 S/m, 6.6, 60°, and 45°, respectively. To that end, a framework was designed with 45°-dipping elliptical TIVAR discs of 0.75-inch thickness, as shown in Figure 3.17, to make synthetic whole core of θ of 45°. The spaces between the dipping elliptical TIVAR discs were filled with 1.16-S/m conductivity brine. Now, the bilaminar TIVAR-brine whole core has σ_{hor} of 0.88 (calculated using series-parallel resistivity formulation) and λ_{c} of 6.6. The synthetic core was placed in the WCEMIT conduit at an azimuthal orientation of 60° with respect to the *xz*-plane formed by the *x*-directed and z-directed transmitter coil axes. Therefore, the value of β associated with the synthetic core is 60°.

All the nine coupling responses of the WCEMIT to the bilaminar synthetic core were measured to obtain the complex conductivity of

$$\boldsymbol{\Sigma} = \begin{bmatrix} 0.2633 & -0.0722 & -0.0643 \\ -0.0722 & 0.3467 & 0.1114 \\ -0.0077 & 0.0133 & 0.7131 \end{bmatrix} \mathrm{S/m},$$

which has non-zero off-diagonal terms due to the effect of non-zero θ and β of the bilaminar core. As the first step of the inversion scheme, I rotated the $\boldsymbol{\Sigma}$ tensor to minimize the cost functional to obtain the value of β. Cost functional is the square root of sum of squares of

the four non-diagonal terms of the $\boldsymbol{\Sigma}$, namely *xy*, *yx*, *yz*, and *zy* terms. Figure 3.18 shows the angle of rotation required to minimize the cost functional. Therefore, the estimate of β of the synthetic core is 60.1°, as shown in Figure 3.18. After this tensor rotation, the original $\boldsymbol{\Sigma}$ tensor reduced to

$$\boldsymbol{\Sigma}_{\mathrm{rot}} = \begin{bmatrix} 0.3884 & -0.0001 & -0.1286 \\ -0.0004 & 0.2216 & 0.0001 \\ -0.0154 & -0.0001 & 0.7131 \end{bmatrix} \mathrm{S/m},$$

which was then inverted to obtain estimates of σ_{hor}, λ_{c}, and θ of 0.887 S/m, 6.65, and 46.19°, respectively, of the bilaminar core (Figure 3.19). The estimated values honor the true values of synthetic core that were known a priori.

3.4 SIMULATION-BASED INVESTIGATION OF PETROPHYSICAL APPLICATIONS

In this section, I investigate two novel petrophysical applications of WCEMIT based on the numerical simulation of WCEMIT response. I was not able to obtain geological or synthetic whole core samples for purposes of demonstrating the WCEMIT applications proposed in this section. Therefore, I use the FE and SA forward models to simulate the applications. Specifically, in the first investigation, I use the SA model to quantify the WCEMIT response to variations in the dielectric properties and dielectric dispersion parameters of whole core samples. In another investigation, I use the FE model to simulate the WCEMIT response to a novel whole core logging process conducted at 58.5 kHz. Using the FE model predictions of whole core logging measurements, I develop an inversion algorithm to estimate the conductivity of a 24-inch whole core at 1-inch vertical resolution. In both the model investigations, the assumed diameters of the cylindrical volumes, identifying a whole core, are 4 inches.

3.4.1 Dielectric properties

Subsurface EM induction frequency measurements are influenced by interfacial polarization phenomena in geomaterials (Anderson et al., 2008). Due to interfacial polarization phenomena, geomaterials exhibit large frequency dispersive and directional permittivity and dispersive conductivity. Complex conductivity of a geomaterial can be expressed as

$$\sigma^* = \sigma - \mathrm{i}\omega\varepsilon_0\varepsilon_\mathrm{r}^* \tag{6}$$

where σ is the conductivity (related to flow of charges), ε_0 is vacuum permittivity, ε_r^* is the complex dielectric relative permittivity (related to storage of charges), and ω is the operating angular frequency. In the operating frequency range of subsurface electromagnetic measurements and in the absence of clay and conductive minerals, the σ is assumed to be non-dispersive with respect to frequency and $\omega\varepsilon_0\varepsilon_\mathrm{r}^*$ is assumed to be negligible. However, when a geomaterial is susceptible to interfacial polarization phenomena, its σ is frequency dispersive and complex dielectric relative permittivity of the geomaterial can be expressed as

$$\varepsilon_\mathrm{r}^* = \varepsilon_\mathrm{r}(\omega)[1 + i\delta(\omega)] \tag{7}$$

where $\varepsilon_\mathrm{r}(\omega)$ is the frequency-dependent relative dielectric permittivity (or dielectric constant) and $\delta(\omega)$ is the frequency-dependent dielectric loss factor of the geomaterial.

The FE model predicts that whole core samples of ε_r more than 10^4 will produce substantial negative X-signal response. Similar observations were made by Anderson et al. (2006) for triaxial EM induction tool measurements that were acquired at 26 kHz. It is important to note that large ε_r values of the sample do not affect the R-signal response; it is the dielectric loss factor and the frequency dispersive behavior of σ that give rise to significant changes in R-signal response. For example, in Figure 3.21a, the blue curve

indicates that the R-signal response to a whole core of σ_{hor} of 1 S/m, λ_{c} of 1, λ_{p} of 1, and $\varepsilon_{\mathrm{r,hor}}$ of 10^5 is close to 1 S/m and is not at all affected by the large $\varepsilon_{\mathrm{r,hor}}$ of the sample. Nonetheless, the X-signal response to that whole core sample exhibits large negative, frequency-dispersive values in the EM induction frequency, as shown by the blue curve in Figure 3.21b. On the other hand, Figure 3.22 describes that the R-signal response is severely affected due to the dielectric loss factor of the whole core sample.

In order to investigate the petrophysical application of the WCEMIT to characterize dielectric properties of whole core samples, I first implement the SA model to compute R-signal response of the *yy*-coupling to a cylindrical volume of σ_{hor} of 1 S/m, λ_{p} of 1, and ε_{r} of 1 for various values of λ_{c}. The *xx*- and *yy*-coupling responses are affected by the variation in λ_{c}. Also, both the coupling responses are equal in magnitude due to the assumption of transverse isotropy of the whole core sample. The *zz*-coupling response however is not at all affected by the variation in λ_{c} because in this simulation case the σ_{hor} is held constant and the σ_{vert} is varied to vary the λ_{c}. Because the *zz*-coupling response is a constant value, I did not plot it. At a constant σ_{hor}, a decrease in σ_{vert} gives rise to an increase in λ_{c}. Figure 3.20 shows that the R-signal response of the *yy*-coupling decreases with increase in λ_{c} which corresponds to the decrease in the conductivity in vertical direction. I don't show the X-signal response in Figure 3.20 because at ε_{r} of 1 the X-signal response is close to zero.

In geoscience and petrophysics, much work has been done on quantifying and measuring the effects of conductivity anisotropy ratio on EM induction measurements. However, only limited investigation has been done on the effects of permittivity anisotropy on the EM induction measurements because typical conventional formations do not give rise to interfacial polarization phenomena; as a result, only negligible values of $\omega\varepsilon_0\varepsilon_{\mathrm{r}}^*$ exist.

Nonetheless, current E&P activities have increased in organic shales, hydrocarbon-bearing mudstones, and shaly formations that are susceptible to interfacial polarization phenomena. Therefore, the effects of dielectric permittivity and permittivity anisotropy should not be ignored during the resistivity characterization of such geomaterials. It is known that interfacial polarization in geomaterial is a direction-dependent phenomenon resulting from the shape and texture of the interfaces (e.g., Zhdanov, 2008). Consequently, geomaterials will also exhibit permittivity anisotropy due to direction-dependent storage of charges on the interfaces. Figure 3.21 illustrates the effects of variation of permittivity anisotropy (λ_{p}) on the R- and X-signal responses of the *yy*-coupling. I define $\lambda_{\mathrm{p}} = \varepsilon_{\mathrm{r,hor}}/\varepsilon_{\mathrm{r,vert}}$, where $\varepsilon_{\mathrm{r,hor}}$ and $\varepsilon_{\mathrm{r,vert}}$ are the horizontal and vertical relative permittivity of the sample. Figure 3.21a highlights that the effects of λ_{p} on the R-signal response are larger for values of λ_{p} lower than 1 than that for values of λ_{p} higher than 1. Further, Figure 3.21b shows that the X-signal response in EM induction frequency range decreases with an increase in λ_{p} for values of λ_{p} higher than 0.5. However, for λ_{p} of 0.2, the sample shows a peak in X-signal response. R-signal response decreases with an increase in λ_{p} from 0.2 of 1, beyond which R-signal response slowly increases with an increase in λ_{p}. Figure 3.21 indicates that the WCEMIT response is highly sensitive to variation in λ_{p} for samples exhibiting large dielectric permittivity due to interfacial polarization, especially for values of λ_{p} lower than 1.

Next, I examine the WCEMIT response to variation in dielectric loss factor (δ) of the whole core sample. In my work, the dielectric loss factor arises due to the energy required to reorient the accumulated ions at the interfaces at each alternation of the applied electrical field (Loftness, 1952). The energy required to reorient the interfacial polarization increases with increase in frequency of alternation of the electric field until a frequency is

reached where the polarization no longer reorients itself fully with each alternation. After that, the energy required reduces with further increase in the frequency of the applied electric field. Dielectric loss factor values ranging from 0.01 to 1 in the frequency range of 1 to 10^6 Hz were measured by Stillman et al. (2010) for mixtures of silicates and brine. Schwartz et al. (2009) emphasized the need to include dielectric loss factor in estimating water content of soil samples based on electromagnetic measurements. Figure 3.22 shows the SA model predictions of the R- and X-signal responses of the *zz*-coupling to a cylindrical volume of σ_{hor} of 1 S/m, λ_{c} of 1, λ_{p} of 1, and $\varepsilon_{\mathrm{r,hor}}$ of 10^5 for various values of δ. Figure 3.22 indicates that δ has negligible effect on the X-signal response, while the R-signal response is drastically influenced due to the variation in δ. A cylindrical volume of δ of 1 exhibits more than 50% increase in the R-signal response compared to that of sample of negligible δ at 58.5 kHz. The effect of δ increases with an increase in frequency, resulting in more than 200% increase of the R-signal response compared to that of sample of negligible δ at 261 kHz. Only R-signal response of the WCEMIT is sensitive to variation in δ for samples exhibiting large dielectric permittivity due to interfacial polarization, especially for values of δ more than 0.1. Therefore, accurate resistivity interpretation of the R-signal response to a whole core sample of large permittivity should account for the effect of dielectric loss factor.

3.4.2 Dispersive dielectric properties

Interfacial polarization is a frequency dispersive phenomena that leads to frequency dispersion of effective conductivity and permittivity of geomaterials. Understanding complex conductivity behavior as a function of frequency helps to correct the real part of the resistivity for the dispersion effects, which otherwise would be interpreted as change of the formation resistivity due to hydrocarbons. The Cole-Cole empirical model is widely

used to interpret dielectric dispersion measurements of geomaterials (Dias, 2000; Ghorbani et al., 2009). However, there is no direct relationship between the parameters of the Cole-Cole model and petrophysical properties. The Cole-Cole model is expressed as

$$\varepsilon_{\mathrm{r}}^{*} = \varepsilon_{\mathrm{r},\infty} + \frac{\varepsilon_{\mathrm{r,s}} - \varepsilon_{\mathrm{r},\infty}}{1 + (\mathrm{i}\omega\tau)^{(1-\alpha)}}, \tag{8}$$

where $\varepsilon_{\mathrm{r}}^{*}$ is the frequency dependent complex relative permittivity, $\varepsilon_{\mathrm{r},\infty}$ is the relative dielectric permittivity at high frequency (~GHz), $\varepsilon_{\mathrm{r,s}}$ is the relative dielectric permittivity at low frequency (~mHz), ω is operating angular frequency (s^{-1}), τ is time constant (s), and (1-α) is the frequency dispersion parameter.

There have been several experimental studies on correlating the Cole-Cole model parameters to petrophysical properties (e.g., Ghorbani et al., 2009). The chargeability (*M*), defined as $\varepsilon_{\mathrm{r,s}} - \varepsilon_{\mathrm{r},\infty}$, depends on the grain size, type of minerals, distribution of minerals, mobility of charge carriers in pore fluid, interfacial effects, surface area within specific pore volume, pore space, and geometrical distribution of pores. Pelton et al. (1978) observed that geomaterials containing disseminated minerals exhibit a lower chargeability and time constant compared to materials containing veinlet mineralization. Geomaterials with low electrical connectivity exhibit a small time constant. Klein and Sill (1982) showed that the time constant increases with an increase in the grain size of clay minerals. Further, dry geomaterials exhibit a low frequency dispersion parameter; therefore, the phase responses exhibit a broad peak. Luo and Zhang (1998) showed that an increase in the heterogeneity reduces the frequency dispersion parameter, and for homogeneous mixtures the frequency dispersion parameter is in the range of 0.7 to 0.9. They also demonstrated that the time constant increases with an increase in grain size.

In this section, I utilize the SA model to predict the R- and X-signal responses to a cylindrical volume of σ_{hor} of 1 S/m, λ_{c} of 1, and λ_{p} of 1 for various values of the Cole-

Cole parameters, namely τ, α, and $\varepsilon_{r,s} - \varepsilon_{r,\infty}$, that describe the dielectric dispersion characteristics of the cylindrical volume. I notice that R-signal response is highly sensitive to variation in Cole-Cole parameter. Accurate resistivity interpretation of samples exhibiting dielectric dispersion should jointly interpret both the R- and X-signal responses by coupling the Cole-Cole empirical model with the forward model of the WCEMIT response, in this case the SA model. Figure 3.23 shows that the peak of X-signal response, corresponding to the loss of complete polarization, shifts to lower frequencies with an increase in τ. Also, both R- and X-signal responses increase with decrease in τ, which generally correlates to a decrease in size of inclusions. Substantial increases in R- and X-signal responses occur for samples of τ smaller than 2×10^{-5} s. Figure 3.23 also indicates that R- and X-signal responses to samples of τ greater than 10^{-4} s approach those of uncontaminated sample that are free from effects of dielectric permittivity and dielectric dispersion.

Next, I study the R- and X-signal responses by varying only the low-frequency relative permittivity $\varepsilon_{r,s}$ and keeping other Cole-Cole parameters at a fixed value. Substantial increase in R- and X-signal responses occurs only for $\varepsilon_{r,s}$ greater than 10^5 (Figure 3.24). The frequency dispersion in R- and X-signal responses increases with an increase in $\varepsilon_{r,s}$ due to greater storage of charges. Finally, I model the effects of variation in frequency dispersion parameter (1-α) on the R- and X-signal responses of WCEMIT while keeping other Cole-Cole parameters constant (Figure 3.25). A decrease in α, corresponding to an increase in homogeneity of the sample, reduces the R- and X-signal responses due to the reduction of surfaces producing interfacial polarization. Interestingly, a sample of α of 0.05 exhibits a frequency dispersion of X-signal response that reduces X-signal response with an increase in frequency, while a sample of α of 0.25 exhibits a frequency dispersion

of X-signal response that increases X-signal response with an increase in frequency. In other words, peak of X-signal response shifts to higher frequencies with increase in α that honors the effect of increase in heterogeneity of the sample. This relationship of X-signal response to α can be used to quantify the degree of heterogeneity of a mixture. This model investigation highlights the sensitivity of the R- and X-signal responses of WCEMIT to the variation in dielectric dispersion parameters of a sample of high dielectric permittivity.

3.4.3 Whole-core logging of multi-laminar samples

This section presents the second simulation-based investigation of a petrophysical application of the WCEMIT. I present a whole core logging procedure to improve the accuracy of laminated sand shale analysis in non-dipping multi-layered formations. It is known that geological formations are deposited in layers. Current E&P activities encounter hydrocarbon-bearing layered formations, such as turbidites and deltaic formations. Conventional resistivity interpretation in layered formations rely on laminated sand shale analysis to accurately quantify the hydrocarbon-bearing sand fraction below the resolution of the subsurface EM tool. Nonetheless, such formations also contain resistive or conductive streaks that reduce the accuracy of laminated sand shale analysis.

I simulate a new whole core logging method designed for a non-dipping, 24-inch-long, 4-inch-diameter whole core using only coaxial *z*-directed transmitter, bucking, and receiver coils. The whole core sample is translated in *z*-direction. This procedure can estimate the values of resistivity of a whole core at 1-inch vertical resolution and at 51.28 kHz. For modeling and inversion purposes, z=0 is selected such that the transmitter and receiver coils are equidistant from z=0. First, the whole core is coaxially placed such that its top is at z=-11 inches and the induced voltage response of *zz* coupling to the whole core is measured at that position. Then, the whole is coaxially translated by 1-inch along the +*z*-

axis and the zz-coupling response is again measured at the new position of the whole core. This process of translating and measuring is repeated in intervals of +1 inch till the top of the whole is at z=+32 inches. In doing so, the whole core logging of single whole core produces 44 measurements of the whole core as the whole is coaxially translated inside the z-directed coils.

The forward model to simulate whole core logging procedure can be expressed as

$$G(\boldsymbol{m}) = \boldsymbol{d}, \tag{9}$$

where $\boldsymbol{m}$ is a vector of conductivity of 24 1-inch-thick layers of a whole core, $\boldsymbol{d}$ is vector of the induced voltage response of *zz*-coupling for the 44 positions of the whole core, and G is the FE model described in Chapter 2 that is used to numerically simulate the WCEMIT's whole core logging measurements $\boldsymbol{d}$ as a function of $\boldsymbol{m}$.

The main purpose of the inversion is to estimate the values of conductivity ($\boldsymbol{m}$) of the 24 individual layers in the whole core that best reconstruct the WCEMIT whole core logging measurements $\boldsymbol{d}$. This amounts to minimizing the residual form $\|G(\boldsymbol{m}) - \boldsymbol{d}\|_2^2$. This requires coupling of the FE model (G) with the inversion scheme. Processing the FE model, which is based on the COMSOL AC/DC module, is computationally intensive; it takes 1 hour to compute the induced voltage response of the *zz*-coupling for 1 position of the whole core. Therefore, I replaced the FE forward model G with a transformation matrix, $\boldsymbol{A}$, in the inversion scheme. Transformation matrix $\boldsymbol{A}$ approximates the FE model predictions of whole core logging measurements.

Transformation matrix $\boldsymbol{A}$ is built on three approximations:

(1) FE model prediction of the induced voltage response of the *zz* coupling to a 24-inch-long 0°-dip whole core sample (Figure 3.26a) at any given position is approximately equal to the FE model prediction of the induced voltage response

of the *zz* coupling to 24 0°-dip, juxtaposed, coaxial 1-inch-thick circular discs constituting a 24-inch-long cylinder at the same position (Figure 3.26b). I tested this approximation for its validity for conductivity in the range of 0.002 S/m to 10 S/m, as elaborated in Table 3.5. Near zero phase angles in Table 3.5 indicate that the bucking coil efficiently eliminates the direct transmitter-receiver coupling.

(2) FE model prediction of the induced voltage response of the *zz* coupling to a 1-inch-thick circular disc of conductivity of *n* S/m at any given position is approximately equal to *n* times the FE model prediction of the induced voltage response of the *zz* coupling to 1-inch-thick circular disc of 1-S/m conductivity at the same position. I tested this approximation for conductivity in the range of 0.1 S/m to 10 S/m, as demonstrated in Figure 3.27. In that figure, at any given location, the induced voltage response of the *zz* coupling to a 1-inch-thick circular disc is linearly related to the conductivity of the disc.

(3) FE model prediction of the induced voltage response of the *zz* coupling to a 24-inch-long 0°-dip whole core at any given position is approximately equal to the sum of the induced voltage responses of the *zz* coupling to 24 coaxial, juxtaposed, 0°-dip 1-inch-thick circular disc that constitute the 24-inch-long cylinder at the same position. I tested this approximation for conductivity in the range of 0.01 S/m to 1 S/m, as elaborated in Table 3.6. In that table, the second last column sums the induced voltage responses of the *zz*-coupling to the 1-inch-thick circular disc for various locations of the disc that range from -12 to 11. The sum for each value of the conductivity of the 1-inch disc (Table 3.6), namely 0.01 S/m, 0.1 S/m, and 1 S/m, are nearly equal to the induced voltage

response of the *zz*-coupling to a 24-inch-long cylinder of equivalent conductivity.

To lend stability to the possibly ill-posed whole core logging problem, I seek to minimize the damped least squares problem of the form

$$F(\boldsymbol{m}) = \|(\boldsymbol{A} \times \boldsymbol{m}) - \boldsymbol{d}\|_2^2 + \alpha^2 \|\boldsymbol{m}\|_2^2, \quad (10)$$

where α is the regularization parameter and $\boldsymbol{A}$ is the transformation matrix that replaces the FE model G for fast inversion. This inversion scheme is developed for non-dipping whole core logging measurements. I select Occam's method to perform the minimization and dynamically adjust α to avoid exceeding the value of misfit so that the effect of the regularization is progressively diminished as the algorithm reaches convergence. The most basic form of Occam's inversion algorithm can be expressed as

$$[\boldsymbol{J}(\boldsymbol{m}^k)^{\mathrm{T}}.\boldsymbol{J}(\boldsymbol{m}^k) + \alpha^2 \boldsymbol{I}]\boldsymbol{m}^{k+1} = \boldsymbol{J}(\boldsymbol{m}^k)^{\mathrm{T}}[\boldsymbol{d} - (\boldsymbol{A} \times \boldsymbol{m}^k) + \boldsymbol{J}(\boldsymbol{m}^k)\boldsymbol{m}^k] \quad (11)$$

where $\boldsymbol{m}^k$ is the vector of model properties at iteration *k*, $\boldsymbol{m}^{k+1}$ is the updated trial model at iteration *k*+1, $\boldsymbol{J}$ is the Jacobian matrix, which constitutes first order derivatives of the measurement vector with respect to model properties, $\boldsymbol{A} \times \boldsymbol{m}^k$ is numerically modeled set of whole core logging measurements for the trial $\boldsymbol{m}^k$, α is the updated regularization parameter, and $\boldsymbol{d}$ is the measurement vector consisting the whole core logging measurements known a priori.

Figure 3.28a shows CT scan and UV fluorescence image of a whole core from a typical turbiditic sequence comprising variable distribution of hydrocarbon-bearing sand, shale, and cemented layers. Figure 3.28b is a model of the conductivity of the layers of the turbiditic sequence shown in figure 3.28a. The model is made by dividing the 24-inch-long whole core into 1-inch-thick layers and assigning each layer a conductivity of 1, 0.4, or 0.01 S/m that identify shale, hydrocarbon-bearing sand, and cemented layers, respectively.

The proposed whole core logging of such a whole core sample will generate 44 measurements of the whole core as it is coaxially translated from -11 inches to +32 inches with respect to the top of the whole core from the center of the *z*-directed transmitter coil. Figure 3.29 shows the FE model predictions of the induced voltage response measured during the whole core logging of the whole core sample shown in Figure 3.28b. The modeled values of induced voltage response in Figure 3.29 constitutes the measurement vector $\boldsymbol{d}$. This measurement vector is inverted using the inversion scheme described earlier to estimate conductivity of each of the 24 layers in the whole core shown in Figure 3.28b. Figure 3.30 shows the results of the inversion of the 44 values in the measurement vector. Inversion results converge at three conductivity values 0.01, 0.4, and 1 S/m, as expected. Figure 3.31 compares the estimated conductivity of the synthetic model of turbiditic sequence against the assigned values of conductivity of each layer. The inversion scheme is able to reproduce the original conductivity values of each of the layers. I found that using whole core logging measurements with a *z*-directed bucking coil significantly improves the accuracy of inversion-based estimation of conductivity of individual layers. Table 3.7 compares the estimation of conductivity of individual layers with and without the *z*-directed bucking coil for a whole core with random distribution of 1-S/m and 0.01-S/m conductivity layers. The values in red in Table 3.7 indicate that the estimated value without the z-directed bucking coil deviates from the true conductivity of a layer.

3.5 CONCLUSIONS

In this chapter, I successfully validated the calibrated WCEMIT measurements by comparing the responses of various WCEMIT couplings with the SA model predictions. Isotropic and polar anisotropic synthetic whole core samples were prepared and implemented for further validation of the WCEMIT measurements. Laboratory

investigation corroborates the use of the WCEMIT for estimating the true conductivity, Archie's porosity exponent, and formation factor of isotropic whole cores. Also, I present the applications of WCEMIT for quantifying bed conductivity, horizontal conductivity, anisotropy ratio, dip, and azimuth of bilaminar whole core samples. The WCEMIT was also used to estimate the host conductivity of a vuggy whole core containing uniformly distributed non-conductive vugs. All estimations of electrical properties based on the laboratory WCEMIT measurements of whole cores conformed well to the known values of those properties. The simulation-based investigations of two petrophysical applications of the WCEMIT were advanced in this chapter. These applications extend the WCEMIT capabilities beyond conventional whole core resistivity analysis. Using the SA model, the simulation work first showed that the WCEMIT response is suitable for measuring the effects of dielectric properties, such as permittivity, dielectric loss factor, and permittivity anisotropy, and the effects of dielectric dispersion characteristic of the whole sample, denoted by the parameters of the Cole-Cole model. Then, I simulated a new whole core logging procedure using the FE model and developed a fast inversion scheme for the whole core logging measurements to estimate layer conductivity of 24-inch-long whole cores at a resolution of 1 inch and at 58.5 kHz. This new approach was applied to identifying cemented streaks in a trilaminar whole core. The WCEMIT measurements facilitated estimation of various electrical properties significant to improved subsurface resistivity interpretation in geologically-complex reservoirs.

Table 3.1: Brine conductivity (σ_w) used to obtain specific conductivity anisotropy (λ_c) for the 0°-dip and 45°-dip bilaminar TIVAR-brine synthetic cores at 58.5 kHz.

σ_w (mS/m)	λ_c
50	1
360	2
1165	5
2500	10

Table 3.2: Estimated values of true conductivity (σ_t) and porosity exponent (m) of various glass-bead packs at 58.5 kHz.

Pack #	σ_w (mS/m)	ϕ_{tot} (%)	σ_t (mS/m)	m
1	2620	38.7	740	1.33
2	2620	37.5	710	1.33
3	2620	37	705	1.32
4	2620	27	455	1.34
5	2620	18.9	280	1.34

Table 3.3: Estimated values of bed conductivity ($\sigma_{t,b}$) of bed-1 and bed-2 of bilaminar glass-bead packs measured at 58.5 kHz.

Pack #	**Bed-1 ϕ_t (%)**	**Bed-2 ϕ_t (%)**	**Est. σ_{hor} (mS/m)**	**λ_c**	**Est. bed-1 $\sigma_{t,b}$ (mS/m)**	**Est. bed-2 $\sigma_{t,b}$ (mS/m)**
6	38	27	572	1.08	425	720
7	38	18.9	490	1.19	270	710
8	27	18.9	360	1.11	245	475

Table 3.4: Measured values of true conductivity (σ_t) and estimated values of host conductivity (σ_h) of 100%-brine-saturated vuggy glass-bead packs.

ϕ_i (%)	**Meas. σ_t (S/m)**	**Est. σ_h (mS/m)**
0	0.754	0.753
6.6	0.685	0.758
13	0.607	0.744
13.3	0.614	0.755
18	0.553	0.736
23	0.539	0.781
28	0.46	0.728

Table 3.5: Comparison of the induced voltage response of the *zz* coupling to a 24-inch-long cylinder, as shown in Figure 3.26a, against that to 24 1-inch-thick circular discs constituting a 24-inch cylinder, as shown in Figure 3.26b.

	Induced voltage response of the *zz* coupling to a 24-inch-long cylinder, as shown in Figure 3.26a		**Induced voltage response of the *zz* coupling to 24 1-inch-thick circular discs constituting a 24-inch cylinder, as shown in Figure 3.26b**	
Conductivity of the whole cores (S/m)	**Magnitude (nV)**	**Phase (°)**	**Magnitude (nV)**	**Phase (°)**
Air	0.0000		0.0000	
0.002	0.0488	-0.141	0.0488	0.259
0.005	0.1950	-0.068	0.1950	0.073
0.01	0.4388	-0.035	0.4388	0.025
0.02	0.9264	-0.019	0.9263	0.009
0.05	2.3892	-0.009	2.3888	0.001
0.1	4.8271	-0.007	4.8263	-0.002
0.2	9.7029	-0.007	9.7013	-0.005
0.5	24.3305	-0.013	24.3263	-0.012
1	48.7097	-0.025	48.7013	-0.024
2	97.4681	-0.048	97.4513	-0.048
5	243.7432	-0.118	243.7011	-0.117

Table 3.6: Induced voltage response of the *zz* coupling to a 1-inch-thick circular disc for various values of conductivity of the disc and for various locations.

	Induced voltage response of zz coupling (nV)		
Location of the 1-inch-thick circular disc (in.)	**0.01-S/m conductivity disc**	**0.1-S/m conductivity disc**	**1-S/m conductivity disc**
-12	0.00015	0.00171	0.01727
-11	0.00026	0.00291	0.02936
-10	0.00046	0.00513	0.05183
-9	0.00086	0.00946	0.09549
-8	0.00166	0.01824	0.1841
-7	0.00333	0.03663	0.3697
-6	0.00675	0.07433	0.75009
-5	0.01206	0.13273	1.33935
-4	0.00366	0.0403	0.4067
-3	-0.06103	-0.67129	-6.77386
-2	-0.12232	-1.34554	-13.57767
-1	-0.18612	-2.04733	-20.65936
0	-0.08316	-0.91469	-9.23005
1	0.17339	1.90731	19.24656
2	0.32299	3.55291	35.85213
3	0.24605	2.70661	27.3122
4	0.07662	0.84289	8.50559
5	0.02567	0.28244	2.85015
6	0.0097	0.10678	1.07752
7	0.00409	0.04498	0.45394
8	0.00188	0.02077	0.20957
9	0.00094	0.01034	0.10437
10	0.0005	0.00548	0.05532
11	0.00027	0.00306	0.03088
Sum of induced voltage responses for various locations of the disc	0.43866	4.82616	48.7017
Induced voltage response of a 24-inch cylinder of equivalent conductivity, as mentioned in Table 3.5	0.4388	4.8271	48.7097

Table 3.7: Comparison of the estimated values of conductivity of individual layers with and without the *z*-directed bucking coil for a whole core with random distribution of 1-S/m and 0.01-S/m conductivity layers.

Layer # (top to bottom)	**True Conductivity (S/m)**	**Estimated conductivity, without buck coil (S/m)**	**Estimated conductivity, with buck coil (S/m)**
1	1	1.0068	1.0024
2	1	0.9989	1.0023
3	0.01	0.0168	0.0112
4	1	0.9998	1.0021
5	0.01	0.0111	0.011
6	0.01	0.0144	0.0109
7	0.01	0.008	0.0108
8	0.01	0.015	0.0107
9	1	1.0013	1.0016
10	0.01	0.0091	0.0105
11	1	1.0075	1.0014
12	1	0.9953	1.0013
13	0.01	0.0188	0.0102
14	0.01	0.0062	0.0101
15	1	1.0038	1.001
16	0.01	0.0101	0.0099
17	0.01	0.0084	0.0098
18	0.01	0.0147	0.0097
19	0.01	0.0048	0.0096
20	0.01	0.0164	0.0095
21	0.01	0.0041	0.0094
22	1	1.0052	1.0003
23	1	0.9973	1.0002
24	0.01	0.0124	0.0091

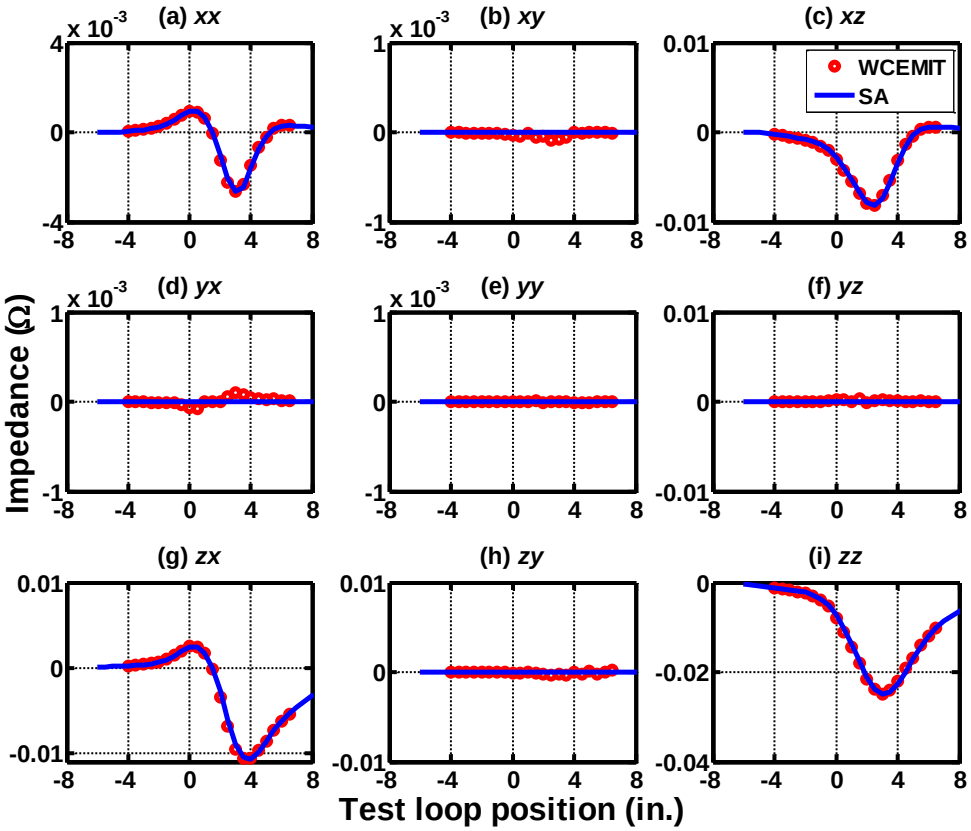

Figure 3.1: Comparison of the measured values against the SA model predictions of the WCEMIT impedance response at 58.5 kHz to a TTL at 0°-azimuthal orientation for various positions of the TTL along the tool axis.

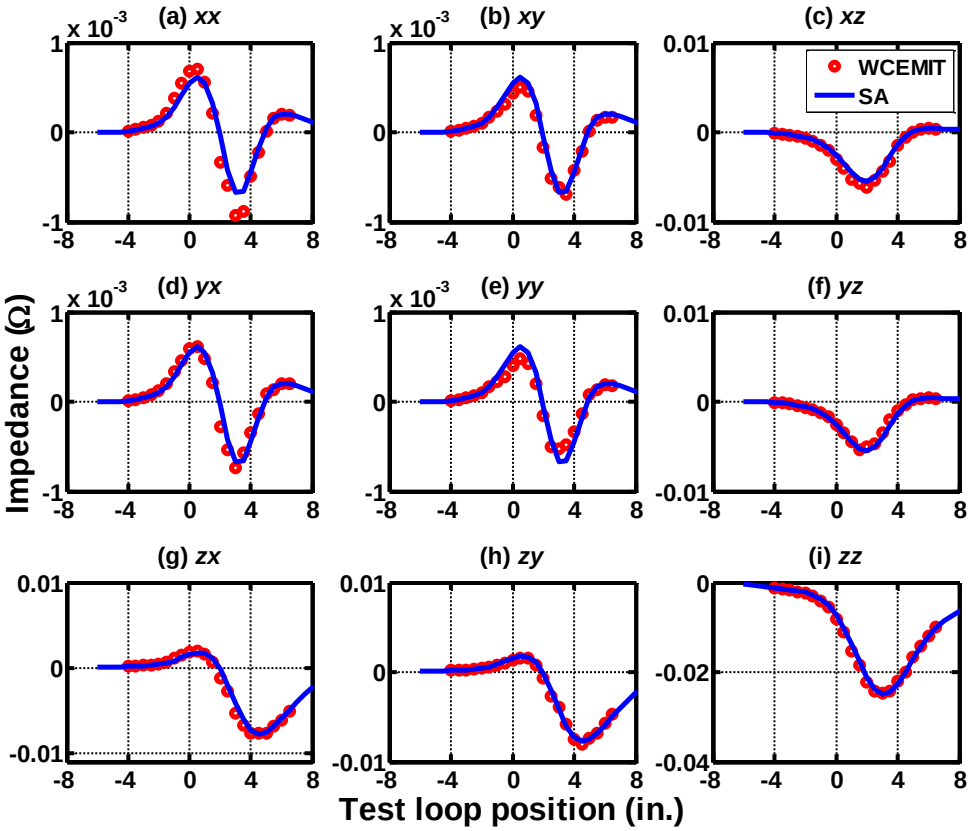

Figure 3.2: Comparison of the measured values against the SA model predictions of the WCEMIT impedance response at 58.5 kHz to a TTL at 45°-azimuthal orientation for various positions of the TTL along the tool axis.

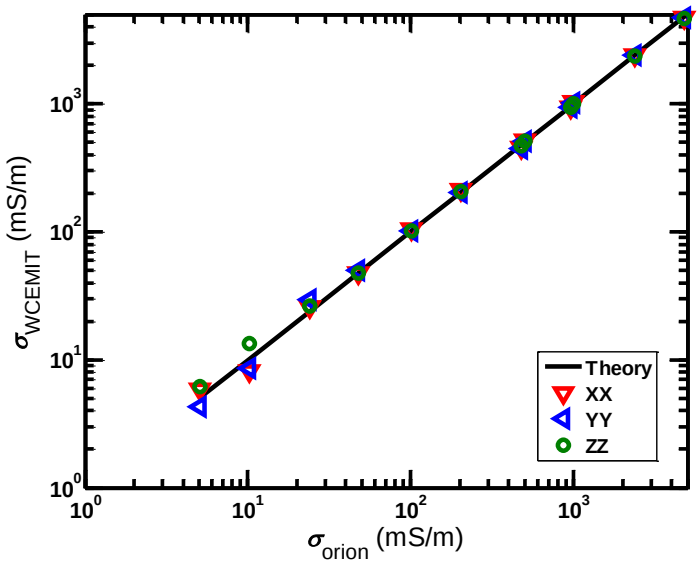

Figure 3.3: Comparison of the apparent conductivity response of the WCEMIT *xx*, *yy*, and *zz* couplings at 58.5 kHz against the conductivity response of Orion conductivity meter to an isotropic cylindrical volume of brine for varying values of conductivity of the brine, ranging from 5 mS/m to 5 S/m.

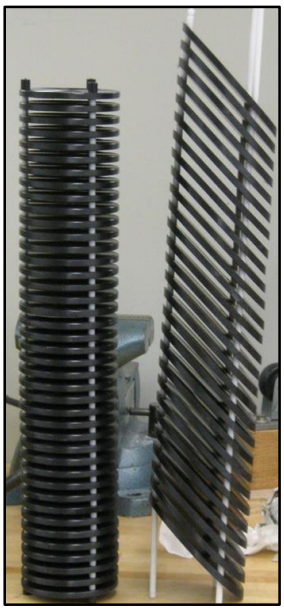

Figure 3.4: Frameworks of two synthetic bilaminar whole core samples of 0°-dip (left) and 45°-dip (right), respectively.

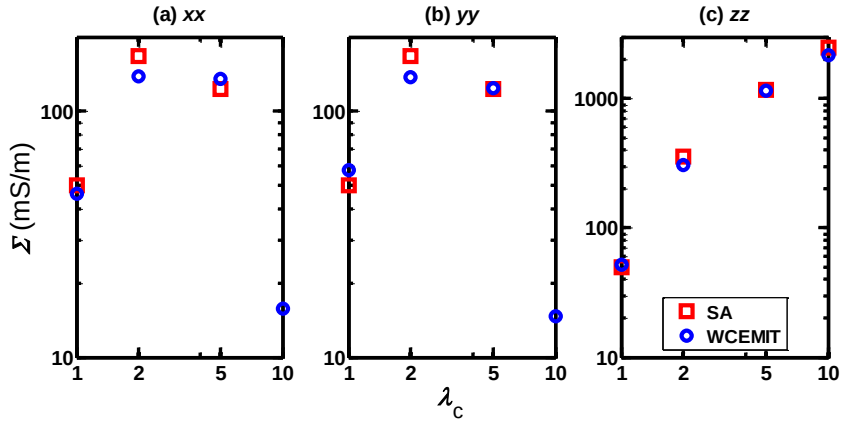

Figure 3.5: Comparison of the FE model predictions against the measured apparent conductivity responses of the *xx*, *yy*, and *zz* couplings at 58.5 kHz to four 0°-dip bilaminar synthetic cores of λ_c of 1, 2, 5, and 10, respectively.

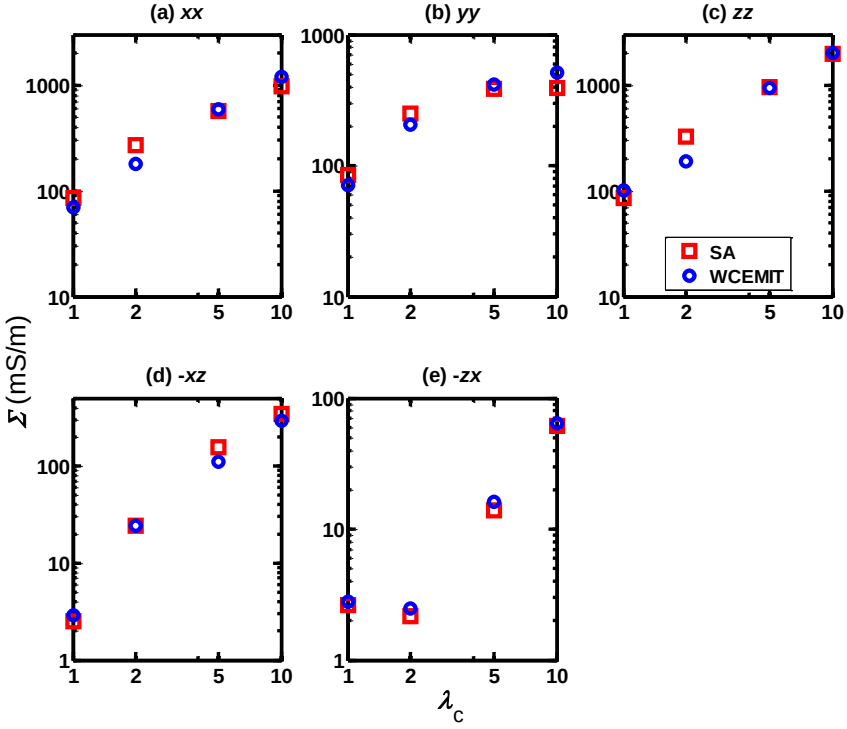

Figure 3.6: Comparison of the FE model predictions against the measured apparent conductivity responses of the *xx*, *yy*, *zz*, *-xz*, and *-zx* couplings at 58.5 kHz to four 45°-dip, 0°-azimuth bilaminar synthetic cores of λ_c of 1, 2, 5, and 10, respectively.

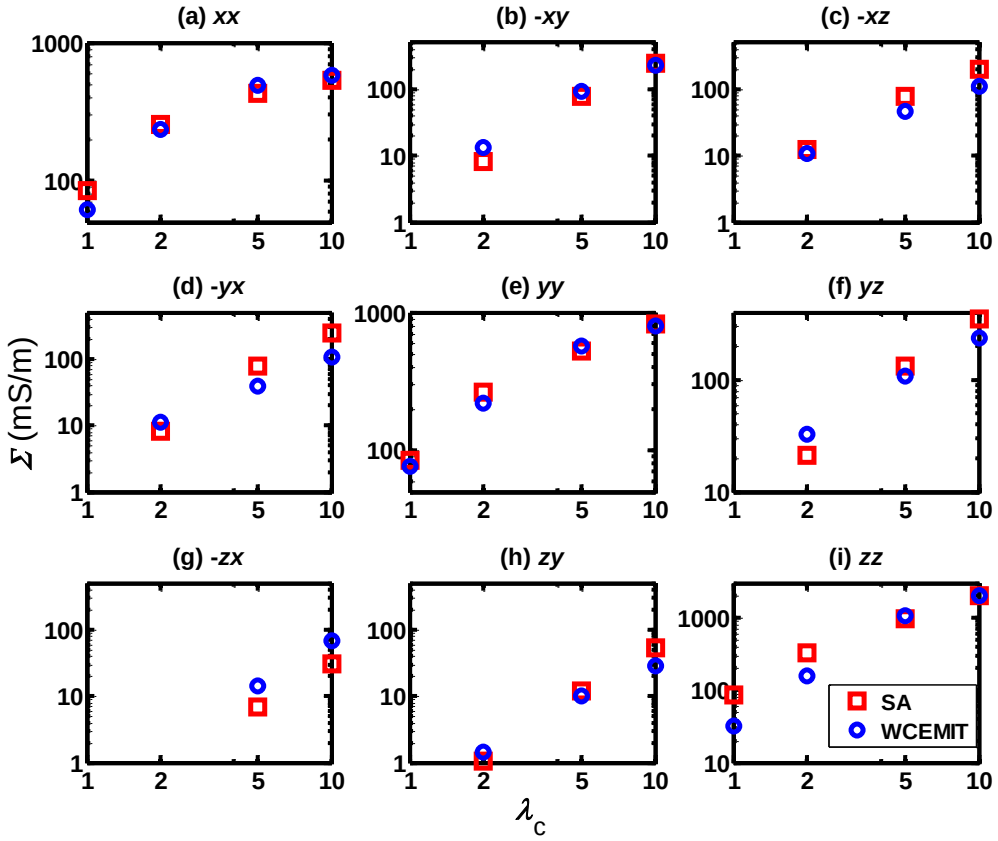

Figure 3.7: Comparison of the FE model predictions against the measured apparent conductivity responses of all nine couplings at 58.5 kHz to four 45°-dip, 60°-azimuth bilaminar synthetic cores of λ_c of 1, 2, 5, and 10, respectively.

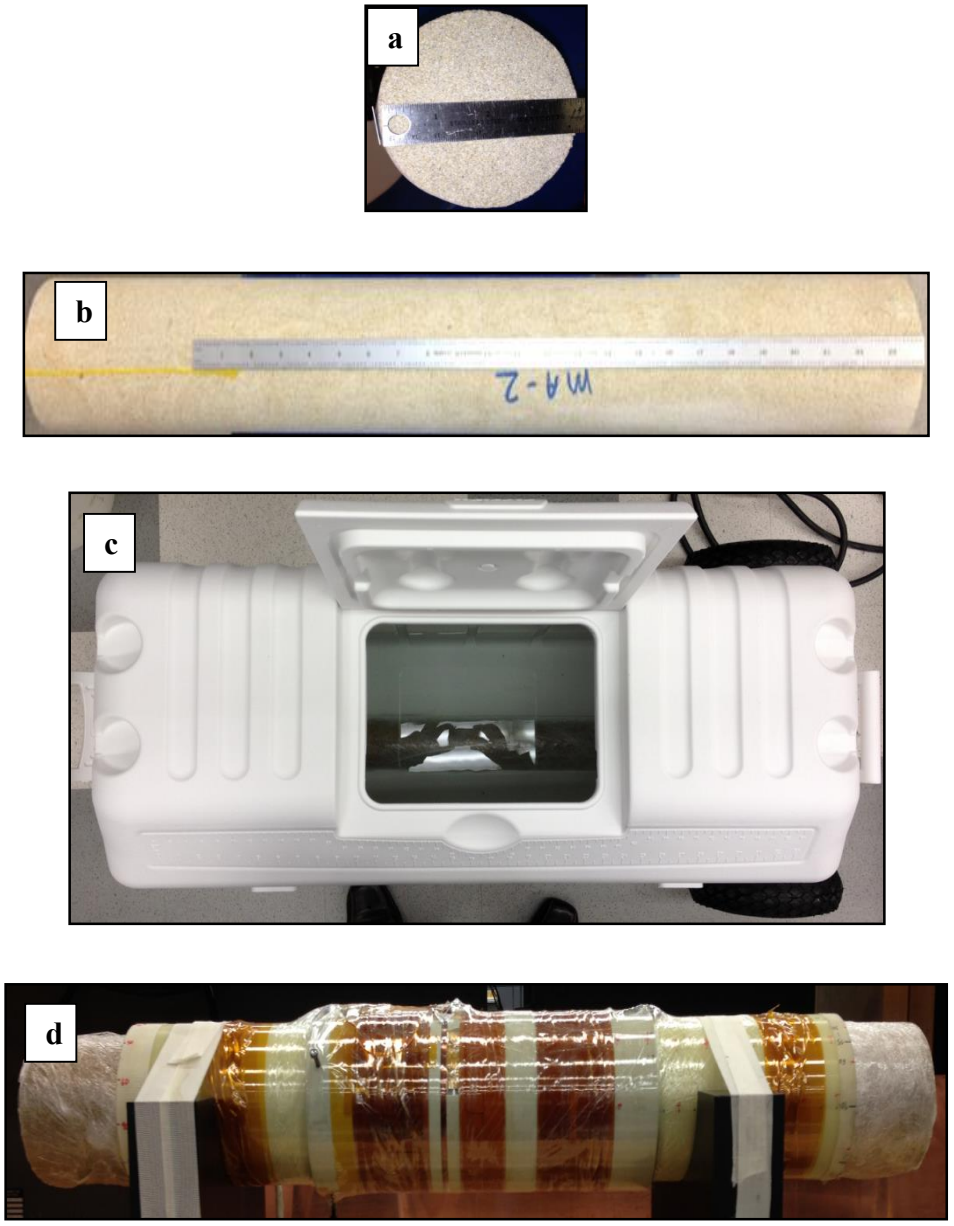

Figure 3.8: Photograph of (a) side view and (b) top view of the 4-inch-diameter Berea whole core sample. (c) Fully saturated Berea whole core samples stored in 7.64-S/m-conductivity brine. (d) Berea whole core sample placed inside the WCEMIT conduit for the conductivity tensor measurement.

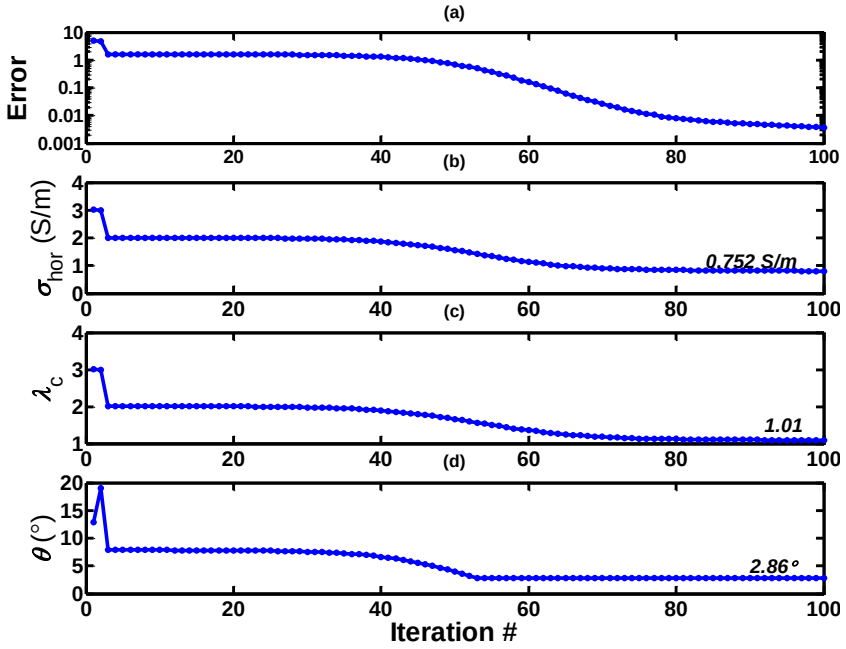

Figure 3.9: Convergence of the estimates of (a) error, (b) σ_{hor}, (c) λ_{c}, and (d) θ during the inversion of rotated conductivity tensor of the Berea whole core sample.

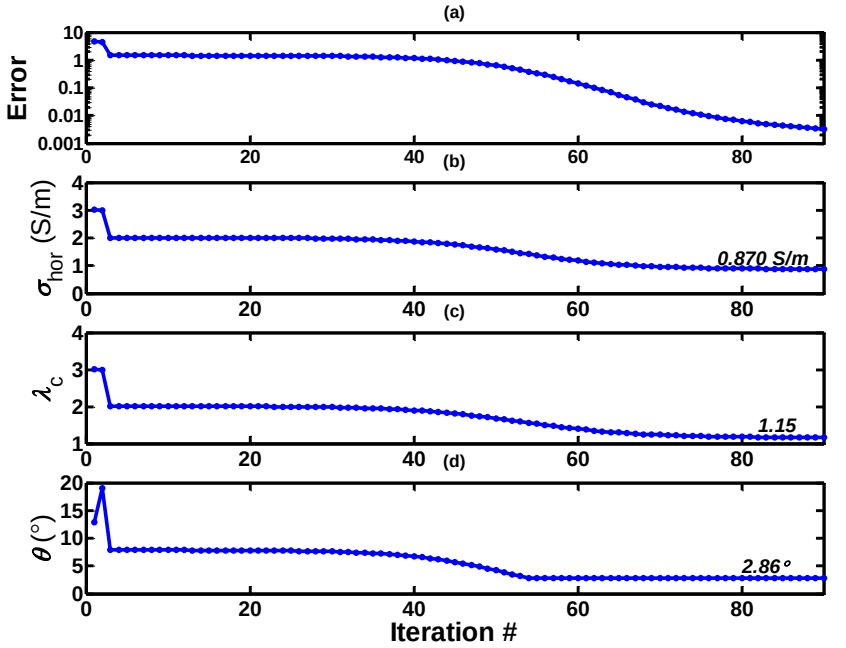

Figure 3.10: Convergence of the estimates of (a) error, (b) σ_{hor}, (c) λ_{c}, and (d) θ during the inversion of rotated conductivity tensor of Boise whole core sample.

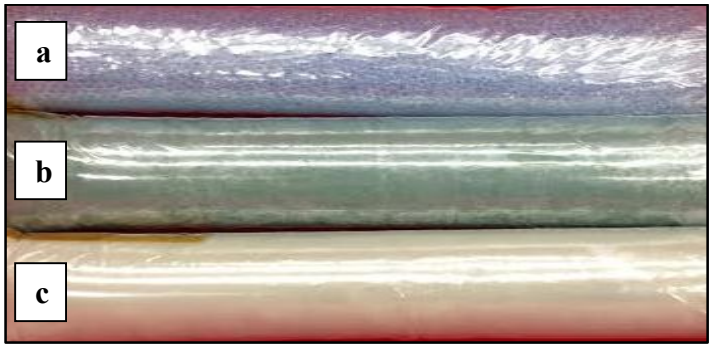

Figure 3.11: Side view of the three 2-feet-long, 4-inch-diameter brine-filled glass-bead packs made of (a) 6-mm, (b) 1.15-mm, and (c) 0.25-mm-diameter glass beads that are referred to as Pack-1, Pack-2, and Pack-3, respectively.

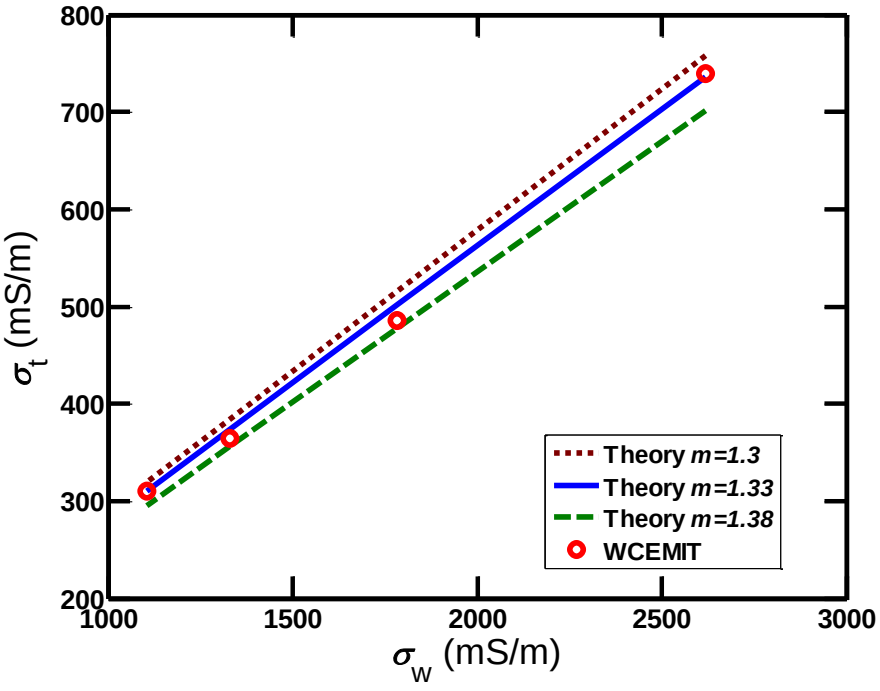

Figure 3.12: Relationship of the true conductivity (σ_t) of brine-saturated glass-bead packs made of 6-mm-diameter glass beads and pore-filling brine conductivity (σ_w). Theoretical predictions based on the Archie's equation are plotted for the porosity exponent (m) values of 1.3, 1.33, and 1.38.

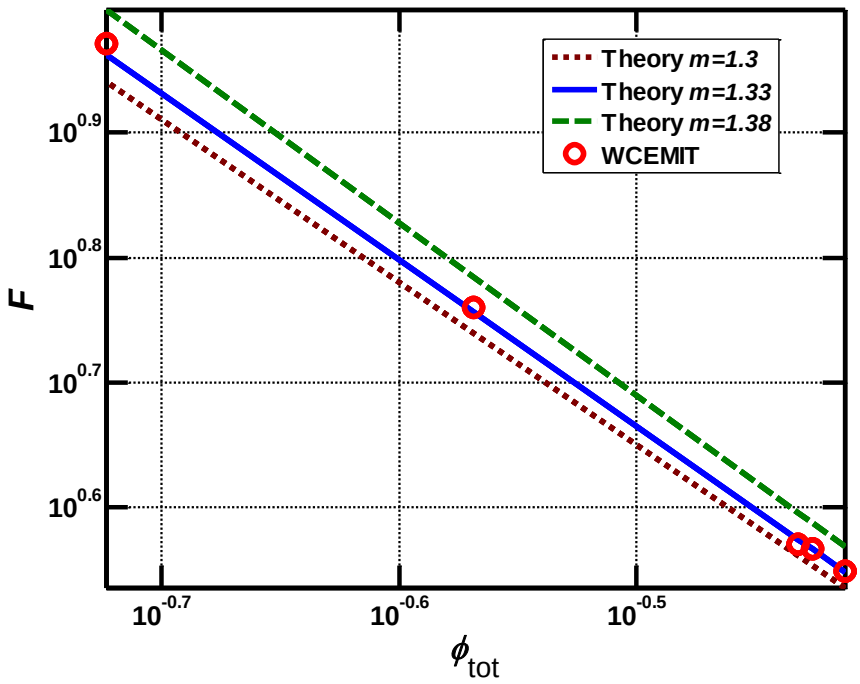

Figure 3.13: Relationship of the formation factor (F) of brine-saturated glass-bead packs and the brine-filled total porosity (ϕ_{tot}). Theoretical predictions based on the Archie's equation are plotted for porosity exponent (m) values of 1.3, 1.33, and 1.38.

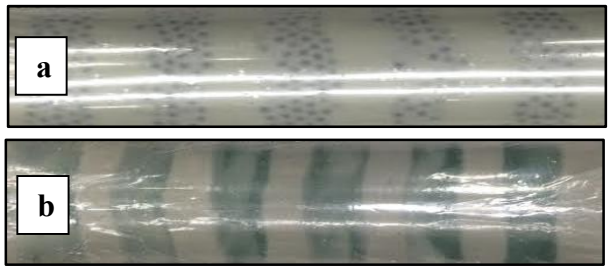

Figure 3.14: Side view of 2-feet-long, 4-inch-diameter brine-filled bilaminar glass-bead packs: (a) Pack-6 and (b) Pack-7.

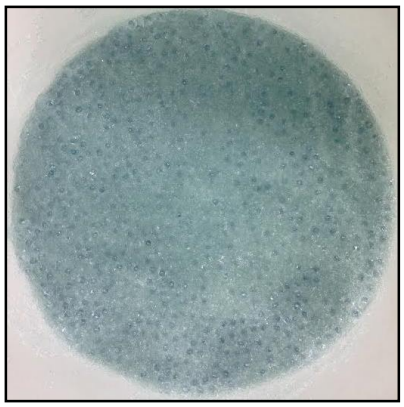

Figure 3.15: Top view of 4-inch-diameter brine-filled glass-bead pack identifying vuggy isotropic whole core. Uniformly distributed 6-mm glass beads identify non-conductive vugs, and the remaining brine-filled volume made of 1.15-mm-diameter glass beads identifies the fluid-saturated porous matrix.

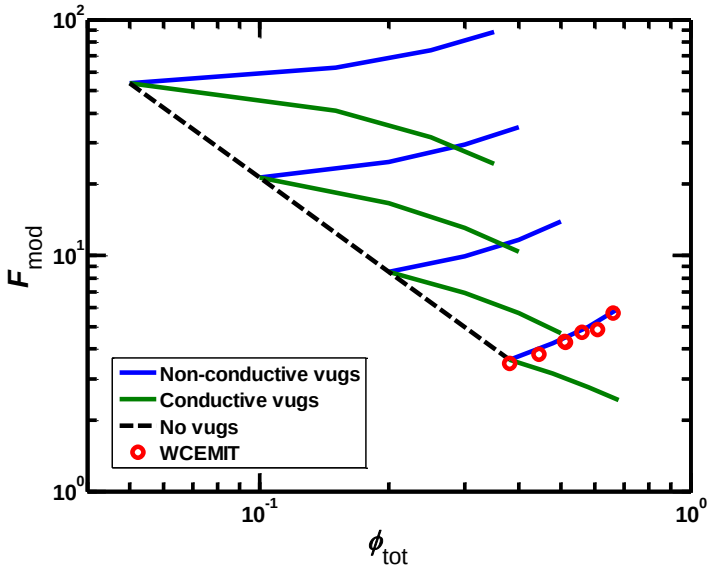

Figure 3.16: Comparative plot of deviation of the formation factor (F_{mod}) of glass-bead packs containing conductive (green curve) or non-conductive (blue curve) vugs from the Archie's formation factor (F) of packs containing no vugs (dashed line) for various values of total porosity (ϕ_{tot}) of the mixture. ϕ_{tot} includes inter-granular porosity (ϕ_{h}) and isolated vuggy porosity (ϕ_{i}). The value of ϕ_{tot} at which blue and green curves deviate from the black line indicates the ϕ_{h} of the pack, and $\phi_{\mathrm{t}} - \phi_{\mathrm{h}}$ indicates the vuggy porosity of the pack.

Figure 3.17: (a) A 2-feet-long, 4-inch-diameter synthetic whole core comprising 0.25-inch TIVAR elliptical discs separated by 0.75 inches and oriented at 45°-dip. (b) Schematic of such a whole core.

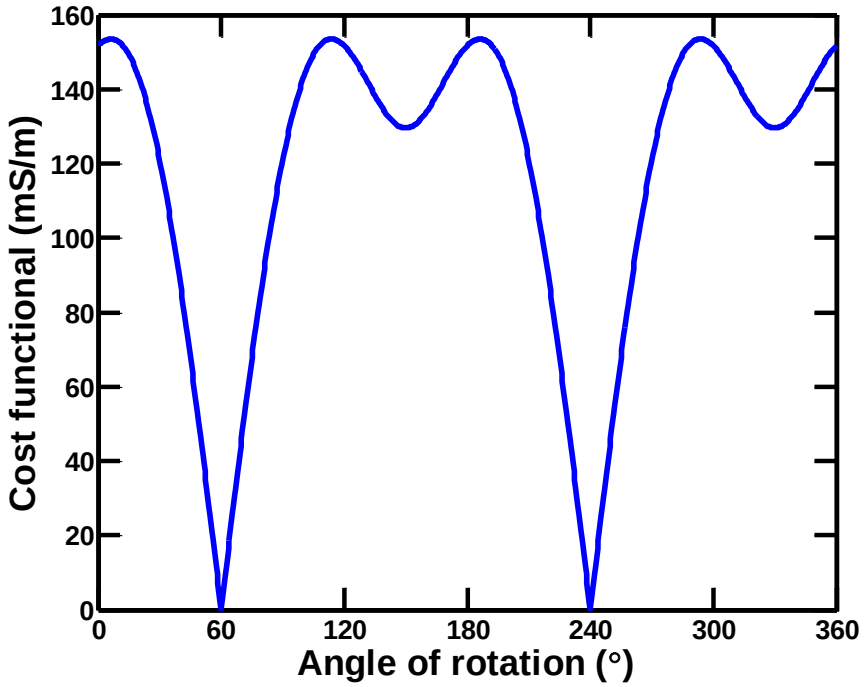

Figure 3.18: The cost functional as a function of angle of rotation of the complex conductivity tensor.

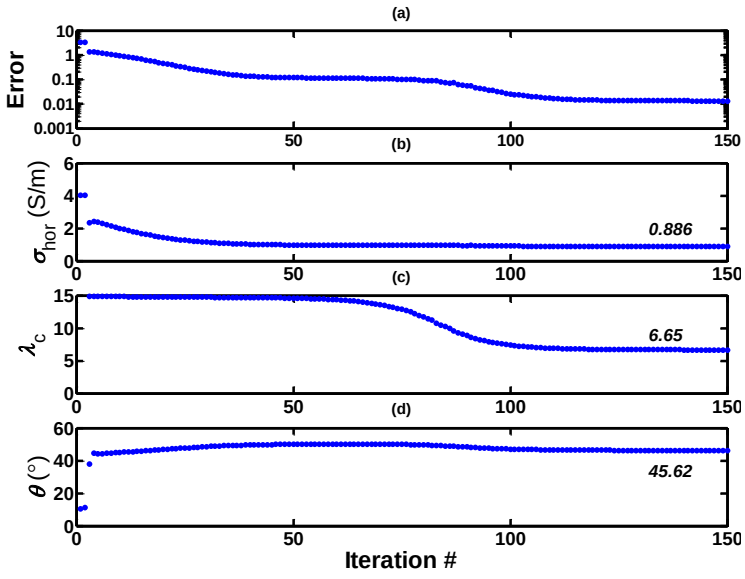

Figure 3.19: Convergence of the estimates of (a) error, (b) σ_{hor}, (c) λ_{c}, and (d) θ during inversion of the rotated conductivity tensor of 45°-dipping bilaminar TIVAR-brine synthetic core.

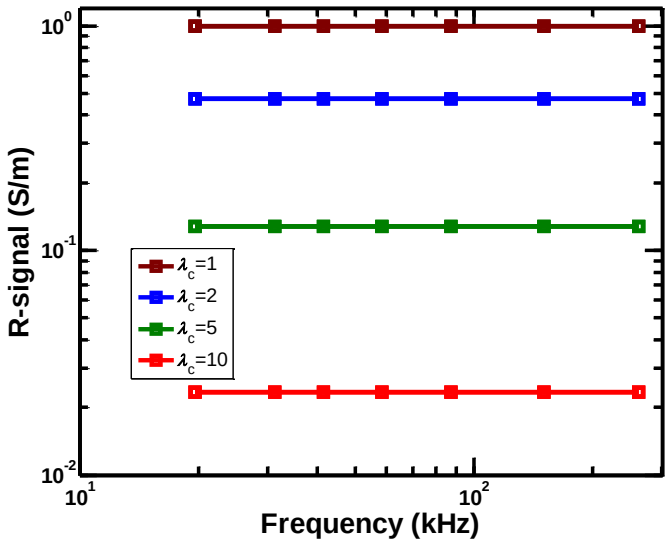

Figure 3.20: SA model predictions of the WCEMIT R-signal response of *yy*-coupling to a cylindrical volume of σ_{hor} of 1 S/m, λ_{p} of 1, and $\varepsilon_{\mathrm{r,hor}}$ of 1 for various values of conductivity anisotropy ratio (λ_{c}) of the cylindrical volume.

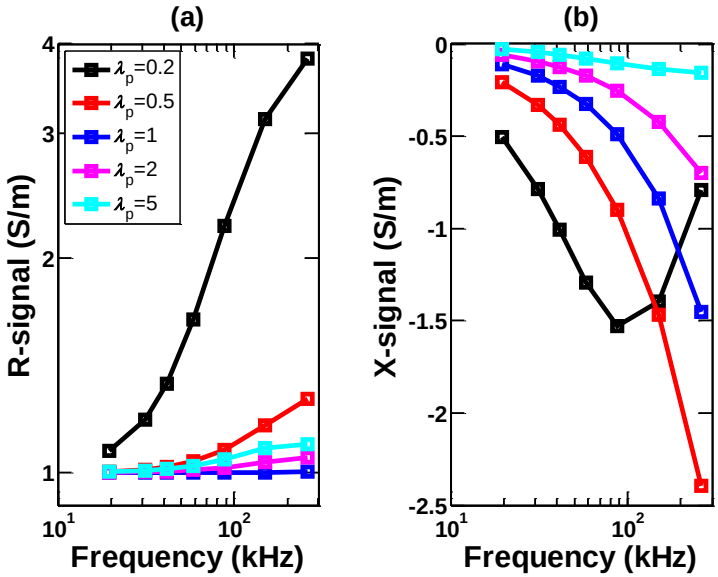

Figure 3.21: SA model predictions of the (a) R-signal and (b) X-signal responses of the *yy*-coupling to a cylindrical volume of σ_{hor} of 1 S/m, λ_c of 1, and $\varepsilon_{r,hor}$ of 10^5 for various values of λ_p of the cylindrical volume.

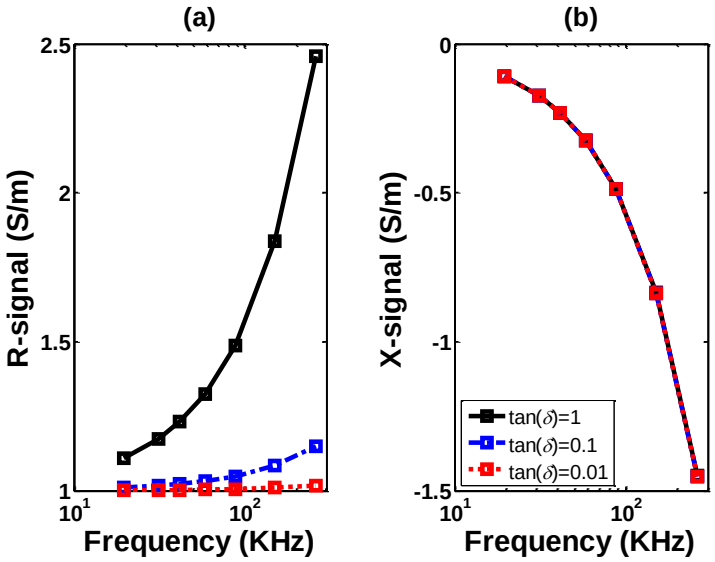

Figure 3.22: SA model predictions of the (a) R-signal and (b) X-signal responses of the *zz*-coupling to a cylindrical volume of σ_{hor} of 1 S/m, λ_c of 1, λ_p of 1, and $\varepsilon_{r,hor}$ of 10^5 for various values of dielectric loss factor (δ).

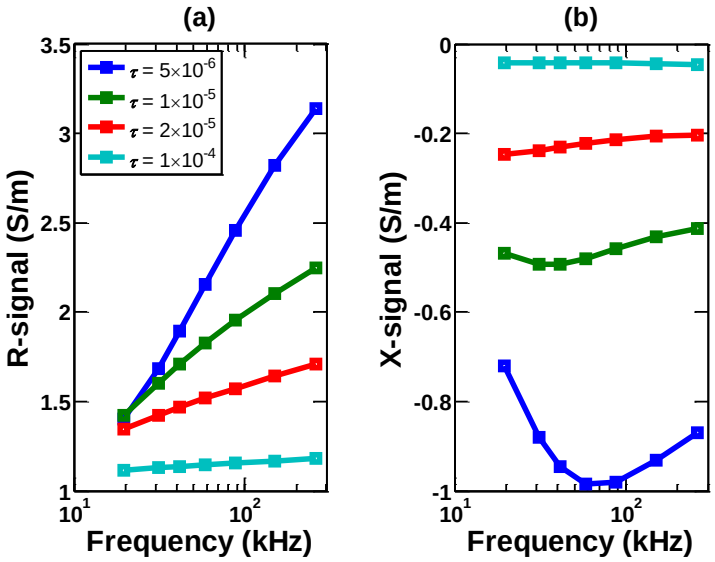

Figure 3.23: SA model predictions of the (a) R-signal and (b) X-signal responses of the *zz*-coupling to an isotropic cylindrical volume of σ_{hor} of 1 S/m, λ_c of 1, λ_p of 1, $\varepsilon_{r,s}$ of 10^6, and α of 0.15 for various values of τ (s).

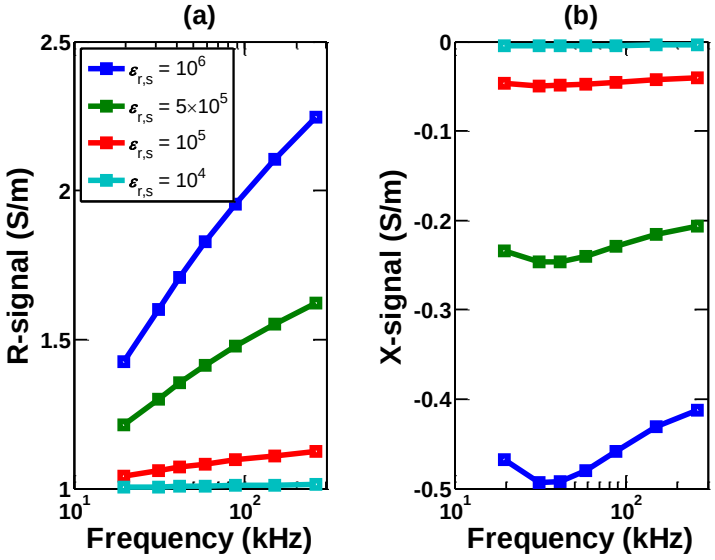

Figure 3.24: SA model predictions of the (a) R-signal and (b) X-signal responses of the *zz*-coupling to an isotropic cylindrical volume of σ_{hor} of 1 S/m, λ_c of 1, λ_p of 1, τ of 10^{-5} s, and α of 0.15 for various values of $\varepsilon_{r,s}$.

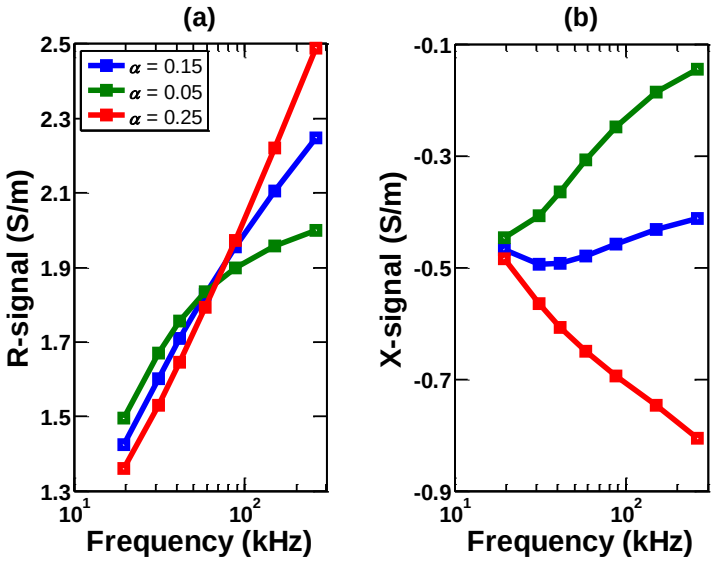

Figure 3.25: SA model predictions of the (a) R-signal and (b) X-signal responses of the *zz*-coupling to an isotropic cylindrical volume of σ_{hor} of 1 S/m, λ_c of 1, λ_p of 1, τ of 10^{-5} s, and $\varepsilon_{r,s}$ of 10^6 for various values of α.

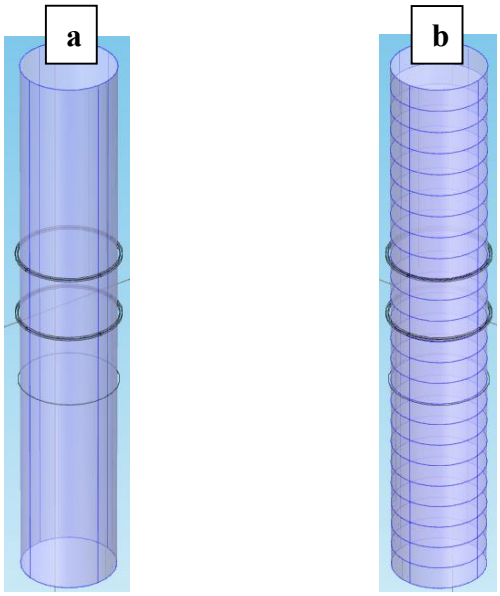

Figure 3.26: (a) A 24-inch-long cylinder placed coaxially inside the coaxial *z*-directed transmitter, receiver, and bucking coils (schematic representation). (b) 24 1-inch-thick, juxtaposed, circular discs that are placed coaxially inside the transmitter, receiver, and bucking coils to constitute a 24-inch-long cylinder.

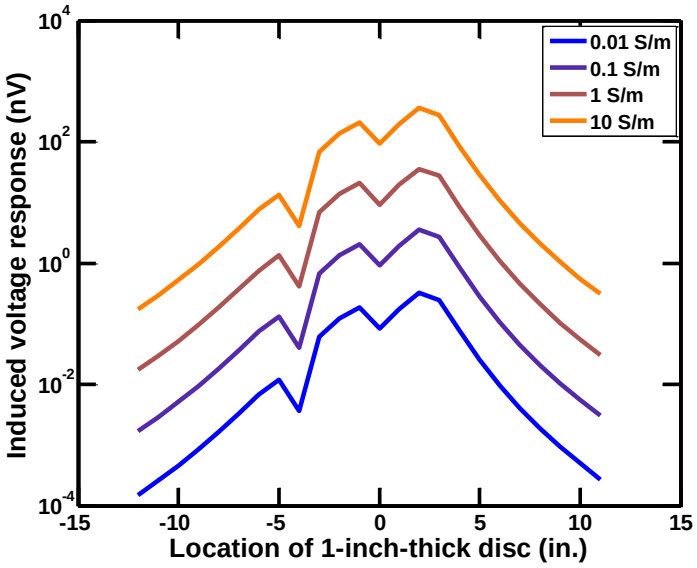

Figure 3.27: Induced voltage response of the *zz* coupling to 1-inch-thick 0°-dip coaxial circular disc located at various distance from z=0.

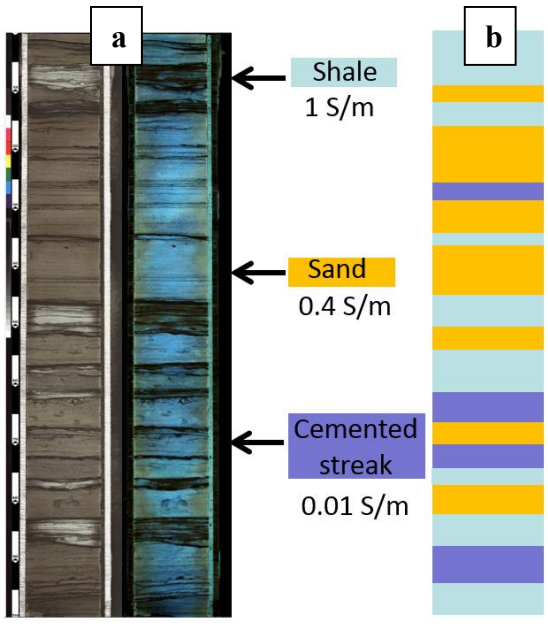

Figure 3.28: (a) A CT scan and UV fluorescence image of a whole core from a turbidite reservoir comprising sand, shale, and cemented layers. (b) A conductivity model of the turbiditic whole core for purposes of computing the whole core logging measurements.

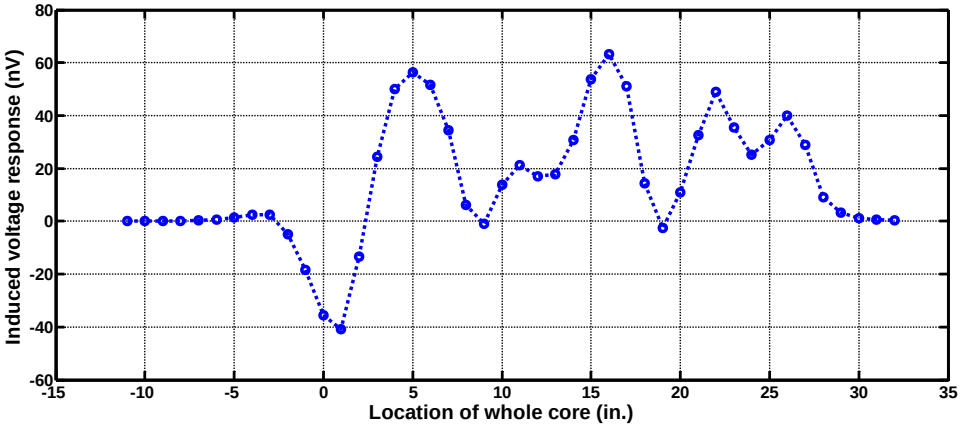

Figure 3.29: Modeled induced voltage response to synthetic whole core shown in Figure 3.28b as the whole core is coaxially translated from -11 to +32 inches.

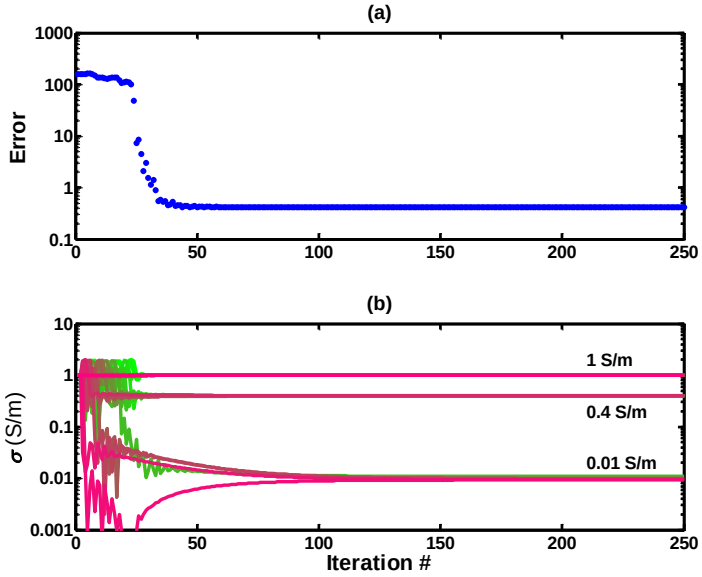

Figure 3.30: Convergence of the estimates of (a) error and (b) σ of each layer during inversion of the whole core logging measurements on synthetic whole core shown in Figure 3.28b.

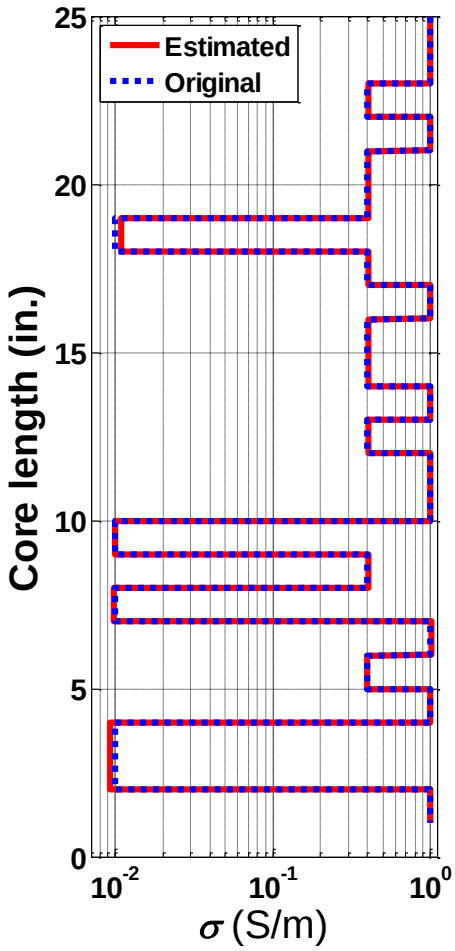

Figure 3.31: Comparison of estimated conductivity of the synthetic model of the turbiditic sequence in Figure 3.28b with the true conductivity of each layer.

Chapter 4: Effective Electrical Conductivity and Dielectric Permittivity of Samples Containing Disseminated Mineral Inclusions

Organic-rich mudrock and source-rock formations generally contain electrically conductive pyrite and graphitic-precursor mineralization in the form of veins, laminations, flakes, and grains. In redox-inactive subsurface conditions, when an external electromagnetic (EM) field is applied to geomaterials containing conductive mineral inclusions, ions in the pore-filling brine and charge carriers in the electrically conductive mineral inclusions, namely electrons and holes, accumulate/deplete at impermeable host-inclusion interfaces giving rise to perfectly-polarized interfacial polarization (PPIP) phenomena (explained in detail in Chapter 5). Such polarization phenomena influence the diffusion, accumulation, and migration of charge carriers in a geomaterial; thereby, altering its effective electrical conductivity (σ_{eff}) and effective relative dielectric permittivity ($\varepsilon_{r,eff}$). In addition, the relaxation process associated with the interfacial polarization phenomena and the time required to fully develop the field-induced polarization give rise to the frequency dispersive σ_{eff} and $\varepsilon_{r,eff}$ of mudrocks and source rocks containing pyrite and graphitic-precursor inclusions. I investigate the effects of the PPIP phenomena exhibited by pyrite-bearing and graphite-bearing samples on their directional and frequency dispersive electrical properties. To that end, I first use the WCEMIT to measure the directional multifrequency EM response of 4-inch-diameter, 2-ft-long glass-bead packs containing uniformly distributed pyrite and graphite inclusions. The semi-analytic EM forward model (SA Model) was then implemented to estimate the σ_{eff} and $\varepsilon_{r,eff}$ of the conductive-mineral-bearing glass-bead packs. I observe significant frequency dispersion of the estimated electrical properties, large values of effective relative permittivity, and significant alteration in the effective conductivity due to the variation in volume content

and size of conductive mineral inclusions. Also, conductive-mineral-bearing packs exhibit conductivity anisotropy and permittivity anisotropy due to the effects of polarization of the disseminated mineral inclusions.

4.1 INTRODUCTION

Organic-rich mudrocks and source-rock formations containing conductive mineral inclusions, clay minerals, and clay-sized particles exhibit frequency dispersive effective electrical conductivity and large effective dielectric permittivity in the EM induction frequency range due to the interfacial polarization phenomena at host-inclusion interfaces. The interfacial polarization phenomena significantly influence charge-carrier migration, accumulation, and diffusion processes (Schmuck and Bazant, 2012; Wong, 1979). Anderson et al. (2006), Wang and Poppitt (2013), and Misra et al. (2015d) mentioned that limited laboratory and numerical modeling work has been published on the effects of interfacial polarization of electrically conductive inclusions on subsurface galvanic, EM induction, and EM propagation measurements. Conventional resistivity interpretation methods typically give rise to inaccurate results in pyrite-bearing sedimentary formations (Altman et al., 2008), pyrite-bearing mudrocks (Kethireddy et al., 2014), and pyrite-bearing and graphitic-precursor-bearing source-rock formations (Anderson et al., 2008).

Passey et al. (2010) mentioned the challenges in resistivity interpretation due to the presence of conductive pyrite and graphitic-precursor inclusions in source-rock formations and shale gas reservoirs. Witkowsky et al. (2012) emphasized that there is a linear correlation of the total organic content (TOC) and pyrite content, and resistivity measurements should be corrected for the effects of pyrite content prior to using resistivity measurements in the delta logR method. Recently, Chen and Heidari (2014) showed that

the directional dielectric permittivity estimation is strongly affected by the presence and connectivity of mature organic matter and pyrite inclusions.

Clavier et al. (1976) measured the effect of pyrite inclusions on various resistivity logging measurements. They observed a strong dependence of the resistivity measurements on the distribution of pyrite inclusions and operating frequency of the logging tool. Despite the absence of electrical connectivity of the pyrite phase, an increase in frequency of electrical measurements led to an increase in electrical conductivity of the mixture. Clavier et al. (1976) also showed that the frequency dispersion of conductivity response of a pyrite-bearing mixture depends on the operating frequency, pyrite volume fraction, and pore-filling brine salinity. Recently, Clennell et al. (2010) observed that the disseminated pyrite inclusions in sandstones resulted in a drastic decrease in resistivity when pyrite content exceeded 5% volume fraction. They used the Hanai-Bruggeman equation in the 1 Hz to 100 kHz frequency range to model the experimentally-measured effective conductivity and dielectric permittivity response of sandstones containing disseminated pyrite grains. However, Clennell et al. (2010) neglected the effects of interfacial polarization of pyrite inclusions. More recently, Yu et al. (2014) showed that both the laboratory and downhole measurements in high TOC marine shale formations exhibited frequency dispersion of the 0.1 Hz to 10 kHz frequency range due to the presence of pyrite inclusions of weight fraction in the range of 1 to 5 wt%. They suggested that the implementation of a complex resistivity method could improve resistivity interpretations in marine shale gas formations. Further, they used the empirical dual Cole-Cole model (instead of a mechanistic formulation) to analyze their data.

Al Duhailan et al. (2014) observed anomalous reversal in resistivity-thermal maturity relationship in Niobrara formation when the formation changes from wet-gas

window to dry-gas window. They explained the decrease in resistivity as a consequence of the change in wettability of the formation from oil-wet to water-wet state with the over-maturation of the organic-rich source rocks. However, I propose that the generation of graphitic-carbon (carbonization) during kerogen maturation as the reason for the reduction in resistivity of organic-rich mudrocks and source rocks with the maturation of the interstitial kerogen. Walters et al. (2014) performed high resolution transmission electronic microscopy (HRTEM) experiments on shales of thermal maturity in the range of 0.6 to >4.5%Ro. They found isolated turbostatic carbon nanostructures whose volume content increased with increase in the maturity of the shale rock. Also, the presence of such carbon nanostructures corresponded to the mature zones exhibiting anomalously high electrical conductivity in the well logs. They concluded that the frequency of occurrence of carbon nanostructures correlated with the abundance of organic carbon, its maturity, and macroscopic electrical conductivity. Also, Romero-Sarmiento et al. (2014) performed HRTEM experiments on powdered Barnett shale rocks and isolated kerogen samples. The HRTEM-generated images showed nanoscale polyaromatic layers and carbon nanostructures in mature organic-rich shale rock samples.

Since 1980s, the generation of graphitic-carbon due to carbonization and/or graphitization of kerogen has been experimentally observed when kerogen is synthetically matured by increasing the applied temperature and pressure (Spötl et al., 1998). Al Duba (1983) performed laboratory-maturation experiments on Green River Shale rocks. He observed that the initial bulk conductivity of 10^{-7} S/m started increasing around 400 °C, which corresponded to the onset of hydrocarbon generation and aromatization of the residual kerogen. The bulk conductivity reached a maximum conductivity value of 10 S/m at 700 °C, which was attributed to the graphitic-precursor generated during the maturation

process. Recently, Buseck and Beyssac (2013) mentioned that the graphitic-precursor can be used for geothermometry to quantify low-grade metamorphism (330 °C). They showed that the graphitization of organic matter resulted in wide variety of intimately mixed conductive structures that exhibit microporous, ring, lamellar, and planar nanostructures. Allan et al. (2013) observed 82% decrease in resistivity measurements on organic-rich shale rocks upon thermal maturation to the wet-gas window. The baseline resistivity measurements of those rocks before the maturation were extremely high, in the order of 20000 ohm-m, because of the lack of connected conductive pore fluid. Consequently, Allan et al. (2013) attributed the decrease in the resistivity measurements with maturation to the carbonization of the kerogen and the conversion of smectite to illite.

The primary objective of this Chapter is to describe the effects of interfacial polarization of conductive mineral inclusions on the EM response of WCEMIT in the EM induction frequency range of 10 kHz to 300 kHz. WCEMIT allows non-contact, directional, multi-frequency, inductive-complex conductivity measurements on whole core samples containing pyrite and/or graphite inclusions. I analyze the WCEMIT measurements (R- and X-signal responses) using the SA model, introduced in Chapter 2. In doing so, I estimate $\varepsilon_{r,eff}$ and σ_{eff} of the conductive-mineral-bearing glass-bead packs. I also compare the measured responses and estimated values of electrical properties of the packs containing graphite inclusions with those containing pyrite inclusions. This comparison can facilitate discrimination of pyrite and graphite based on the WCEMIT response. Finally, I study the WCEMIT response to layered glass-bead packs having layers containing pyrite or graphite inclusions alternating with uncontaminated layers. This study will test the accuracy of laminated shale sand analysis in layered formations, wherein some layers exhibit high dielectric permittivity and frequency dispersive electrical properties.

4.2 MATERIALS AND METHODS

Two 4-inch-outer-diameter, 3.8-inch-inner-diameter, 2-ft-long cylindrical glass vases were used to prepare the glass-bead packs. An inclusion-free glass-bead pack (Figure 4.1a) was prepared by filling the glass vase with 575-μm-radius glass beads and then fully saturating the pore spaces between the glass beads with 3.75-S/m-conductivity brine. A conductive-mineral-bearing pack (Figures 4.1b and 4.1c) was prepared by filling the glass vase with a mixture of 575-μm-radius glass beads and conductive mineral inclusions of a particular size to obtain a 2-inch thick layer. Following that, 3.75-S/m-conductivity brine is poured into the glass vase to fully saturate the 2-inch thick layer. The vase was then vibrated using a mechanical hand-held shaker to consolidate the mixture, remove trapped air bubbles, and uniformly distribute the pore-filling brine. The three above-mentioned steps were repeated until the entire glass vase was tightly-filled with glass beads, inclusions, and brine. I consistently prepared 2-ft-long glass-bead packs having brine-filled porosity of approximately 38%. Two sizes of nearly-spherical pyrite inclusions were used for this study, namely the Pyrite Red (average diameter = 50 μm) and Pyrite Yellow (average diameter = 130 μm) grains manufactured by Washington Mills (http://www.washingtonmills.com/products/iron-pyrite/). Two sizes of flaky graphite inclusions were used in this work, namely the #2 flake graphite (50×200 mesh size, average surface area = 0.02 mm^2) and the #1 flake graphite (50×80 mesh size, average surface area = 0.06 mm^2) manufactured by Dixon Graphite. The glass beads used in this work are 1.15-mm-diameter Megalux beads manufactured by Swarco Company (http://www.swarco.com/en/Products-Services/Traffic-Materials/Glass-Beads).

Multi-frequency inductive-complex conductivity measurements were obtained with the WCEMIT, described in Chapter 2. The WCEMIT operates at seven frequencies

in the frequency range of 10 kHz to 300 kHz. The WCEMIT measurements on the conductive-mineral-bearing glass-bead packs were inverted using the SA model to obtain the $\varepsilon_{r,eff}$ and σ_{eff}. Prior to performing the WCEMIT measurements on conductive-mineral-bearing glass-bead packs, the WCEMIT system was calibrated for each of the seven operating frequencies and for each of the nine transmitter-receiver coupling using the tilted-test loop method, as described in Chapter 3. Following that, the directional conductivity measurements were performed on the brine samples of known conductivity for each of the seven operating frequencies, as described in Chapter 3. After the WCEMIT calibration, the brine-saturated inclusion-free glass-bead pack (Figure 1a) was measured to record the variations in the R- and X-signal responses of each of the nine transmitter-receiver couplings at each of the seven operating frequencies. This frequency-dependent variations in the R- and X- signal responses to the inclusion-free glass-bead packs are associated with the undesirable polarization of glass beads and the vase, and is also associated with the frequency-dependent magnitude and phase changes due to the peripheral electronics of the system. These variations in the R- and X-signal responses of each of the nine couplings at the seven operating frequencies were used for the final gain corrections on subsequent measurements of R- and X-signal responses to glass-bead packs containing inclusions.

In the laboratory, one can measure weights of the inclusion and host phases more accurately than their volumes because the volume measurements require correction for the volume occupied by air. Measured weights are converted to volumes using the measured densities of the host and inclusion phases to obtain the volume fraction of the inclusion phase. I present my laboratory results as a function of the volume fraction of the inclusion phase to enable petrophysicists and geoscientists to better correlate the results of my

findings with subsurface and laboratory measurements, which are generally carried out as a function of the volume fraction. I measured that 308.65 g of the air-filled unconsolidated pack of glass beads occupied 210 cm^3, and the density of the air-filled unconsolidated pack of glass beads is 1.47 g/cm^3 (bulk density), while that of only the glass beads is 2.37 g/cc (density), assuming 40% air-filled porosity of the glass-bead packs. These values are in the range of the bulk density of 1.2 to 1.8 g/cc and that of the density of 2.2 to 2.6 g/cc of the Megalux Beads as reported in the Swarco Safety Data Sheet (2004). I also measured that 15 g of air-filled unconsolidated pack of graphite flake #2 occupied 20 cm^3, which amounts to a density of 0.75 g/cm^3 of the air-filled unconsolidated pack of graphite flake #2. This value is in agreement with the bulk density of graphite flakes as reported in several publications (e.g., Franklin Miller Inc., 2015). Further, I measured that 93 g of the air-filled unconsolidated pack of Pyrite Red particles occupied 68 cm^3, which amounts to a density of 1.37 g/cm^3 of the air-filled unconsolidated pack of Pyrite Red particles. This value is in agreement with the bulk density of pyrite powder as reported in several publications (e.g., Ken and Stewart, 1999).

4.3 EFFECTS OF UNIFORMLY DISTRIBUTED PYRITE INCLUSIONS

4.3.1 R- and X-signal responses

Using the WCEMIT system, I first measured the R- and X-signal responses of the *zz* (Figure 4.2) and *yy* (Figure 4.3) couplings to the glass-bead packs containing uniformly distributed Pyrite Red inclusions for volume fractions of the inclusion phase of 0.5%, 1.5%, 2.5%, and 5%. In Figures 4.2 and 4.3, the frequency dispersions of the R- and X-signal responses increase with an increase in the volume fraction of Pyrite Red inclusions because the difference between the static and high-frequency limits of effective conductivity and

relative permittivity increases with increase in the volume content of pyrite inclusions. As observed in many subsurface EM tool measurements (e.g., Anderson et al., 2006; Wang and Poppitt, 2013), large negative X-signal responses were measured for the pyrite-bearing glass-bead packs, which indicates that the presence of pyrite inclusions gives rise to a substantial dielectric permittivity associated with the interfacial polarization phenomena. Notably, the R- and X-signal responses obtained for the *yy* coupling (Figure 4.3) are distinct from those obtained for the *zz* coupling (Figure 4.2), implying that the pyrite-bearing glass-bead packs possess both conductivity and permittivity anisotropy. R-signal response mostly decreases, while the negative X-signal response increases in magnitude with an increase in the volume fraction of the inclusion phase.

Using the WCEMIT system, I also measured the R- and X-signal responses of the *zz* (Figure 4.4) and *yy* (Figure 4.5) couplings to the glass-bead packs containing uniformly distributed Pyrite Red (average radius = 25 μm) or Pyrite Yellow (average radius = 65 μm) inclusions for volume fractions of the inclusion phase of 1.5% and 5%. In Figures 4.4 and 4.5, the frequency dispersions of R- and X-signal responses increase with an increase in the size of pyrite inclusions because larger-sized conductive inclusions fail to fully polarize at much low frequencies compared to smaller-sized conductive inclusions. Glass-bead packs containing larger-diameter Pyrite Yellow inclusions exhibit a peak in X-signal response of the *zz* coupling (Figure 4.4b). Both R- and X-signal responses mostly increase with an increase in the size of inclusion phase.

The sensitivity of the R-signal responses of the *yy* and *zz* couplings to the variations in size and volume fraction of pyrite inclusions in the glass-bead packs decreases, while that of the negative X-signal responses of the *yy* and *zz* couplings increases in magnitude with an increase in the operating frequency. At an operating frequency of 58.5 kHz, the

presence of 1.5% volume fraction of pyrite inclusions in the glass-bead packs resulted in approximately 5% decrease in the R-signal response with respect to the R-signal response to inclusion-free glass-bead pack, and produced an X-signal response of approximately -25 mS/m. Further, at an operating frequency of 58.5 kHz and at a volume fraction of 1.5% of pyrite inclusions in the glass-bead packs, a 160% increase in the size of the inclusions from 25 µm to 65 µm, resulted in a 3% increase in the R-signal response and a 50% increase in the magnitude of the negative X-signal response.

4.3.2 Directional effective electrical conductivity and relative dielectric permittivity

Frequency-dependent horizontal and vertical effective electrical properties of the pyrite-bearing glass-bead packs are estimated by tweaking the SA model input values of conductivity and relative permittivity to obtain the best match of the SA model predictions to the multi-frequency *zz* coupling response and to the multi-frequency *yy* coupling response, respectively. Figures 4.6 and 4.7 show the frequency dispersions of both the σ_{eff} and $\varepsilon_{r,eff}$ of the pyrite-bearing packs. The estimated values of $\varepsilon_{r,eff}$ of the pyrite-bearing packs are in the order of 10^3 to 10^4, which are similar to the large permittivity values estimated by Anderson et al. (2006) and Wang and Poppitt (2013). Further, the vertical values of σ_{eff} and $\varepsilon_{r,eff}$ are less dispersive than the horizontal values. Interestingly, for low operating frequencies, the σ_{eff} of the pyrite-bearing packs decreased with an increase in the volume fraction of the pyrite inclusions, which indicates that the pyrite inclusions are acting as non-conductive particles. However, for higher operating frequencies, the pyrite inclusions act as conductive particles giving rise to an increase in the σ_{eff} with an increase in the pyrite content. The counter-intuitive behavior of the σ_{eff} of the pyrite-bearing glass-bead packs containing pyrite inclusions with respect to operating frequency can be explained on the basis of perfectly-polarized interfacial polarization of pyrite inclusions

(Misra et al., 2015c; Revil et al., 2015) due to which conductive inclusions behave as non-conductive particles at very low frequencies and as highly-conductive particles at high frequencies.

Figures 4.8 and 4.9 depict the estimated horizontal and vertical σ_{eff} and $\varepsilon_{r,eff}$ of the glass-bead packs containing disseminated Pyrite Red (average radius = 25 μm) or Pyrite Yellow (average radius = 65 μm) inclusions for volume fraction of the inclusion phase of 1.5% and 5%. In Figures 4.8 and 4.9, the frequency dispersions of σ_{eff} and $\varepsilon_{r,eff}$ of pyrite-bearing packs is larger for packs containing Pyrite Yellow inclusions than that containing Pyrite Red inclusions because larger-sized conductive inclusions fail to fully polarize at lower frequencies compared to smaller-sized conductive inclusions; thereby exhibiting frequency dispersion at lower operating frequencies.

For operating frequencies around 58.5 kHz or lower, the σ_{eff} and $\varepsilon_{r,eff}$ of pyrite-bearing glass-bead packs made of 25-μm pyrite inclusions are close to the static limits as predicted by Maxwell-Garnett effective medium model. Importantly, the effects of interfacial polarization of 25-μm pyrite inclusions on the accuracy of estimation of σ_{eff} based on Maxwell-Garnett effective medium model is negligible for operating frequencies around 58.5 kHz or lower. Comparison of Figures 4.6 and 4.7 indicates that the frequency dispersion effects of interfacial polarization of 25-μm pyrite inclusions are lower in the vertical direction than that in the horizontal direction. A probable explanation of that behavior is that there is a greater reduction in the surface area of pyrite inclusions susceptible to interfacial polarization in the vertical direction compared to that in the horizontal direction due to the tighter packing under gravity in the vertical direction that results in increased contact of pyrite inclusions with adjacent glass beads in the vertical direction. Notably, the effects of interfacial polarization of 5%-volume-fraction of 65-μm

pyrite inclusions on the accuracy of estimation of σ_{eff} based on Maxwell-Garnett effective medium model is non-negligible for operating frequencies around 58.5 kHz or lower. The effects of interfacial polarization on the σ_{eff} and $\varepsilon_{r,eff}$ of pyrite-bearing glass-bead packs in the EM induction frequency range increases with an increase in the volumetric content and size of the pyrite inclusions.

4.3.3 Conductivity and permittivity anisotropy ratio

Based on the results shown in Figures 4.6, 4.7, 4.8, and 4.9, pyrite-bearing glass-bead packs exhibit both effective conductivity and permittivity anisotropy. In Figure 4.10, conductivity anisotropy ratio (λ_c) of the pyrite-bearing packs increase, while effective permittivity anisotropy ratio (λ_p) decrease with an increase in operating frequency. These trends in λ_c and λ_p are attributed to the frequency dispersion behavior of σ_{eff}, which increases with an increase in operating frequency, and that of $\varepsilon_{r,eff}$, which decreases with an increase in the operating frequency. Further, the sensitivity of λ_p to variations in volume fraction of pyrite inclusions is negligible, while that of λ_c strongly depends on the volume fraction of pyrite inclusions, as illustrated in Figure 4.10. However, the frequency dependence of λ_p of pyrite-bearing packs is larger compared to that of λ_c, wherein λ_c is in the range of 1 to 1.2, and λ_p is in the range of 1.7 to 2.8.

Figure 4.11 compares λ_c and λ_p of pyrite-bearing packs containing uniformly distributed Pyrite Red (25 μm) against those containing uniformly distributed Pyrite Yellow (65 μm) inclusions for volume fraction of the inclusion phase of 1.5% and 5%. An increase in the size of pyrite inclusions increases the λ_c but decreases the λ_p. For operating frequencies around 58.5 kHz or lower, a 160% increase in the size of the inclusions from 25 μm to 65 μm, resulted in a 9% increase in the λ_c and an 18% decrease in the λ_p. Interestingly, I observe a peak in the λ_p for the packs containing Pyrite Yellow inclusions,

which can be attributed to the peak of relaxation time of the interfacial polarization of those pyrite inclusions. The experimental results suggest that the values of λ_c are close to 1 and their effects on resistivity interpretation can be neglected; however, the values of λ_p are close to 2 and resistivity interpretation methods should account for possible effects of permittivity anisotropy.

4.4 EFFECTS OF UNIFORMLY DISTRIBUTED GRAPHITE INCLUSIONS

4.4.1 R- and X-signal responses

Using the WCEMIT system, I first measured the R- and X-signal responses of the *zz* and *yy* couplings to the glass-bead packs containing uniformly distributed #2 graphite flake inclusions for volume fractions of the inclusion phase of 2%, 4%, 6%, and 10%. In Figure 4.12, the frequency dispersions of the R- and X-signal responses increase with an increase in the volume fraction of #2 graphite flake inclusions. The magnitude of the negative X-signal responses of the graphite-bearing packs are much larger than that of the pyrite-bearing packs. Notably, the R- and X-signal responses obtained for the *yy* coupling (dotted) are distinct from those obtained for the *zz* coupling (solid), implying that the graphite-bearing glass-bead packs possess both conductivity and permittivity anisotropy. Unlike the R- and X-signal responses of packs containing pyrite inclusions, both the R-signal response and the negative X-signal response increase in magnitude with an increase in the volume fraction of the inclusion phase. This indicates that the graphite inclusions act as conductive particles in the EM induction frequency range. Moreover, the difference in R-signal response of packs containing pyrite inclusions from those containing graphite inclusions highlight that the graphite inclusions have higher relaxation times compared to those containing pyrite inclusions. Gurin et al. (2015) reported that graphite-bearing

samples have higher relaxation times compared to those of pyrite-bearing samples. For volume fraction of 10% of graphite inclusions, the packs exhibit very large frequency-dispersive R- and X-signal responses. However, such rocks containing volume fraction of graphite more than 4% are not associated with productive hydrocarbon-bearing rocks.

Using the WCEMIT system, I also measured the R- and X-signal responses of the *zz* (solid) and *yy* (dotted) couplings to the glass-bead packs containing uniformly distributed #1 graphite flake inclusions. Figure 4.13 compares the response of a pack containing #1 graphite flake inclusions (average surface area = 0.06 mm^2) against that containing #2 graphite flake inclusions (average surface area = 0.02 mm^2) for the volume fraction of the inclusion phase of 2%. The *zz* coupling exhibits larger sensitivity of the R-signal response to the variation in the operating frequency compared to that of the *yy* coupling, which is similar to that observed for pyrite-bearing packs. Further, at a given volume fraction, the R-signal responses and the magnitude of the negative X-signal responses of packs containing #2 graphite flake inclusions are larger compared to those containing #1 graphite flake inclusions.

At an operating frequency of 58.5 kHz, the presence of 2% volume fraction of #2 graphite inclusions in the glass-bead packs resulted in approximately 20% increase in the R-signal response with respect to the R-signal response to inclusion-free glass-bead pack, and produced an X-signal response of approximately -150 mS/m. Further, at an operating frequency of 58.5 kHz and at a volume fraction of 2% of graphite inclusions in the glass-bead packs, a 200% increase in the surface area of the representative graphite inclusion from 0.02 mm^2 to 0.06 mm^2, resulted in a 4% decrease in the R-signal response and a 12% decrease in the magnitude of the negative X-signal response.

4.4.2 Effective electrical conductivity and relative dielectric permittivity

Frequency-dependent horizontal and vertical effective electrical properties of the graphite-bearing glass-bead packs are estimated by tweaking the SA model input values of conductivity and relative permittivity to obtain the best match of the SA model predictions to the multi-frequency *zz* coupling response (solid) and to the multi-frequency *yy* coupling response (dotted), respectively. Figure 4.14 shows the frequency dispersions of both the σ_{eff} and $\varepsilon_{r,eff}$ of the graphite-bearing packs. The estimated values of the $\varepsilon_{r,eff}$ of the graphite-bearing packs are in the order of 10^4 to 10^6, which are one to two order of magnitude higher than those of pyrite-bearing packs. This indicates that the presence of graphite inclusions gives rise to higher accumulation of charges compared to pyrite inclusions mostly due their larger surface area. Owing to the higher diffusion coefficient (approximately around 10^{-3} m^2s^{-1}) and higher conductivity of graphite (10^5 S/m) than that compared to those of pyrite of 10^{-6} m^2s^{-1} and 10^3 S/m, respectively, the $\varepsilon_{r,eff}$ and σ_{eff} values of the graphite-bearing inclusions are much larger than that of pyrite-bearing packs (Revil et al., 2015a). Moreover, a large dielectric loss factor is associated with such large $\varepsilon_{r,eff}$ gives rise to the substantial increase in the σ_{eff}. Further, the vertical values of σ_{eff} are less dispersive than the horizontal values, similar to those of pyrite-bearing packs. However, both horizontal and vertical values of the $\varepsilon_{r,eff}$ have similar magnitude of frequency dispersion and exhibit a power-law relationship with the operating frequency. Unlike the σ_{eff} of pyrite-bearing packs, the σ_{eff} of the graphite-bearing packs increase with an increase in the volume fraction of the graphite inclusions, which indicates that the graphite inclusions are acting as conductive particles in the EM induction frequency range.

Figures 4.15 and 4.16 depict the estimated horizontal and vertical σ_{eff} and $\varepsilon_{r,eff}$ of the glass-bead packs containing disseminated #2 graphite flake inclusions (average surface

area = 0.02 mm^2) and #1 graphite flake inclusions (average surface area = 0.06 mm^2) inclusions for volume fraction of the inclusion phase of 2% and 10%, respectively. In Figures 4.15 and 4.16, the frequency dispersions of σ_{eff} and $\varepsilon_{r,eff}$ of graphite-bearing packs are similar for packs containing #2 graphite flake inclusions and those containing #1 graphite flake inclusions. Nonetheless, at any given operating frequency and volume fraction of graphite inclusions, the packs containing #2 graphite flake inclusions show higher values of $\varepsilon_{r,eff}$ and σ_{eff} compared to those containing #1 graphite flake inclusions. This behavior suggests that the packs containing #2 graphite flake inclusions produces larger interfacial polarization effects than those containing #1 graphite flake inclusions. For pyrite-bearing packs, increase in size of spherical pyrite inclusions shifted the relaxation time to higher values; thereby increasing the values of $\varepsilon_{r,eff}$ and σ_{eff} compared to those containing smaller-sized inclusions. However, for graphite-bearing packs, an increase in the size of a flaky graphite inclusion increases the surface area; thereby increasing the $\varepsilon_{r,eff}$ and the associated dielectric factor that increases the σ_{eff}. Also, the pack containing #2 graphite inclusions and that containing #1 graphite inclusion exhibit a large increase in the horizontal σ_{eff} at frequencies above 88 kHz.

For operating frequencies around 58.5 kHz or lower, the σ_{eff} of the glass-bead pack containing 2% volume fraction of #2 graphite flake inclusions is 20% more than the host conductivity, while that of the pack containing 10% volume fraction of #2 graphite flake inclusions is 350% more than the host conductivity. These large differences in the values of σ_{eff} compared to the host conductivity is attributed to the large dielectric loss factor associated with the large vales of $\varepsilon_{r,eff}$ of 5×10^4 and 5×10^5, respectively, that substantially increases the σ_{eff} values. Importantly, the effects of interfacial polarization of #2 graphite flake inclusions severely reduces the accuracy of estimation of σ_{eff} for operating

frequencies around 58.5 kHz or lower. Figures 4.15 and 4.16 indicate that the frequency dispersion effects of interfacial polarization of #2 graphite flake inclusions are much lower in the vertical direction than those in the horizontal direction, similar to the responses of the pyrite-bearing packs. The effects of interfacial polarization of graphite inclusions on the σ_{eff} and $\varepsilon_{r,eff}$ of the graphite-bearing glass-bead packs in the EM induction frequency range increases with an increase in the volumetric content and size of the graphite inclusions.

4.4.3 Conductivity and permittivity anisotropy ratio

Based on the estimation of $\varepsilon_{r,eff}$ and σ_{eff}, graphite-bearing packs exhibit both effective conductivity and permittivity anisotropy. In Figure 4.17, λ_c values of the graphite-bearing packs increase, while λ_p values decrease with an increase in the operating frequency, similar to that of pyrite-bearing inclusions. Further, the sensitivity of λ_p and λ_c to variations in volume fraction of graphite inclusions is non-negligible, unlike that observed for pyrite-bearing packs. The frequency dependence of λ_p of graphite-bearing packs is comparable to that of λ_c, wherein λ_c is in the range of 1 to 1.6 and λ_p is in the range of 1 to 1.8. Graphite-bearing packs exhibit smaller values of $\varepsilon_{r,eff}$ in the EM induction frequency range compared to the pyrite-bearing packs.

Figure 4.17 also compares the λ_c and λ_p of graphite-bearing packs containing uniformly distributed #2 graphite flakes against those containing uniformly distributed #1 graphite flakes for volume fraction of the inclusion phase of 2% and 10%. An increase in the surface area of the representative graphite inclusion deceases both the λ_c and λ_p, which is due to the increase in the randomness of the orientation of larger-sized inclusions. For operating frequencies around 58.5 kHz or lower and volume fraction of 2%, a 200% increase in the surface area of the representative graphite inclusion from 0.02 mm^2 to 0.06

mm^2, resulted in a 1% decrease in the λ_c and an 10% decrease in the λ_p. In my experiments, at volume fractions of 2%, the values of λ_c and λ_p are close to 1, both λ_c and λ_p have low sensitivity to variations in the size, volume fraction, and operating frequency.

4.5 EFFECTS OF PYRITE- AND GRAPHITE-BEARING LAYERS

In this section, I measure the WCEMIT response to bi-laminar glass-bead packs that have alternating layers of different volume fractions of graphite (e.g., Figures 4.18a and 4.18b) or pyrite inclusions (e.g., Figure 4.18c). Figure 4.19 compares the horizontal and vertical σ_{eff} and $\varepsilon_{r,eff}$ of a bi-laminar pack made of alternating 0-vol% and 10-vol% of uniformly distributed #2 graphite-bearing layers (red) against those of two homogeneous packs of 5-vol% and 10-vol%, respectively, of uniformly distributed #2 graphite inclusions. In that figure, the horizontal and vertical σ_{eff} of the bi-laminar pack is approximately 8% more, while the horizontal and vertical $\varepsilon_{r,eff}$ is approximately 250% more than those of the homogeneous 5-vol% graphite-bearing pack. Though the overall volume fraction of graphite in the bi-laminar pack is equal to that of the homogeneous 5-vol% graphite-bearing pack, Figure 4.19 indicates a large difference in their $\varepsilon_{r,eff}$ values, which can be attributed to the larger accumulation by the alternating 10-vol% graphite-inclusion-bearing layers compared to that of the homogeneous, uniformly distributed 5-vol% of graphite inclusions. Further, the horizontal and vertical $\varepsilon_{r,eff}$ of the homogeneous 10-vol% graphite-bearing pack is 300% more, whereas the horizontal and vertical σ_{eff} of the homogeneous 10-vol% graphite-bearing pack is 200% more than those of the bi-laminar pack. Notably, the bi-laminar pack shows no noticeable increase in the horizontal σ_{eff} for operating frequencies higher than 88 kHz, as exhibited by the homogeneous 10-vol% graphite-bearing pack.

Figure 4.20 compares the horizontal and vertical σ_{eff} and $\varepsilon_{r,eff}$ of a bi-laminar pack made of alternating 0-vol% and 10-vol% of uniformly distributed #1 graphite-bearing layers (red) against those of a homogeneous pack of 10-vol% of uniformly distributed #1 graphite inclusions (green). Here, the bi-laminar pack exhibits a large increase in the horizontal σ_{eff} for operating frequencies higher than 88 kHz, as exhibited by the homogeneous 10-vol% graphite-bearing pack. Also, the values of horizontal σ_{eff} of the bilaminar pack (red, solid) are 14% more than the values of effective horizontal conductivity calculated using the series conductivity model for the 0-vol% and 10-vol% graphite-inclusion-bearing layers (magenta, solid). Similarly, the values of horizontal $\varepsilon_{r,eff}$ of the bilaminar pack (red, solid) are 40% more than the values of effective horizontal relative permittivity calculated using the series permittivity model for the 0-vol% and 10-vol% graphite-inclusion-bearing layers (magenta, solid). Further, the values of vertical σ_{eff} of the bi-laminar pack (red, dotted) are 23% more than the values of effective vertical conductivity calculated using the parallel conductivity model for the 0-vol% and 10-vol% graphite-inclusion-bearing layers (magenta, dotted). Although the series-parallel model is not applicable for the bi-laminar pack because of the complex conductivity exhibited by the bilaminar pack, the calculated values based on the series-parallel model is relatively close to the estimated effective conductivity and permittivity values. Also, in Figure 4.20b, the $\varepsilon_{r,eff}$ values of the bilaminar pack in the horizontal direction are much larger than those in the vertical direction, unlike the vertical and horizontal $\varepsilon_{r,eff}$ values of the homogeneous 10-vol% graphite-bearing pack.

Figure 4.21 compares the horizontal and vertical σ_{eff} and $\varepsilon_{r,eff}$ of a bi-laminar pack made of alternating 0-vol% and 6-vol% of uniformly distributed #1 graphite-bearing layers (red) against those of a homogeneous pack of 6-vol% of uniformly distributed #1 graphite

inclusions (green). Notably, the bi-laminar pack exhibits a large increase in the horizontal σ_{eff} for operating frequencies higher than 88 kHz, as exhibited by the homogeneous 6-vol% graphite-bearing pack. Also, the values of horizontal σ_{eff} of the bi-laminar pack (red, solid) are 22% more than the values of effective horizontal conductivity calculated using the series conductivity model for the 0-vol% and 6-vol% graphite-inclusion-bearing layers (magenta, solid). Similarly, the values of horizontal $\varepsilon_{r,eff}$ of the bi-laminar pack (red, solid) are 43% more than the values of effective horizontal relative permittivity calculated using the series permittivity model for the 0-vol% and 6-vol% graphite-inclusion-bearing layers (magenta, solid). Further, the values of vertical σ_{eff} of the bi-laminar pack (red, dotted) are 16% more than the values of effective vertical conductivity calculated using the parallel conductivity model for the 0-vol% and 6-vol% graphite-inclusion-bearing layers (magenta, dotted). Also, in Figure 4.21b, the $\varepsilon_{r,eff}$ values of the bi-laminar pack in the horizontal direction (red, solid) are much larger than those in the vertical direction (red, dotted), unlike the vertical and horizontal $\varepsilon_{r,eff}$ values of the homogeneous 6-vol% graphite-bearing pack. Therefore, a layered graphite-bearing pack exhibits large values of permittivity anisotropy ratio.

Figure 4.22 shows that the bi-laminar pack containing alternating 0-vol% and 10-vol% of uniformly distributed #1 graphite-bearing layers (blue) exhibits larger λ_c and λ_p compared to the homogeneous 5-vol% #1 graphite-bearing pack (green). Although overall the volume fraction of graphite inclusions is equal in both packs, both λ_c and λ_p are larger for the bi-laminar pack. The increase λ_c in is negligible around an operating frequency of 58.5 kHz or lower; however, there is 120% increase in λ_p for those frequencies. This observation confirms that the bi-laminar packs contribute to increase in permittivity anisotropy in the pack.

4.6 COMPARISON OF THE EFFECTS OF UNIFORMLY DISTRIBUTED PYRITE-BEARING PACKS AGAINST UNIFORMLY DISTRIBUTED GRAPHITE-BEARING PACKS

Several researchers have investigated the differences in the frequency dispersion of conductivity and permittivity of samples containing graphite and pyrite inclusions (e.g., Gurin et al. 2015; Pelton et al., 1978) for purposes of mineral discrimination. Shale-gas reservoirs are prone to the presence of graphitic-precursors and pyrite (Laughrey et al., 2011; Passey et al., 2010). Therefore, in this section, I investigate qualitative differences in the effective conductivity and permittivity of packs containing only graphite inclusions, only pyrite inclusions, and mixture of graphite and pyrite inclusions.

Figure 4.23 compares the horizontal and vertical σ_{eff} and $\varepsilon_{r,eff}$ of the graphite-bearing pack (green) containing uniformly distributed 1.5-vol% of graphite inclusions against those of pyrite-bearing pack (red) containing uniformly distributed 1.5-vol% of pyrite inclusions. The σ_{eff} of the graphite-bearing pack is 16% more than that of the pyrite-bearing packs. I observe that the presence of pyrite inclusions tends to decrease the σ_{eff} to values below the host conductivity for various volume fractions of pyrite inclusions (Figure 4.6), while the presence of graphite inclusions tends to increase the σ_{eff} to values higher than the host conductivity for various volume fractions of graphite inclusions (Figure 4.14). Further, the $\varepsilon_{r,eff}$ of the graphite-bearing pack is 400% more than that of the pyrite-bearing pack. Moreover, the λ_c of the graphite-bearing pack is larger than that of the pyrite-bearing pack that increases with an increase in the operating frequency, whereas the λ_p of pyrite-bearing pack is larger than that of the graphite-bearing pack that decreases with a decrease in the operating frequency.

Figure 4.24 compares the horizontal and vertical σ_{eff} and $\varepsilon_{r,eff}$ of a graphite-bearing pack (green) containing uniformly distributed 2-vol% of graphite inclusions, a pyrite-bearing pack (red) containing uniformly distributed 2.5-vol% of pyrite inclusions, and

mixed-mineral-bearing pack containing uniformly distributed 2-vol% of graphite and 2.5-vol% of pyrite inclusions (magenta). In that figure, the σ_{eff} values of the 2.5-vol% pyrite-bearing pack are lower than the host conductivity (blue), whereas the 2-vol% graphite-bearing pack exhibits a σ_{eff} value that is approximately 15% more than the host conductivity. Notably, the mixed-mineral-bearing pack exhibits a value of σ_{eff} that is much larger than the sum of the σ_{eff} values of the pyrite-bearing pack and graphite-bearing pack for all the operating frequencies. Also, the mixed-mineral-bearing pack exhibits larger values of λ_c compared to those of the pyrite-bearing pack and graphite-bearing pack that increases with an increase in the operating frequency. Further, the mixed-mineral-bearing pack exhibits horizontal and vertical $\varepsilon_{r,eff}$ that is slightly more than the sum of the $\varepsilon_{r,eff}$ values of the pyrite-bearing pack and graphite-bearing pack. Comparison of the σ_{eff} and $\varepsilon_{r,eff}$ data indicate the non-additive nature of the effects of interfacial polarization of different types of mineral inclusions.

Figure 4.25 compares the horizontal and vertical σ_{eff} and $\varepsilon_{r,eff}$ of the mixed-mineral-bearing pack containing uniformly distributed 5-vol% of #2 graphite inclusions and 2.5-vol% of Pyrite Red inclusions (red) against those of the mixed-mineral-bearing pack containing uniformly distributed 2-vol% of #1 graphite inclusions and 2.5-vol% of Pyrite Red inclusions (magenta). In Figure 4.25, the mixed-mineral-bearing pack containing 7.5-vol% of conductive mineral inclusions exhibited 30% increase in the horizontal σ_{eff} and 75% increase in the vertical $\varepsilon_{r,eff}$ compared to those of the mixed-mineral-bearing pack containing 4.5-vol% of conductive mineral inclusions. The packs containing only pyrite inclusions have distinct σ_{eff} and $\varepsilon_{r,eff}$ responses compared to the packs containing graphite inclusions. Moreover, the packs containing both graphite and pyrite inclusions exhibit σ_{eff} and $\varepsilon_{r,eff}$ responses that are qualitatively similar to packs containing only graphite

inclusions, wherein the effects of pyrite inclusions are altered such that the effects of pyrite inclusions on σ_{eff} and $\varepsilon_{r,eff}$ are comparable to those of graphite inclusions.

4.7 CONCLUSIONS

Glass-bead packs containing homogeneously dispersed pyrite and/or graphite inclusions exhibited frequency dispersion of their R- and X-signal responses due to the interfacial polarization of electrically conductive mineral inclusions. The R-signal response of conductive-mineral-bearing packs were significantly different from those of the inclusion-free glass-bead packs; consequently, accurate resistivity interpretation methods for samples containing pyrite or graphite inclusions must account for the effects of interfacial polarization. Also, negative values of X-signal response were observed for glass-bead packs containing more than 1%-volume-fraction of graphite or pyrite inclusions, which is indicative of the dielectric behavior (charge accumulation) of these packs due to the interfacial polarization phenomena. I successfully estimated the effective conductivity and effective relative permittivity of the conductive-mineral-bearing glass-bead packs using the Semi-Analytic EM forward model. The estimated values of the effective relative permittivity were in the range of 10^3 to 10^4 for the pyrite-bearing glass-bead packs and 10^4 to 10^6 for the graphite-bearing glass-bead packs. The effective electrical conductivity and dielectric relative permittivity of the conductive-mineral-bearing packs are strongly dependent on the operating frequency, mineral type, and volume fraction and size of mineral inclusions. The multi-frequency effective conductivity and relative permittivity of graphite-bearing packs were significantly different compared to those of the pyrite-bearing packs due to the large difference in the diffusion coefficients of charge carriers, bulk conductivity values, and shapes of pyrite and graphite inclusions. Further, the packs containing homogeneously dispersed conductive inclusions exhibit conductivity

anisotropy ratios, in the range of 1 to 1.7, and permittivity anisotropy ratios, in the range of 1.1 to 2.8. Consequently, resistivity interpretation methods for formations containing uniformly dispersed pyrite or graphite inclusions must account for the effects of effective conductivity and effective permittivity anisotropy due to interfacial polarization of the inclusion phase. Notably, the packs containing alternating layers of different volume fraction of conductive mineral inclusions have significantly different effective conductivity and relative permittivity compared to those of packs containing homogeneously distributed mineral inclusions of the same mineral type, size, total volume fraction, and shape. Therefore, accurate resistivity interpretation in formations containing conductive minerals will require accurate knowledge of shape, size, mineral type, conductivity, and distribution of the inclusion phase.

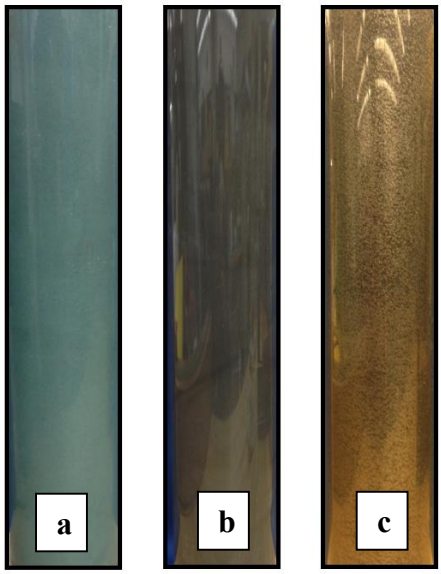

Figure 4.1: Photographs of the 4-inch-diameter, 24-inch-long, glass-bead packs containing (a) no inclusions, (b) 2.5% volume fraction of uniformly distributed pyrite inclusions, and (c) 3-wt% of uniformly distributed graphite inclusions fully saturated with 3.75-S/m-conductivity brine.

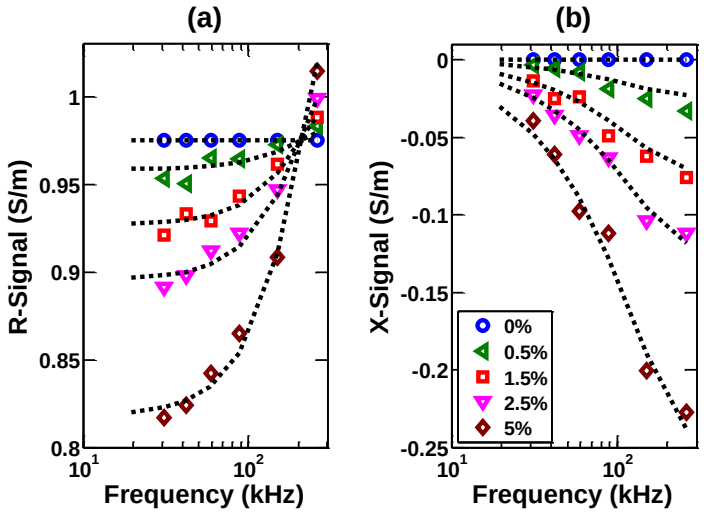

Figure 4.2: Multi-frequency (a) R-signal and (b) X-signal responses, identified with discrete points, of *zz* coupling to packs containing disseminated Pyrite Red inclusions for various volume fractions of the inclusion phase. The dotted curves identify SA model predictions that best fit the WCEMIT response.

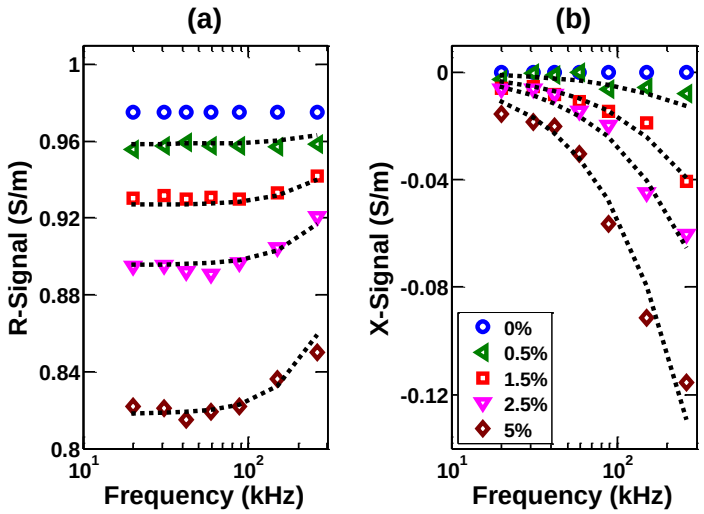

Figure 4.3: Multi-frequency (a) R-signal and (b) X-signal responses, identified with discrete points, of *yy* coupling to packs containing disseminated Pyrite Red inclusions for various volume fractions of the inclusion phase. The dotted curves identify SA model predictions that best fit the WCEMIT response.

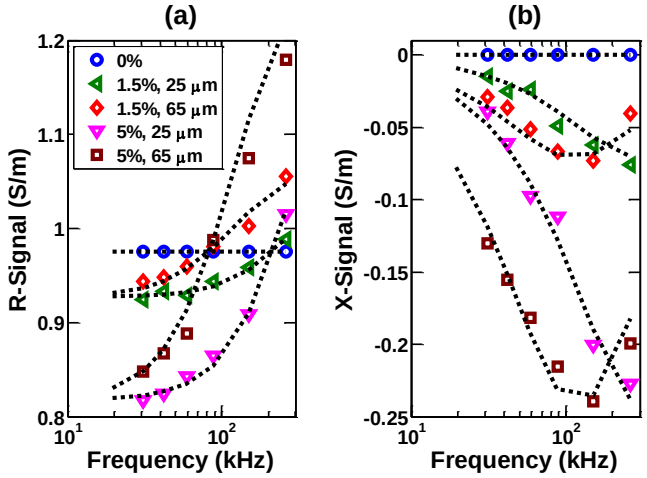

Figure 4.4: Multi-frequency (a) R-signal and (b) X-signal responses, identified with discrete points, of the *zz* coupling to packs containing disseminated Pyrite Red (25 µm) or Pyrite Yellow (65 µm) inclusions for various volume fractions of the inclusion phase. The dotted curves identify the SA model predictions that best fit the WCEMIT response.

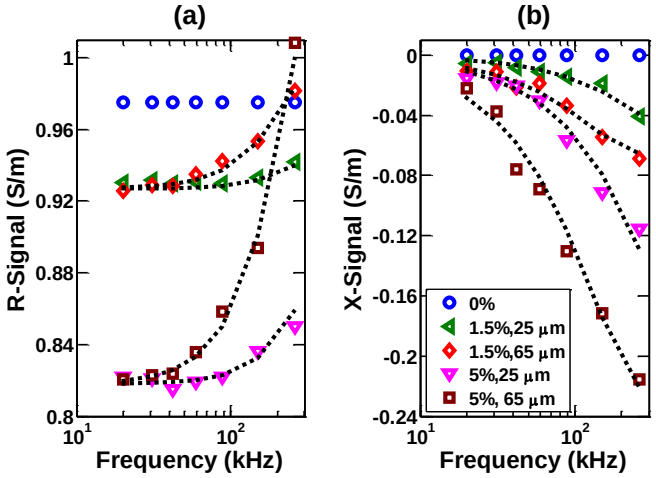

Figure 4.5: Multi-frequency (a) R-signal and (b) X-signal responses, identified with discrete points, of the *yy* coupling to packs containing disseminated Pyrite Red (25 µm) or Pyrite Yellow (65 µm) inclusions for various volume fractions of the inclusion phase. The dotted curves identify the SA model predictions that best fit the WCEMIT response.

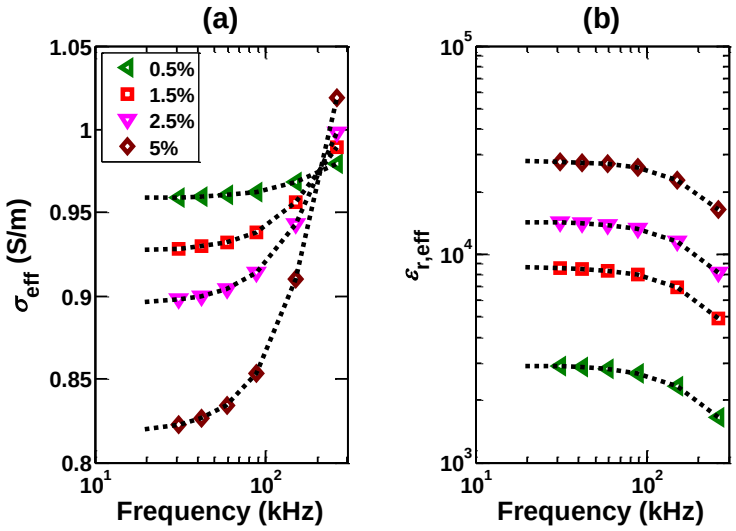

Figure 4.6: Estimated values of the horizontal (a) σ_{eff} and (b) $\varepsilon_{r,eff}$ of the packs containing disseminated Pyrite Red inclusions for various volume fractions of the inclusion phase.

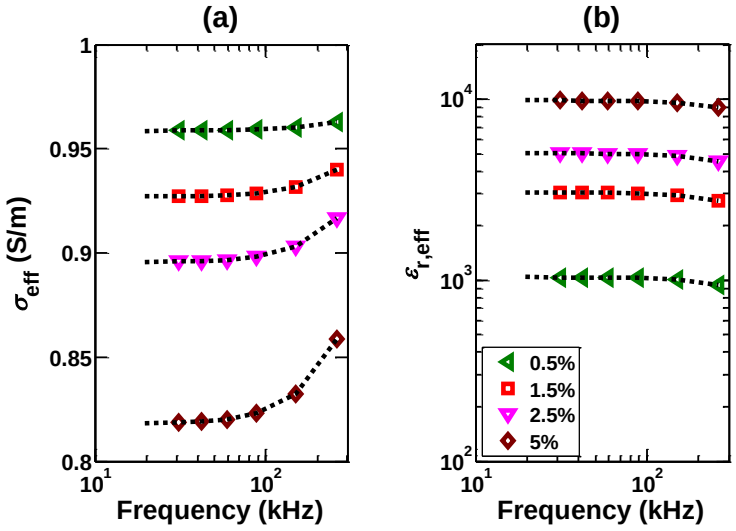

Figure 4.7: Estimated values of the vertical (a) σ_{eff} and (b) $\varepsilon_{r,eff}$ of the packs containing disseminated Pyrite Red inclusions for various volume fractions of the inclusion phase.

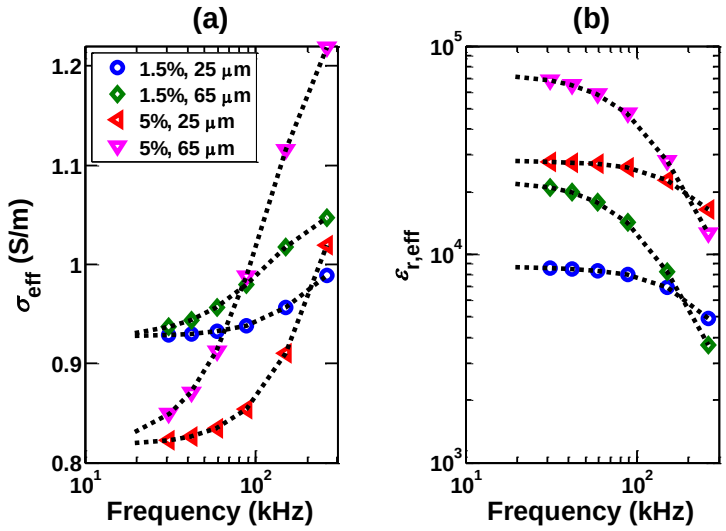

Figure 4.8: Estimated values of the horizontal (a) σ_{eff} and (b) $\varepsilon_{r,eff}$ of the packs containing disseminated Pyrite Red (25 µm) or Pyrite Yellow (65 µm) inclusions for various volume fractions of the inclusion phase.

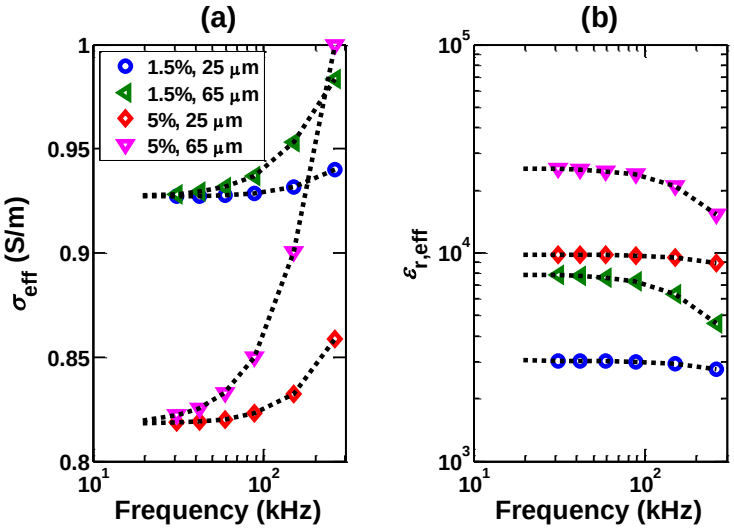

Figure 4.9: Estimated values of the vertical (a) σ_{eff} and (b) $\varepsilon_{r,eff}$ of the packs containing disseminated Pyrite Red (25 µm) or Pyrite Yellow (65 µm) inclusions for various volume fractions of the inclusion phase.

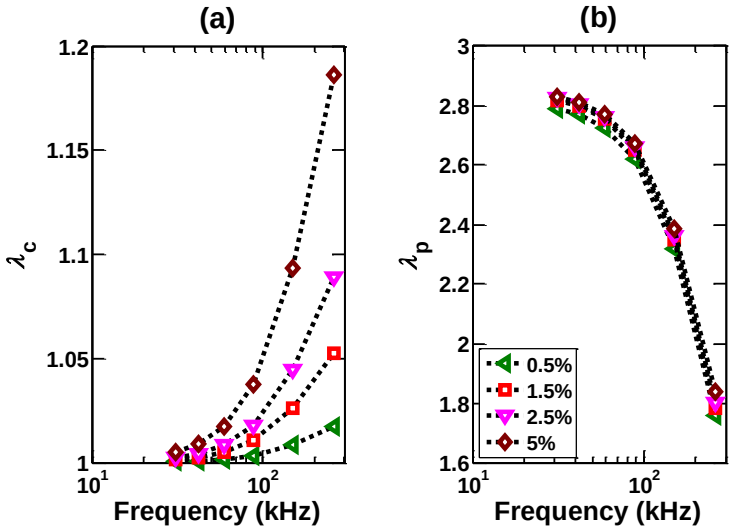

Figure 4.10: Estimated values of the (a) λ_c and (b) λ_p of the packs containing disseminated Pyrite Red inclusions for various volume fractions of the inclusion phase.

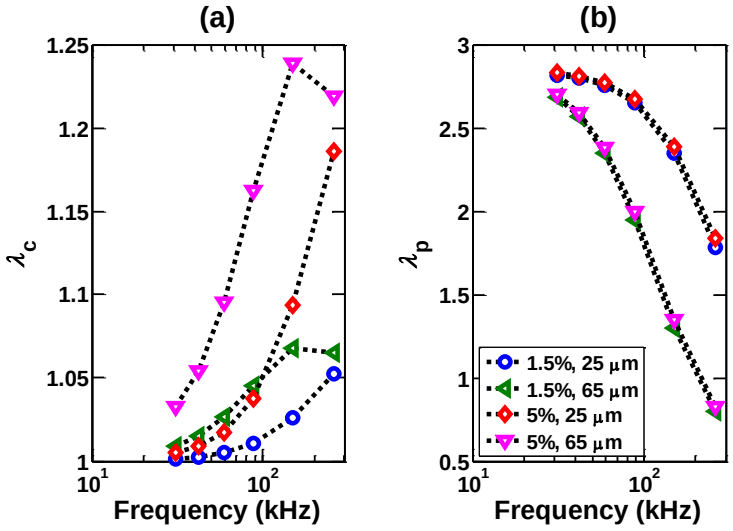

Figure 4.11: Estimated values of the (a) λ_c and (b) λ_p of the packs containing disseminated Pyrite Red (25 µm) or Pyrite Yellow (65 µm) inclusions for various volume fractions of the inclusion phase.

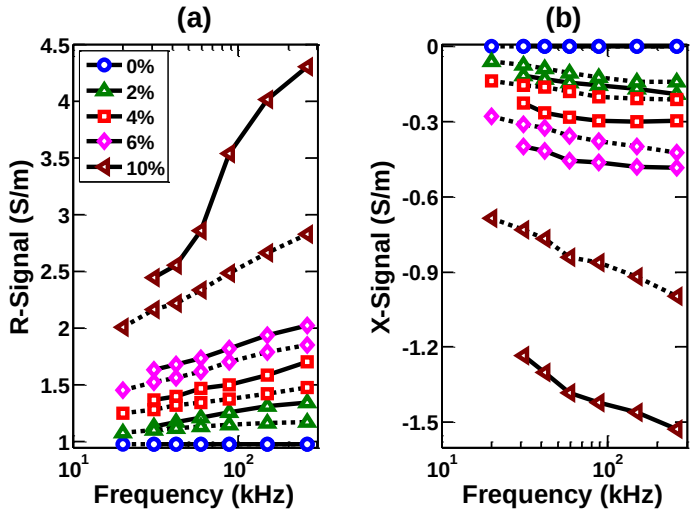

Figure 4.12: Multi-frequency (a) R-signal and (b) X-signal responses, identified with discrete points, of *zz* coupling (solid) and of *yy* coupling (dotted) to packs containing disseminated #2 graphite flakes for various volume fractions of the inclusion phase. The solid and dotted curves identify the SA model predictions that best fit the WCEMIT response.

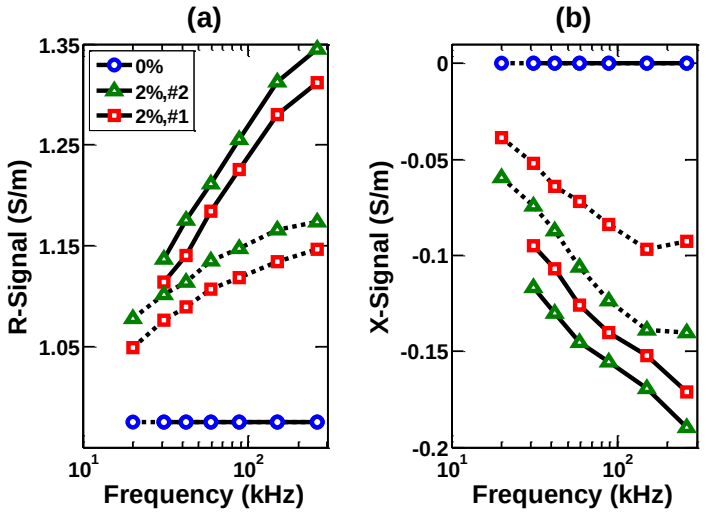

Figure 4.13: Multi-frequency (a) R-signal and (b) X-signal responses of *zz* coupling (solid) and of *yy* coupling (dotted) to two packs containing #2 graphite (0.02 mm^2) inclusions and #1 graphite (0.06 mm^2) inclusions, respectively.

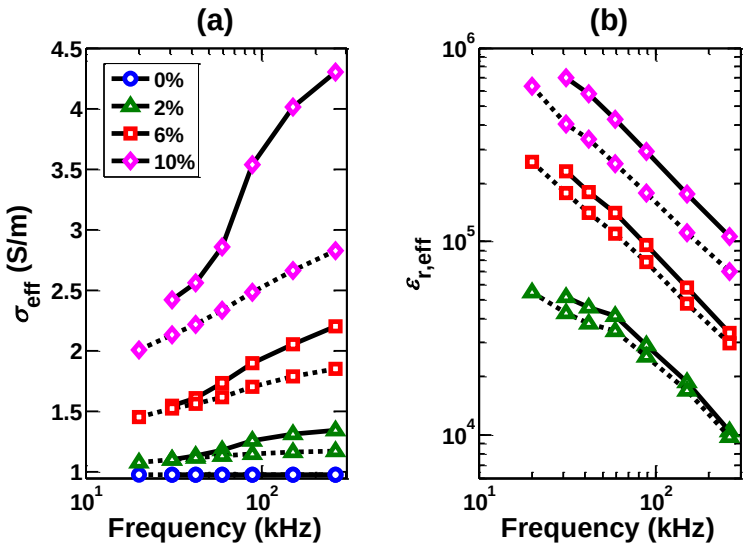

Figure 4.14: Estimated values of the horizontal (solid) and vertical (dotted) (a) σ_{eff} and (b) $\varepsilon_{r,eff}$ of the packs containing #2 graphite flakes inclusions for various volume fractions of the inclusion phase.

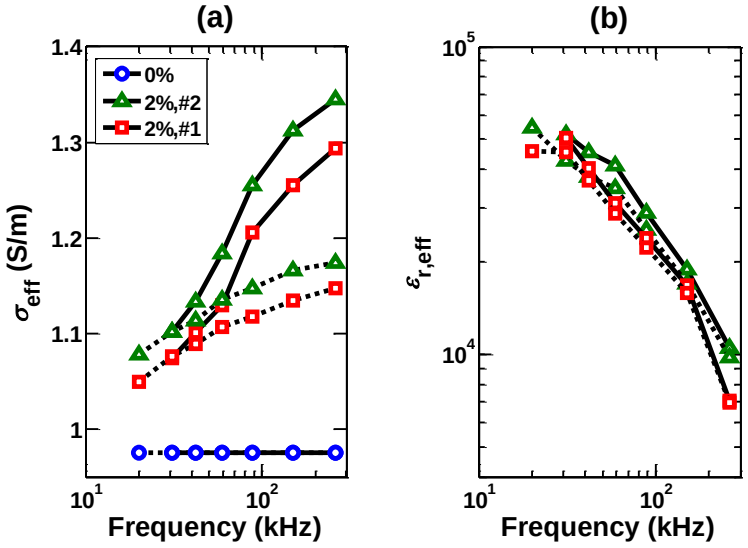

Figure 4.15: Estimated values of the horizontal (solid) and vertical (dotted) (a) σ_{eff} and (b) $\varepsilon_{r,eff}$ of two packs containing disseminated #2 graphite (0.02 mm^2) inclusions and disseminated #1 graphite (0.06 mm^2) inclusions, respectively.

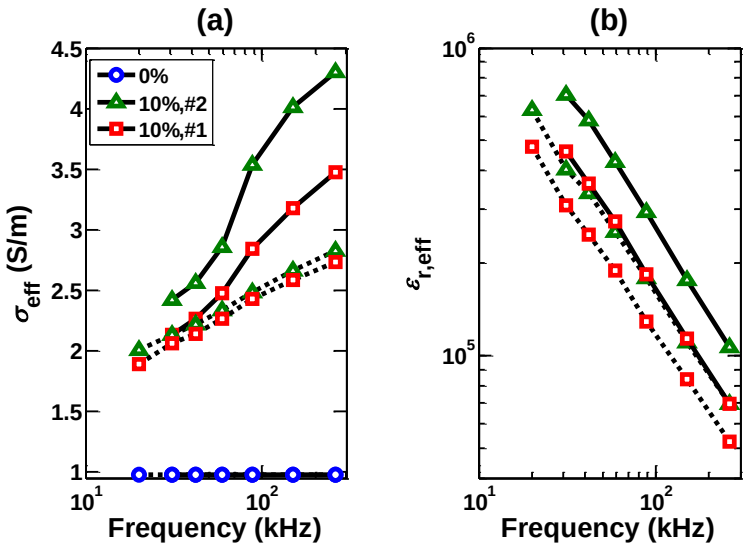

Figure 4.16: Estimated values of the horizontal (solid) and vertical (dotted) (a) σ_{eff} and (b) $\varepsilon_{r,eff}$ of two packs containing disseminated #2 graphite (0.02 mm^2) inclusions and disseminated #1 graphite (0.06 mm^2) inclusions, respectively.

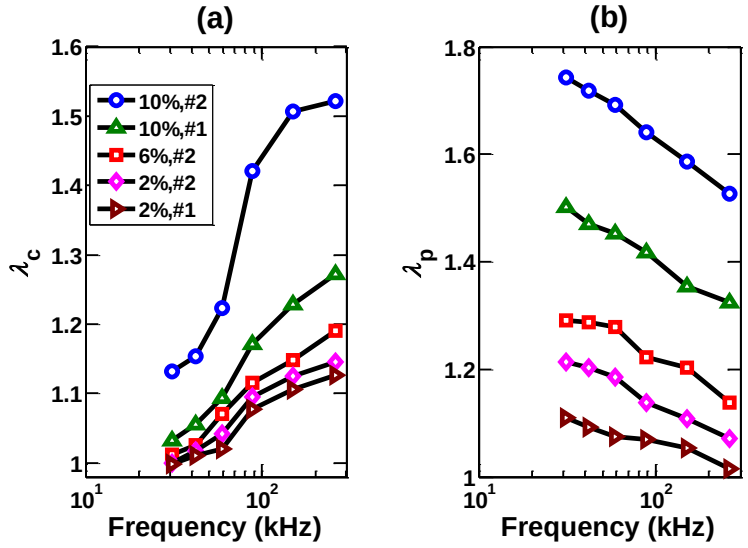

Figure 4.17: Estimated values of the (a) λ_c and (b) λ_p of the packs containing disseminated graphite flakes for various volume fractions and sizes of the inclusion phase.

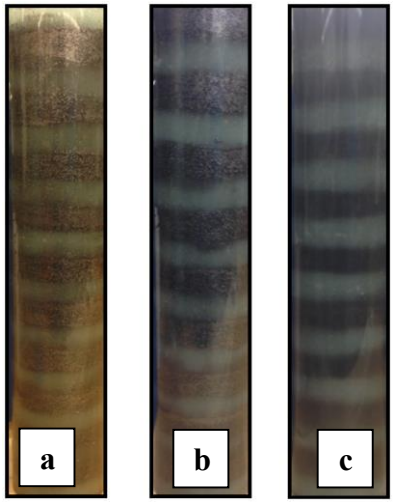

Figure 4.18: Photographs of the 4-inch-diameter, 24-inch-long, glass-bead packs containing alternating (a) 0-vol% and 6-vol% of dispersed graphite-bearing layers, (b) 0-vol% and 10-vol% of dispersed graphite-bearing layers, and (c) 0-vol% and 5-vol% of dispersed pyrite-bearing layers fully saturated with 3.75-S/m-conductivity brine.

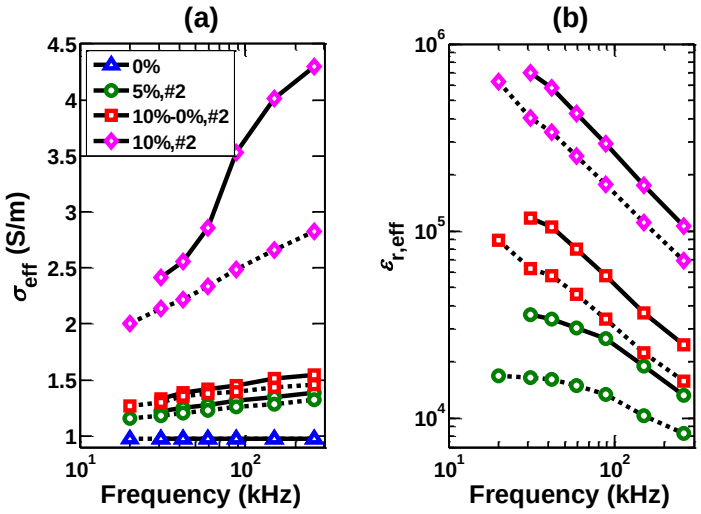

Figure 4.19: Estimated values of the horizontal (solid) and vertical (dotted) (a) σ_{eff} and (b) $\varepsilon_{r,eff}$ of three packs containing 5-vol% of uniformly distributed #2 graphite inclusions, 10-vol% of uniformly distributed #2 graphite inclusions, and alternating 0-vol% and 10-vol% of uniformly distributed #2 graphite-bearing layers, respectively.

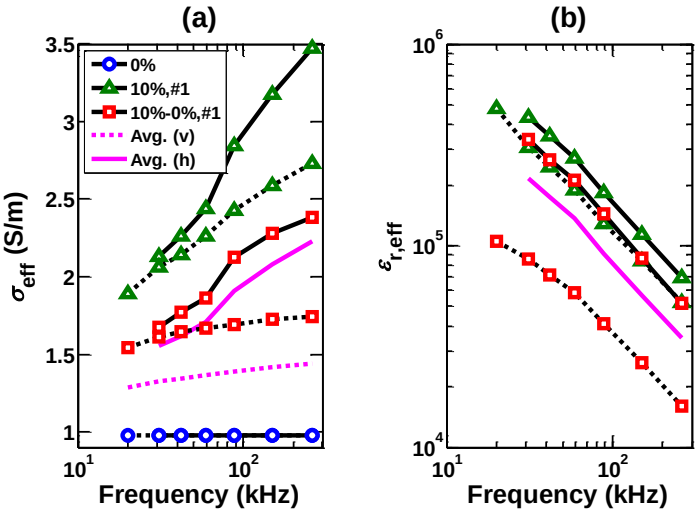

Figure 4.20: Estimated values of the horizontal (solid) and vertical (dotted) (a) σ_{eff} and (b) $\varepsilon_{r,eff}$ of two packs containing 10-vol% of uniformly distributed #1 graphite inclusions and alternating 0-vol% and 10-vol% of uniformly distributed #1 graphite-bearing layers, respectively.

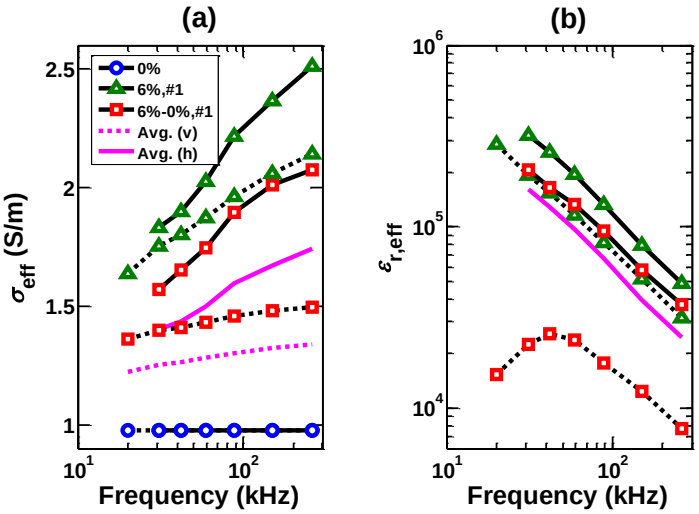

Figure 4.21: Estimated values of the horizontal (solid) and vertical (dotted) (a) σ_{eff} and (b) $\varepsilon_{r,eff}$ of two packs containing 6-vol% of uniformly distributed #1 graphite inclusions and alternating 0-vol% and 6-vol% of uniformly distributed #1 graphite-bearing layers, respectively.

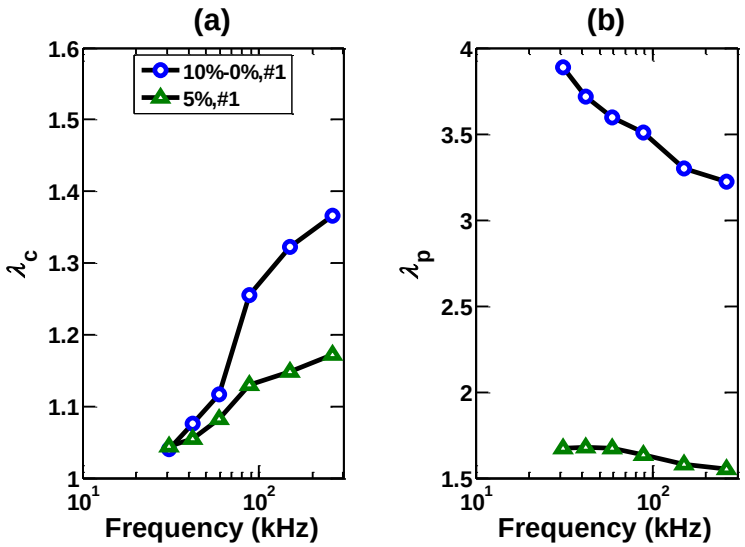

Figure 4.22: Estimated values of the (a) λ_c and (b) λ_p of two packs containing 5-vol% of uniformly distributed #1 graphite inclusions and alternating 0-vol% and 10-vol% of uniformly distributed #2 graphite-bearing layers, respectively.

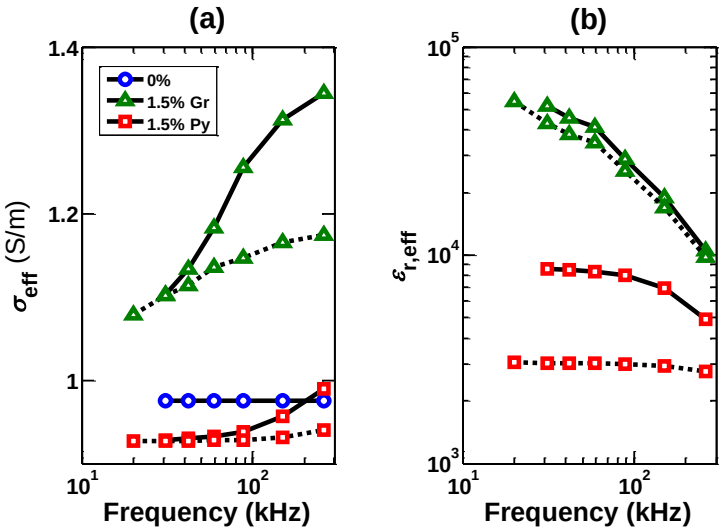

Figure 4.23: Estimated values of the horizontal (solid) and vertical (dotted) (a) σ_{eff} and (b) $\varepsilon_{r,eff}$ of two packs containing 1.5-vol% of uniformly distributed Pyrite Red inclusions (red) and #2 graphite inclusions (green), respectively.

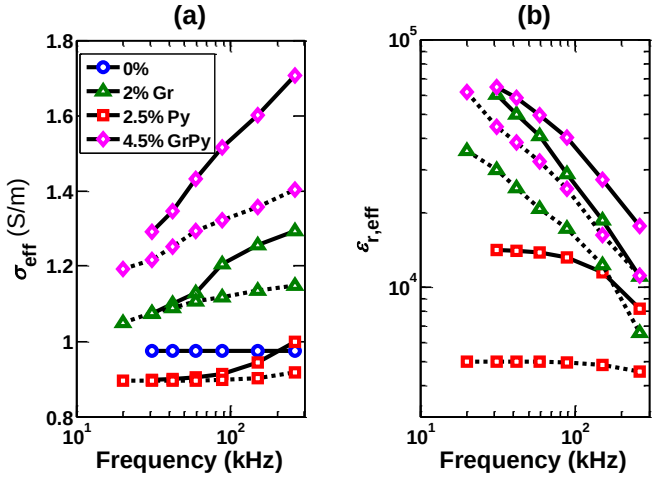

Figure 4.24: Estimated values of the horizontal (solid) and vertical (dotted) (a) σ_{eff} and (b) $\varepsilon_{r,eff}$ of three packs containing 2.5-vol% of uniformly distributed Pyrite Red inclusions (red), 2-vol% of uniformly distributed #1 graphite inclusions (green), and uniformly distributed mixture of 2-vol% of #1 graphite inclusions and 2.5-vol% of Pyrite Red inclusions (magenta), respectively.

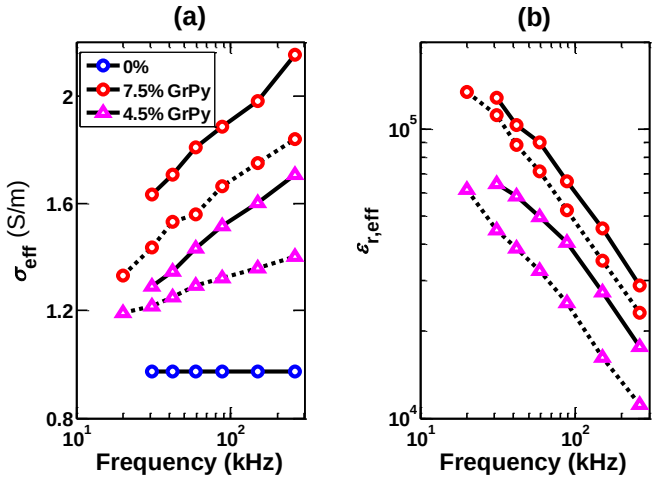

Figure 4.25: Estimated values of the horizontal (solid) and vertical (dotted) (a) σ_{eff} and (b) $\varepsilon_{r,eff}$ of two packs containing uniformly distributed mixture of 5-vol% of #2 graphite inclusions and 2.5-vol% of Pyrite Red inclusions (red) and uniformly distributed mixture of 2-vol% of #1 graphite inclusions and 2.5-vol% of Pyrite Red inclusions (magenta), respectively.

Chapter 5: Mechanistic Model of Interfacial Polarization of Disseminated Conductive Minerals in Absence of Redox-Active Species

Electrically conductive mineral inclusions are commonly present in organic-rich mudrock and source-rock formations as veins, laminations, rods, grains, flakes, and beds. Laboratory and subsurface electromagnetic (EM) measurements performed on geomaterials containing electrically conductive inclusions generally exhibit frequency dispersion due to interfacial polarization phenomena at host-inclusion interfaces. In absence of redox-active species, surfaces of electrically conductive mineral inclusions are impermeable to the transport of charge carriers, inhibit the exchange of charges, and behave as perfectly polarized (PP) interfaces under the influence of an externally applied EM field. Interfacial polarization phenomena involving charge separation, migration, accumulation/depletion, and relaxation around PP interfaces is referred to as perfectly polarized interfacial polarization (PPIP); it influences the magnitude and direction of the electric field and charge carrier migration in the geomaterial. I develop a mechanistic model to quantify the complex-valued electrical conductivity response of geomaterials containing electrically conductive mineral inclusions, such as pyrite and magnetite, uniformly distributed in a fluid-filled, porous matrix made of non-conductive grains possessing surface conductance, such as silica and clay grains. The model first uses a linear approximation of Poisson-Nernst-Planck's (PNP) equations of dilute solution theory to determine the induced dipole moment of a single isolated conductive inclusion and that of a single isolated non-conductive grain surrounded by an electrolyte. A consistent effective-medium formulation is then implemented to determine the effective complex-valued electrical conductivity of the geomaterial. Our model predictions are in good agreement with laboratory measurements of multi-frequency complex-valued electrical conductivity,

relaxation time, and chargeability of mixtures containing electrically conductive inclusions.

5.1 INTRODUCTION

Interfacial polarization phenomena influence electromigration, charge carrier accumulation/depletion, and electrodiffusion processes in host materials (Wong, 1979; Schmuck and Bazant, 2012). A resistivity interpretation method that neglects interfacial polarization effects will lead to inaccurate estimation of petrophysical properties of formations containing electrically conductive inclusions. However, there are limited publications related to laboratory investigations and numerical modeling of the effects of interfacial polarization of electrically conductive mineral inclusions on subsurface galvanic resistivity, EM induction, and EM propagation measurements (Anderson et al., 2006; Anderson et al., 2008; Wang and Poppitt, 2013). Existing resistivity interpretation techniques for the three above-mentioned EM measurements do not account for the effects of interfacial polarization of electrically conductive mineral inclusions (Anderson et al., 2007; Corley et al., 2010). As a result, conventional resistivity interpretations in pyrite-rich sedimentary rocks (Altman et al., 2008) and pyrite- and graphite-rich organic source rocks (Anderson et al., 2008) typically give rise to inaccurate estimates.

In geomaterials, charge carriers in a porous brine-filled host are ions, while those in an electrically conductive mineral inclusion are holes and electrons (Chu and Bazant, 2006). Redox-active conditions allow charge transfer and charge carrier transport to occur at host-inclusion interfaces (common surfaces between conductive mineral inclusions and host). Such redox-active conditions exist only when (a) the pore-filling electrolyte is in contact with the outer surfaces of electrically conductive inclusions, (b) redox-active species (for example, Fe^{3+}, O_2, and H^+ are redox-active species with respect to pyrite) are

present in the electrolyte (Placencia-Gomez and Slater, 2014), and (c) the magnitude of the externally applied EM field is above a certain threshold value (Chu and Bazant, 2006). Consequently, host-inclusion interfaces in geomaterials containing conductive inclusions are typically impermeable to charge transport, inhibit charge transfer, and behave as perfectly polarized interfaces in the presence of weak or moderate externally applied electric fields.

In this chapter, I focus on the interfacial polarization phenomena occurring in redox-inactive conditions. I develop and test a new mechanistic electrochemical model, referred to as the PPIP model, to analyze the EM response of geomaterials containing uncharged perfectly polarizable spherical, rod-like, and/or sheet-like electrically conductive inclusions surrounded by either pore-filling conductive/non-conductive fluid or non-conductive matrix. Notably, the PPIP model is coupled with a surface-conductance-assisted interfacial polarization (SCAIP) model that accounts for the complex-valued conductivity response of fluid-filled, porous matrix made of non-conductive spherical grains possessing surface conductance (Σ_s). This work is technically significant as exploration and production activities are shifting toward geologically complex reservoirs and computationally inexpensive resistivity interpretation methods are required for purposes of accurate estimation of water saturation, conductivity of formation water, and organic content.

5.2 INTERFACIAL POLARIZATION PHENOMENA

When the surface of a non-metallic (non-conductive) mineral, such as clay minerals and silica grains, is exposed to electrolytes, it acquires charges due to ionic adsorption, protonation/deprotonation of the hydroxyl groups, and dissociation of other potentially active surface groups (e.g., Leroy and Revil, 2004). In contrast, in redox-inactive

conditions, the surface of a metallic or semi-metallic (electrically conductive) mineral, such as pyrite, graphite, magnetite, and siderite, does not possess surface charge when exposed to an electrolyte (Chu and Bazant, 2006). However, in presence of an external EM field, charge carriers (holes and electrons) in electrically conductive mineral inclusions accumulate at host-inclusion interfaces; consequently, charges are induced on surfaces of electrically conductive inclusions. It is important to note that the process by which non-metallic particles acquire surface charges is significantly different from that of metallic and semi-metallic particles. In this chapter, the mechanism of interfacial polarization and its effect associated with non-metallic particles is referred to as the SCAIP phenomena, while that associated with conductive particles is referred to as the PPIP phenomena.

In presence of an externally applied electric field, non-metallic and conductive particles both develop a counterion cloud and diffused-charge distribution around host-inclusion interfaces. Variations in the external electric field perturb the charge distribution around host-inclusion interfaces from its equilibrium state. Therefore, in the presence of a time-varying electric field, electromigration, charge carrier accumulation/depletion, and diffusion processes require a certain time, referred to as the relaxation time, to attain the equilibrium state. Dynamics of accumulation/depletion of charge carriers, relaxation process, and distribution of charge carrier concentrations around host-inclusion interfaces influence the magnitude, phase, and frequency dispersion of the EM response of geomaterials containing electrically conductive inclusions.

5.2.1 Mathematical models of interfacial polarization phenomena

Various mathematical models of accumulation/depletion and relaxation of charge carriers around surfaces of non-conductive spherical particles possessing surface conductance have been developed for applications in colloidal (Grosse and Barchini,

1992), electrochemical (Chu and Bazant, 2006), microfluidic, biological (Zheng and Wei, 2011), and geophysical (Revil, 2012; Placencia-Gomez and Slater, 2014) measurements. Modeling of interfacial polarization can be done using circuit (Dias, 2000), empirical (Tarasov and Titov, 2013), phenomenological (Wait, 1986), or mechanistic models (Schmuck and Bazant, 2012; Revil et al., 2015a; Revil et al., 2015b). A physically consistent model must satisfy Kramers-Kronig relations (Olhoeft et al., 1994; Toumelin et al., 2008).

Schwarz (1962) modeled the interfacial polarization mechanism around charged particles as a diffusion of counterions moving along the surface of a charged particle. This modeling framework neglected all the bulk diffusion effects by calculating the potential outside the counterion layer as a solution of Laplace's equation rather than Poisson's equation. Dukhin et al. (1974) developed a new approach to this problem based on the concept of a diffused double layer. Non-linearity of the Dukhin et al.'s (1974) equation led to mathematical complexity which does not provide analytical expressions for the interfacial polarization process in terms of various relaxation parameters. Subsequently, Grosse and Foster (1987) developed a simplified model which led to an analytical solution of interfacial polarization of charged spherical particles in an electrolyte. Previous theories were improved by Grosse and Barchini (1992) and Wong (1979) for infinitely conductive spherical particles in an electrolyte with semi-permeable membranes capable of electrochemical reactions. Different from the above-mentioned models, our model couples interfacial polarization of uniformly distributed spherical, rod-like, and sheet-like finitely conductive inclusions in redox-inactive conditions, with the interfacial polarization of the electrolyte-filled, porous host medium made of spherical, silt- and/or clay-sized grains possessing surface conductance.

5.3 PPIP-SCAIP MODEL

The PPIP model is based on the PNP equations for a dilute solution in a weak electrical field regime. Using the PNP equations, I analyze the EM response of a representative volume comprising a single, isolated electrically conductive inclusion surrounded by the host material (Zheng and Wei, 2011). Subsequently, I employ a consistent effective-medium formulation to determine the effective complex conductivity (K_{eff}) of the entire mixture (Grosse and Barchini, 1992). I claim that the PPIP model is reliable for studying the EM response of mixtures containing uniformly distributed inclusions of characteristic length < 1 mm, conductivity < 10^5 S/m, relative permittivity < 20, relative magnetic permeability equal to 1, and volume fraction < 20% in the frequency range of 100 Hz to 100 MHz. Beyond these limits, the PPIP model predictions will incur significant discrepancies with measurements due to the skin effect of the inclusion phase. The skin effect is primarily governed by the operating frequency and conductivity of the inclusion phase. PPIP model predictions are physically consistent only when the estimated skin depth is an order of magnitude larger than the characteristic length of the inclusions. For example, at an operating frequency of 100 kHz, an inclusion phase of conductivity of 10^3 S/m and ε_r of 10 exhibits a skin depth of 50 mm. Therefore, the PPIP model can be used to compute the complex conductivity response of a geological mixture containing such an inclusion phase at 100 kHz only when the characteristic length of the inclusion phase is smaller than 5 mm.

The PPIP model is coupled with the SCAIP model for consistent petrophysical applications. Likewise, the SCAIP model quantifies the complex conductivity response of fluid-filled, porous host medium, while the PPIP model quantifies the complex conductivity response of an electrically conductive inclusion phase that is uniformly

distributed in the fluid-filled, porous host medium. The integrated PPIP-SCAIP model assumes negligible EM coupling and dipole-dipole interaction between adjacent polarizable particles, namely conductive inclusions and non-conductive particles possessing surface conductance. This chapter develops the mathematical formulation of the PPIP model for the three geometries, namely sphere, long cylinder, and thin sheet, while that of the SCAIP model will be documented in a forthcoming publication. For purposes of model simplification, electrically conductive mineral grains, dispersed clay mineral grains, and silt- and clay-sized grains of the host medium are identified as isolated spheres. Further, pore-throat-filling and rod-like mineralization are identified as isolated parallelly aligned long cylinders; fractures, mineral veins, mineral laminations, and thin beds are identified as isolated parallelly aligned thin sheets.

Figure 5.1 shows the three types of geological mixtures that can be analyzed using the PPIP model. Figures 5.2 and 5.3 are schematic depictions of PPIP phenomena in a representative volume of a dilute mixture of uniformly distributed electrically conductive spherical, rod-like, or sheet-like inclusions in an electrolyte-saturated host medium. The representative volume illustrated in Figure 5.2 describes the geological mixtures shown in Figures 5.1a and 5.1b while that in Figure 5.3 describes the geological mixture shown in Figure 5.1c. For the representative volume of a mixture containing spherical inclusions (Figure 5.1a), as shown in Figure 5.2, interfacial polarization is independent of the direction of the externally applied electric field due to spherical symmetry. On the other hand, for the representative volume of a mixture containing rod-like inclusions (Figure 5.1b), as shown in Figure 5.2, interfacial polarization exists only in the transverse radial direction and is negligible in the axial direction (y-axis). Owing to the azimuthal symmetry of a rod-like inclusion, interfacial polarization at the cylindrical surface is independent of the

azimuth of the incident electric field. By contrast, for the representative volume of a mixture containing sheet-like inclusions (Figure 5.1c), as shown in Figure 5.3, interfacial polarization only develops across the *XY*-plane along the *z*-axis. In order to exhibit interfacial polarization, sheet-like inclusions require that the component of the externally applied electric field along the *z*-axis be non-zero. Directionality of interfacial polarization of rod-like and sheet-like inclusions gives rise to electrical anisotropy in formations containing such inclusions.

The phenomenological basis of interfacial polarization considered in our work builds on the mechanistic descriptions outlined by Revil et al. (2015a) (see also Placencia-Gomez and Slater, 2014). Charge carriers in conductive minerals have higher mobility compared to ions in porous geomaterials. In the presence of an externally applied EM field, charge carriers in the disseminated electrically conductive inclusions migrate faster and accumulate at impermeable interfaces. Consequently, electrically conductive inclusions behave as dipoles in the presence of an externally applied electric field. Subsequently, charge carriers in the host medium migrate and accumulate on host-inclusion interfaces under the influence of the externally applied electric field and that of the induced charges in conductive inclusions. Unlike Wong's (1979) model, the newly developed PPIP model integrates the dynamics and distribution of charge carriers inside and outside electrically conductive inclusions. Therefore, the PPIP model predicts the large dielectric enhancement and complex conductivity dispersion behavior of mixtures containing conductive inclusions uniformly distributed in a porous, electrolyte-saturated host.

In the absence of an externally applied electric field, a Guoy-Chapman layer is assumed around the silt- and clay-sized grains and clay mineral inclusions. A negligible initial surface charge is also assumed on electrically conductive inclusions. Thus, there is

no double layer around the surface of electrically conductive inclusions, whereby the surface conductance of a conductive inclusion is negligible. Similar assumptions are made in electrochemistry and colloid science with respect to electrochemical relaxation around metallic surfaces (Chu and Bazant, 2006). Also, I assume absence of redox-active species and neglect the influence of pH of pore water (Revil et al., 2015a). The host and inclusion phases can be modeled as an electrically conductive, insulating, or dielectric material. Also, pore-filling fluid can be modeled as electrically conductive or non-conductive material. The host, inclusion, and pore-filling fluid are assumed to have homogeneous, isotropic, and non-dispersive electrical properties. Therefore, the frequency dispersion and dielectric enhancement predicted by the PPIP model solely stem from the PPIP phenomenon around electrically conductive inclusions.

5.3.1 Poisson-Nernst-Planck's Equations

The PNP equations have been applied to model electromigration and diffusion of ionic charge carriers in electrolytes (e.g., Zheng and Wei, 2011) and that due to holes and electrons in semiconductors (e.g., Schmuck and Bazant, 2012). It is based on a mean-field approximation of charge carrier interactions and continuum descriptions of concentration and electrostatic potential. I apply the PNP equations to model charge dynamics and relaxation in the representative volume (Figures 5.2 and 5.3) containing only two phases, namely the host medium, denoted by subscript *h*, and the electrically conductive inclusion phase, denoted by subscript *i*. The host medium can be either an electrolyte or the non-conductive matrix. At time $t < 0$, it is assumed that there is no external electric field exciting the representative volume. Also, spontaneous initial accumulation of charges is assumed to be absent on the host-interfaces. At time $t < 0$, electro-neutrality is assumed throughout the system. Initial charge carrier densities at equilibrium conditions in both the host and

inclusion phases are denoted as $N_{0,j}$, where subscript *j* takes the form of *i* for the inclusion phase and *h* for the host phase. At time $t = 0$, the representative volume experiences an uniform externally applied electric field $E = E_0 e^{i\omega t}$, where E_0 is the amplitude of the externally applied electric field, i is square root of -1, and ω is the frequency of the externally applied electric field. Under a weak field approximation, charge carrier densities in host and inclusion phases are perturbed from their equilibrium conditions near the host-inclusion interfaces, resulting in a new linearly approximated charge distribution given by

$$N_j^{\pm}(r) = N_{0,j} + c_j^{\pm}(r) e^{i\omega t} \cos(\theta) , \quad (1)$$

such that $\left|c_j^{\pm}\right| \leq N_{0,j}^{\pm}$, $c_j^{\pm}$ is the charge density variation due to the externally applied electric field near the host-inclusion interface in medium j, r is the distance along the normal to the interface, and θ is the angle between the normal to the interface and the incident external electric field. Further, the symbol "+" identifies positive-charge carriers such as holes and cations, while the symbol "-" identifies negative-charge carriers such as electrons and anions.

I use a low-frequency approximation that requires that ω be much smaller than $a^2/{\lambda_D}^2$, where λ_D is the Debye screening length and a is the characteristic length of the inclusion phase. The characteristic length a is equal to the radius of spherical inclusion, radius of rod-like inclusion, or half of the thickness of sheet-like inclusion. Mathematically, $\lambda_D = \sqrt{\varepsilon_h k_B T/(2Z_h^+ Z_h^- q^2 N_{0,h})}$, where ε_h is dielectric permittivity of the host, k_B is Boltzmann's constant, T is absolute temperature, $Z_h^{\pm}$ is charge number of positive and negative charge carriers in the host, and q is the elementary charge. One of our simplifying assumptions is that all the charge carriers bear unitary charge and that both host and inclusion phases bear binary, symmetric charge carriers. In other words,

$$Z_j^{\pm} = 1, \mu_h^+ = \mu_h^- = \mu_h, \mu_i^+ = \mu_i^- = \mu_i, N_{0,i}^+ = N_{0,i}^- = N_{0,i} ; N_{0,h}^+ = N_{0,h}^- = N_{0,h}, \quad (2)$$

where $\mu_j^{\pm}$ is the electrical mobility of positive and negative charge carriers in medium *j*, and $Z_j^{\pm}$ is charge number of positive and negative charge carriers in medium *j*.

The current density of each charge carrier type in the host and inclusion phases is the sum of current density due to drift current and diffusion current. In the absence of generation/recombination reactions, the transport equation representing conservation laws for charge-carrying species can be written as

$$\mathbf{j}_j^{\pm} = \mathbf{j}_{j,\text{drift}}^{\pm} + \mathbf{j}_{j,\text{diffusion}}^{\pm} = \mathrm{q}N_j^{\pm}\mu_j\mathbf{e}_j \mp \mathrm{q}D_j^{\pm}\nabla N_j^{\pm}, \tag{3}$$

where $\mathbf{j}_j^{\pm}$ is the current density of positive and negative charge carriers, respectively, in medium *j*, $\mathbf{e}_j$ is the net electric field vector in medium *j*, and $D_j^{\pm}$ is diffusion coefficient of positive and negative charge carriers, respectively, in medium *j*. When using the simplifying assumption for electrical mobility of charge carriers, as mentioned in equation 2, and Einstein's relationship of diffusion coefficient with electrical mobility, namely $D_j = (\mu_j \mathrm{k_B} T)/\mathrm{q}$, I obtain

$$D_h^+ = D_h^- = D_h,\ D_i^+ = D_i^- = D_i. \tag{4}$$

By substituting $\mathbf{e}_j = -\nabla\varphi_j$ into the low-frequency limit of Maxwell's equations (induction neglected) and substituting equation 4 into equation 3, I express the charge species conservation condition as

$$\mathbf{j}_j^{\pm} = -\mathrm{q}N_j^{\pm}\mu_j\nabla\varphi_j \mp \mathrm{q}D_j\nabla N_j^{\pm}, \tag{5}$$

where φ_j is the electrical potential in medium *j*. Equation 5 is Nernst-Planck's equation that describes the relationship of the flux of charge-carrying species to its concentration gradient and that to the applied electrical potential gradient in a given medium. Nernst-Planck's equation can alternatively be expressed as

$$\mathbf{j}_j^{\pm} = -D_j^{\pm}N_j^{\pm}\nabla\varphi_{cj}^{\pm}, \tag{6}$$

where $\varphi_{cj}^{\pm} = \mathrm{k_B}T\ln(N_j^{\pm}) \pm \mathrm{q}Z_j^{\pm}\varphi_j$ is the electrochemical potential of charge carriers.

The continuity equation for charge carrier density based on mass conservation for each charge carrier type in an incompressible medium without any convective flow can be written as

$$\mp \mathrm{q}\frac{\partial N_j^{\pm}}{\partial t} = \nabla \cdot \mathbf{j}_j^{\pm}. \tag{7}$$

By applying equation 5 and Einstein's relationship to equation 7, I obtain

$$\frac{\partial N_j^{+}}{\partial t} = \nabla \cdot \left(D_j \nabla N_j^{+} + \frac{\mathrm{q}D_j}{\mathrm{k_B}T} N_j^{+} \nabla \varphi_j \right), \tag{8}$$

and

$$\frac{\partial N_j^{-}}{\partial \mathrm{t}} = \nabla \cdot \left(D_j \nabla N_j^{-} - \frac{\mathrm{q}D_j}{\mathrm{k_B}T} N_j^{-} \nabla \varphi_j \right). \tag{9}$$

Using equation 1, the right-hand side of equation 7 can be re-written as

$$\frac{\partial N_j^{\pm}}{\partial t} = \mathrm{i}\omega c_j^{\pm}. \tag{10}$$

I apply equation 10 to the right-hand side of equations 8 and 9, and subtract the new form of equation 8 from equation 9 to obtain

$$-\mathrm{iq}\omega d_j = -2\mathrm{q}N_{0,j}\mu_j \Delta\varphi_j - \mathrm{q}s_j\mu_j\Delta\varphi_j - \mathrm{q}D_j\Delta d_j, \tag{11}$$

where $d_j = \ c_j^{+} - c_j^{-}$, $s_j = \ c_j^{+} + c_j^{-}$, and Δ (∇^2) is Laplace's operator. Also, because of the electroneutrality condition assumed for time $t < 0$, I assume $d_j = \ c_j^{+} - c_j^{-} = 0$ for the far-field regime at all times $t \geq 0$. Under the influence of an externally applied EM field, the distribution of charge carriers within both media leads to a time-varying electric potential that is expressed as $\varphi_j(r, \theta, t) = \varphi_j(r) e^{\mathrm{i}\omega t} \cos(\theta)$. Using Gauss' law and equation 1, I obtain

$$\nabla \cdot (\varepsilon_j \mathbf{e}_j) = \ P_{\mathrm{f},j} = \ \mathrm{q}\left(N_j^{+} - N_j^{-}\right) = \ \mathrm{q}\left(c_j^{+} - c_j^{-}\right) = \ \mathrm{q}d_j, \tag{12}$$

where $P_{f,j}$ is the net free charge in medium j due to charge redistribution in the presence of an externally applied EM field. Equation 12 relates the spatial distribution of electric charge to the time-varying electric field.

Assuming that both media are linear, isotropic, and homogeneous, and that the electric field can be defined by a scalar electrical potential field, φ_j, I obtain

$$\nabla \cdot \left(\varepsilon_j \mathbf{e}_j\right) = -\nabla \cdot \left(\varepsilon_j \nabla \varphi_j\right) = -\varepsilon_j \Delta \varphi_j. \tag{13}$$

By combining equations 12 and 13, I obtain an alternate expression of Poisson's equation, given by

$$\Delta \varphi_j = -\frac{\mathrm{q} d_j}{\varepsilon_j}. \tag{14}$$

Poisson's equation is applied to describe the electric field in terms of the electrical potential, the gradient of which governs electromigration in both media. Under the weak field approximation, by substituting equation 14 into equation 11, I obtain the PNP equations, given by

$$-\mathrm{iq}\omega d_j = {2\mathrm{q}^2 N_{0,j} \mu_j d_j}\Big/{\varepsilon_j} - \mathrm{q} D_j \Delta d_j, \tag{15}$$

which can be re-written as

$$\Delta d_j = \left(\frac{\mathrm{i}\omega}{D_j} + \frac{\sigma_j}{\varepsilon_j D_j}\right) d_j, \tag{16}$$

where σ_j=$2N_{0j}\mu_j$q is the electrical conductivity of medium j, $\varepsilon_j = \varepsilon_{\mathrm{r},j}\varepsilon_0$ is the dielectric permittivity of medium j, $\varepsilon_{r,j}$ is the relative permittivity of medium j, and $\varepsilon_0 = 8.854 \times 10^{-12}$ F/m is vacuum permittivity. I rewrite equation 16 as

$$\Delta d_j = \gamma_j{}^2 d_j, \tag{17}$$

where

$$\gamma_j{}^2 = \left(\frac{\mathrm{i}\omega}{D_j} + \frac{\sigma_j}{\varepsilon_j D_j}\right). \tag{18}$$

Equation 17 is a Helmholtz partial differential equation that can be solved by separation of variables in Cartesian, cylindrical, or spherical coordinates to obtain an analytical expression for d_j in the host and inclusion phases around the perfectly polarized

host-inclusion interface of a sheet-like inclusion [Appendix A], rod-like inclusion [Appendix B], and spherical inclusion [Appendix C].

After obtaining the analytical expression for d_j, I apply the following two boundary conditions to generate the particular solution: (a) d_j is finite everywhere in the representative volume and (b) d_j is zero in the host medium at a distance far away from the interface due to electroneutrality. In doing so, I obtain two distinct analytical expressions of d_j for the host and inclusion phases, respectively. Subsequently, equation 17 is inserted into equation 14 to obtain the following Laplace partial differential equation that can be solved for the electric potential field in the representative volume:

$$\Delta\vartheta_j = 0, \tag{19}$$

where

$$\vartheta_j = \varphi_j + {(\mathrm{q}d_j)}\Big/{(\gamma_j^2\varepsilon_j)}. \tag{20}$$

Appendices A, B and C describe the solution of equation 19 in Cartesian, cylindrical and spherical coordinates, respectively. Equation 19 is solved using the following boundary conditions:

(a) Assuming a zero intrinsic capacitance of the host-inclusion interface, the electric potential must be continuous at the interface.

(b) The normal component of the displacement field must be continuous at the interface. This condition corresponds to the fact that there is no surface-charge distribution on an electrically conductive inclusion phase.

(c) The normal component of the current density must vanish at the interface for both media. This condition expresses the fact that in the absence of transport of charge carriers and exchange of charges along the interface, the diffusive and electro-migrative currents must cancel each other at the interface. Our focus is perfectly polarizable or

completely blocking interfaces without Faradic processes, wherein fluxes of charge carriers must vanish on both sides of the interface.

A limitation of the PNP equations arises from the omission of the finite volume effect of charge carriers, mutual interactions and steric effects, effects due to transport of ions in confined channels of the pore system, and correlation effects (Chu and Bazant, 2006). Another limitation arises because the model is developed only for symmetric, binary charge carriers in both the host and inclusion phases. This assumption simplifies the analytical complexity of the PNP formulations. Another drawback of the PNP formulations is that the analysis is performed for materials that contain completely dissociated charge carriers at low concentration values. Moreover, in this chapter, unlike Chu and Bazant (2006), I only consider the linear response to weak fields where exact solutions are possible.

5.3.2 Effective medium model

In geophysical applications, it is desirable to treat a mesoscopically heterogeneous mixture as a macroscopically homogeneous medium. Such homogenization is done by constructing the final macroscale material incrementally from a starting microscopic material. First, microscopic electrical properties around a single inclusion/scatter are computed using the PNP equations, as explained in the previous section. Dipolarizability (dipole moment), $f(\omega)$, of the representative volume, as shown in Appendices A, B, and C for different geometries of the inclusion, are computed using the PNP equations. In our derivations of the PNP equations, the effect of multipoles are neglected as their magnitude decreases with inverse power of distance (Sihvola, 2007). Also, I neglect monopole effects because there is zero net charge due to the assumed electroneutrality of the mixture. After calculating the dipolarizability of the representative volume, the global macroscopic

electrical properties are computed using effective-medium formulations which are based on the concept that a material composed of a mixture of distinct homogeneous media can be considered as a homogeneous material at a sufficiently large observation scale (Giordano, 2003). Modeling of effective electrical properties of heterogeneous materials requires information about (a) the number of phases constituting the mixture; (b) geometrical shapes and sizes of individual phases; and (c) the electrical properties of individual phases, their distribution, and their interfacial properties.

In this chapter, I primarily focus on estimating effective electrical properties of mixtures having less than 20% volume fraction of electrically conductive inclusions, which lies within the limits of Maxwell-Garnett effective-medium formulations. Moreover, for purposes of petrophysical studies, reservoir rocks have less than 10% volume fraction of conductive mineral inclusions. Therefore, I implement a Maxwell-Garnett-type effective-medium formulation to obtain the effective electrical properties. Such a formulation neglects EM interactions between heterogeneities. Due to the assumed dilution of the uniformly distributed inclusion phase, individual elements of the dispersed phase are assumed to be isolated and not in contact with each other. Similar to other mixing theories, our model includes the assumption that the magnitude of spatial variations of the electric field is smaller than the magnitude of variations in the intrinsic electrical properties and geometrical structures. Moreover, all calculations are performed using a quasi-static assumption that requires the size of heterogeneities to be much smaller than the wavelength of the applied EM field (Cosenza et al., 2009). Also, when dealing with a lossy medium, the skin depth of the EM wave must be considered to avoid strong attenuation of the field amplitudes in the heterogeneities. Most importantly, due to the implementation of the PNP

equations, and unlike other theories (e.g., Giordano, 2003), our effective-medium formulations explicitly account for the characteristic lengths of heterogeneities.

For a monodispersed mixture of ellipsoidal inclusions, the effective-medium model of the mixture can be written in terms of the complex-valued conductivity (Giordano, 2003) as

$$\frac{K_{\hat{n},\text{eff}} - K_h}{K_{\hat{n},\text{eff}} + n_{\hat{n}} K_h} = \phi_i \frac{K_i - K_h}{K_i + n_{\hat{n}} K_h}, \tag{21}$$

which can also be expressed as

$$\frac{K_{\hat{n},\text{eff}} - K_h}{K_{\hat{n},\text{eff}} + n_{\hat{n}} K_h} = \phi_i f_{\hat{n}}(\omega), \tag{22}$$

where $K = \sigma + \mathrm{i}\omega\varepsilon$ is a representation of the complex conductivity of a material, $K_{\hat{n},\text{eff}}$ is the effective complex conductivity of the geological mixture along the $\hat{n}$ unit vector that can be measured with respect to the component of the externally applied electric field directed along the $\hat{n}$ unit vector, K_h is the complex-valued conductivity of the homogenous isotropic host material that surrounds the inclusions, K_i is the complex-valued conductivity of the homogenous isotropic inclusion material, ϕ_i is the volume fraction of the inclusion phase in the mixture, $n_{\hat{n}}$ is the shape factor of the inclusion phase along the $\hat{n}$ unit vector, and $f_{\hat{n}}(\omega)$ is the dipolarizability of the representative volume along the direction of $\hat{n}$ unit vector. Dipolarizability of the representative volume is derived in Appendices A, B, and C using the PNP equations. In the absence of interfacial polarization, equation 21 is used for purposes of Maxwell-Garnett's effective-medium formulation (Sihvola, 2007). However, for our study, where I model large induced dielectric polarization phenomena, equation 21 will lead to erroneous results because K_i is drastically altered due to interfacial polarization around the electrically conductive inclusions. Therefore, equation 22 should be used for

effective-medium formulations of the PPIP model (Wong, 1979; Grosse and Barchini, 1992). Additionally, in equations 21 and 22, the shape factor can be expressed as

$$n_{\hat{n}} = \frac{1 - L_{\hat{n}}}{L_{\hat{n}}}, \tag{23}$$

where $L_{\hat{n}}$ is the depolarization factor of the inclusion phase in the direction of the $\hat{n}$ unit vector (Sihvola, 2007).

As derived in Appendix A, for a sheet-like inclusion (Figure 5.3) that comprises the representative volume of a formation containing uniformly distributed, parallelly aligned, thin beds, laminations, veins, or induced fractures (Figure 5.1c), the dipolarizability can be expressed as

$$f(\omega) = \left(1 - \frac{K_h}{K_i}\right) + \frac{\mathrm{i}}{\omega a}\left[\frac{K_h}{K_i}\frac{\sigma_i}{\varepsilon_i}\frac{F_i}{H_i} - \frac{\sigma_h}{\varepsilon_h}\frac{E_h}{G_h}\right]. \tag{24}$$

Additionally, the directional K_{eff} response for a mixture containing sheet-like inclusions can be computed by substituting equation 24 into equation 22, and next by implementing the following expressions for the depolarization factor, as mentioned in Giordano (2003):

$$L_{\hat{x}} = L_{\hat{y}} = 0;\ L_{\hat{z}} = 1,$$

and

$$n_{\hat{x}} = n_{\hat{y}} = \infty;\ n_{\hat{z}} = 0.$$

As a result, the K_{eff} of such a mixture (Figure 5.1c) is significantly altered along the *z*-axis and negligibly altered along the *x*- and *y*-axes.

Similarly, as derived in Appendix B, for a rod-like inclusion (Figure 5.2) that comprises the representative volume of a formation containing uniformly distributed pore-throat-filling or rod-like mineralization (Figure 5.1b), the dipolarizability can be expressed as

$$f(\omega) = -1 + \frac{2\mathrm{i}\omega}{\left[\frac{1}{a}\frac{K_h}{K_i}\frac{\sigma_i}{\varepsilon_i}\frac{F_i}{H_i} - \frac{1}{a}\frac{\sigma_h}{\varepsilon_h}\frac{E_h}{G_h} + \mathrm{i}\omega\left(\frac{K_h}{K_i} + 1\right)\right]}. \tag{25}$$

The directional K_{eff} properties for a mixture containing rod-like inclusions can be computed by substituting equation 25 into equation 22, and by implementing the following expressions for the depolarization factor, as mentioned in Giordano (2003):

$$L_{\hat{y}} = 0; L_{\hat{x}} = L_{\hat{z}} = \frac{1}{2},$$

and

$$n_{\hat{y}} = \infty;\ n_{\hat{x}} = n_{\hat{z}} = 1.$$

As a result, the K_{eff} of such a mixture is significantly altered along the *x*- and *z*-axes, and altered negligibly along the *y*-axis.

Similarly, as derived in Appendix C, for a spherical inclusion (Figure 5.2) that comprises the representative volume of a formation containing uniformly distributed grain mineralization and vugs (Figure 5.1a), the dipolarizability can be expressed as

$$f(\omega) = -\frac{1}{2} + \frac{3}{2}\frac{\mathrm{i}\omega}{\left[\frac{2}{a}\frac{\sigma_h}{\varepsilon_h}\frac{E_h}{G_h} - \frac{2}{a}\frac{K_h}{K_i}\frac{\sigma_i}{\varepsilon_i}\frac{F_i}{H_i} + \mathrm{i}\omega\left(\frac{2K_h}{K_i} + 1\right)\right]}. \tag{26}$$

The directional K_{eff} properties for a mixture containing spherical inclusions can be computed by substituting equation 26 into equation 22, and by implementing the following expressions for the depolarization factor, as mentioned in Giordano (2003):

$$L_{\hat{x}} = L_{\hat{y}} = L_{\hat{z}} = \frac{1}{3},$$

and

$$n_{\hat{x}} = n_{\hat{y}} = n_{\hat{z}} = 2.$$

As a result, the K_{eff} of such a mixture is significantly altered along all three orthogonal directions.

Finally, I extended Wong's (1979) effective-medium formulation and implement the new formulation to model the complex conductivity response of multiphase mixtures containing *m* distinct ellipsoidal structures, for instance, a mixture of spherical, rod-like,

and sheet-like inclusion constitutes 3 different phases. The new mixing law that leads to consistent effective electrical properties for a multiphase mixture of *m* distinct ellipsoidal structures can be expressed as

$$\sum_{\mathrm{u}=1}^{\mathrm{m}} \left[\frac{K_{\hat{n},\mathrm{eff}} - K_{\mathrm{h}}}{K_{\hat{n},\mathrm{eff}} + n_{\hat{n},u} K_{\mathrm{h}}} \times \frac{\phi_{i,u}}{\left(\sum_{l=1}^{m} \phi_{i,l} \right)} \right] = \sum_{\mathrm{u}=1}^{\mathrm{m}} \phi_{i,u} f_{\hat{n},u}(\omega), \qquad (27)$$

where $n_{\hat{n},u}$ is the shape factor of the *u*-th inclusion phase belonging to a particular ellipsoidal structure along the $\hat{n}$ unit vector, $\phi_{i,u}$ is the volume fraction of *u*-th inclusion phase in the multiphase mixture, and $f_{\hat{n},u}(\omega)$ is the dipolarizability of *u*-th inclusion along the $\hat{n}$ unit vector. I applied equation 27 to mixtures containing two different sizes of electrically conductive spherical inclusions or those containing two different shapes of electrically conductive inclusions. The resulting expression for $K_{\hat{n},\mathrm{eff}}$ is in quadratic form and leads to consistent K_{eff} values as shown in the final section of this chapter that describes the petrophysically adverse alterations of resistivity and permittivity estimates due to PPIP of disseminated conductive inclusions.

5.4 PPIP-SCAIP MODEL VALIDATION

In this section, PPIP-SCAIP model predictions are compared to experimental data obtained from various peer-reviewed published materials. I observe the following salient features of the PPIP model predictions: (1) presence of uniformly distributed inclusions in an electrolyte-filled, porous mixture significantly alters its complex conductivity response, (2) the estimated diffusion coefficient of charge carriers in electrically conductive inclusions is similar to that of the *p*- and *n*-charge carriers in the inclusion material, (3) the peak frequency of the quadrature conductivity (σ") and the phase response (Θ) of a mixture containing uniformly sized electrically conductive spherical inclusions is inversely related to the radius of inclusions and is a function of both the diffusion coefficient of charge

carriers in the inclusion phase and that in the electrolyte-filled host material, and (4) the σ'' and chargeability (M) scales linearly with the volume content of the inclusion phase.

The following assumptions are made for purposes of comparison of the PPIP-SCAIP model predictions: (1) the concentration of the inclusion phase is below the percolation threshold, (2) magnetic effects are neglected, (3) host-inclusion interfaces are electrochemically inactive and smooth, (4) redox-inactive conditions persist in the mixtures under investigation, and (5) the operating frequency is such that the characteristic length of the inclusion phase is much smaller than the wavelength of the applied electromagnetic field.

In the following section, I first compare the spectral response computed using the PPIP-SCAIP modeling scheme to that measured in various laboratory experiments (e.g., Abdel Aal et al., 2014). Then, I compare the estimation of relaxation time, critical frequency, and chargeability calculated based on the PPIP-SCAIP model to those obtained from experimental measurements (e.g., Wong, 1979).

5.4.1 Spectral response

Schwan et al. (1962) conducted laboratory investigations of dielectric enhancement and dielectric dispersion of colloidal suspensions of polystyrene spheres of uniform size in an ionic electrolyte. Their experiments considered the frequency range from 10 Hz to several MHz. For modeling purposes, they used a frequency-dependent surface admittance circuit model to explain their laboratory measurements. In that paper, the authors mentioned the need to develop a mechanistic model to predict experimental data. Figure 5.4 compares the PPIP model predictions and experimental data from Schwan et al. (1962). PPIP model predictions are in good agreement with experimental results for input values that are similar to published ones. Using similar values for electrical properties of the

polystyrene particles and electrolyte, I obtain good agreement for the computed ε_r of the suspension with another set of experimental results mentioned in Schwan et al. (1962), as shown in Figure 5.5. Figures 5.4 and 5.5 imply that the presence of dispersed polystyrene particles produces drastic dielectric enhancement and dispersion due to interfacial polarization phenomena because neither the host nor the inclusion individually possess dielectric characteristics comparable to that measured in the experiments. On the other hand, Figures 5.4 and 5.5 indicate relatively smaller conductivity dispersion in the order of 1% relative difference between the high- and low-frequency values of conductivity, which is attributed to the absence of high-mobility charge carriers in the inclusion phase. Further, Figure 5.5 shows that PPIP modeling results match EM measurements of oil-in-water emulsions performed by Hanai et al. (1959).

Hanai et al. (1979) measured the EM response of suspensions of bovine erythrocytes in a NaCl solution. These biological suspensions of erythrocyte cells exhibit dielectric relaxation due to interfacial polarization at insulating host-inclusion interfaces formed of thin-lipidic cell membranes. The representative volume of this mixture is formed of conducting cytoplasm surrounded by a non-conducting shell of lipidic membrane immersed in an ionic electrolyte. PPIP modeling of the EM response of such biological suspensions (Hanai et al., 1979) showed good agreement between the PPIP modeling results and measured values, as shown in Figure 5.6. In this experiment, cell walls act as perfectly polarized interfaces. Further, I modeled experiments performed by Delgado et al. (1998), who worked on identifying laboratory techniques to differentiate surface from volume diffusion mechanisms. They carried out dielectric dispersion measurements on suspensions of polymer latex balls in a KCl solution. PPIP modeling results matched

experimental results for two different volume fractions of polymer latex balls in a KCl solution, as shown in Figure 5.7.

Mahan et al. (1986) measured the complex resistivity responses of synthetic samples containing quartz grains of various sizes and conductive sulphide particles of different materials that were fully saturated with electrolytes with or without active ions (e.g., Cu^{2+} ions are active ions with respect to chalcopyrite mineral inclusions). Active ions results in charge transfer across host-inclusion interfaces due to oxidation-reduction reactions. Mahan et al. (1986) were successful in matching laboratory measurements of the complex resistivity of synthetic samples using Wong's (1979) model in the frequency range where frequency dispersion and peak of Θ occur. A limitations of Wong's (1979) model is the assumption that inclusions have infinite conductivity and the host behaves as a non-polarizable ionic material rather than as a mixture of electrolyte and silica grains that exhibit interfacial polarization arising from electrochemical effects of surface conductance (also, referred to as the SCAIP phenomenon). The PPIP-SCAIP model does not suffer from the limitations of Wong's (1979) model. Unlike Mahan et al.'s (1986) modeling procedure, the PPIP-SCAIP model takes into account the effects of surface conductance of uniformly distributed 80-μm diameter spherical silica grains that are fully saturated with pore-filling fluid. As shown in Figure 5.8a, the PPIP-SCAIP model predictions match very well the computed results from Mahan et al. (1986) for the complex conductivity response of a mixture of chalcopyrite and silica grains fully saturated with a NaCl solution that contains no active ions. The PPIP-SCAIP model predicts a Debye-type dispersion response in the absence of active ions. On the other hand, for the mixture of quartz and pyrite grains fully saturated with a NaCl solution that contains active ions, electrochemical charge transfer reactions occur at interfaces giving rise to a Warburg-type response, as shown in Figure

5.8b. As a result, the agreement between PPIP-SCAIP model predictions and experimental results worsens at higher frequencies for this mixture. Electrochemical charge transfer reaction at the interface due to active ions alters the boundary conditions at the interface assumed in our present study.

Importantly, the PPIP-SCAIP model was implemented to estimate the diffusion coefficient of charge carriers in the inclusion phase and the resistivity of inclusions. These estimated values are in good agreement with the physical properties of the inclusion materials, as mentioned in Revil et al. (2015a). The estimated resistivity of pyrite is 5 times higher than that of chalcopyrite, while the diffusion coefficient of charge carriers in pyrite is an order of magnitude larger than that of chalcopyrite. Due to the dynamics of charge carriers in the electrically conductive inclusion, I observe 13% relative difference between low- and high-frequency resistivity values, which is significantly larger than that obtained for mixtures containing non-conductive inclusions (e.g., Schwan et al., 1962).

Abdel Aal et al. (2014) performed laboratory experiments to investigate the complex conductivity signatures of five minerals, namely pyrite, magnetite, goethite, hematite, and siderite, disseminated in porous media under variable iron mineral content and grain size. PPIP-SCAIP model predictions are in good agreement with laboratory measurements. The PPIP-SCAIP model was implemented to estimate the diffusion coefficient of charge carriers in pyrite inclusions to be 1×10^{-6} m^2s^{-1}, which is comparable to the diffusion coefficient of charge carriers in metallic grains equal to 2.5×10^{-5} m^2s^{-1} for p-charge carriers and 3×10^{-6} m^2s^{-1} for n-charge carriers as estimated from laboratory measurements carried out by Revil et al. (2015a). Figure 5.9 shows that PPIP-SCAIP modeling results agree with experimental values for uniformly distributed pyrite mineral inclusions in sand matrix fully saturated with a NaCl solution. I observe an increase in the

magnitude of the peak of σ" and a progressive shift in relaxation peak toward higher frequencies with a decrease in the diameter of pyrite inclusions. Also, I observe that the increase in in-phase conductivity (σ') is much smaller than that of the σ" because of the low values of conductivity of the pore-filling electrolyte.

Tirado and Grosse (2006) performed broadband dielectric measurements on suspensions of spherical polystyrene particles having high surface charge distribution in an aqueous solution. Instead of using the PPIP-SCAIP model, I used only the SCAIP model to quantify the dielectric enhancement and dispersion behavior of suspensions measured by Tirado and Grosse (2006). Interfacial polarization phenomena in their experiment is dominated by surface conductance effects due to high surface charge of polystyrene particles. Figure 5.11 shows a good agreement between Tirado and Grosse's (2006) measurements and SCAIP model predictions. This agreement validates the use of the SCAIP model in quantifying the interfacial polarization arising from surface conductance effects of quartz and clay grains.

5.4.2 Relaxation time and critical frequency

PPIP model predictions generate a complex conductivity response having Debye-like characteristics that is consistent with various laboratory measurements on mixtures containing conductive inclusions (e.g., Wong, 1979). As shown in Figure 5.13a, the PPIP model predicts a linear relationship between relaxation time (τ) and radius of electrically conductive spherical inclusions. This linear relationship can also be expressed as an inverse relationship of critical frequency and radius of conductive spherical inclusions, as illustrated in Figure 5.12, which compares PPIP model predictions against Wong's (1979) modeling results. Specifically, Figure 5.12 implies that an inverse relationship exists only when active ions are not present in the electrolyte and when the radius of uniformly

distributed conductive spherical inclusions are lower than 50 μm. Further, PPIP model predictions of the linear relationship of τ with radius of conductive spherical inclusions is in accordance with the theoretical derivation by Shilov and Borkovskaya (2010), where they show that the critical frequency of β-dispersion (Maxwell-Wagner-type relaxations) is inversely related to the radius of conductive spherical inclusions for medium and high frequencies. On the other hand, at low frequencies, Shilov and Borkovskaya (2010) show that the critical frequency of α-dispersion (concentration polarization due to surface conductance) for a mixture containing only non-conductive inclusions possessing surface conductance is related to the radius of inclusions by an inverse square law, also determined by Dukhin et al. (1974). Furthermore, unlike previously published research work describing PPIP phenomena, the PPIP model predicts an inverse logarithmic dependence of relaxation time on the diffusion coefficient (D) of charge carriers in the inclusion phase and also to that of charge carriers in the host, as shown in Figure 5.13b. In agreement with previous experimental work (Abdel Aal et al., 2014; Revil et al., 2015b), I find in Figure 5.13c that relaxation time is negligibly dependent on the volume concentration of electrically conductive spherical inclusions.

5.4.3 Chargeability

Chargeability of a mixture is expressed as

$$M = (\sigma_\infty - \sigma_0)/\sigma_\infty, \tag{28}$$

where σ_∞ is effective conductivity (σ_{eff}) of a mixture at very high frequency (~GHz), and σ_0 is σ_{eff} of a mixture at very low frequency (~Hz). Figures 5.14a and 5.14b describe the chargeability values as measured by several researchers based on electrical experiments conducted on mixtures of various host conductivity values, inclusion materials, and sizes of the inclusion phase. Figures 5.14a and 5.14b imply that the chargeability of a mixture

derived from PPIP modeling predictions of the complex conductivity response indicates that the estimated chargeability is a function of the volume fraction of electrically conductive spherical inclusions and is independent of both the size of spherical inclusions and conductivity of the host. It should be noted that, in Figures 5.14a and 5.14b, PPIP model predictions are independent of the radius of the spherical inclusions and conductivity of the host medium. The PPIP model predicts that chargeability is independent of the variations in conductivity of the host medium for values close to or higher than 0.01 S/m, as shown in Figure 5.14c. This host-conductivity-independent behavior is in good agreement with the observations by Revil et al. (2015a) and the experimental comparisons carried out by Revil et al. (2015b). However, for conductivities of the host medium close to 0.001 S/m or lower, as illustrated in Figure 5.14c, I notice deviations of computed chargeability estimates from the host-conductivity-independent behavior. In other words, the PPIP model predicts that, for low values of conductivity of the host medium, the chargeability will deviate from the host-conductivity-independent behavior that has been documented by several researchers.

5.5 CONCLUSIONS

I derived an analytical formulation, referred to as the PPIP model, to compute the complex-valued electrical conductivity of geomaterials containing uniformly distributed electrically conductive inclusions in the shape of a sphere, long rod, or thin sheet. Furthermore, the PPIP model was integrated with the SCAIP model for consistent petrophysical applications. The integrated PPIP-SCAIP model quantifies the complex-valued conductivity response of non-conductive grains possessing surface conductance and that due to uniformly distributed perfectly polarizable conductive inclusions. It is important to note that the PPIP-SCAIP model quantifies the complex-valued conductivity response

only in the direction along the characteristic length of the inclusion phase. The PPIP-SCAIP model suffers from the inherent limitations of the PNP equations and a Maxwell-Wagner type effective-medium formulation. Nonetheless, the PPIP-SCAIP model was successfully validated in the frequency range from 100 Hz to 100 MHz for a characteristic length of the inclusion phase ranging from 0.1 μm to 1 mm. It predicts that the chargeability of a mixture depends only on the volumetric content of electrically conductive inclusions when the host conductivity is close to or higher than 0.01 S/m. Unlike the well-established relaxation-time versus characteristic length relationship for interfacial polarization arising from surface conductance effects of non-conductive spheres, the PPIP relaxation time is linearly related to the radius of spherical inclusions and is inversely related to both the diffusion coefficient of charge carriers in the host and that of the inclusion phase. Notably, the estimated values of diffusion coefficient of charge carriers in the electrically conductive inclusion phase were consistent with the electrical mobility of *p*- and *n*-charge carriers in the inclusion material. It was found that the high-frequency effective conductivity increases while the low-frequency effective conductivity decreases with an increase in the concentration of metallic inclusions that give rise to PPIP phenomena.

The next chapter quantifies the petrophysically adverse effects of PPIP phenomena on effective complex-valued conductivity estimates obtained based on subsurface galvanic, EM induction, and EM propagation tool measurements in formations containing uniformly distributed conductive inclusions of various shapes, materials, and sizes.

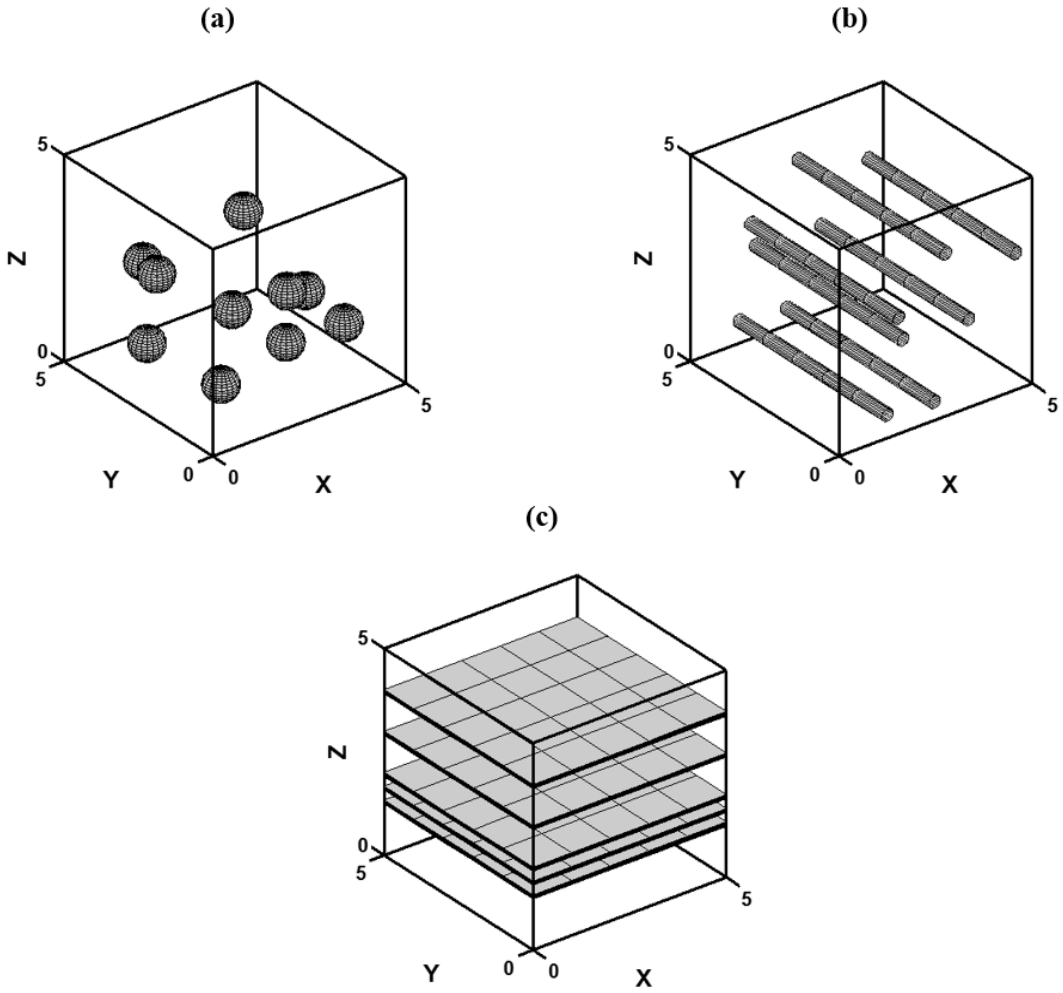

Figure 5.1: Illustration of the three types of geological mixtures that can be analyzed using the PPIP model. The total volume of each of the three mixtures is 125 (reference unit)^3. (a) Mixture contains 10 isolated spherical inclusions, each having a radius of 0.4 reference unit, that occupy 2.14% volume fraction, (b) mixture contains 7 isolated parallel long rod-like inclusions, each having a radius of 0.15 reference unit and a length of 5 reference unit, that occupy 1.98% volume fraction, and (c) mixture contains 5 isolated parallel thin sheet-like inclusions, each having a thickness of 0.099 reference unit, that occupy 9.9% volume fraction.

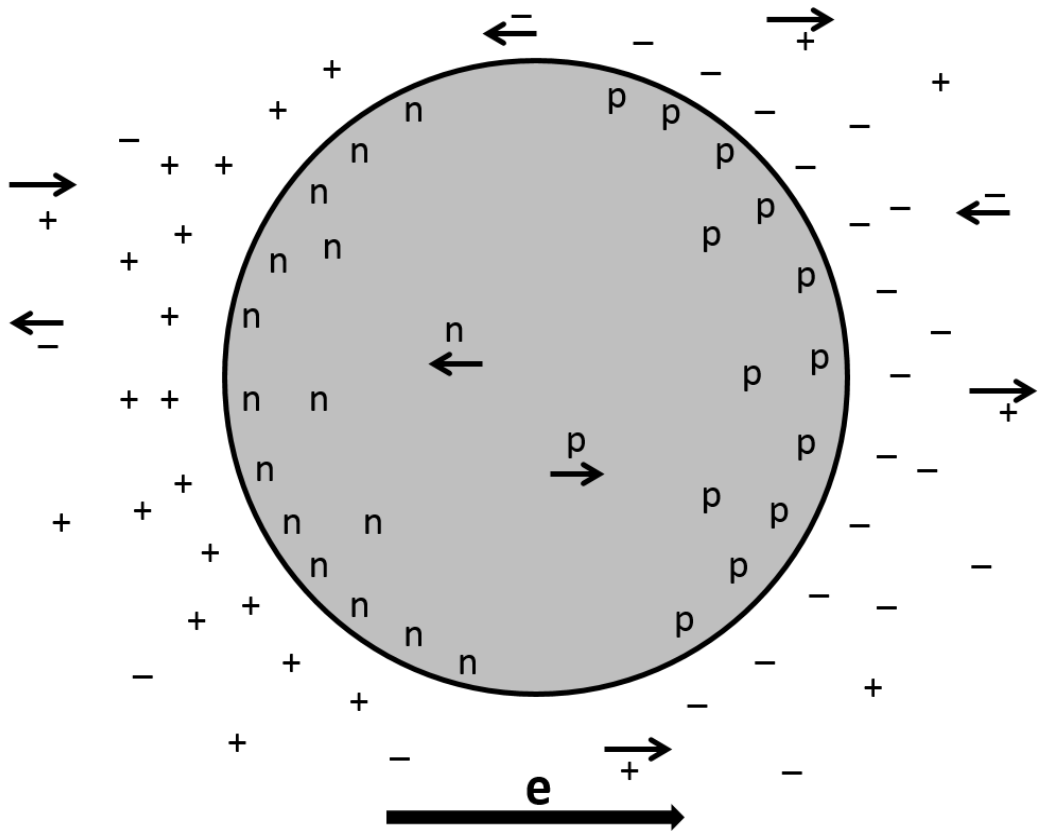

Figure 5.2: Cross-section of a perfectly polarized conductive spherical or rod-like inclusion surrounded by an ionic host medium. Charge carriers in the ionic host medium are cations, identified by "+" symbol, and anions, identified by "-" symbol. Charge carriers in the conductive sheet-like inclusion are *n*- and *p*-charge carriers, identified by symbol "n" and "p", respectively. The direction of the externally applied electrical field, **e**, is identified with a bold arrow next to the symbol "e". The direction of movement of the four different types of charge carriers is represented by the arrow next to the symbols of the charge carriers.

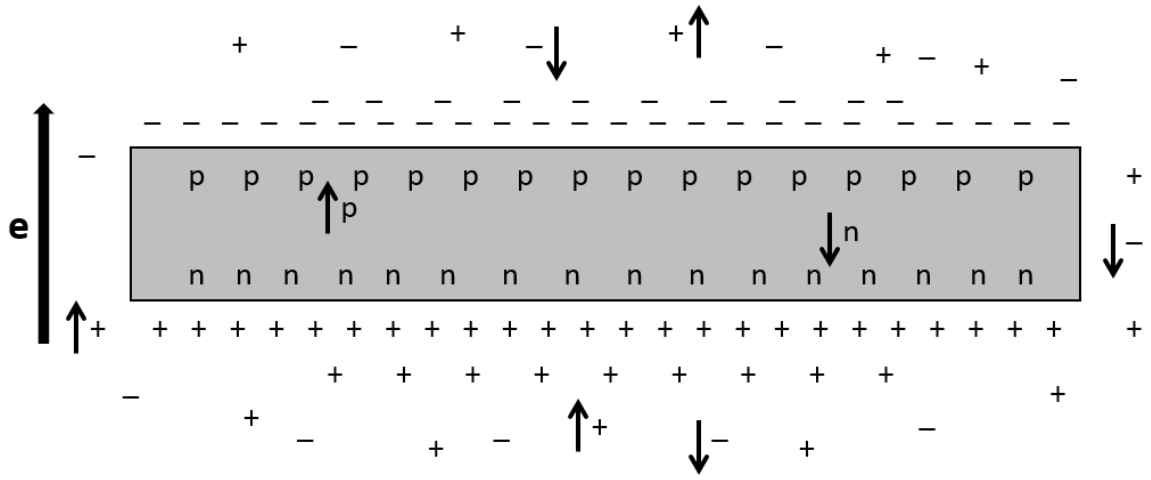

Figure 5.3: Cross-section of a perfectly polarized conductive sheet-like inclusion surrounded by an ionic host medium. Charge carriers in the ionic host medium are cations, identified by "+" symbol, and anions, identified by "-" symbol. Charge carriers in the conductive sheet-like inclusion are *n*- and *p*-charge carriers, identified by symbol "n" and "p", respectively. The direction of the externally applied electrical field, **e**, is identified with a bold arrow next to the symbol "e" that is along the thickness of the sheet. The direction of movement of the four different types of charge carriers is represented by the arrow next to the symbols of the charge carriers.

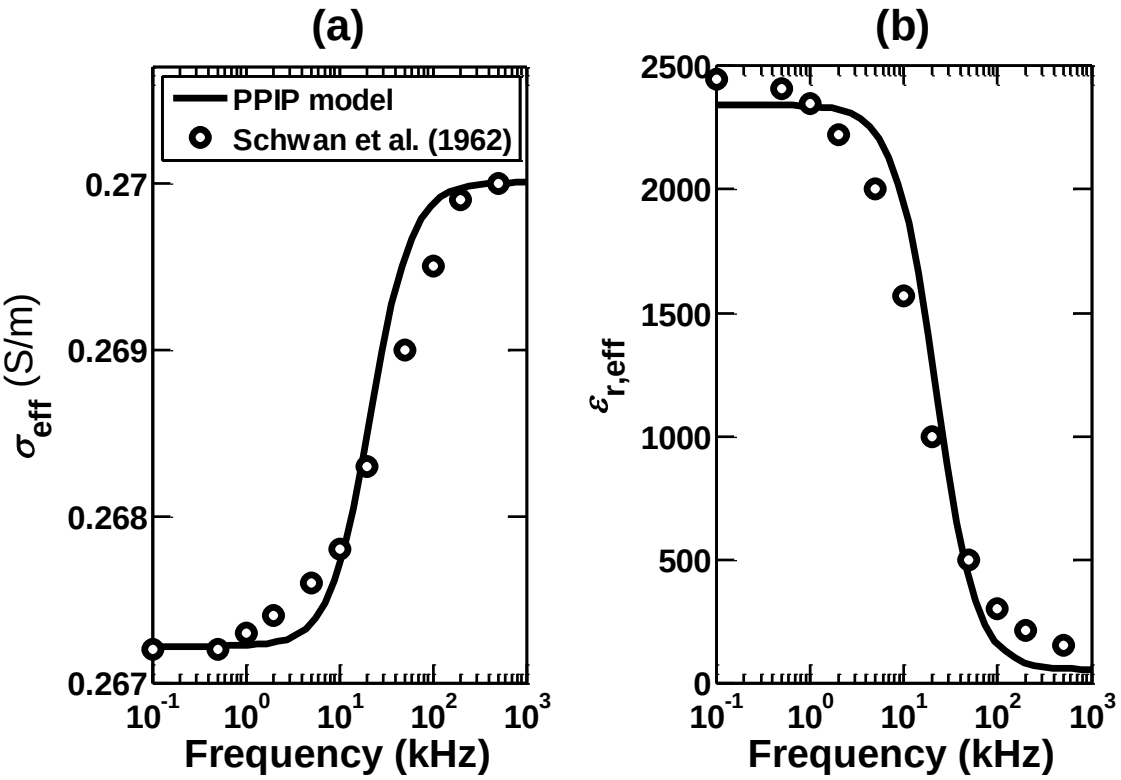

Figure 5.4: Comparison of the PPIP model predictions of (a) σ_{eff} and (b) $\varepsilon_{r,eff}$ against that measured by Schwan et al. (1962) for a colloidal suspension of 30% volume fraction of 0.188-μm diameter polystyrene balls uniformly distributed in 0.439 S/m KCl solution. ε_r of a polystyrene ball is 10 and that of the KCl solution is 78. Diffusion coefficient of ions in the KCl solution is 1.3×10^{-9} m^2/s.

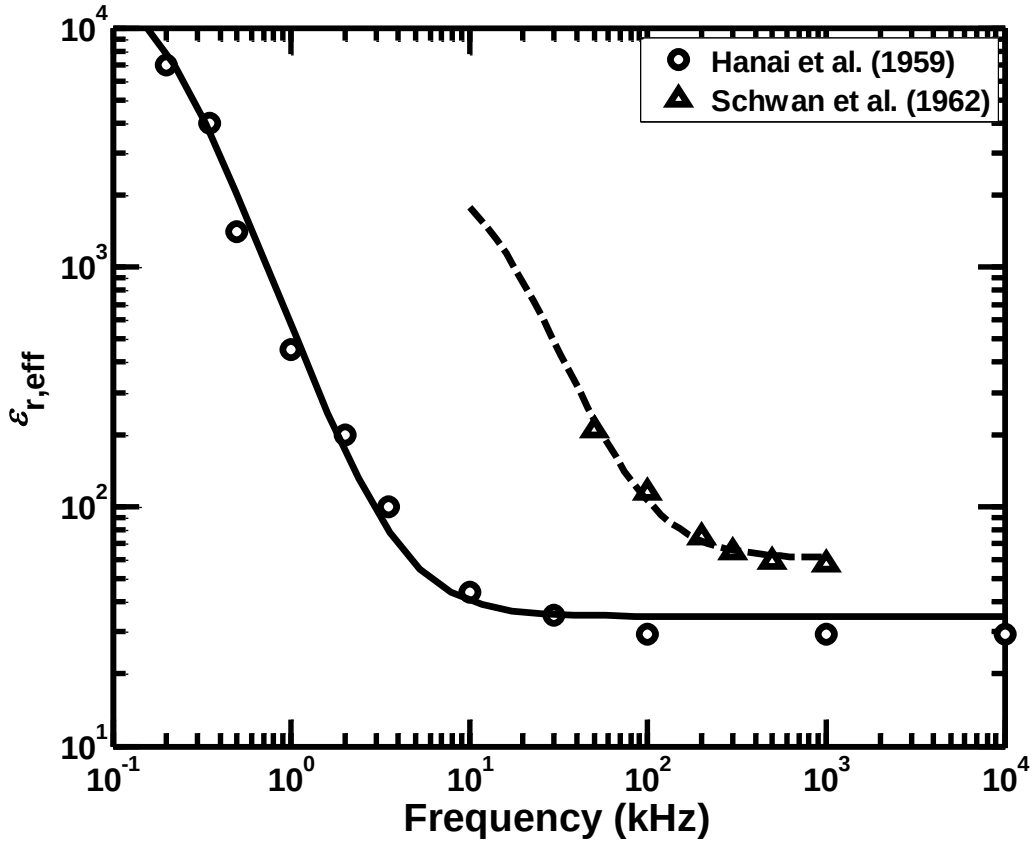

Figure 5.5: Comparison of the PPIP model predictions of $\varepsilon_{r,eff}$ against that measured by Schwan et al. (1962) and Hanai et al. (1959) for a colloidal suspension of polystyrene balls in KCl solution and oil-in-water emulsion, respectively. The colloidal suspension mentioned in Schwan et al. (1962) is made of 19.5% volume fraction of 0.56-μm diameter polystyrene balls of ε_r of 10 uniformly distributed in 0.125 S/m KCl solution. The oil-in-water emulsion mentioned in Hanai et al. (1959) is made of 50% volume fraction of 7-μm diameter oil droplets of ε_r of 5 uniformly distributed in 0.002 S/m solution. Both the KCl solutions have ε_r of 78, and diffusion coefficient of ions in both the KCl solutions is 1.3×10^{-9} m^2/s.

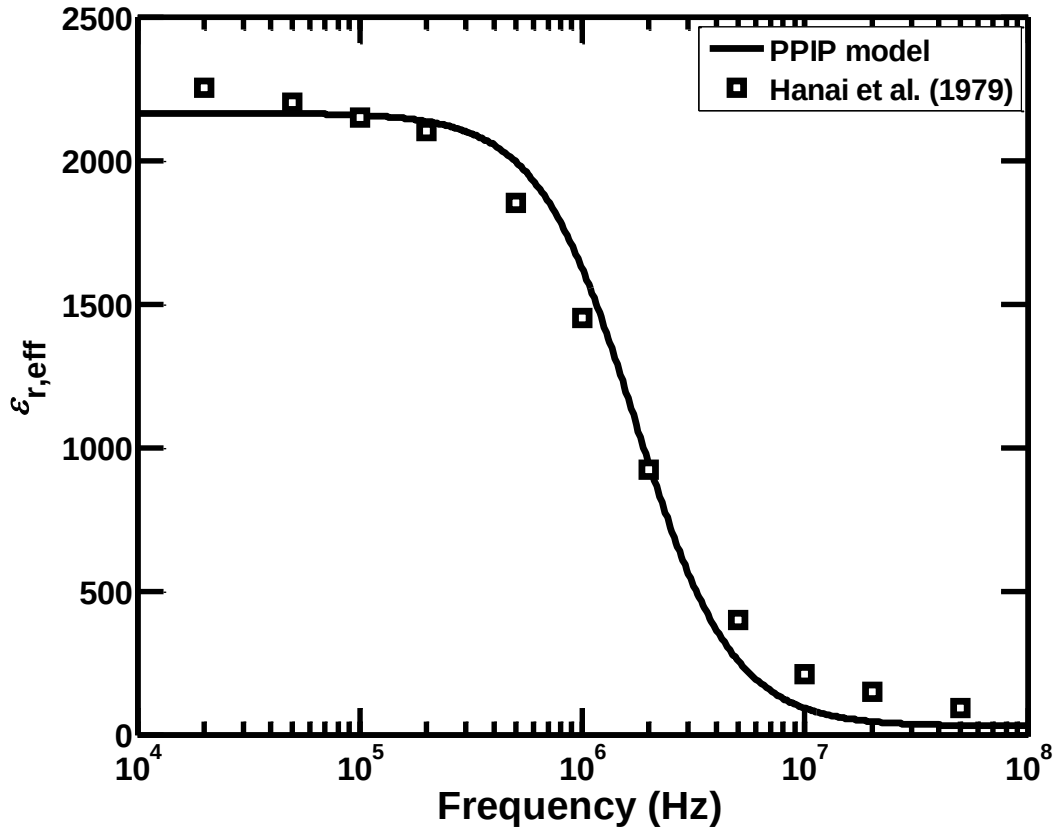

Figure 5.6: Comparison of the PPIP model predictions of $\varepsilon_{r,eff}$ against that measured by Hanai et al. (1979) for a suspension of 59.5% volume fraction of 0.9-μm diameter erythrocyte cells uniformly distributed in 0.4346-S/m conductivity NaCl solution. ε_r of an erythrocyte cell is 3 and that of the NaCl solution is 77. Diffusion coefficient of ions in the NaCl solution is 2×10^{-9} m^2/s. Conductivity of the region of erythrocyte cell inside the cell wall is 0.284 S/m.

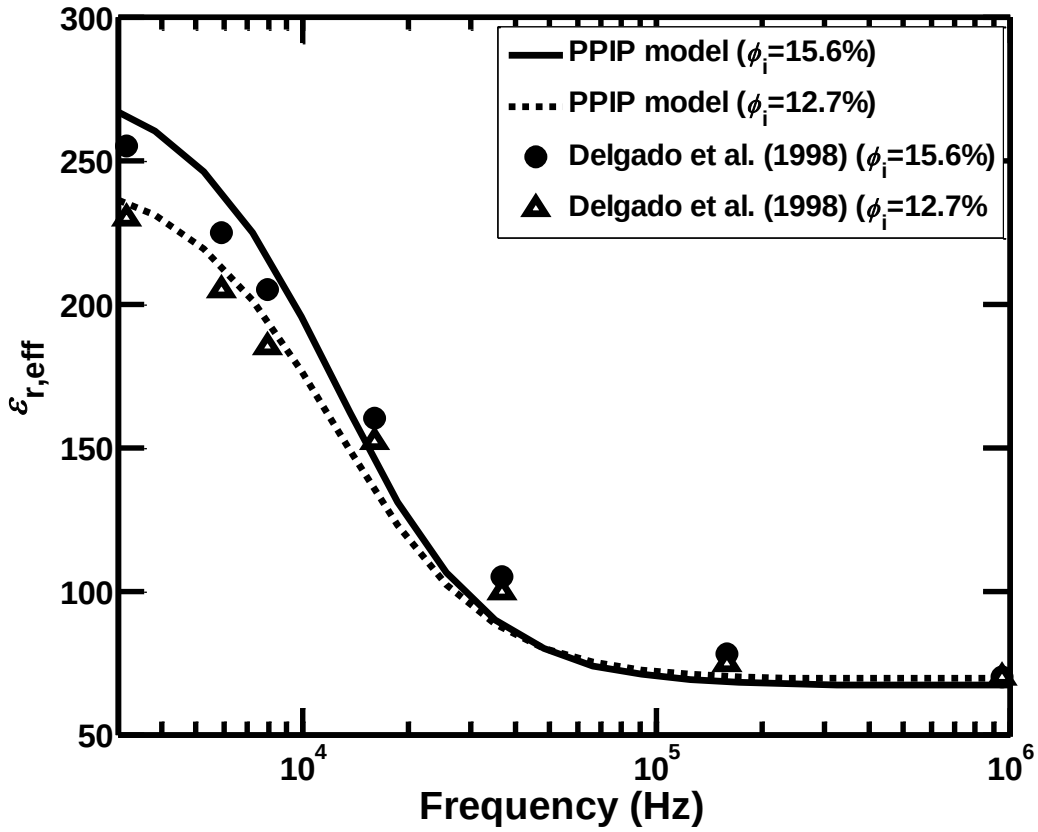

Figure 5.7: Comparison of the PPIP model predictions of $\varepsilon_{r,eff}$ against that measured by Delgado et al. (1998) for two suspensions having 12.7% and 15.6% volume fraction, respectively, of 115-μm diameter polymer latex balls uniformly distributed in 0.0147-S/m conductivity KCl solution. ε_r of a latex ball is 15 and that of the KCl solution is 78. Diffusion coefficient of ions in the KCl solution is 0.8×10^{-9} m^2/s.

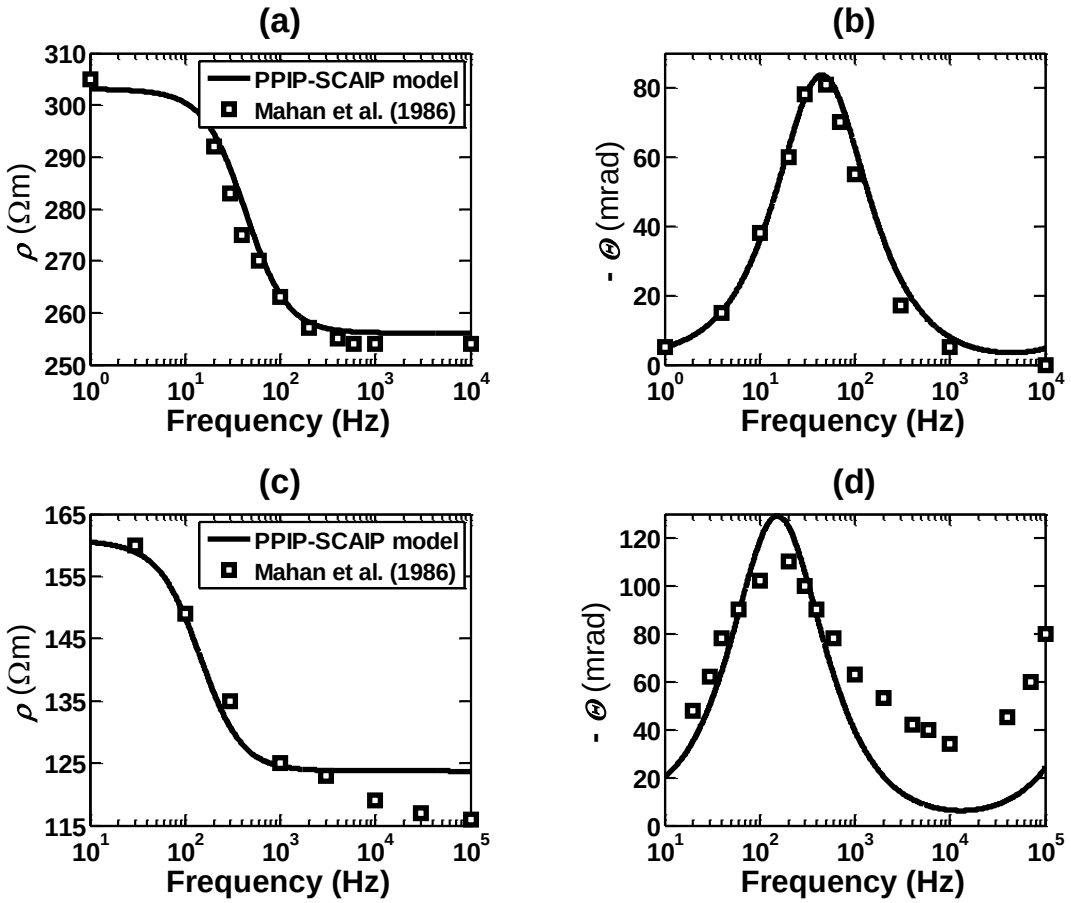

Figure 5.8: Comparison of the PPIP-SCAIP model predictions of (a) resistivity (ρ) and (b) phase angle (Θ) against that measured by Mahan et al. (1986) for mixtures containing 80-µm diameter quartz grain matrix and uniformly distributed 3.75% volume fraction of 276-µm diameter, 1000-S/m conductivity chalcopyrite grains fully saturated with 34% volume fraction of 0.0094-S/m conductivity NaCl solution without any active ions. Comparison of the PPIP-SCAIP model predictions of (c) resistivity (ρ) and (d) phase angle (Θ) against that measured by Mahan et al. (1986) for mixtures containing 80-µm diameter quartz grain matrix and uniformly distributed 5.8% volume fraction of 98-µm diameter, 5000-S/m conductivity pyrite grains fully saturated with 37% volume fraction of 0.0094-S/m conductivity NaCl solution with active ions. ε_r of chalcopyrite and pyrite is 10 and 15, respectively, and that of the NaCl solution is 80. Diffusion coefficient of charge carriers in chalcopyrite and pyrite is 10^{-7} and 10^{-6} m^2/s, respectively, and that of ions in the NaCl solution is 2×10^{-11} m^2/s.

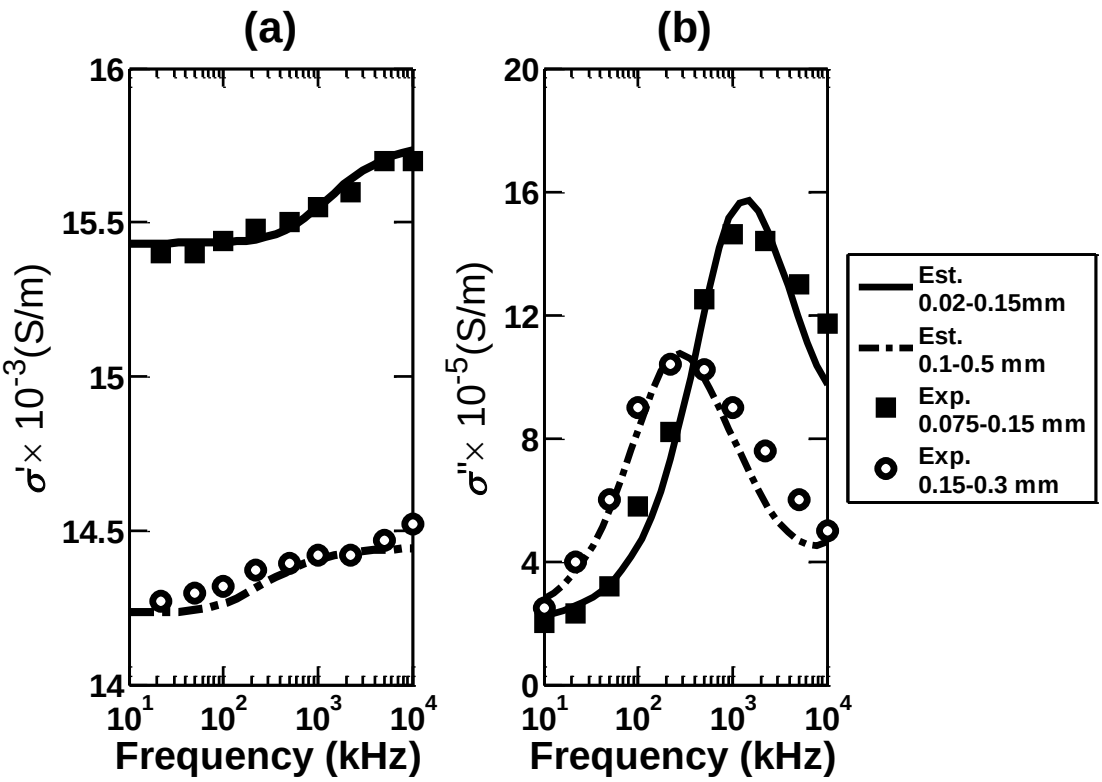

Figure 5.9: Comparison of the PPIP-SCAIP model predictions of (a) in-phase conductivity (σ') and (b) quadrature conductivity (σ'') against that measured by Abdel Aal et al. (2014) for two mixtures containing 0.3% volume fraction of 5000-S/m conductivity pyrite inclusions of varying grain diameter ranging from 0.075 to 0.15 mm and 0.15 to 0.3 mm, respectively. Pyrite inclusions were uniformly distributed in porous sand matrix that is fully saturated with 0.0256 S/m NaCl solution. ε_r of pyrite is 12 and that of the NaCl solution is 80. Diffusion coefficient of charge carriers in pyrite is 10^{-6} m^2/s and that of ions in the NaCl solution is 10^{-9} m^2/s.

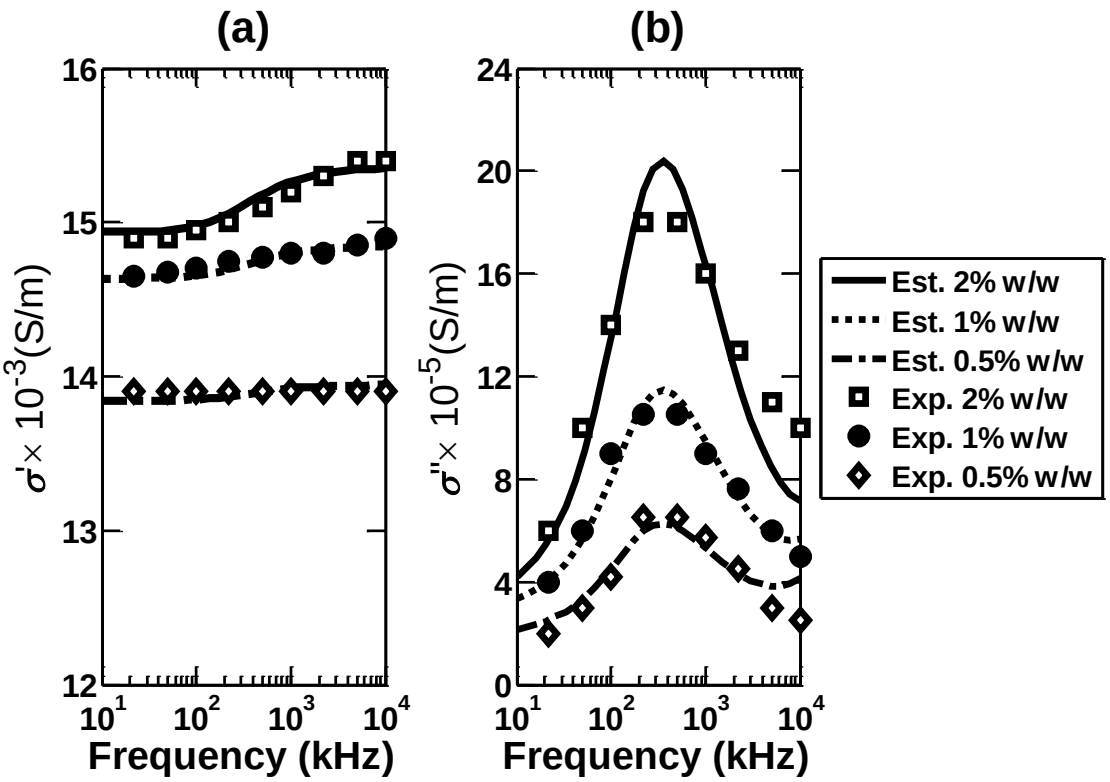

Figure 5.10: Comparison of the PPIP-SCAIP model predictions of (a) in-phase conductivity (σ') and (b) quadrature conductivity (σ'') against that measured by Abdel Aal et al. (2014) for three mixtures containing 0.5%, 1%, and 2% weight fraction, respectively, of 450-μm diameter pyrite inclusions uniformly distributed in porous sand matrix fully saturated with 0.0256-S/m conductivity NaCl solution. ε_r of pyrite is 12 and that of the NaCl solution is 80. Diffusion coefficient of charge carriers in pyrite is 10^{-6} m^2/s and that of ions in the NaCl solution is 10^{-9} m^2/s.

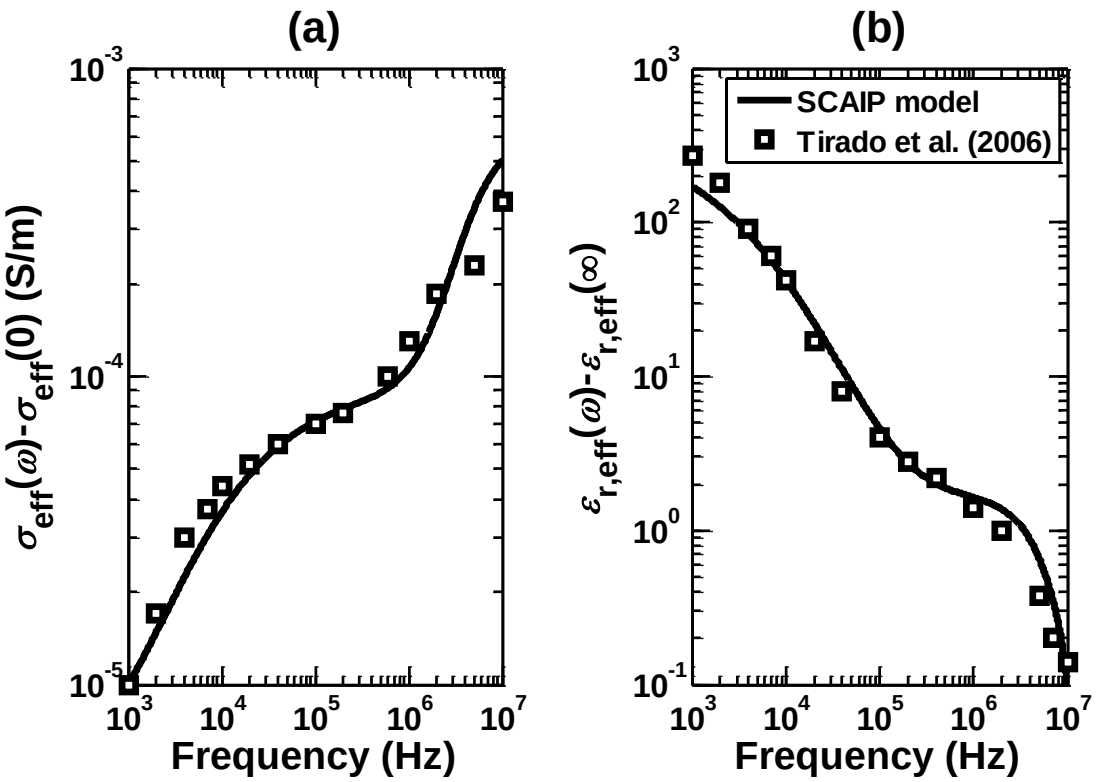

Figure 5.11: Comparison of the SCAIP model predictions of (a) change in effective conductivity ($\sigma_{eff}(\omega)$-$\sigma_{eff}(0)$) and (b) change in effective relative permittivity ($\varepsilon_{r,eff}(\omega)$-$\varepsilon_{r,eff}(\infty)$) against that measured by Tirado and Grosse (2006) for 1% volume fraction of 1-μm diameter polystyrene particles possessing Σ_s of 9×10^{-9} S, uniformly distributed in 0.0055-S/m conductivity NaCl solution. ε_r of polystyrene ball is 10 and that of the KCl solution is 80. Diffusion coefficient of ions in the KCl solution is 2×10^{-9} m^2/s.

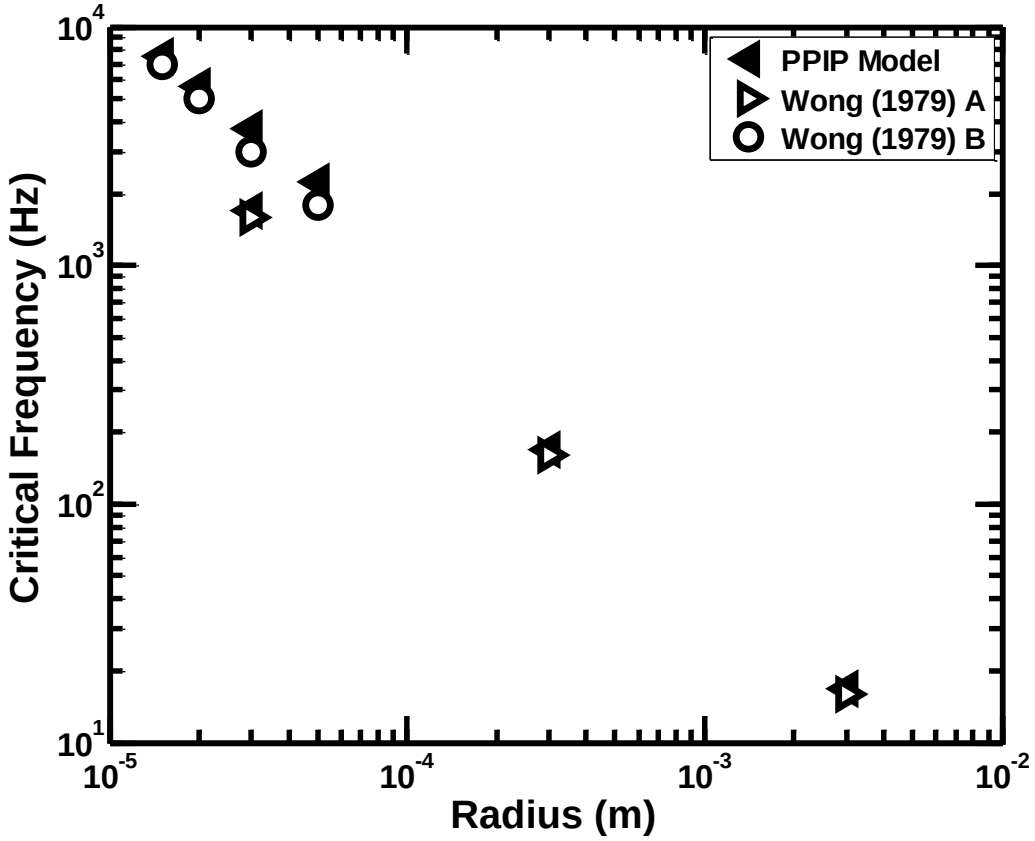

Figure 5.12: Comparison of the PPIP model predictions of critical frequency of induced frequency dispersion against that of Wong's (1979) modeling results for mixtures A and B containing conductive mineral inclusions of 5000-S/m conductivity that are uniformly distributed in the electrolytic host medium. Mixture A contains 8.3% volume fraction of conductive inclusions distributed in the 0.002-S/m conductivity electrolytic host having diffusion coefficient of ions of 10^{-9} m^2/s. Mixture B contains 6% volume fraction of conductive inclusions distributed in the 0.01-S/m conductivity electrolytic host having diffusion coefficient of ions of 2×10^{-9} m^2/s. For both the mixtures, ε_r of conductive inclusion is 15 and that of the host is 12. Also, for both the mixtures, the diffusion coefficient of charge carriers in the conductive inclusions is 10^{-6} m^2/s.

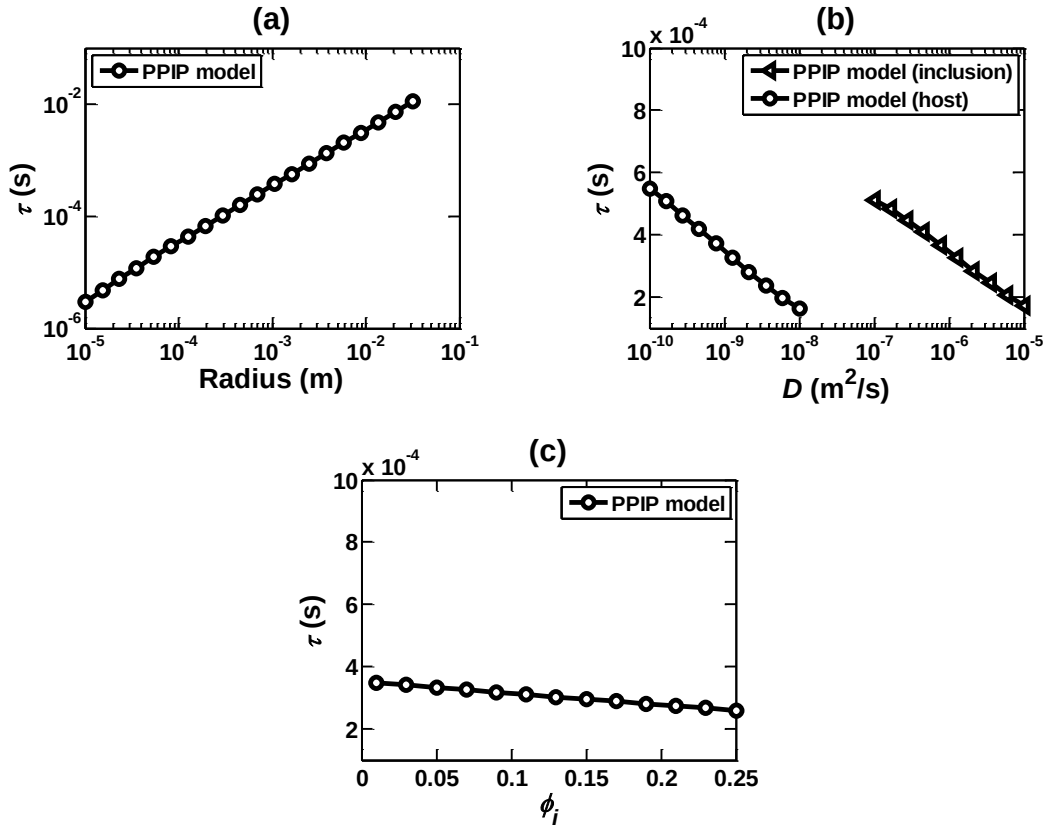

Figure 5.13: PPIP model predictions of the effect of PPIP phenomenon on the relaxation time (τ) as a function of (a) radius of the spherical conductive inclusions, (b) diffusion coefficient (D) of charge carriers in the host and inclusion phases, and (c) volume fraction (ϕ_i) of spherical conductive inclusion phase. Default mixture is assumed to contain 1% volume fraction of 100-S/m conductivity, 200-μm diameter conductive inclusions uniformly distributed in 0.01-S/m conductivity electrolytic host medium. ε_r of conductive inclusion phase is 10 and that of the host is 80. Diffusion coefficient of charge carriers in conductive inclusion is 10^{-6} m^2/s and that of ions in the host is 10^{-9} m^2/s.

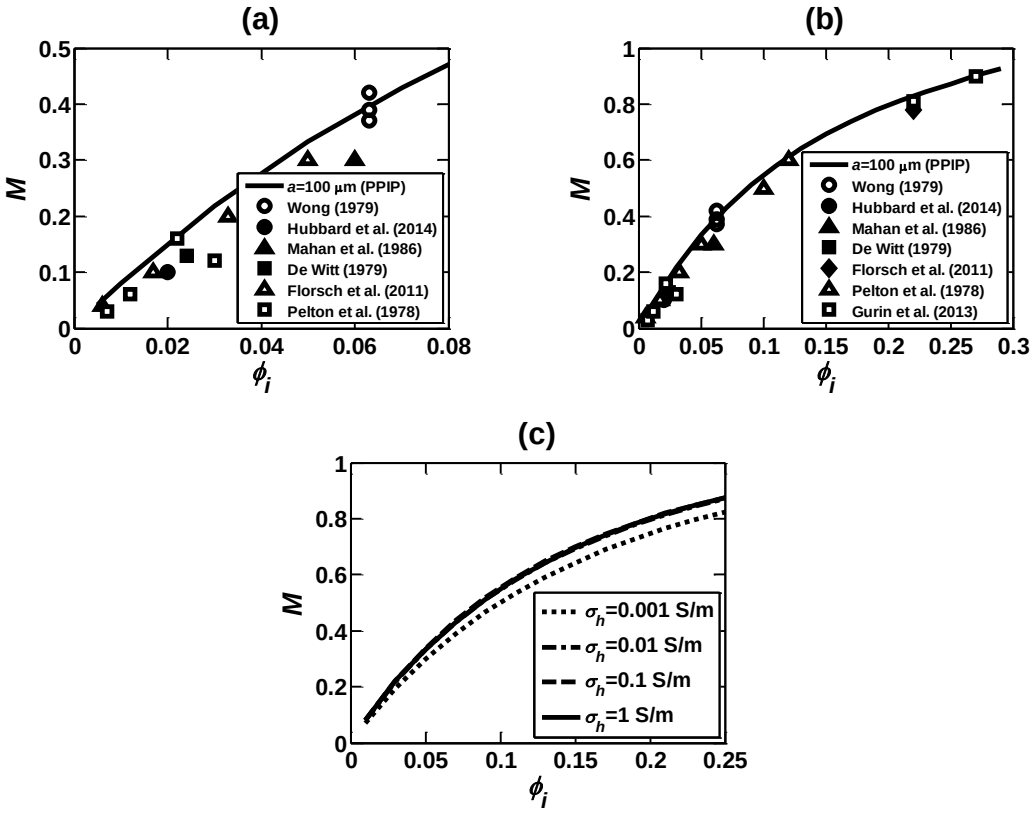

Figure 5.14: Comparison of the PPIP model predictions of chargeability (M) against that estimated from various laboratory measurements of the complex resistivity response of synthetic and geological samples for varying volume fractions (ϕ_i) of conductive mineral inclusions in the range of (a) 0 to 8% and (b) 0 to 30% uniformly distributed in the host medium. (c) PPIP model predictions of chargeability of mixtures containing varying volume fractions, in the range of 0 to 25%, of conductive inclusions uniformly distributed in the host medium for four different values of host conductivity. Default mixture is assumed to contain 200-μm diameter conductive inclusions of 100-S/m conductivity uniformly distributed in 0.01-S/m conductivity electrolytic host medium. ε_r of the conductive inclusion phase is 10 and that of the host is 80. Diffusion coefficient of charge carriers in conductive inclusion is 10^{-6} m^2/s and that of ions in the host is 10^{-9} m^2/s.

Chapter 6: Effects of Disseminated Conductive Mineral Inclusions on Subsurface Electrical Measurements

Hydrocarbon-bearing conventional formations, mudrock formations, and source-rock formations generally contain clays, pyrite, magnetite, graphite-like carbon, and/or other electrically conductive mineral inclusions. Under redox-inactive conditions, these inclusions give rise to perfectly polarized interfacial polarization (PPIP) when subjected to an externally applied electric field. Effective electrical conductivity and dielectric permittivity of geomaterials containing such inclusions are frequency-dependent (dispersive) properties due to the electric-field-induced interfacial polarization and associated charge relaxation processes around host-inclusion interfaces. Existing resistivity interpretation techniques do not account for the effects of PPIP phenomena, and hence can lead to inaccurate estimation of water saturation, total organic content, and conductivity of formation water based on subsurface galvanic resistivity, EM induction, and EM propagation measurements in geological formations containing conductive mineral inclusions. In Chapter 5, I derived a mechanistic electrochemical model, the PPIP model, and validated the PPIP-SCAIP model for purposes of quantifying the frequency-dependent electrical complex conductivity of geomaterials. In this chapter, I use the PPIP-SCAIP model to evaluate the dependence of effective complex-valued conductivity of geological mixtures on (a) operating frequency, (b) conductivity of host medium (σ_h), and (c) material, size, and shape of inclusion phase. Notably, I use the PPIP-SCAIP model to identify petrophysical conditions that give rise to significant differences in effective conductivity (σ_{eff}) and effective relative permittivity ($\varepsilon_{r,eff}$) of conductive-inclusion-bearing mixtures from those of conductive-inclusion-free homogeneous media. I estimate that for a mixture containing as low as 5% volume fraction of disseminated conductive inclusions, the low-

frequency effective conductivity of the mixture is in the range of -30% to +100% with respect to the host conductivity for operating frequencies between 100 Hz and 100 kHz. Further, the high-frequency effective relative permittivity of that mixture is in the range of -10% to +90% with respect to the host permittivity for operating frequencies between 100 kHz and 10 MHz.

6.1 INTRODUCTION

Interfacial polarization phenomena significantly influence charge-carrier migration, accumulation, and diffusion processes in geomaterials (Schmuck and Bazant, 2012). For a porous fluid-filled geomaterial containing conductive mineral inclusions, charge carrier species in formation brine are ions, while those in conductive inclusions are electrons and holes. In redox-inactive conditions, there is no charge transfer and charge carrier transport across host-inclusion interfaces (Misra et al., 2015c). Consequently, these interfaces are electrochemically inactive, possess negligible surface charges, and are perfectly polarizable (Chu and Bazant, 2006).

Extensive studies have been carried out to describe interfacial polarization phenomena arising from the effects of surface conductance (Σ_s) of surface-charge-bearing, non-conductive spherical inclusions (e.g. Dukhin et al., 1974; Grosse, 1988). However, laboratory investigations and numerical modeling work on interfacial polarization phenomena arising from the effects of bulk conductivity of conductive mineral inclusions disseminated in geomaterials are limited in the open literature (e.g. Misra et al., 2015b). Anderson et al. (2006), Anderson et al. (2008), and, more recently, Wang and Poppitt (2013) emphasize the need to model and measure the effects of interfacial polarization of conductive inclusions for purposes of improving resistivity interpretation of subsurface galvanic resistivity, EM induction, and EM propagation measurements. Existing resistivity

interpretation techniques for the three above-mentioned geo-electromagnetic measurements neglect the effects of interfacial polarization of conductive mineral inclusions (Anderson et al., 2007; Corley et al., 2010). Consequently, conventional resistivity interpretation techniques tend to be inaccurate in pyrite-bearing sedimentary rocks (Clavier et al., 1976; Altman et al., 2008), pyrite-bearing mudrocks (Misra et al., 2015a), and organic source rocks that contain precursors to graphite (Anderson et al., 2008).

Maxwell-Wagner, electrical-double-layer, and electrochemical polarization phenomena occur in organic-rich mudrocks and source rock formations under the influence of an externally applied electric field. Garrouch (1998) observed substantial differences in measurements between wireline induction (~kHz) and LWD propagation (~MHz) tools in clean-sand and shaly-sand formations due to Maxwell-Wagner and electrical-double-layer polarization. Josh et al. (2012) observed that even at quite high frequencies up to 100s of MHz, there is significant space-charge polarization effects in shale rocks. This behavior is a consequence of the large surface area of clays and muds that carry surface charges. As a result, the dielectric dispersion measurements in MHz to GHz frequency range are significantly influenced by the volumetric content of brine and rock texture. Contrary to several observations made in clean sands and shaly-sand formations, Josh (2014) observed low correlation between high frequency dielectric permittivity (~GHz) and water content of Schlattingen shales. Chen and Heidari (2014) demonstrated the effects of directional connectivity of pyrite and organic matter on high frequency dielectric permittivity measurements. They modified the CRIM model using a tortuosity-dependent coefficient to obtain better fit with dielectric dispersion measurements in organic-rich mudrocks. Revil et al. (2013) mentioned that tight-oil mudrock formations can be better characterized by

implementing an effective complex electrical conductivity model specific for shales and mudrocks. According to them, such a model should incorporate the relative effects of porosity, water saturation, kerogen content, conductive minerals, Maxwell-Wagner polarization, clay types, clay content, and tortuosity tensor. Most importantly, Wang and Poppitt (2013) produced first-of-its-kind continuous broadband subsurface electromagnetic dispersion logging data. It was found that the measured X-signal responses are as large as -30 mS/m and the inverted dielectric permittivity values are in the order of 40000 in the pyrite-rich zones of the shale gas formations. They also emphasized the need to develop a broadband electromagnetic dispersion interpretation methodology to estimate petrophysical properties such as clay content, clay type, CEC, water salinity, water-filled porosity, and kerogen content.

In this Chapter, I quantify the σ_{eff} and $\varepsilon_{\text{r,eff}}$ of geomaterials containing uniformly distributed conductive spherical, rod-like, and sheet-like inclusions by accounting for the effects of PPIP phenomena. More importantly, petrophysical conditions that produce significant differences between effective EM properties of geological mixtures and those of conductive-inclusion-free, fluid-filled, porous host media are described in this chapter. It is worth noting that the EM properties of conductive-inclusion-free, fluid-filled, porous host media are vital to the accurate estimation of water saturation and total organic content, but EM tools measure effective EM properties, which can be significantly different from the EM properties of conductive-inclusion-free, fluid-filled, porous host media due to PPIP phenomena. The PPIP model, one of the two models incorporated in the PPIP-SCAIP model, quantifies the EM response of mixtures containing uncharged, perfectly polarizable spherical, rod-like, and/or sheet-like conductive inclusions surrounded by either pore-filling electrolyte or non-conductive matrix/fluid. On the other hand, the SCAIP model (the

second component of the PPIP-SCAIP model) quantifies the complex-valued conductivity response of conductive-inclusion-free, fluid-filled, host media comprising spherical grains that possess surface conductance.

6.2 COMPARISON OF THE PPIP-SCAIP MODEL TO EMPIRICAL MODELS

In this section, the PPIP model predictions are first compared against the SCAIP model predictions of the low-frequency (LF) σ_{eff} and high-frequency (HF) $\varepsilon_{r,eff}$ (Figure 6.1) of conductive-inclusion-free mixtures comprising varying volume fractions of 1-mm diameter, non-conductive spherical grains, possessing negligible surface conductance, that are uniformly distributed in an electrolyte. Then, the PPIP-SCAIP model predictions are compared against two well-established electrical model predictions of the LF σ_{eff} and HF $\varepsilon_{r,eff}$ (Figure 6.2) of conductive-inclusion-free mixtures comprising varying volume fractions of 1-mm diameter, non-conductive spherical grains, possessing negligible surface conductance, that are uniformly distributed in an electrolyte.

Figure 6.1 illustrates the LF σ_{eff} and HF $\varepsilon_{r,eff}$ of three electrolyte-saturated, conductive-inclusion-free mixtures W, S1 and S2 containing 0%, 20%, and 70% volume fraction, respectively, of non-conductive spherical grains. Owing to the absence of conductive inclusions and grains possessing surface conductance, none of the three curves exhibit frequency dispersion in the LF σ_{eff} and HF $\varepsilon_{r,eff}$. Curve W, identifying 100% volume fraction of 0.1-S/m conductivity water, indicates consistent LF σ_{eff} of 0.1 S/m and HF $\varepsilon_{r,eff}$ of 80. For curve S1, the LF σ_{eff} is reduced to 0.072 S/m and the HF $\varepsilon_{r,eff}$ is reduced to 60 owing to the presence of 20% volume fraction of non-conductive spherical grains of low relative permittivity. For mixture S2, containing 70% volume fraction of non-conductive spherical grains, I observe further reduction in the LF σ_{eff} of the mixture to 0.022 S/m and the HF $\varepsilon_{r,eff}$ reduces to 22 due to reduction in interconnected electrolyte-filled porosity.

Curves W, S1, and S2 are generated using the PPIP model. These curves identify mixtures comprising non-conductive spherical grains possessing no surface conductance. Subsequently, curves W*, S1*, and S2* are generated using the SCAIP model for the three above-mentioned mixtures, namely 0%, 20%, and 70% volume fraction, respectively, of non-conductive spherical grains. Curves W*, S1*, and S2* identify mixtures comprising non-conductive spherical grains possessing low values of Σ_s of 10^{-9} S (representative of Σ_s of silica grains). As illustrated in Figure 6.1, the SCAIP model predictions are in good agreement with the PPIP model predictions of the σ_{eff} and $\varepsilon_{r,eff}$ of conductive-inclusion-free mixtures comprising only non-conductive spherical grains and electrolyte. This agreement is a consequence of the absence of conductive inclusions and grains possessing surface conductance.

Figures 6.2a and 6.2b depict a good agreement between the computed LF σ_{eff} and HF $\varepsilon_{r,eff}$ values, respectively, with Archie's model and Lichtenecker-Rother's model (e.g. Zakri et al., 1998), respectively. Despite the limitations of the PPIP-SCAIP model for non-dilute mixtures containing volume fractions of inclusion phase greater than 20%, the predictions of LF σ_{eff} and HF $\varepsilon_{r,eff}$ using the two empirical models agree well with those of the PPIP-SCAIP model. Assuming 100%-electrolyte-saturated mixture, Archie's model used for purposes of our comparison is described as

$$\sigma_{\text{eff}} = \sigma_{\text{w}}(1 - \phi_{\text{i}})^{m}, \tag{1}$$

where σ_{w} is the conductivity of electrolyte filling the pore space of the mixture, ϕ_{i} is volume fraction of spherical non-conductive grains, and *m* is the porosity exponent of the mixture. Experimental and numerical works have shown that the value of *m* is close to 1.3 for electrolyte-filled unconsolidated packs of non-conductive spherical grains (Jackson et al., 2008; Revil and Skold, 2011). Accordingly, the PPIP-SCAIP model predicts that the

LF σ_{eff} of such mixtures agrees with the Archie's model predictions for porosity exponent value of 1.25, as shown in Figure 6.2a.

With respect to HF $\varepsilon_{\text{r,eff}}$ of sand packs and other granular materials, experimental investigations have shown that HF $\varepsilon_{\text{r,eff}}$ can be modeled using Lichtenecker-Rother's model (Achour et al., 1999; Sabouroux and Ba, 2011), which is expressed as

$$(\varepsilon_{\text{eff}}^{*})^{\alpha} = \phi_{\text{i}}(\varepsilon_{\text{i}}^{*})^{\alpha} + (1-\phi_{\text{i}})(\varepsilon_{\text{h}}^{*})^{\alpha}, \quad (2)$$

where $\varepsilon_{\text{eff}}^{*}$ is effective complex-valued permittivity of the mixture, $\varepsilon_{\text{i}}^{*}$ is complex-valued permittivity of the non-conductive spherical grains, $\varepsilon_{\text{h}}^{*}$ is complex-valued conductivity of the host medium comprising the pore-filling electrolyte, ϕ_{i} is volume fraction of spherical grains, and the non-vanishing α is the geometrical arrangement factor that ranges from -1 to 1 (Lee, 2010). The value of α presents the relationship between the direction of effective layering of the components to that of the applied electric field (Lee, 2010). When the electric field is parallel to the composite layers, the value of α = 1, giving a direct weighted average of dielectric permittivity values of constituent phases, while when the field is perpendicular to the composite layers, α = -1 gives a harmonic weighing of the dielectric permittivity values of individual phases (Leao et al., 2015). Moreover, Leao et al. (2015) mention that when using $\alpha = \frac{1}{3}$ in equation 2, one obtains Looyenga's formula, whereas $\alpha = \frac{1}{2}$ reduces equation 2 to the CRIM model, which is suitable for isotropic homogeneous media. The CRIM model has been extensively used to interpret high-frequency dielectric measurements of geological formations (Seleznev et al., 2004; Hizem et al., 2008). In Figure 6.2b, our mechanistic model predictions of the HF $\varepsilon_{\text{r,eff}}$ of electrolyte-saturated mixtures comprising different volume fractions of uncharged, non-conductive spherical grains agree with Lichtenecker-Rother's model predictions for α = 0.69. Values of α of 0.66 and 0.7 are reported in the literature survey by Lee (2010). The agreement of PPIP-

SCAIP model predictions with the two empirical electrical models, as shown in Figure 6.2, supports the mechanistic and mathematical robustness of the improved modeling scheme discussed in this work.

6.3 COMPLEX ELECTRICAL CONDUCTIVITY RESPONSE OF GEOMATERIALS CONTAINING DISSEMINATED INCLUSIONS

In this section, the complex-valued conductivity response of mixtures containing uniformly distributed inclusions is modeled using the PPIP model. In doing so, I identify petrophysical properties that govern PPIP phenomena around conductive inclusions. In the first half of this section, I study the interfacial polarization of conductive spherical inclusions in absence of redox-active species. Unlike those in previously published research works (Wong, 1979; Placencia-Gomez and Slater, 2014), the inclusion phase in this wrok are assumed to be finitely conducting with inherent dielectric properties; similar considerations were made by Revil et al. (2015a). Additionally, I study the sensitivity of complex-valued conductivity to the dispersity of inclusion sizes (Beltramo and Furst, 2012), distribution of inclusion sizes (Arroyo et al., 1999), and material of the inclusion phase. In the latter half of this section, I model PPIP phenomena around conductive sheet-like and rod-like inclusions. Numerical studies of interfacial polarization phenomena around conductive inclusions of such shapes for applications in geosciences are limited in the open literature (e.g. Grosse, 1988; Sihvola, 2007). All model predictions reported in this section are supported by theoretical explanations based on first principles.

6.3.1 Material of Inclusion Phase

In this study, the inclusion phase differs in its conductivity, relative permittivity, and diffusion coefficient of charge carriers. Figure 6.3 depicts the computed σ_{eff} and $\varepsilon_{\text{r,eff}}$ responses of mixtures containing spherical inclusions of different materials. In that figure,

curves G, P, C, X, Y, and H identify six mixtures containing only graphite inclusions, pyrite inclusions, chalcopyrite inclusions, low-conductivity material inclusions, 0.1-S/m conductivity inclusions, and non-conductive inclusions, respectively, uniformly distributed in a 0.1-S/m conductivity electrolyte. The assumed values of conductivity, relative permittivity, and diffusion coefficient of charge carriers of these six materials are reported in Table 6.1.

I observe significant dispersion in the computed σ_{eff} and $\varepsilon_{r,eff}$ responses of mixtures G, P, C, and Y. Also, Figure 6.3b shows large dielectric enhancements in the low-frequency limits for all the mixtures except mixture H. Interestingly, Figure 6.3a shows that LF σ_{eff} values of all mixtures converge to a value lower than the σ_h of 0.1 S/m, which results from the dielectric behavior of conductive inclusions with perfectly polarizable surfaces at low frequencies. Similar reduction in the LF σ_{eff} values below σ_h were observed by Revil et al. (2015b). Conductive inclusions behave as dielectric material at low frequencies (< 1 kHz) owing to charge accumulation at the host-inclusion interfaces. On the other hand, the HF σ_{eff} of mixtures G, P, and C converge to a value higher than σ_h, which is indicative of the high conductivity behavior of such inclusions at higher frequencies. Another interesting feature shown in Figure 6.3a is that for mixture Y, containing 0.1-S/m conductivity (equal to σ_h) inclusions, the HF σ_{eff} values are equal to σ_h, whereas the LF σ_{eff} values are much lower than σ_h due to the accumulation of charges at the electrochemically inactive surfaces of these inclusions in accordance with PPIP model assumptions. In contrast, in Figure 6.3b mixture H, containing non-conductive inclusions, exhibits a non-dispersive EM response due to the absence of interfacial polarization.

From a theoretical stand point, an increase in the metallic nature of inclusion material implies an increase in the concentration of charge carriers and an increase in the

mobility of charge carriers in the inclusion phase. In this study, mixture G contains inclusions of the highest metallic nature followed by mixture P and then mixture C (e.g. Pridmore and Shuey, 1976). Among the mixtures used in our study, mixture G undergoes the highest accumulation of charges around the host-inclusion interfaces at low frequencies due to the highest charge carrier concentration, thereby giving rise to largest dielectric enhancement and largest LF $\varepsilon_{r,eff}$, as shown in Figure 6.3b. Moreover, mixture G exhibits higher HF σ_{eff} than those of mixtures P and C, as illustrated in Figure 6.3a, because graphite inclusions have higher mobility and concentration of charge carriers. It is noteworthy that, an increase in the metallic nature of the disseminated inclusion phase results in faster alignment of the field-induced polarization with the externally applied electric field, whereupon the frequency dispersion for mixture G occurs at much lower frequencies than those of mixtures P and C (e.g. Pelton et al., 1978; Gurin et al., 2015).

Figures 6.3a and 6.3b show an intuitive conductivity response wherein the σ_{eff} of the graphite mixture is higher than that of the pyrite mixture, which in turn is higher than that of the chalcopyrite mixture over the entire frequency range. However, Figure 6.4a illustrates a counter-intuitive conductivity response, wherein mixtures G, P, and C exhibit similar σ_{eff} responses, despite dissimilarities in the metallic nature of the inclusion materials. I claim that this counterintuitive behavior is a consequence of the equal ratio of the conductivity of inclusion phase to the diffusion coefficient of charge carriers in the inclusion phase for the three mixtures, as shown in the last column of Table 6.2. Nonetheless, the PPIP model predictions in Figure 6.4a indicate that mixtures containing conductive inclusions of bulk conductivity values close to or lower than 1 S/m, for instance mixtures X and Y, the σ_{eff} responses diverge from the counter-intuitive converging responses, as exhibited by mixtures G, P, and C.

Organic-rich and hydrocarbon-bearing geological rocks typically contain more than one type of conductive mineral inclusions. In this section, the complex-valued conductivity response of mixtures containing uniformly distributed conductive inclusions of one or more different type of materials is quantified using the PPIP-SCAIP model. Figure 6.5 shows the modeled EM response of various mixtures containing 70% volume fraction of 100-μm diameter non-conductive spherical grains mixed with various volume fractions of 100-μm diameter, conductive inclusions of one or more types of materials uniformly distributed in a 0.1-S/m electrolyte. In Figure 6.5, the computed EM responses of four mixtures, namely mixtures S, G, P, and C, are provided as references to compare the effects of the presence of more than one type of materials as the inclusion phase. Mixtures S, G, P, and C identify mixtures containing no inclusions, only 2% volume fraction of graphite inclusions, only 2% volume fraction of pyrite inclusions, and only 2% volume fraction of chalcopyrite inclusions, respectively. In Figure 6.5a, mixture S, which contains no conductive inclusions, exhibits a non-dispersive response that agrees with Archie's prediction. Further, mixtures G, P, and C, which contain conductive inclusions of different type of materials, give rise to significantly distinct Θ responses, owing to the dissimilarity in the metallic nature of the materials (Gurin et al., 2015). For example, Figure 6.5b illustrates that the peak of the Θ response of mixture G is at 5 kHz, that of mixture P is at 20 kHz, and that of mixture C is at 50 kHz.

On the other hand, mixture CG, which was obtained by mixing 2% volume fraction of graphite with 2% volume fraction of chalcopyrite, exhibits a Θ response having two peaks corresponding to the constituent materials of the inclusion phase in the resulting mixture. Interestingly, the Θ responses of mixtures containing inclusions of two or more materials are broader than those of mixtures containing inclusions of only one material.

Further, mixtures containing inclusions of two different materials that are not significantly different in their electrical properties and metallic nature show only a single peak in the Θ response. For instance, the Θ response of mixture PG, which contains a 2% volume fraction of graphite inclusions and a 2% volume fraction of pyrite inclusions, exhibits only a single peak. Furthermore, for mixture CPG, which contains a 2% volume fraction of inclusions of each of the three materials, namely chalcopyrite, pyrite, and graphite, I observe a sharp frequency dispersion in the conductivity response (Figure 6.5a), a broad single-peak Θ response (Figure 6.5b), and a significant difference in LF and HF effective conductivity (Figure 6.5a), corresponding to the increase in volume fraction of conductive inclusions due to the volumetric mixing in equal concentrations.

6.3.2 Dispersed clay particles v/s conductive mineral inclusions

In this section, I compare the EM response of mixtures containing non-conductive particles possessing surface conductance, which identify clay minerals, clay-sized particles, and silt-sized particles, against that of mixtures containing conductive/semi-conductive inclusions, which identify pyrite and magnetite inclusions. Clay minerals, clay-sized particles, and silt-sized particles have negligible bulk conductivity and possess surface charges that give rise to surface conductance (Revil, 2012). In contrast, conductive/semi-conductive metallic mineral inclusions possess high bulk conductivity without surface charges under redox inactive conditions (Chu and Bazant, 2006). Clay-like minerals undergo surface-conductance-assisted interfacial polarization phenomena that follow a significantly different mechanisms than those of semi-conductive/conductive minerals, which undergo perfectly polarized interfacial polarization under redox-inactive conditions (Misra et al., 2015c). In Figure 6.6b, PPIP-SCAIP model predictions indicate that mixtures containing conductive inclusions exhibit dispersion responses that are

markedly distinct from those of mixtures containing non-conductive inclusions possessing surface conductance. Mixtures P and G, which contain 2% volume fraction of uniformly distributed conductive pyrite and graphite inclusions, respectively, exhibit much larger peaks of the Θ response than that of mixture Cl2, which contains 10% volume fraction of uniformly distributed non-conductive spherical grains possessing Σ_s of 10^{-8} S, identifying a shaly sand. Moreover, mixture Cl1, which contains 70% volume fraction of uniformly distributed non-conductive spherical grains possessing Σ_s of 10^{-8} S (identifying a mudrock) exhibits a significantly lower peak in its Θ response than those of mixtures P and G.

As shown in Figure 6.6b, the critical frequency of mixture P is at 3 kHz and that of mixture G is at 1 kHz, which is approximately two orders of magnitude higher than those of mixtures Cl1 and Cl2 of 50 Hz. Such differences in peaks of the Θ responses were predicted by Anderson et al. (2006) and in their subsequent papers. Also, comparisons of experimental observations made by Jougnot et al. (2010) on clay rocks against those made by Gurin et al. (2015) on mixtures containing electronic conductors support our model predictions. Significant variations in the peak and critical frequency of the Θ response are due to the difference in SCAIP and PPIP phenomena. The dispersive Θ response of mixtures containing non-conductive inclusions possessing surface conductance is dominant at frequencies between 1 Hz and 100 Hz (Shilov and Borkovskaya, 2010). On the other hand, mixtures containing metallic inclusions have a dominant dispersive response in the 1-50 kHz frequency range (Wong, 1979; Grosse and Barchini, 1992).

The PPIP-SCAIP model predictions, as shown in Figure 6.6, indicate that at operating frequencies of downhole induction logging tools in the range of 1 kHz to 50 kHz, the EM response will be substantially influenced by interfacial polarization of conductive mineral inclusions and relatively unaffected by the interfacial polarization of clay-like

inclusions. However, at operating frequencies of galvanic resistivity tools around 100 Hz, the EM response is influenced by interfacial polarization of both clay-like inclusions and conductive mineral inclusions. Figure 6.6a illustrates that presence of 10% volume fraction dispersed clays, as in mixture Cl2, will lower σ_{eff} to values smaller than σ_h in the entire frequency range of 1 Hz to 1 MHz. Moreover, presence of 2% volume fraction of pyrite inclusions, as in mixture P, or graphite inclusions, as in mixture G, gives rise to frequency dispersion of conductivity responses in the frequency range of 1 Hz to 1 MHz, wherein the LF σ_{eff} values are substantially lower and the HF σ_{eff} values are substantially higher than the conductivity of the host medium. Further, mixture Cl1 identifying with a mixture containing 70% volume fraction of clay-like particles possessing Σ_s of 10^{-8} S, exhibits 120% higher σ_{eff} values than that of inclusion-free mixture S, due to the effects of surface conductance of clay-like particles present at a high volumetric concentration.

6.3.3 Size of inclusions

Relaxation mechanisms associated with PPIP phenomena strongly depend on the surface area (or the characteristic length) of the disseminated conductive inclusion phase. In this section, I investigate the influence of inclusion size, distribution of inclusion sizes, and dispersity of inclusion sizes on the EM response of mixtures containing 10% volume fraction of 500-S/m conductivity spherical inclusions uniformly distributed in a 0.01-S/m conductivity electrolyte. Figure 6.7 illustrates that the frequency dispersion curve shifts toward higher frequencies by approximately an order of magnitude for every order of magnitude reduction in the size of inclusions. Peaks of the Θ responses for mixtures M1, M2, and M3, which contain 10-μm, 100-μm, and 1000-μm diameter conductive spherical inclusions, respectively, are at 12 kHz, 1.2 kHz, and 0.12 kHz, respectively. From a theoretical standpoint, at a constant volume fraction of conductive inclusions, a decrease

in size of conductive inclusions in the mixture results in faster build-up of charge accumulation at interfaces. Therefore, interfacial polarization of smaller-sized inclusions follows the time-varying externally applied electric field at higher frequencies; consequently, the frequency dispersion of a mixture containing smaller-sized inclusions appears at higher frequencies than that of a mixture containing larger-sized inclusions. Figure 6.7 illustrates the EM response of mixtures M4 and M5, which contain conductive spherical inclusions with a uniform distribution of sizes (±90% variation) about a mean diameter of 10 μm varying from 1 to 19 μm and that about a mean diameter of 100 μm varying from 10 to 190 μm, respectively. The magnitudes of peaks of the Θ responses of mixtures M4 and M5, which have variations in sizes of the inclusions, decreases by approximately 10% with respect to those of mixtures M1 and M2, which have uniform sizes of inclusions. However, the critical frequency remains nearly unchanged for mixtures M1 and M4 and for M2 and M5.

Instead of being a monodisperse mixture, a geological mixture can be bidisperse or polydisperse. Figure 6.8 illustrates the computed complex-valued conductivity response of mixtures containing more than one size (dispersivity) of conductive inclusions. The Θ response of the bidisperse mixture M7, which contains 5% volume fractions of 10-μm and 1000-μm diameter conductive spherical inclusions, respectively, exhibits two distinct peaks, as shown in Figure 6.8b, owing to the two sizes of inclusions present in the mixture that are more than an order of magnitude different from each other. However, the Θ response of mixture M6, which contains 5% volume fractions of 10-μm and 100-μm diameter conductive spherical inclusions, respectively, exhibits two peaks that are closely spaced and can be distinguished only through a high-resolution spectral measurement. Further, Figure 6.8b shows that the polydisperse mixture M8, which contain 3.33% volume

fractions of 10-µm, 100- µm, and 1000-µm diameter conductive spherical inclusions, respectively, exhibits broader Θ responses than those of mixtures containing monodisperse and bidisperse inclusion sizes. Similar behavior is also exhibited by mixture M9, which contains 2.5% volume fractions of 1-µm, 10-µm, 100- µm, and 1000-µm diameter conductive spherical inclusions, respectively. Also, Figure 6.8a indicates that an increase in the dispersivity of inclusion sizes leads to an increase in the spread and decrease in steepness of conductivity dispersion. Interestingly, the magnitude of the peak of the Θ response is higher for mixtures containing inclusions of sizes that are less than an order of magnitude different from each other; for instance, the magnitude of the peak of the Θ response of mixture M6 is higher than that of mixture M7, as shown in Figure 6.8b.

6.3.4 Laminations, veins, fractures, and beds

In this and the next section, I model the EM responses of mixtures containing sheet-like and rod-like conductive inclusions, respectively. To the best of our knowledge, PPIP phenomena around uniformly distributed rod-like and sheet-like inclusions have not been investigated for purposes of petrophysical applications. Beds, laminations, pore-filling mineralization, fractures, and veins typically present in geological mixtures are comparable to the two inclusion geometries under investigation in this and the next section.

PPIP model predictions indicate that the complex-valued conductivity response of mixtures containing conductive sheet-like inclusions (e.g., thin-beds and laminations) strongly depends on σ_h. In Figures 6.9a and 6.9b, frequency dispersion shifts to higher frequencies with an increase in conductivity of the electrolytic-host medium. An increase in the conductivity of electrolyte surrounding the inclusion increases the number of ions in the electrolyte, which in turn increases charge accumulation at the outer surface of the inclusions, resulting in an increase in phase at low frequencies. Consequently, in Figure

6.9b, the LF Θ response at 10 Hz is highest for the mixture having a 1-S/m conductivity host. Additionally, the field-induced polarization of sheet-like inclusions follows the applied electric field until higher frequencies for mixtures having higher host conductivity owing to the greater mobility of charge carriers (ions) in the electrolytic host, which easily accumulate at the outer surface under the combined influence of dipole moment of the inclusion and the externally applied electric field and generate complete polarization. Unlike the behavior of mixtures containing spherical and rod-like inclusions, a mixture containing sheet-like inclusions under redox-inactive conditions acts as an insulator at low frequencies. Therefore, for sheet-like conductive inclusions, the LF σ_{eff} values are close to zero and the LF Θ values are close to 90-degrees for the mixture having a 1-S/m conductivity host, which indicates the perfect dielectric behavior of that mixture.

The thickness of sheet-like inclusions significantly affects the EM response of mixtures containing such inclusions. In Figures 6.9c and 6.9d, the frequency dispersion characteristics shift to higher frequencies with a decrease in the thickness of sheet-like inclusions. Irrespective of the thickness, all the curves in Figure 6.9c exhibit similar LF and HF limits for the σ_{eff} and Θ values, which honors the mixing law predictions for insulating and infinitely conductive behavior of sheet-like inclusions at low (~ Hz) and high frequencies (~ GHz), respectively. PPIP model predictions in Figure 6.9c indicate that 2 mm or thicker beds uniformly distributed in geological host will not exhibit dispersion characteristics for frequencies higher than 100 Hz. As a result, subsurface EM induction and EM propagation measurements can be interpreted using laminated sand analysis when the thickness of disseminated parallelly aligned sheet-like inclusions is greater than or close to 2 mm. However, for accurate well-log interpretation in thinly laminated systems

(thickness < 1 mm), the effects of PPIP phenomena should be accounted when quantifying the frequency dispersion of the σ_{eff} and Θ responses.

Finally, Figure 6.9f shows that the magnitude of the Θ response increases with an increase in the volume fraction of sheet-like inclusions. In Figures 6.9e and 6.9f, for a mixture containing 1% volume fraction of sheet-like inclusions, the Θ response is negligible and σ_{eff} values are close to σ_h, respectively. However, for a mixture with higher volume fractions of sheet-like inclusions, the complex-valued conductivity response exhibits drastic alteration in both the Θ and σ_{eff} responses, as illustrated in Figures 6.9e and 9f. Also, the HF σ_{eff} response of mixtures containing sheet-like inclusions increases with an increase in volume fraction of the inclusion phase in accordance with mixing law predictions. As demonstrated by the explanation provided in the earlier part of this section, an increase in volume fraction of sheet-like inclusions in the mixture leads to a decrease in the LF σ_{eff} response of the mixture, as illustrated in Figures 6.9e.

6.3.5 Pore-throat-filling and rod-like mineralization

In this section, I focus on mixtures containing uniformly distributed, parallelly aligned, rod-like inclusions. In Figures 6.10a and 6.10b, the frequency dispersion response of rod-like inclusions is significantly different from those of sheet-like inclusions shown in the previous section. At low frequencies (~ Hz), charge carriers in the uniformly distributed rod-like inclusions accumulate at host-inclusion interfaces and migration of charge carriers only occurs in the electrolytic host medium. Also, displacement currents are much smaller than conduction currents at low frequencies. Nonetheless, the Θ response of such mixtures strongly depends on σ_h, as shown in Figure 6.10b. Mixtures having a low-conductivity host exhibit frequency dispersion at low frequencies. Such dispersion characteristics shift to higher frequencies with an increase in σ_h. It is important to remember

that the $\varepsilon_{r,eff}$ (the charge storage potential) of these mixtures decreases with an increase in operating frequency. The Θ response of mixtures being a ratio of displacement current to conduction current, a minimum follows a maximum Θ response. Interestingly, in Figure 6.10b the magnitude of the peak of the Θ response is almost equal for all the different values of σ_h.

In Figures 6.10c and 6.10d mixtures containing larger diameter rod-like inclusions exhibit frequency dispersion at much lower frequencies than those containing smaller diameter inclusions. Consequently, mixtures containing smaller-diameter rod-like inclusions will exhibit lower conductivity values than those containing larger-diameter rod-like inclusions for a considerably larger frequency range. This behavior is attributed to the relatively shorter distances that charge carriers in the inclusion phase are required to travel inside the smaller-diameter inclusions. Consequently, mixtures containing smaller diameter inclusions undergo complete polarization of inclusions for much higher frequencies and exhibit lower values of σ_{eff}. Also, in Figure 6.10d, the magnitude of the peak of the Θ response is relatively independent of the diameter of rod-like inclusions. Finally, Figure 6.10e shows that, at a 5% volume fraction of rod-like inclusions, the frequency dispersion in σ_{eff} results in LF σ_{eff} values 10% lower and HF σ_{eff} values 10% higher than σ_h, in accordance with mixing law predictions. Moreover, in Figure 6.10f, the magnitude of the peak of the Θ response increases with an increase in volume fraction of rod-like inclusions, while the critical frequency associated with the peak of the Θ response remains relatively unaltered.

6.4 EFFECTS OF PPIP AND SCAIP PHENOMENA ON SUBSURFACE ELECTRICAL MEASUREMENTS

Petrophysicists and geoscientists typically interpret EM measurements of low-frequency electrical conductivity, high-frequency conductivity phase and attenuation, and high-frequency dielectric permittivity of inclusion-free geological samples to assess water saturation, total organic content, formation electrical anisotropy, formation water salinity, and other electrical properties. They employ galvanic resistivity (e.g., laterolog measurements) and EM induction methods (e.g., array induction measurements) to assess the LF conductivity of formations, EM propagation methods for measuring high-frequency phase and attenuation of formations, and dielectric methods for measuring high-frequency permittivity of formations. However, when a porous geological host contains inclusions in the form of grains, vugs, patches, pore throat-filling structures, fractures, and/or laminations, the accumulation/depletion and relaxation of charges around host-inclusion interfaces significantly alter the electromigration, charge storage, and electrodiffusion processes in the host medium. As a result, resistivity interpretation techniques that do not account for the effects of PPIP phenomena lead to inaccurate assessment of petrophysical properties of geological formations. The PPIP-SCAIP model quantifies the alteration of EM measurements due to SCAIP and PPIP phenomena. In this section, I use the PPIP model to identify the petrophysical conditions that lead to significant alterations of galvanic resistivity, EM induction, and EM propagation measurements in the frequency range from 100 Hz to 100 MHz.

The computed EM response of each mixture is presented as two set of plots, namely effective conductivity (σ_{eff}) plot and effective relative permittivity ($\varepsilon_{r,eff}$) plot. All σ_{eff} plots are depicted for low frequency measurements that range from 0.1 kHz to 100 kHz. All $\varepsilon_{r,eff}$ plots are depicted for high frequency measurements that range from 1 MHz to 100 MHz.

Consequently, curves presented in the σ_{eff} plot are comparable to LF σ_{eff} estimates based on galvanic resistivity and EM induction measurements. On the other hand, curves presented in the $\varepsilon_{r,eff}$ plot are comparable to HF $\varepsilon_{r,eff}$ estimates based on EM propagation and dielectric propagation measurements. For all the plots, a non-dispersive response of the inclusion-free mixture S is presented as a reference curve for visualizing the severity of alterations due to the presence of conductive inclusions. When the LF σ_{eff} and HF $\varepsilon_{r,eff}$ responses of a mixture deviate from the reference curve, it indicates that conventional resistivity interpretation of galvanic resistivity, EM induction, and EM propagation measurements in formations similar to the mixture will not yield accurate petrophysical assessments. Unlike other previous works on modeling interfacial polarization phenomena (Wong, 1979; Mahan et al., 1986), I ensure petrophysically consistent modeling by coupling the SCAIP model to the PPIP model, thereby quantifying the effects of polarization due to the background material (matrix) made of non-conductive grains possessing surface conductance and those due to the perfectly polarizable inclusions uniformly distributed in the mixture.

6.4.1 Shape of inclusions and conductivity of pore-filling fluid

Pyrite mineralization tends to be associated with hydrocarbon bearing formations, sedimentary rocks, and source rocks. In this section, I assign electrical properties to the inclusion phase comparable to that of conductive pyrite mineral. For the inclusion phase, the assumed value of bulk conductivity is 5000 S/m, relative permittivity is 12, and the diffusion coefficient of charge carriers in the inclusion phase is 5×10^{-5} m^2/s. Moreover, the assumed value of relative permittivity of non-conductive spherical grains, identifying a sand grains, is 4 and that of non-conductive spherical grains, identifying clay grains, is 8.

The assumed value of Σ_s of representative sand grains is 10^{-9} S and that of the representative clay grains is 10^{-8} S.

Figure 6.11 shows the computed EM response of mixtures SP1, SP2, and SP3 containing 5% volume fraction of conductive inclusions in shape of either 200-μm diameter spherical grains, 20-μm diameter long rods, or 1-mm thick sheets, respectively, uniformly distributed in a matrix made of 70% volume fraction of 1-mm diameter, non-conductive spherical grains that is completely saturated with electrolyte for various electrolyte conductivities. I also present the computed EM response of a mixture SCl made of 70% volume fraction of 1-mm diameter, non-conductive spherical grains containing uniformly distributed 5% volume fraction of 10-μm diameter, non-conductive spherical grains possessing Σ_s of 10^{-8} S that is fully saturated with electrolyte for various electrolyte conductivities. The computed EM response of the inclusion-free mixture S containing only 70% volume fraction of non-conductive spherical grains exhibiting a low value of Σ_s of 10^{-9} S is presented as a reference to visualize the alteration of the EM response due to PPIP effects. Pairs of Figures 6.11a and 6.11b, 6.11c and 6.11d, 6.11e and 6.11f, and 6.11g and 6.11h identify the computed σ_{eff} and $\varepsilon_{r,eff}$ responses of mixtures, respectively, fully saturated with 0.001-, 0.01-, 0.1-, and 1-S/m electrolyte, respectively. It is important to note that the computed EM responses shown in Figure 6.11 are along the direction of characteristic length of the inclusion phase.

Important observations regarding the LF σ_{eff} response are as follows:

(1) Mixtures SP1, SP2, and SP3 undergo significant variations of the LF σ_{eff} and HF $\varepsilon_{r,eff}$ responses with respect to that of the inclusion-free mixture S.

(2) The variations of LF σ_{eff} and HF $\varepsilon_{r,eff}$ responses with respect to the reference curve strongly depend on the conductivity of pore-filling electrolyte because the frequency

dispersion characteristics of a mixture shift to lower frequencies with a decrease in the electrolyte conductivity, as emphasized in previous sections.

(3) For mixtures SP1 and SP2, the variation of LF σ_{eff} with respect to the reference curve and frequency dispersion of the LF σ_{eff} increases with a decrease in electrolyte conductivity.

(4) In the operating frequency range of a typical galvanic resistivity measurement (~ 100 Hz), the variations of LF σ_{eff} responses of mixtures SP1 and SP2 with respect to reference curves are independent of electrolyte conductivity for electrolyte conductivity values higher than or close to 0.01 S/m, as shown in Figures 6.11c, 6.11e, and 6.11g.

(5) The variation of the LF σ_{eff} with respect to the reference curve strongly depends on the shape of inclusions.

(6) For electrolyte conductivity values higher than or close to 0.01 S/m, mixture SCl exhibits LF σ_{eff} values that are lower than that of inclusion-free mixture S, as shown in Figures 6.11c, 6.11e, and 6.11g, because surface conduction is negligible compared to bulk conduction. However, for electrolyte conductivity values lower than or close to 0.001 S/m, the LF σ_{eff} values of mixture SCl are higher than that of the inclusion-free mixture S, as illustrated in Figure 6.11a, because surface conduction dominates bulk conduction. Similar increases in conductivity values in the presence of low conductivity electrolytes around clay grains have been extensively reported in the published petrophysical literature (e.g., Waxman and Smits, 1968).

(7) In the operating frequency range of the EM induction measurements (~ 50 kHz), the LF σ_{eff} increases by 96%, 51%, and 38% with respect to that of inclusion-free

mixture S for mixtures SP1, SP2, and SP3, respectively, owing to the effects of PPIP phenomena.

(8) As illustrated in Figures 6.11c, 6.11e, and 6.11g, for electrolyte conductivity values higher than or close to 0.01 S/m and frequencies close to a typical galvanic resistivity measurements operating at 100 Hz, mixtures SP1 and SP2 exhibit LF σ_{eff} values that are approximately 20% lower than that of inclusion-free mixture S.

(9) Mixture SP3 exhibits an extremely large reduction of LF σ_{eff} values with respect to that of inclusion-free mixture S at frequencies close to 100 Hz and electrolyte conductivity values close to or higher than 1 S/m because sheet-like inclusions act as insulators at low frequencies and high values of electrolyte conductivities, as shown in Figure 6.11g.

(10) As illustrated in Figures 6.11a, 6.11c, and 6.11e, for electrolyte conductivity values lower than or close to 0.1 S/m, mixture SP3 exhibits negligible frequency dispersion in the LF σ_{eff} response and approximately 96% higher values of LF σ_{eff} than that of inclusion-free mixture S.

Additional important observations regarding the HF $\varepsilon_{r,eff}$ response are as follows:

(1)As shown in Figures 6.11b, 6.11d, and 6.11f, for electrolyte conductivity values close to or lower than 0.1 S/m, the HF $\varepsilon_{r,eff}$ of mixtures SP1, SP2, and SP3 are 76%, 43%, or 33% higher, respectively, than that of the inclusion-free mixture S.

(2)Mixtures SP1, SP2, and SP3 exhibit a non-dispersive HF $\varepsilon_{r,eff}$ response for electrolyte conductivity values close to or lower than 0.01 S/m, as shown in Figures 6.11b and 6.11d.

(3)Mixture SCl exhibits a non-dispersive HF $\varepsilon_{r,eff}$ response for electrolyte conductivity values in the range of 0.001 S/m to 1 S/m.

(4)With an increase in electrolyte conductivity, the frequency dispersion of HF $\varepsilon_{r,eff}$ response is observable due to the shift of dispersion characteristics to higher frequencies resulting in an increase in HF $\varepsilon_{r,eff}$, as shown in Figures 6.11f and 6.11g.

(5)As shown in Figures 6.11f and 6.11h, for electrolyte conductivity values close to or higher than 0.1 S/m, HF $\varepsilon_{r,eff}$ values at frequencies close to 100 MHz are relatively independent of the change in electrolyte conductivity, whereas large variations in the HF $\varepsilon_{r,eff}$ response with respect to the reference curve are observed for frequencies close to or lower than 1 MHz.

6.4.2 Non-conductive pore-filling fluid

Figure 6.12 illustrates the computed EM response of various mixtures having non-conductive pore-filling fluid of bulk relative permittivity of 3, which identifies with hydrocarbon. Figure 6.12 shows that the LF σ_{eff} and HF $\varepsilon_{r,eff}$ of mixtures SP1, SP2, and SP3 are all approximately 27% and 12% higher, respectively, than those of the inclusion-free mixture S. There is negligible frequency dispersion of HF $\varepsilon_{r,eff}$ for these mixtures, as illustrated in Figure 6.12b. In contrast, mixture SCl exhibits frequency dispersion of HF $\varepsilon_{r,eff}$ and LF σ_{eff} at frequencies higher than 10 kHz. Mixtures SP1 and SP2 containing spherical and rod-like pyrite inclusions, respectively, exhibit LF σ_{eff} responses that are nearly similar to that of mixture SCl, while the mixture SP3 containing sheet-like inclusions exhibit higher LF σ_{eff} values.

6.4.3 Volume content of inclusion phase

Interfacial polarization is a surface governed phenomenon that strongly depends on the volume content of inclusions in the mixture. Figure 6.13a shows that the LF σ_{eff} of the two SP3-type mixtures containing 1% volume fraction (dotted) and 2% volume fraction

(solid), respectively, of sheet-like conductive inclusions are 27% and 49% higher than that of the inclusion-free mixture S, respectively. These mixtures containing sheet-like inclusions exhibit negligible dispersion characteristics in the LF σ_{eff} response. At frequencies close to 100 Hz, the LF σ_{eff} responses of one SP1-type mixture containing 2% volume fraction of spherical inclusions and SP2-type mixture containing 2% volume fraction of rod-like inclusions are approximately 6% lower than that of the inclusion-free mixture S. In contrast, at 50 kHz, these two mixtures exhibit LF σ_{eff} responses that are 15% higher than that of the inclusion-free mixture S. Further, in Figure 6.13b, the computed HF $\varepsilon_{r,eff}$ of the two SP3-type mixtures containing 1% volume fraction (dotted) and 2% volume fraction (solid), respectively, of sheet-like pyrite inclusions are 24% and 43% higher than that of the inclusion-free mixture S, respectively. Finally, the HF $\varepsilon_{r,eff}$ response of one SP1-type mixture containing 2% volume fraction of spherical inclusions and one SP2-type mixture containing 2% volume fraction of rod-like inclusions are approximately 20% higher than that of the inclusion-free mixture S over the entire HF range.

6.4.4 Inclusion material and shapes

In this section, the PPIP-SCAIP model is used to study the alteration of the LF σ_{eff} and HF $\varepsilon_{r,eff}$ responses of mixtures S, SG, SP, SC, and SX containing no inclusions, 5% volume fraction of graphite (G) inclusions, 5% volume fraction of pyrite (P) inclusions, 5% volume fraction of chalcopyrite (C) inclusions, and 5% volume fraction of inclusions made of a low-conductivity material (X), respectively. The assumed values of electrical properties of these inclusion materials are comparable to the electrical properties of the corresponding minerals, as reported in Table 6.5. In Figure 6.14, plots a and b are associated with mixtures containing spherical inclusions, plots c and d are associated with

mixtures containing rod-like inclusions, and plots e and f are associated with mixtures containing sheet-like inclusions.

Mixtures containing graphite inclusions, irrespective of the shape of the inclusion phase, exhibit conductivity dispersion at low frequencies and do not exhibit permittivity dispersion. Figures 6.14a and 6.14c indicate that spherical and rod-like inclusions of graphite produce the largest conductivity enhancement among all other materials. With a decrease in the metallic nature of the inclusion phase, the conductivity dispersion shifts to higher frequencies and the frequency dispersion of HF $\varepsilon_{r,eff}$ is more evident, as shown in Figures 6.14a and 6.14b, respectively. At operating frequencies close to 50 kHz, mixtures containing sheet-like inclusions of different materials exhibit LF σ_{eff} and HF $\varepsilon_{r,eff}$ values that are 90% and 70% higher than those of inclusion-free mixture S, respectively, as illustrated in Figures 6.14e and 6.14f. In contrast, at operating frequencies close to 50 kHz, mixtures containing spherical and rod-like inclusions show larger variations in LF σ_{eff} values ranging from -25% to +40% for various materials of the inclusion phase. In other words, conductivity dispersion responses of mixtures containing conductive sheet-like inclusions occur at lower frequencies than those containing conductive rod-like and spherical inclusions. Consequently, at operating frequencies close to 1 MHz, mixtures containing spherical and rod-like inclusions exhibit large dielectric enhancement that can represent an increase as high as 150%, as shown in Figures 6.14b and 6.14d, while those containing sheet-like inclusions do not exhibit any dielectric enhancement, as shown in Figure 6.14f. Finally, the dispersion of HF $\varepsilon_{r,eff}$ increases, while that of LF σ_{eff} decreases with a decrease in the metallic nature of the inclusion phase (i.e., graphite>pyrite>chalcopyrite). Figure 6.14 illustrates that the dispersion characteristics of

mixtures shift to higher frequencies with a decrease in the metallic nature of the inclusion phase.

6.4.5 Characteristic length of inclusions

In this section, I investigate the role of characteristic length of the inclusion phase (size of inclusions) in determining the PPIP effects. I computed the EM response of mixtures containing spherical, rod-like, or sheet-like inclusions for four different characteristic lengths of the inclusion phase, as reported in Table 6.6. Mixtures SP1, SP2, SP3, and SP4 contain uniformly distributed inclusion phases of different characteristic lengths, such that the characteristic length of inclusion phase in mixture SP1 is smaller than that in mixture SP2, which in turn is smaller than that in mixture SP3, which is smaller than that in mixture SP4. In Figure 6.15, plots a and b are associated with mixtures containing spherical inclusions, plots c and d are associated with mixtures containing rod-like inclusions, and plots e and f are associated with mixtures containing sheet-like inclusions.

The frequency dispersion of the LF σ_{eff} and HF $\varepsilon_{\text{r,eff}}$ responses shift to higher frequencies with a decrease in the characteristic length of the inclusion phase. At operating frequencies close to 50 kHz, for mixtures containing spherical and rod-like inclusions, the variation of LF σ_{eff} with respect to the reference curve ranges between -20% for smaller inclusion sizes to +35% for larger inclusion sizes, as shown in Figures 6.15a and 6.15c. However, at operating frequencies close to 100 Hz, the LF σ_{eff} responses of spherical and rod-like inclusions are independent of the size of inclusions in the mixture, as shown in Figures 6.15a and 6.15c. On the other hand, at operating frequencies more than 1 kHz, Figures 6.15e and 6.15f show that the LF σ_{eff} and HF $\varepsilon_{\text{r,eff}}$ of mixtures containing sheet-like inclusions, respectively, are relatively independent of the size of inclusions because the

dispersion behavior of such sheet-like inclusions occurs at frequencies much lower than 1 kHz. Finally, at operating frequencies close to 1 MHz, large dielectric enhancements are possible for smaller-sized conductive spherical and rod-like inclusions, as shown in Figures 6.15b and 6.15d.

6.5 CONCLUSIONS

Electrical measurements in formations containing uniformly distributed conductive inclusions are highly sensitive to the variations in volume fraction, material, characteristic length, and shape of the inclusion phase and conductivity of the pore-filling electrolyte. The low-frequency effective conductivity of an electrolyte-saturated geomaterial containing as low as 5% volume fraction of disseminated conductive inclusions is -30% to +100% greater than the host conductivity for operating frequencies between 100 Hz to 100 kHz. Furthermore, the high-frequency effective relative permittivity of that geomaterial is -10% to +90% greater than that of the host for operating frequencies between 100 kHz to 10 MHz. I numerically investigated the effects of charge polarization and relaxation mechanism around sheet-like and rod-like conductive inclusions on subsurface EM measurements. Geomaterials containing sheet-like inclusions exhibit large frequency dispersion in the effective conductivity response for low frequencies that generate exceedingly high galvanic resistivity measurements compared to the true formation resistivity. Conversely, EM induction and EM propagation measurements are less sensitive to variations in properties of sheet-like inclusions. However, EM induction and EM propagation measurements, and not galvanic resistivity measurements, are highly sensitive to variations in the electrical properties of rod-like and spherical inclusions. Moreover, EM propagation measurements at operating frequencies close to or higher than 100 MHz are not susceptible to the effects of PPIP phenomena, whereby a CRIM-type effective medium

formulation can be used to analyze the EM propagations measurements at those frequencies.

PPIP phenomena generally lead to large variations of EM measurements, highly dispersive complex-valued conductivity response, and high sensitivity of EM measurements to the properties of inclusions and conductivity of pore-filling electrolyte. The PPIP-SCAIP model or a similar approach can improve resistivity interpretation of subsurface galvanic resistivity, EM induction, and EM propagation measurements in formations containing conductive mineral inclusions.

Table 6.1: Brine conductivity (σ_w) used to obtain specific conductivity anisotropy (λ_c) for the 0°-dip and 45°-dip bilaminar TIVAR-brine synthetic cores at 58.5 kHz.

Material of inclusion phase	$\boldsymbol{\sigma}$	$\boldsymbol{\varepsilon_r}$	$\boldsymbol{D}$
Graphite (G)	6e4	15	10^{-4}
Pyrite (P)	5e2	12	5×10^{-5}
Chalcopyrite (C)	10	11	8×10^{-6}
Low-conductivity material (X)	1	5	10^{-8}
0.1-S/m conductivity material (Y)	0.1	80	10^{-9}
Non-conductive material (H)	—	3	—

Table 6.2: Conductivity (σ), in S/m, relative permittivity (ε_r), diffusion coefficient (D), in m^2/s, and ratio of conductivity to diffusion coefficient of charge carriers assumed in Figure 6.4.

Material of inclusion phase	$\boldsymbol{\sigma}$	$\boldsymbol{\varepsilon_r}$	$\boldsymbol{D}$	$\boldsymbol{\sigma / D}$
Graphite (G)	1e4	15	10^{-4}	10^{8}
Pyrite (P)	1e3	12	10^{-5}	10^{8}
Chalcopyrite (C)	1e2	11	10^{-6}	10^{8}
Low-conductivity material (X)	1	5	10^{-8}	10^{8}
0.1-S/m conductivity material (Y)	0.1	80	10^{-9}	10^{8}
Non-conductive material (H)	—	3	—	—

Table 6.3: Conductivity (σ), in S/m, relative permittivity (ε_r), and diffusion coefficient (D), in m^2/s, assumed in Figure 6.5.

Material of inclusion phase	$\boldsymbol{\sigma}$	$\boldsymbol{\varepsilon_r}$	$\boldsymbol{D}$
Chalcopyrite (C)	10	11	8×10^{-6}
Pyrite (P)	500	12	5×10^{-5}
Graphite (G)	6e4	15	10^{-4}

Table 6.4: Conductivity (σ), in S/m, relative permittivity (ε_r), and diffusion coefficient (D), in m^2/s, assumed in Figure 6.6.

Material of inclusion phase	σ	ε_r	D	**Model**
Pyrite (P)	500	12	5×10^{-5}	PPIP-SCAIP
Graphite (G)	6e4	15	10^{-4}	PPIP-SCAIP
Clay (Cl2)	—	2	—	SCAIP

Table 6.5: Conductivity (σ), in S/m, relative permittivity (ε_r), and diffusion coefficient (D), in m^2/s, assumed in Figure 6.14.

Material of inclusion phase	σ	ε_r	D
Graphite (SG)	6e4	15	10^{-4}
Pyrite (SP)	500	12	5×10^{-5}
Chalcopyrite (SC)	10	11	8×10^{-6}
Low-conductivity material (SX)	0.5	8	7×10^{-7}

Table 6.6: Characteristic length, in μm, of various shapes of inclusion phase assumed in Figure 6.15.

Material of inclusion phase	Spherical Inclusion	Rod-like inclusion	Sheet-like inclusion
P1 pyrite	2	0.2	200
P2 pyrite	20	2	600
P3 pyrite	200	20	1200
P4 pyrite	2000	100	2400

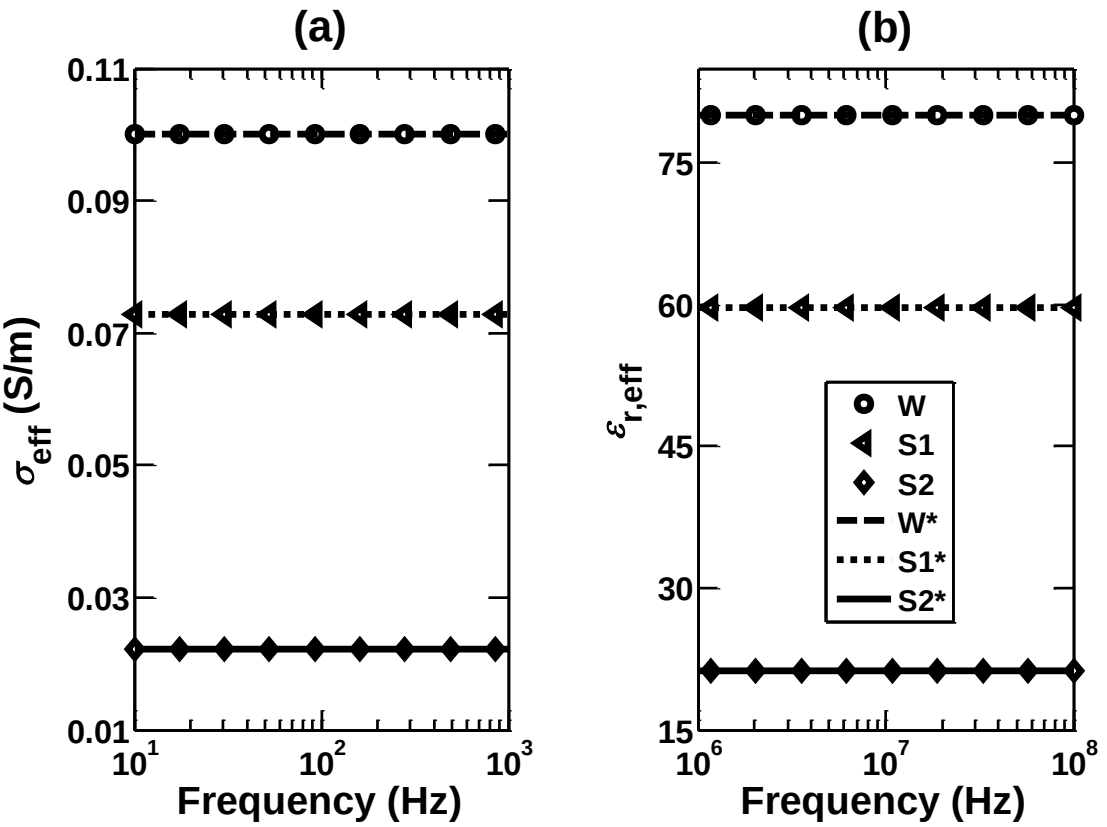

Figure 6.1: Comparison of PPIP and the SCAIP model predictions of the (a) LF effective conductivity (σ_{eff}) and (b) HF effective relative permittivity ($\varepsilon_{r,eff}$) of three mixtures containing 0%, 20%, and 70%, respectively, volume fraction of non-conductive spherical grains that are uniformly distributed in a 0.1-S/m conductivity electrolyte. Curves with the "*" superscript in their names identify mixtures that were analyzed using the SCAIP model, and those without the "*" superscript identify mixtures that were analyzed using the PPIP model. Curves W and W* identify mixtures with 100% volume fraction of the electrolyte, curves S1 and S1* identify mixtures containing 20% volume fraction of non-conductive spherical grains and 80% volume fraction of electrolyte, and curves S2 and S2* identify mixtures containing 70% volume fraction of non-conductive spherical grains and 30% volume fraction of electrolyte. The default mixture is assumed to be made of 1-mm diameter, non-conductive spherical grains possessing Σ_s of 10^{-9} S. Relative permittivity of non-conductive spherical grains is 4 and that of the electrolyte is 80. Diffusion coefficient of ions in the electrolyte is 10^{-9} m^2/s.

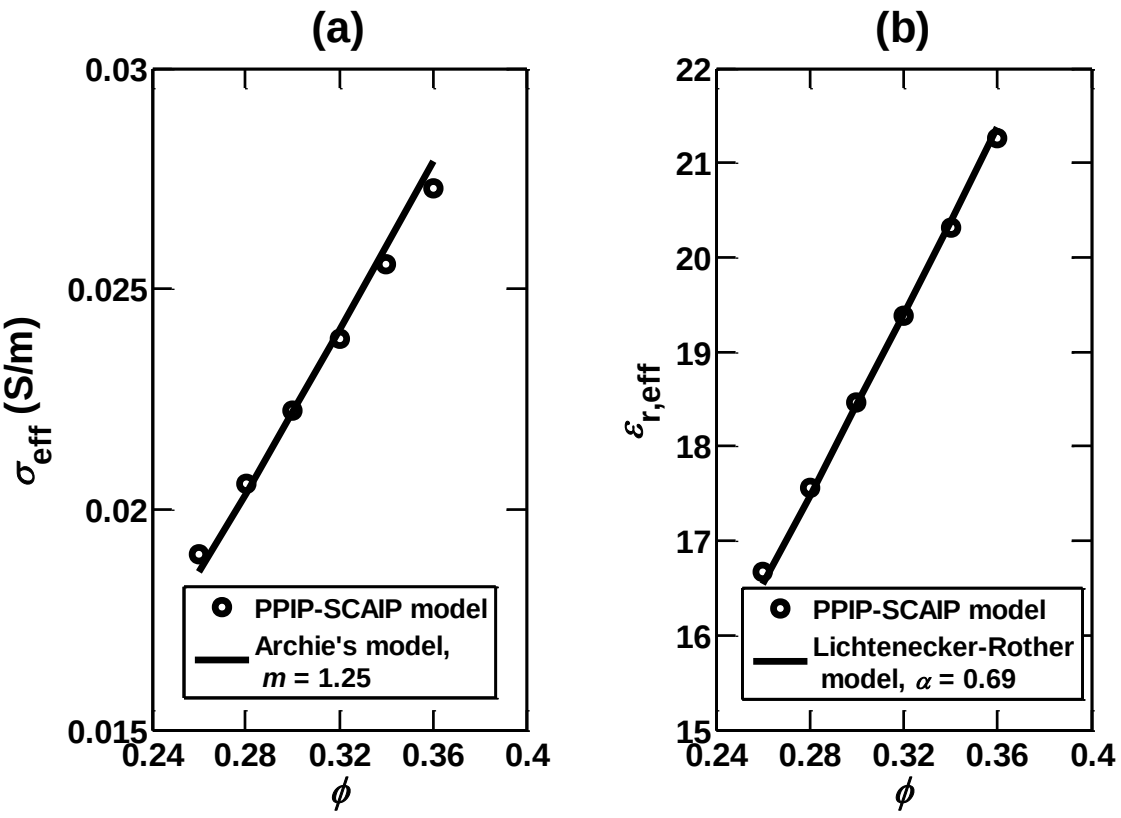

Figure 6.2: Comparison of PPIP-SCAIP model predictions of the (a) LF σ_{eff} against Archie's model predictions (solid) and that of (b) HF $\varepsilon_{r,eff}$ against Lichtenecker-Rother's model predictions (solid) for mixtures containing varying volume fractions, ranging from 64% to 74%, of non-conductive spherical grains that are uniformly distributed in a 0.1-S/m conductivity electrolyte. The default mixture is assumed to contain 1-mm diameter, non-conductive spherical grains possessing Σ_s of 10^{-9} S. Relative permittivity of non-conductive spherical grains is 6 and that of electrolyte is 60. Diffusion coefficient of ions in the electrolyte is 10^{-9} m^2/s.

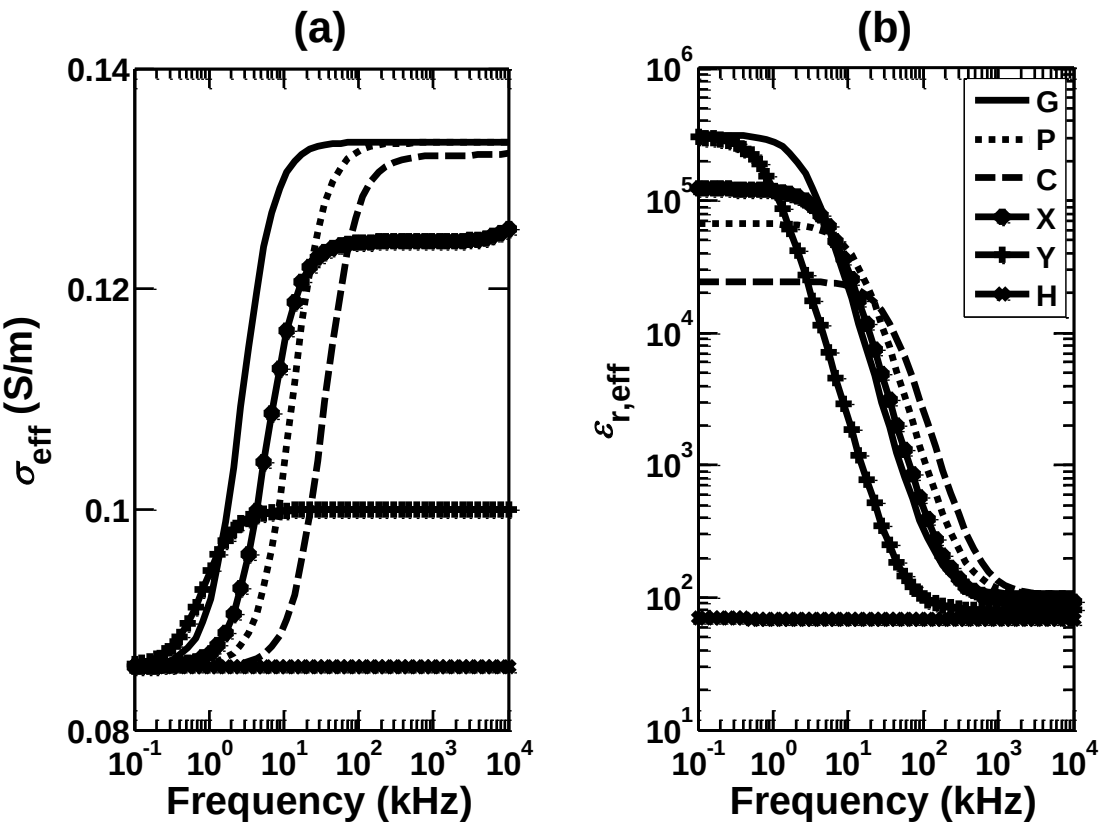

Figure 6.3: Comparison of PPIP model predictions of the (a) σ_{eff} and (b) $\varepsilon_{r,eff}$ of mixtures containing 10% volume fraction of 200-μm diameter, spherical inclusions that are uniformly distributed in a 0.1-S/m conductivity electrolyte for different materials of the inclusion phase. Curves G, P, C, X, Y, and H identify mixtures containing only graphite inclusions, pyrite inclusions, chalcopyrite inclusions, low-conductivity material inclusions, 0.1-S/m conductivity inclusions, and non-conductive inclusions, respectively, uniformly distributed in the electrolyte. Relative permittivity of the electrolyte host is 80 and the diffusion coefficient of ions in the electrolyte is 10^{-9} m^2/s. Table 6.1 describes the assumed electrical properties for materials of the inclusion phase for the above mixtures.

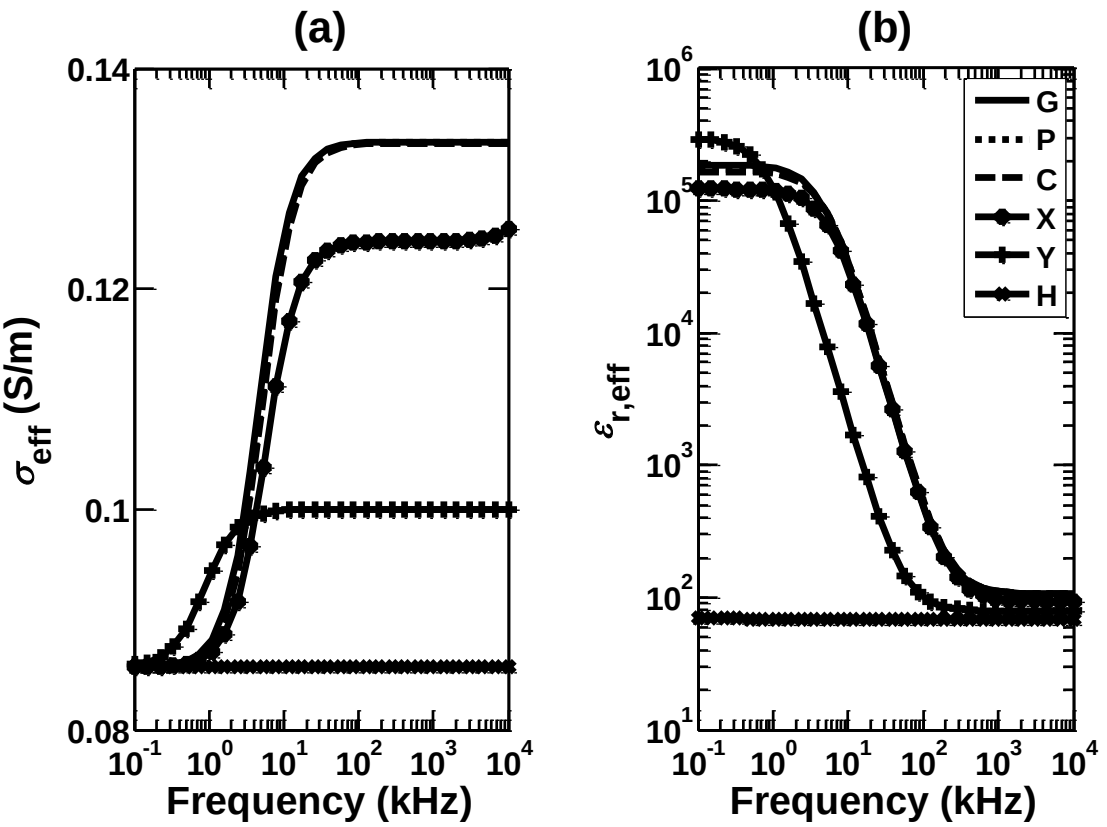

Figure 6.4: Comparison of PPIP model predictions of the (a) σ_{eff} and (b) $\varepsilon_{r,eff}$ of mixtures containing 10% volume fraction of 200-μm diameter, spherical inclusions that are uniformly distributed in a 0.1-S/m conductivity electrolyte for different materials of the inclusion phase. Curves G, P, C, X, Y, and H identify mixtures containing only graphite inclusions, pyrite inclusions, chalcopyrite inclusions, low-conductivity material inclusions, 0.1-S/m conductivity inclusions, and non-conductive inclusions, respectively, uniformly distributed in the electrolyte. Relative permittivity of the electrolyte is 80 and the diffusion coefficient of ions in the electrolyte is 10^{-9} m^2/s. Table 6.2 describes the assumed electrical properties for materials of the inclusion phase for the above mixtures.

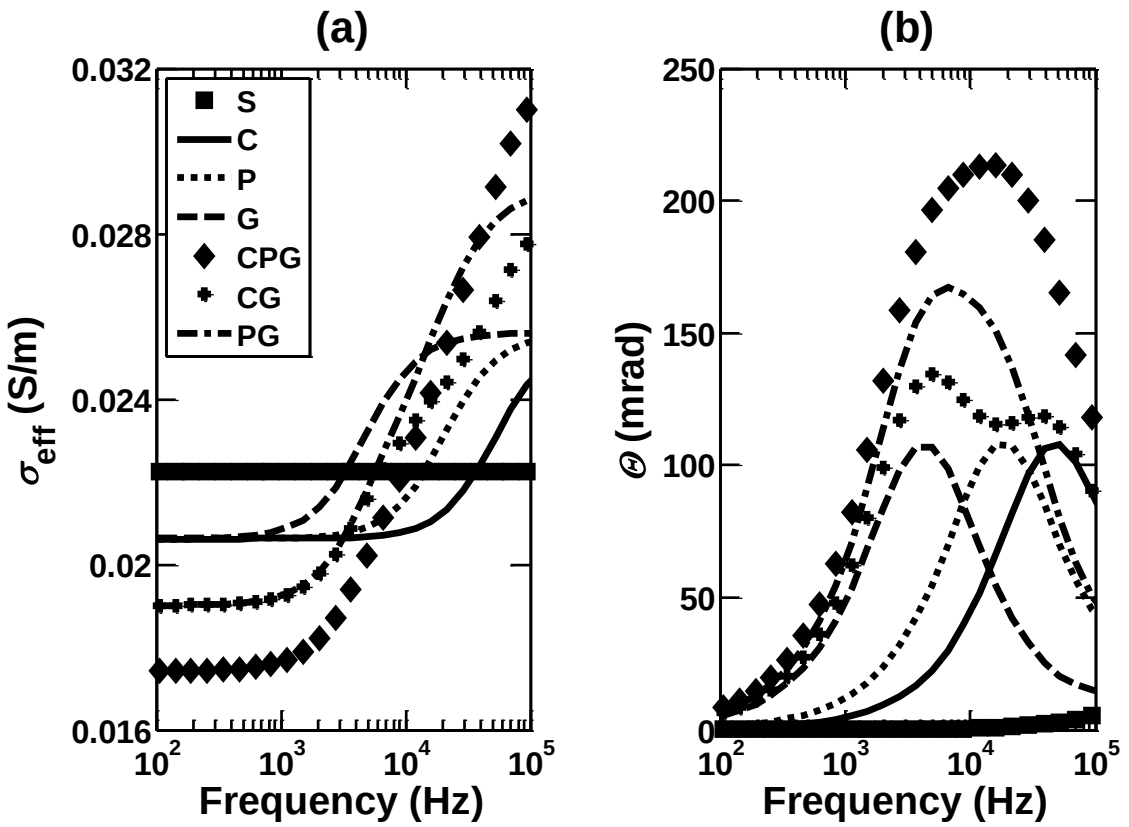

Figure 6.5: Comparison of PPIP-SCAIP model predictions of the (a) σ_{eff} and (b) Θ responses of mixtures containing 70% volume fraction of 100-μm diameter, non-conductive spherical grains and various volume fractions of 100-μm diameter, conductive inclusions of one or more materials that are uniformly distributed in a 0.1-S/m conductivity electrolyte. Curves S, C, P, G, CPG, CG, and PG identify mixtures containing no conductive inclusions, only 2% volume fraction of chalcopyrite inclusions, only 2% volume fraction of pyrite inclusions, only 2% volume fraction of graphite inclusions, 2% volume fractions of pyrite, graphite, and chalcopyrite inclusions, 2% volume fractions of chalcopyrite and graphite inclusions, and 2% volume fractions of pyrite and graphite inclusions, respectively, uniformly distributed in the mixture of electrolyte and non-conductive spherical grains. Relative permittivity of the electrolyte is 80 and the diffusion coefficient of ions in the electrolyte host is 10^{-9} m^2/s. Relative permittivity of non-conductive spherical grains is 5 and its Σ_s is 10^{-9} S. Table 6.3 describes the assumed electrical properties for materials of the inclusion phase for the above mixtures.

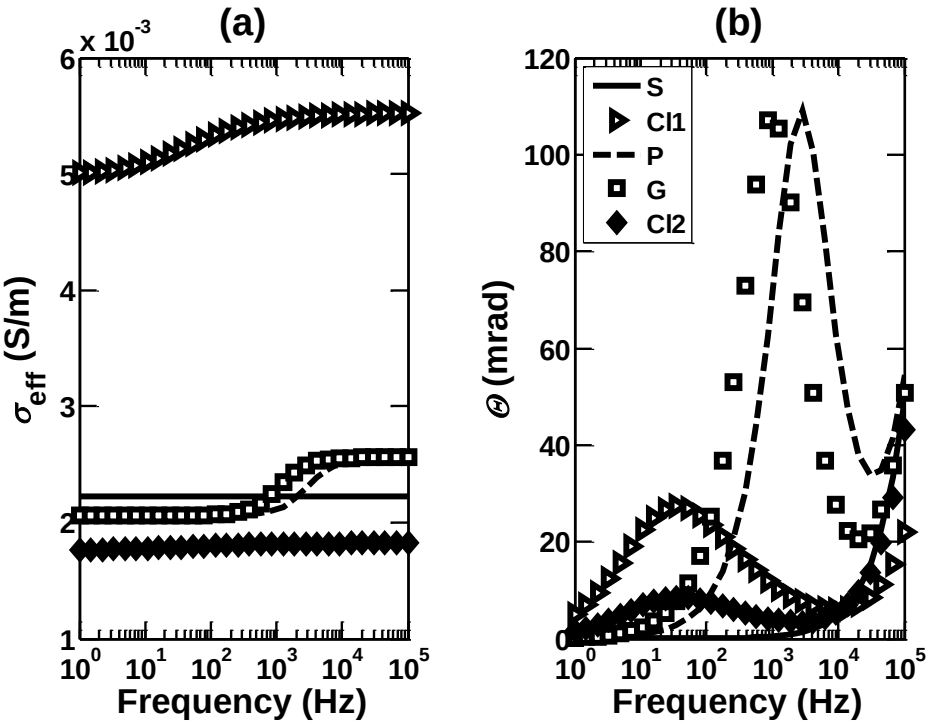

Figure 6.6: Comparison of PPIP-SCAIP model predictions of the (a) σ_{eff} and (b) Θ responses of mixtures containing varying volume fractions of either conductive inclusions or non-conductive spherical grains, possessing surface conductance, uniformly distributed in a matrix comprising of 70% volume fraction of non-conductive spherical grains fully saturated with 0.01-S/m conductivity electrolyte. Curves S and Cl1 identify mixtures containing 70% volume fraction of 1-mm diameter, non-conductive spherical grains, possessing Σ_s of 10^{-9} S, of relative permittivity of 5 and 70% volume fraction of 10-µm diameter, non-conductive spherical grains, possessing Σ_s of 10^{-8} S, of relative permittivity of 5, respectively. Curves P, G, and Cl2 identify mixtures containing 2% volume fraction of 100-µm diameter pyrite inclusions, 2% volume fraction of 100-µm diameter graphite inclusions, and 10% volume fraction of 10-µm diameter non-conductive spherical grains, possessing Σ_s of 10^{-8} S, of relative permittivity of 2, respectively, uniformly distributed in 70% volume fraction of 1-mm diameter, non-conductive spherical grains, possessing Σ_s of 10^{-9} S, of relative permittivity of 5. Relative permittivity of the electrolyte is 80 and the diffusion coefficient of ions in the electrolyte is 10^{-9} m^2/s. Table 6.4 describes the assumed electrical properties for materials of the inclusion phase for the above mixtures.

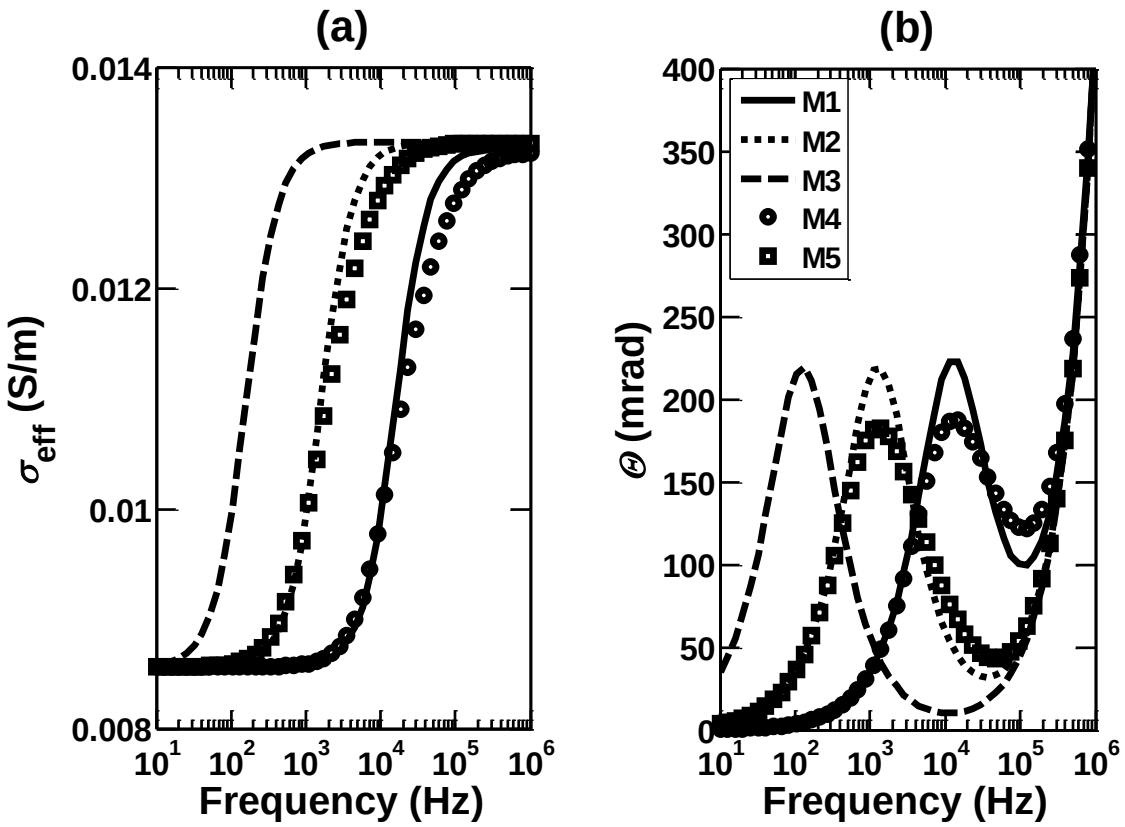

Figure 6.7: Comparison of PPIP model predictions of the (a) σ_{eff} and (b) Θ responses of mixtures containing 10% volume fraction of spherical conductive inclusions uniformly distributed in 0.01-S/m conductivity electrolyte for varying size and distribution of sizes of inclusions. Conductive inclusion phase has a relative permittivity of 12, conductivity of 500 S/m, and diffusion coefficient of charge carriers is 5×10^{-5} m^2/s. Relative permittivity of the electrolyte is 80 and the diffusion coefficient of ions in the electrolyte is 10^{-9} m^2/s. Curves M1, M2, and M3 identify mixtures containing conductive spherical inclusions of 10-μm, 100-μm, and 1000-μm diameter, respectively. Curves M4 and M5 identify mixtures containing conductive spherical inclusions of uniform distribution of sizes that vary ±90% about a mean diameter of 10 μm and 100 μm, respectively.

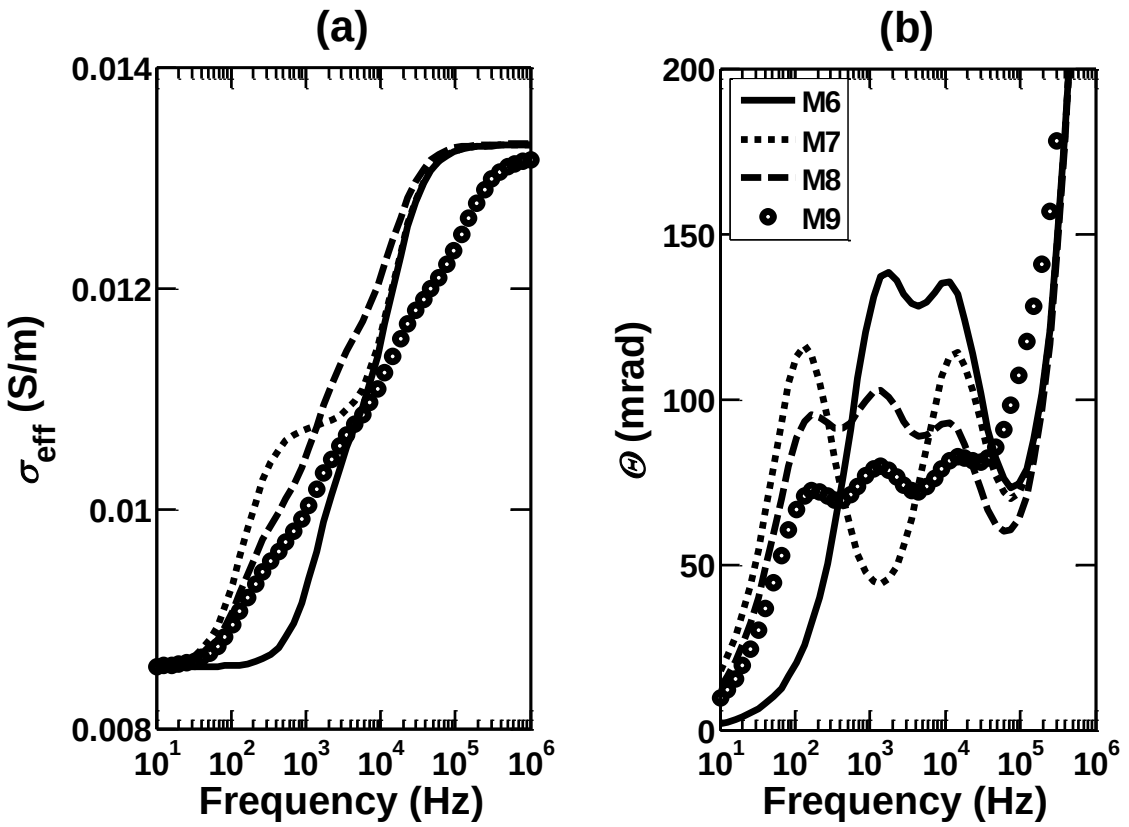

Figure 6.8: Comparison of PPIP model predictions of the (a) σ_{eff} and (b) Θ responses of mixtures containing 10% volume fraction of spherical conductive inclusions uniformly distributed in a 0.01-S/m electrolytic host for varying dispersity of inclusion sizes. The conductive inclusion phase has a relative permittivity of 12, conductivity of 500 S/m, and diffusion coefficient of charge carriers is 5×10^{-5} m^2/s. Relative permittivity of the electrolyte is 80 and the diffusion coefficient of ions in the electrolyte is 10^{-9} m^2/s. Curves M6, M7, M8, and M9 identify mixtures containing 10% volume fraction of conductive inclusions of equal volumetric content of 10-μm and100-μm diameter inclusions; 10-μm and1000-μm diameter inclusions; 10-μm, 100-μm, and1000-μm diameter inclusions; and 1-μm, 10-μm,100-μm, and1000-μm diameter inclusions, respectively.

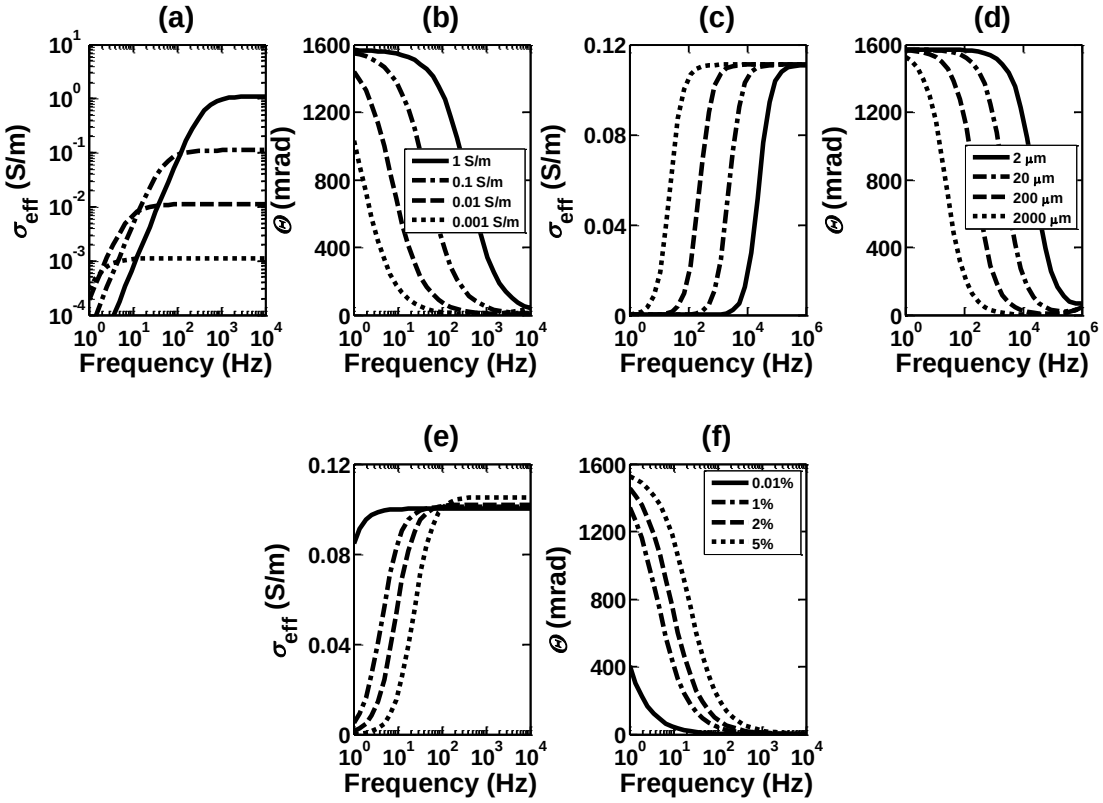

Figure 6.9: Comparison of PPIP model predictions of the (a) σ_{eff} and (b) Θ responses of four mixtures containing 10% volume fraction of 1000-μm thick conductive sheet-like inclusions uniformly distributed in an 1-, 0.1-, 0.01-, and 0.001-S/m conductivity electrolytic host, respectively. Comparison of the PPIP model predictions of the (c) σ_{eff} and (d) Θ responses of four mixtures containing 10% volume fraction of 2-, 20-, 200-, and 2000-μm thick conductive sheet-like inclusions, respectively, uniformly distributed in a 0.1-S/m conductivity electrolytic host. Comparison of PPIP model predictions of the (e) σ_{eff} and (f) Θ responses of four mixtures containing 0.1%, 1%, 2%, and 5% volume fractions, respectively, of 1-mm thick conductive sheet-like inclusions uniformly distributed in a 0.1-S/m conductivity electrolytic host. The conductive inclusion phase has a relative permittivity of 12, conductivity of 5000 S/m, and diffusion coefficient of charge carriers is 5×10^{-5} m^2/s. Relative permittivity of the electrolyte is 80 and the diffusion coefficient of ions in the electrolyte is 10^{-9} m^2/s. Pairs of plots (a) and (b), (c) and (d), and (e) and (f) share the same legends, respectively.

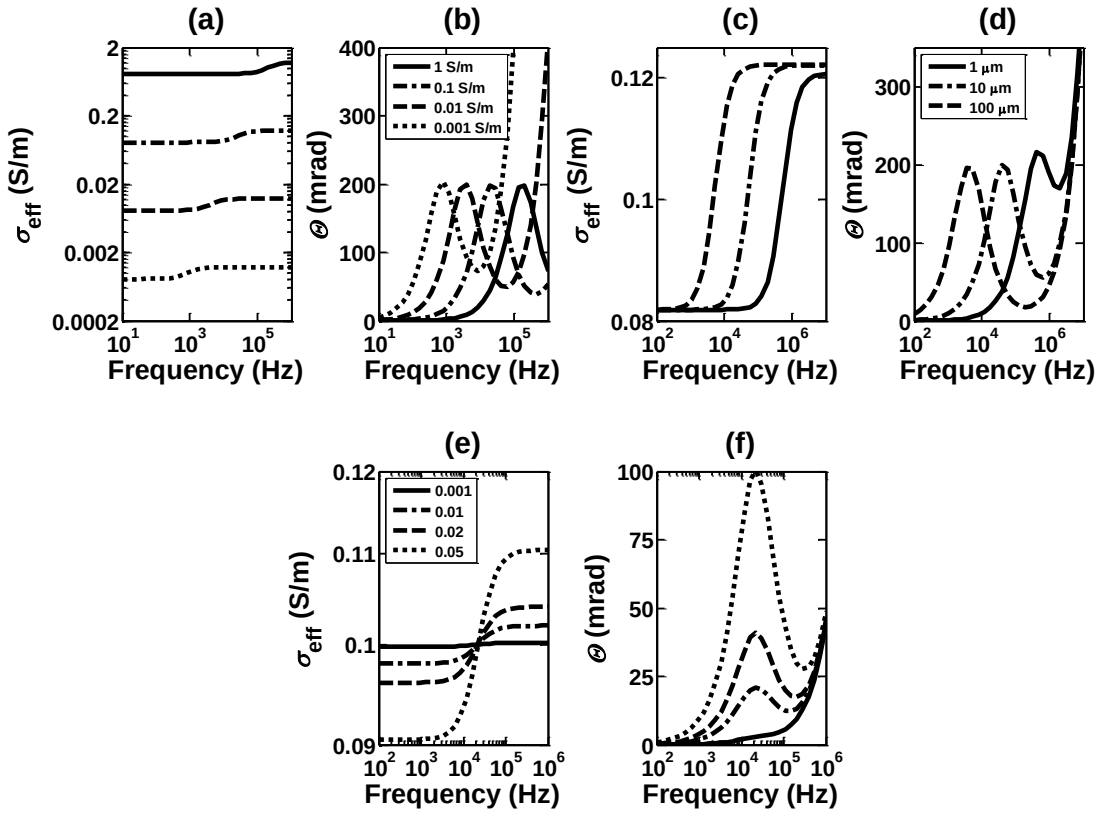

Figure 6.10: Comparison of PPIP model predictions of the (a) σ_{eff} and (b) Θ responses of four mixtures containing 10% volume fraction of 20-μm diameter, conductive rod-like inclusions uniformly distributed in an 1-, 0.1-, 0.01-, and 0.001-S/m conductivity electrolytic host, respectively. Comparison of the PPIP model predictions of the (c) σ_{eff} and (d) Θ responses of three mixtures containing 10% volume fraction of 1-, 10-, and 100-μm thick, conductive rod-like inclusions, respectively, uniformly distributed in a 0.1-S/m electrolytic host. Comparison of PPIP model predictions of the (e) σ_{eff} and (f) Θ responses of four mixtures containing 0.1%, 1%, 2%, and 5% volume fraction, respectively, of 20-μm thick, conductive rod-like inclusions uniformly distributed in a 0.1-S/m conductivity host. The conductive inclusion phase has a relative permittivity of 12, conductivity of 5000 S/m, and diffusion coefficient of charge carriers is 5×10^{-5} m^2/s. Relative permittivity of the electrolyte is 80 and the diffusion coefficient of ions in the electrolyte is 10^{-9} m^2/s. Pairs of plots (a) and (b), (c) and (d), and (e) and (f) share the same legends, respectively.

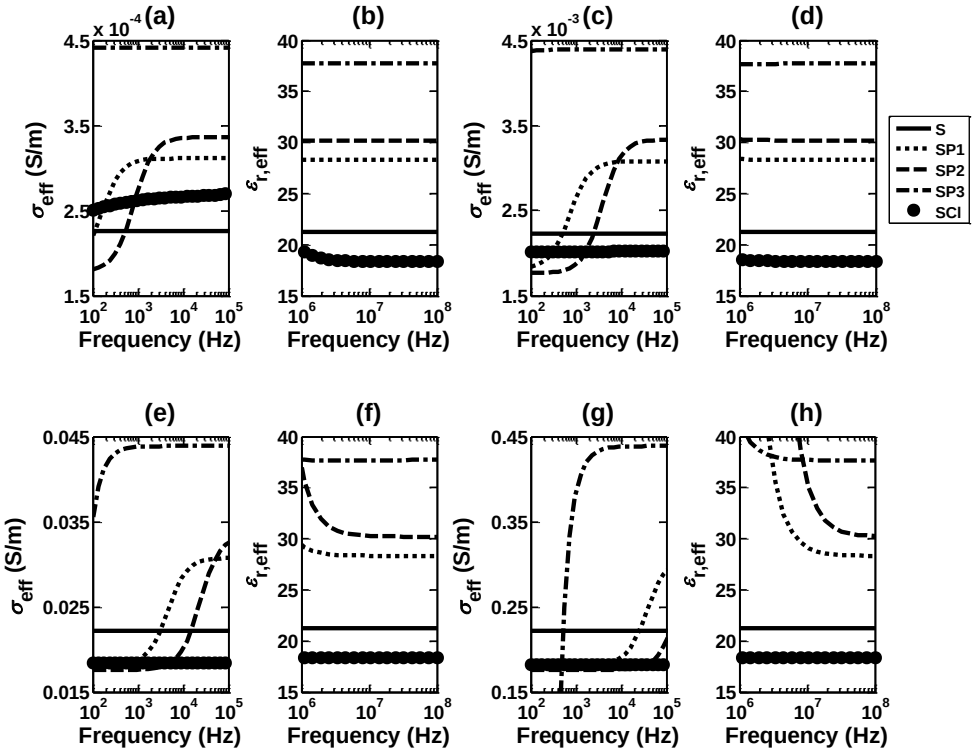

Figure 6.11: Comparison of PPIP-SCAIP model predictions of the LF σ_{eff} and HF $\varepsilon_{r,eff}$ responses of mixtures S, SP1, SP2, SP3, and SCl containing no inclusions, 5% volume fraction of 200-μm diameter spherical grains, 5% volume fraction of 20-μm diameter long rods, 5% volume fraction of 1-mm thick sheets, and 5% volume fraction of 10-μm diameter surface-charge-bearing, non-conductive spherical grains exhibiting Σ_s of 10^{-8} S, respectively, uniformly distributed in a matrix made of 70% volume fraction of 1-mm diameter, non-conductive spherical grains that is completely saturated with electrolyte for various electrolyte conductivities. Pairs of Figures 11a and 11b, 11c and 11d, 11e and 11f, and 11g and 11h identify the computed LF σ_{eff} and HF $\varepsilon_{r,eff}$ of mixtures, respectively, fully saturated with 0.001-, 0.01-, 0.1-, and 1-S/m electrolyte, respectively. The conductive inclusion phase has a relative permittivity of 12, conductivity of 5000 S/m, and diffusion coefficient of charge carriers is 5×10^{-5} m^2/s. Relative permittivity of the electrolyte is 80 and the diffusion coefficient of ions in the electrolyte is 10^{-9} m^2/s. The assumed value of relative permittivity of non-conductive spherical grains possessing Σ_s of 10^{-9} S, identifying sand grains, is 4 and that of non-conductive spherical grains possessing Σ_s of 10^{-8} S, identifying clay grains, is 8. All the plots share the same legend.

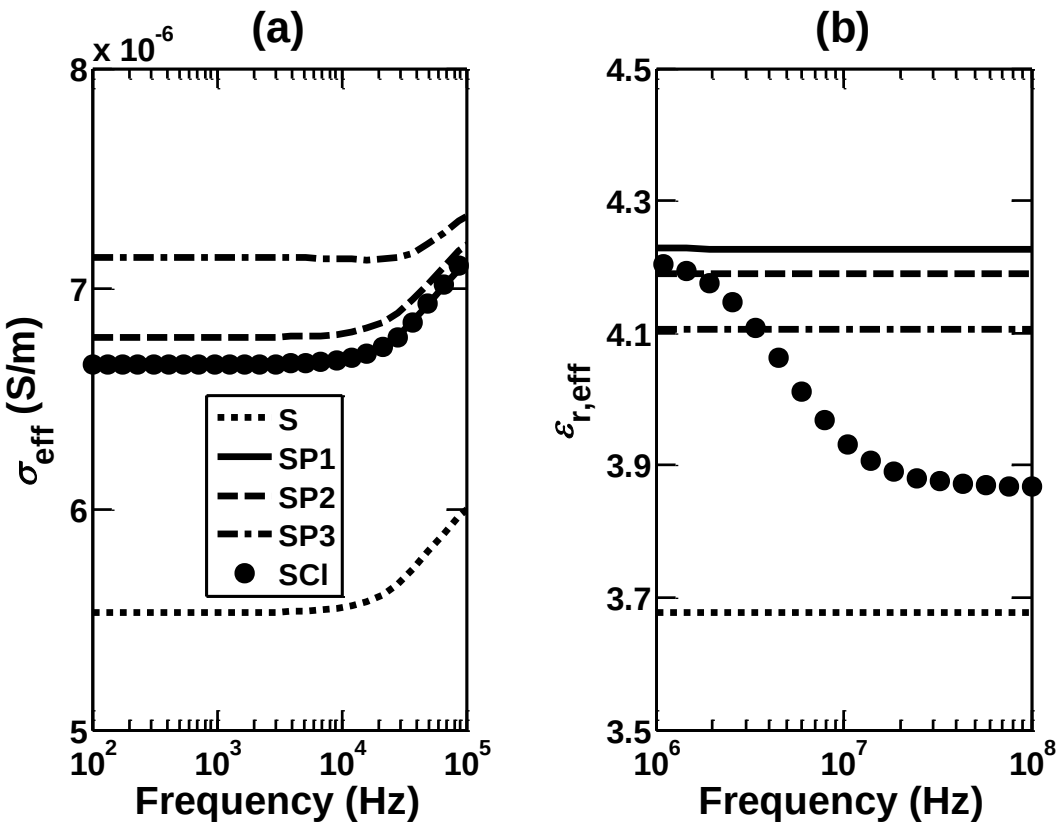

Figure 6.12: Comparison of PPIP-SCAIP model predictions of the (a) LF σ_{eff} and (b) HF $\varepsilon_{r,eff}$ responses of mixtures S, SP1, SP2, SP3, and SCl containing no inclusions, 5% volume fraction of 200-μm diameter conductive spherical inclusions, 5% volume fraction of 20-μm diameter long rod-like conductive inclusions, 5% volume fraction of 1-mm thick sheet-like conductive inclusions, and 5% volume fraction of 10-μm diameter non-conductive spherical inclusions possessing Σ_s of 10^{-8} S, respectively, uniformly distributed in a matrix made of 70% volume fraction of 1-mm diameter, non-conductive spherical grains completely saturated with non-conductive fluid possessing a bulk relative permittivity of 3. The conductive inclusion phase has a relative permittivity of 12, conductivity of 5000 S/m, and diffusion coefficient of charge carriers is 5×10^{-5} m^2/s. The assumed value of relative permittivity of non-conductive spherical grains possessing Σ_s of 10^{-9} S, identifying sand grains, is 4 and that of non-conductive spherical grains possessing Σ_s of 10^{-8} S, identifying clay grains, is 8.

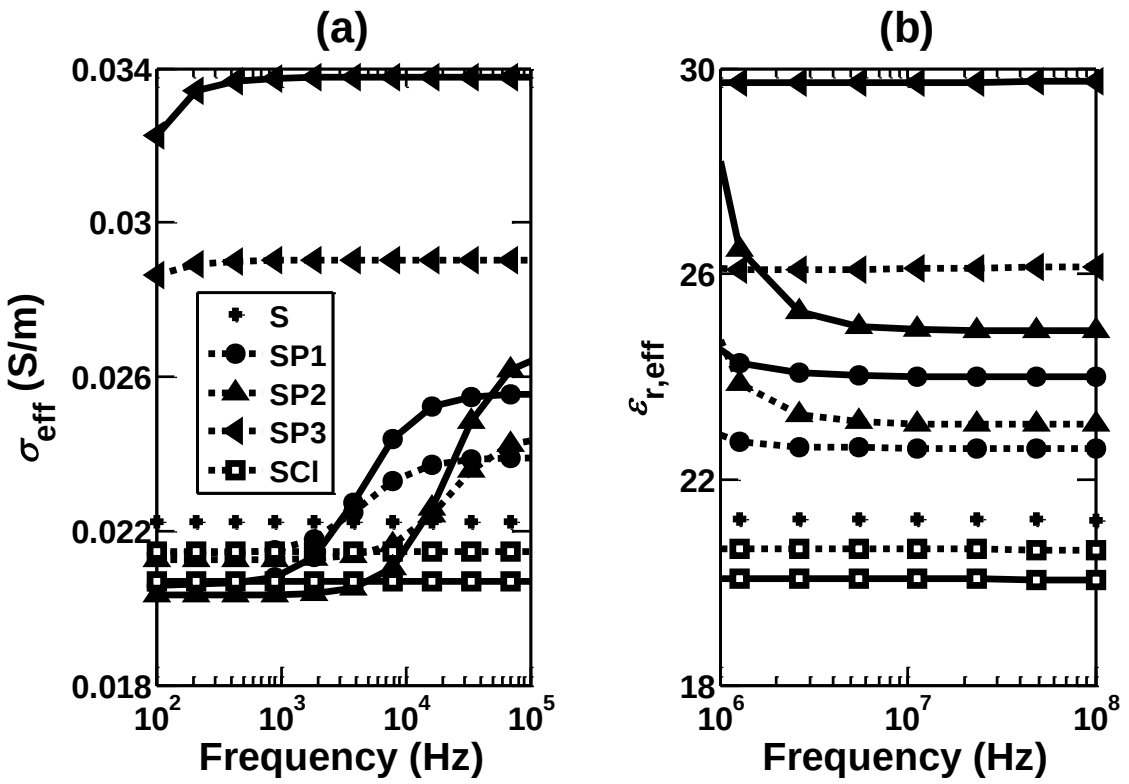

Figure 6.13: Comparison of PPIP-SCAIP model predictions of the (a) LF σ_{eff} and (b) HF $\varepsilon_{r,eff}$ responses of mixtures S, SP1, SP2, SP3, and SCl containing no inclusions, 200-μm diameter conductive spherical inclusions, 20-μm diameter long rod-like conductive inclusions, 1-mm thick sheet-like conductive inclusions, and 10-μm diameter non-conductive spherical grains exhibiting Σ_s of 10^{-8} S, respectively, uniformly distributed in a matrix made of 70% volume fraction of 1-mm diameter non-conductive spherical grains completely saturated with electrolyte for 1% (dotted) and 2% (solid) volume fraction of the inclusion phase. The conductive inclusion phase has a relative permittivity of 12, conductivity of 5000 S/m, and the diffusion coefficient of charge carriers is 5×10^{-5} m^2/s. Relative permittivity of the electrolyte is 80 and the diffusion coefficient of ions in the electrolyte is 10^{-9} m^2/s. The assumed value of relative permittivity of non-conductive spherical grains possessing Σ_s of 10^{-9} S, identifying sand grains, is 4 and that of non-conductive spherical grains possessing Σ_s of 10^{-8} S, identifying clay grains is 8.

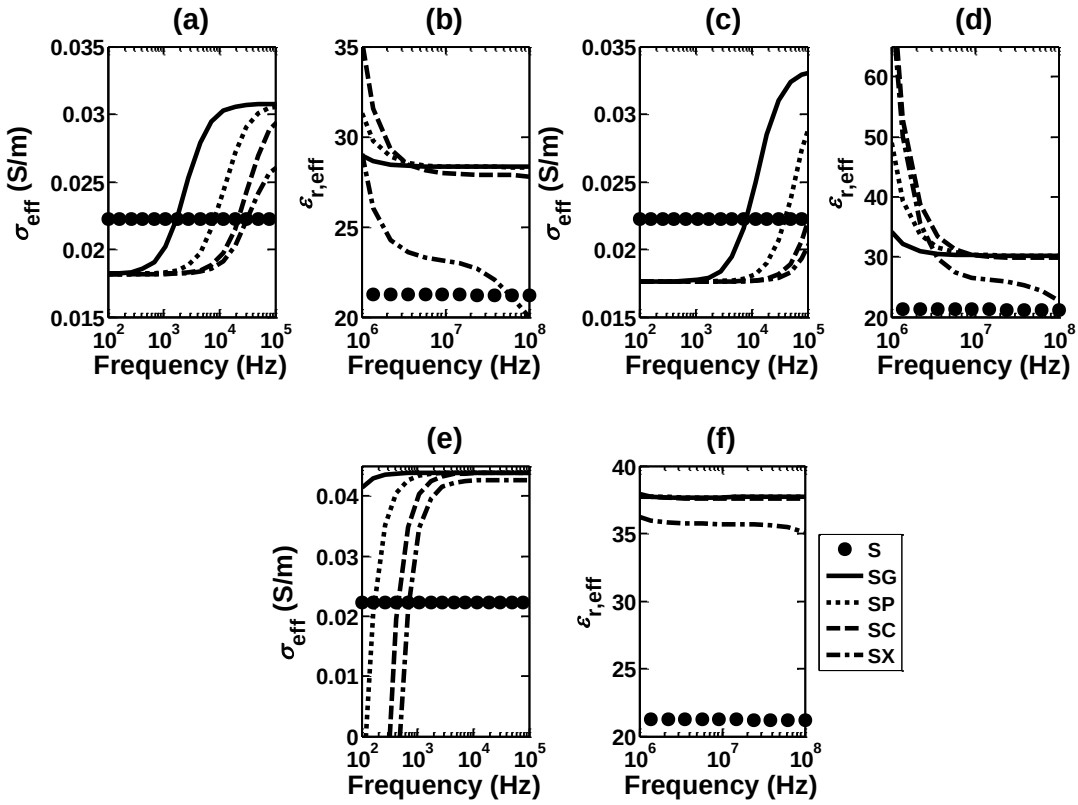

Figure 6.14: Comparison of PPIP-SCAIP model predictions of the LF σ_{eff} and HF $\varepsilon_{r,eff}$ responses of mixtures S, SG, SP, SC, and SX containing no inclusions, 5% volume fraction of graphite inclusions, 5% volume fraction of pyrite inclusions, 5% volume fraction of chalcopyrite inclusions, and 5% volume fraction of inclusions made of a synthetic low-conductivity material, respectively, uniformly distributed in a matrix made of 70% volume fraction of 1-mm diameter, non-conductive spherical grains that is completely saturated with 0.1-S/m conductivity electrolyte. Pairs of Figures 14a and 14b, 14c and 14d, and 14e and 14f identify the computed σ_{eff} and $\varepsilon_{r,eff}$, respectively, of mixtures containing 200-μm diameter spherical inclusions, 20-μm diameter long rod-like inclusions, and 1-mm thick sheet-like inclusions, respectively. Relative permittivity of the electrolytic host is 80 and the diffusion coefficient of ions in the electrolyte host is 10^{-9} m^2/s. The assumed values of relative permittivity of non-conductive spherical grains possessing Σ_s of 10^{-9} S, identifying sand grains, is 4. All the plots share the same legend. Table 6.5 describes the assumed electrical properties for the above materials.

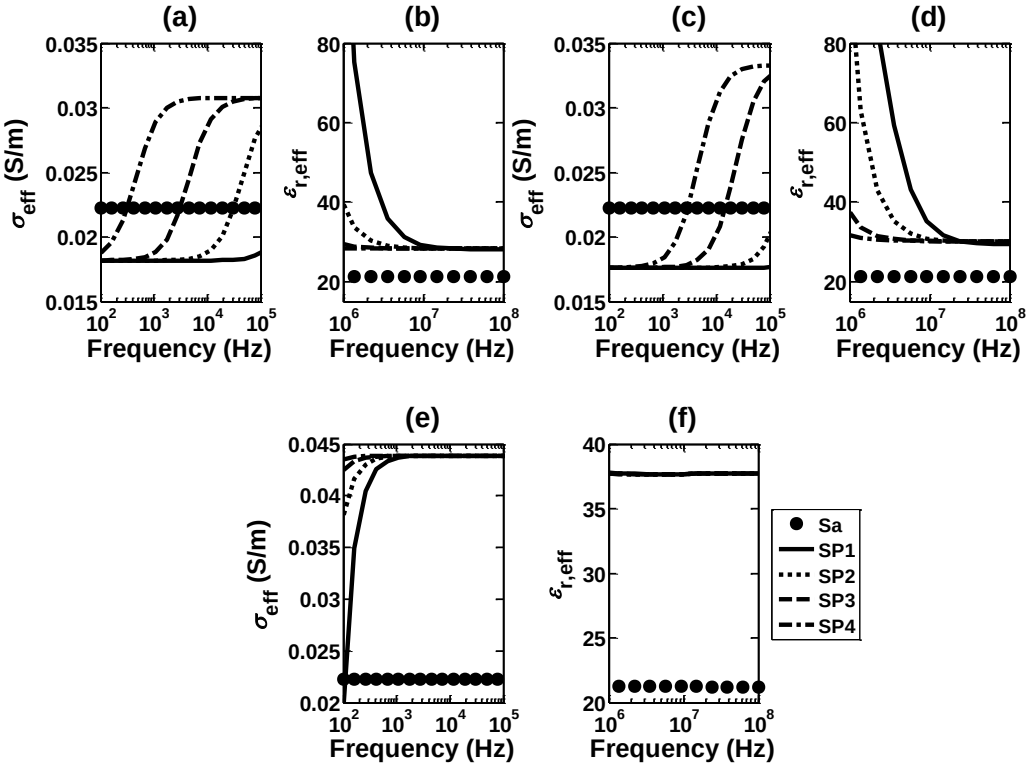

Figure 6.15: Comparison of PPIP-SCAIP model predictions of the LF σ_{eff} and HF $\varepsilon_{r,eff}$ responses of mixtures S, SP1, SP2, SP3, and SP4 containing no inclusions, 5% volume fraction of P1 pyrite inclusions, 5% volume fraction of P2 pyrite inclusions, 5% volume fraction of P3 pyrite inclusions, and 5% volume fraction of P4 pyrite inclusions, respectively, uniformly distributed in a matrix made of 70% volume fraction of 1-mm diameter, non-conductive spherical grains that are completely saturated with a 0.1-S/m conductivity electrolyte. Pairs of Figures 15a and 15b, 15c and 15d, and 15e and 15f identify the computed σ_{eff} and $\varepsilon_{r,eff}$, respectively, of mixtures containing only spherical inclusions, long rod-like inclusions, or sheet-like inclusions, respectively. Table 6.6 reports the characteristic length associated with the P1, P2, P3, and P4 inclusion phase. The conductive inclusion phase has a relative permittivity of 12, conductivity of 5000 S/m, and the diffusion coefficient of charge carriers is 5×10^{-5} m^2/s. Relative permittivity of the electrolyte is 80 and the diffusion coefficient of ions in the electrolyte is 10^{-9} m^2/s. The assumed value of relative permittivity of non-conductive spherical grains possessing Σ_s of 10^{-9} S, identifying sand grains, is 4. All the plots share the same legend.

Chapter 7: Summary, Conclusions, and Recommendations

This final chapter summarizes the developments and technical contributions in the dissertation, draws general conclusions from the results, and provides recommendations for future research.

7.1 SUMMARY

The main thrust of this dissertation was to develop a laboratory measurement technique and a quantitative interpretation method that explicitly account for the effects of interfacial polarization due to conductive minerals, clay-sized particles, and clay minerals uniformly distributed in a fluid-filled porous geological host. To do so, I developed a non-contact and non-invasive laboratory apparatus, the WCEMIT, based on the physics of electromagnetic induction to measure the complex electrical conductivity tensor of whole core samples at multiple frequencies. I developed two EM forward models based on COMSOL-based finite-element (FE) method and a MATLAB-based semi-analytic (SA) method, respectively, of the developed tool. These EM forward models were used for interpreting the WCEMIT measurements to estimate effective conductivity and permittivity of the samples. Several petrophysical applications of the WCEMIT were tested for purposes of whole core analysis of rock samples of various facies. More importantly, the directional complex conductivity of mixtures containing conductive mineral inclusions, such as pyrite and graphite, were estimated in the EM induction frequency range from 10 kHz to 300 kHz. Moreover, a mechanistic electrochemical model, PPIP-SCAIP model, was developed and implemented to quantify the directional complex electrical conductivity of mixtures containing electrically conductive mineral inclusions of various shapes uniformly distributed in a fluid-filled, porous matrix made of non-conductive grains possessing surface conductance. Finally, using the mechanistic model, cases of petrophysically

adverse alteration of subsurface galvanic resistivity, EM induction, and EM propagation logging measurements were identified in formations containing clay particles, clay minerals, and conductive minerals.

I successfully validated and benchmarked the new laboratory tool, the two EM forward models of the developed tool, and the mechanistic electrochemical model against conventional models and laboratory measurements. The WCEMIT facilitated new measurement techniques for purposes of whole core analysis. Also, that apparatus was utilized to measure the dielectric and frequency dispersive properties of pyrite-bearing and graphite-bearing samples. The two EM forward models enabled conventional petrophysical interpretation of whole core measurements and estimation of the directional effective electrical conductivity and dielectric permittivity of pyrite-bearing and graphite-bearing samples. The mechanistic electrochemical model allowed the simulation of petrophysical cases for which standard electromagnetic mixing laws become invalid due to the effects of interfacial polarization of clay particles and conductive minerals. This simulation work emphasized situations where conventional interpretation of subsurface galvanic resistivity, EM induction, and EM propagation logging measurements could not provide accurate petrophysical assessments.

The second chapter of this dissertation introduced the new laboratory apparatus capable of high-resolution multi-frequency complex conductivity tensor measurements on whole core samples and continuous-feed cylindrical volumes in the EM induction (EMI) frequency range of 10 kHz to 300 kHz. The apparatus is primarily a non-invasive and non-contact measurement technique for examining whole core samples in their as-received and re-saturated state. The COMSOL-based finite-element (FE) EM forward model and a MATLAB-based semi-analytic (SA) EM forward model of the developed tool response

were validated. The semi-analytic and finite-element EM forward model predictions were used to calibrate the complex impedance response of the nine transmitter-receiver couplings of the WCEMIT to whole core samples.

In Chapter 3, the WCEMIT was used to measure the multi-frequency inductive-complex electrical conductivity tensor of whole core samples of various rock facies. An inversion scheme was invoked to processes these measurements to estimate the electrical properties of natural and synthetic whole core samples in the EM induction frequency range of 10 kHz to 300 kHz. The Archie's equation, laminated sand-shale model, tensor resistivity model, and Maxwell-Garnett effective medium model were successfully implemented to estimate petrophysically consistent electrical properties of the whole core samples. The effects of large dielectric permittivity, permittivity anisotropy, dielectric loss factor, and frequency dispersive dielectric properties on the WCEMIT measurements were simulated using the semi-analytic EM forward model. Notably, a new whole core logging method that can improve the resistivity characterization of turbiditic and multi-layered formations was numerically investigated using the finite-element EM forward model coupled with a multi-layer resistivity inversion scheme.

Following that, I investigated the effects of the PPIP phenomena exhibited by pyrite-bearing and graphite-bearing samples on their directional and frequency dispersive electrical properties. To that end, I first used the new laboratory apparatus to measure the directional multifrequency EM response of 4-inch-diameter, 2-feet-long glass-bead packs containing uniformly distributed pyrite and graphite inclusions. The semi-analytic EM forward model was then implemented to estimate the effective electrical conductivity and dielectric permittivity of the conductive-mineral-bearing glass-bead packs. The interpretation work in this chapter confirms that the conductive-mineral-bearing samples

exhibit significant frequency dispersion of electrical conductivity and dielectric permittivity, large values of effective relative permittivity, and large alteration in the effective conductivity due to the variations in volume content and size of conductive mineral inclusions.

In the final part of the dissertation that includes Chapters 5 and 6, I developed a mechanistic model to quantify the complex-valued effective electrical conductivity response of geomaterials containing electrically conductive mineral inclusions, such as pyrite and magnetite, uniformly distributed in a fluid-filled, porous matrix made of non-conductive grains possessing surface conductance, such as silica grains, clay particles, and clay-sized grains. Our model predictions are in good agreement with laboratory measurements of multi-frequency complex-valued electrical conductivity, relaxation time, and chargeability of mixtures containing electrically conductive inclusions. Using the mechanistic model, I evaluated the dependence of effective complex-valued conductivity of geological mixtures containing conductive mineral inclusions and clay particles on (a) operating frequency, (b) conductivity of host medium, and (c) material, size, and shape of inclusion phase. The mechanistic model predictions identified the petrophysical conditions that give rise to significant differences of the effective conductivity and effective relative permittivity of conductive-inclusion-bearing geomaterials from the conductivity and relative permittivity, respectively, of the inclusion-free hydrocarbon-bearing host.

7.2 CONCLUSIONS

The conclusions are listed below according to the main objectives of this dissertation.

7.2.1 Laboratory Apparatus for Multi-Frequency Inductive-Complex Conductivity Tensor Measurements

i. The FE model predictions for the *zz*-coupling and *yy*-coupling of the WCEMIT agreed with Maxwell-Garnett effective medium model predictions of the effective conductivity of 1-S/m-conductivity host containing randomly distributed spherical inclusions of conductivity in the range of 0.1 S/m to 100 S/m and radius in the range of 0.35 inches to 0.6 inches.

ii. The real part of the induced voltage response for the *zz*-coupling and *yy*-coupling of the WCEMIT was linearly related to the conductivity of the whole core sample for conductivity values in the range of 0.01 S/m to 10 S/m.

iii. The computed values of geometrical factors of the *zz*-coupling and *yy*-coupling of the WCEMIT at 58.5 kHz were similar to those obtained by Kickhofel et al. (2010) at 51.28 kHz.

iv. The SA model predictions agreed with the FE model predictions of the *zz*-coupling and *yy*-coupling response for various values of conductivity, dielectric permittivity, dielectric loss factor, and operating frequencies in the range of 10 kHz to 300 kHz.

v. Tilted test loop (TTL) method was used to calibrate all the nine couplings of the WCEMIT at seven discrete frequencies, namely 19.6, 31.2, 41.5, 58.5, 87.6, 150, or 261 kHz.

7.2.2 Petrophysical Applications of Multi-frequency Inductive-Complex Conductivity Tensor Measurements on Whole Core Samples

i. The SA model predictions of the WCEMIT responses of all nine transmitter-receiver couplings to the tilted test loop were used to validate the calibrated WCEMIT measurements.

ii. The calibrated WCEMIT measurements were successfully validated by comparing the measured values with the SA model predictions of all nine transmitter-receiver coupling responses to synthetic bi-laminar dipping whole cores oriented at any given azimuth for various operating frequencies.

iii. Laboratory investigation corroborated the use of the WCEMIT for estimating the true host conductivity, Archie's porosity exponent, and formation factor of isotropic whole cores.

iv. The WCEMIT was applied to quantify the bed conductivity, horizontal conductivity, anisotropy ratio, dip, and azimuth of bilaminar whole core samples.

v. The WCEMIT was also used to estimate the host conductivity of vuggy whole cores containing uniformly distributed non-conductive vugs for various volume fractions of non-conductive vugs.

vi. Numerical investigation using the SA model confirmed that the WCEMIT response is suitable for measuring the effects of dielectric properties, such as permittivity, dielectric loss factor, and permittivity anisotropy, and dielectric dispersion characteristics, denoted by the parameters of the Cole-Cole model, arising due to the interfacial polarization phenomena.

vii. A fast inversion scheme for a newly proposed whole core logging measurement was applied to estimate the layer-by-layer conductivity of 24-inch-long whole cores at a vertical resolution of 1 inch and at 58.5 kHz. This method successfully identified cemented streaks in a whole core containing randomly distributed sand, shale, and cemented layers of minimum 1-inch thickness.

7.2.3 Effective Electrical Conductivity and Dielectric Permittivity of Samples Containing Disseminated Mineral Inclusions

i. Glass-bead packs containing homogeneously dispersed pyrite and/or graphite inclusions exhibited frequency dispersion of their R- and X-signal responses due to the interfacial polarization of electrically conductive mineral inclusions.

ii. The R-signal response of conductive-mineral-bearing packs were significantly different from that of the inclusion-free glass-bead packs; consequently, accurate resistivity interpretation methods for samples containing pyrite or graphite inclusions must account for the effects of interfacial polarization.

iii. The effective conductivity and effective relative permittivity of the conductive-mineral-bearing glass-bead packs were successfully estimated using the SA model.

iv. The estimated values of the effective relative permittivity were in the range of 10^3 to 10^4 for the pyrite-bearing glass-bead packs, and were in the range of 10^4 to 10^6 for the graphite-bearing glass-bead packs.

v. The effective electrical conductivity and dielectric relative permittivity of the conductive-mineral-bearing packs were strongly dependent on the operating frequency and mineral type, volume fraction, and size of mineral inclusions.

vi. The multi-frequency effective conductivity and relative permittivity of graphite-bearing packs were significantly different from those of the pyrite-bearing packs due to the large difference in the diffusion coefficients of charge carriers, bulk conductivity values, and shapes of pyrite and graphite inclusions.

vii. The packs containing homogeneously dispersed conductive inclusions exhibited conductivity anisotropy ratio, in the range of 1 to 1.7, and permittivity anisotropy ratio, in the range of 1.1 to 2.8. Consequently, resistivity interpretation methods for formations containing uniformly dispersed pyrite or graphite inclusions must

account for the effects of effective conductivity and effective permittivity anisotropy due to interfacial polarization of the inclusion phase.

viii. The packs containing alternating layers of different volume fraction of conductive mineral inclusions had significantly different effective conductivity and relative permittivity compared to those of packs containing homogeneously distributed mineral inclusions of the same mineral type, size, total volume fraction, and shape.

ix. Accurate resistivity interpretation in formations containing conductive minerals will require accurate knowledge of shape, size, mineral type, conductivity, and distribution of the inclusion phase.

7.2.4 Mechanistic Model of Interfacial Polarization of Disseminated Conductive Minerals in Absence of Redox-Active Species

i. Dipole moment of an inclusion was obtained by solving Poisson-Nernst-Planck's (PNP) equations of dilute solution theory. The calculated dipole moment was coupled with a consistent Maxwell-Garnett effective-medium formulation to determine the effective complex-valued electrical conductivity of the geomaterial containing conductive mineral inclusions, clay particles, and clay-sized grains.

ii. The PPIP-SCAIP model was successfully validated in the frequency range from 100 Hz to 100 MHz for a characteristic length of the inclusion phase in the range of 0.1 μm to 1 mm.

iii. The chargeability of geomaterials depend only on the volumetric content of electrically conductive inclusions for host conductivity close to or higher than 0.01 S/m.

iv. The relaxation time associated with polarization of conductive spherical inclusions was linearly related to the radius of inclusions and is inversely related to the diffusion coefficients of charge carriers in the host and those in the inclusion phase.

v. The estimated values of diffusion coefficient of charge carriers in the electrically conductive inclusion phase were consistent with the electrical mobility of *p*- and *n*-charge carriers in the inclusion material.

vi. High-frequency effective conductivity increases while the low-frequency effective conductivity decreases with an increase in the concentration of metallic inclusions that give rise to the PPIP phenomena.

7.2.5 Effects of Disseminated Conductive Mineral Inclusions on Subsurface Electrical Measurements

i. Electrical measurements in formations containing uniformly distributed conductive inclusions are highly sensitive to the variations in volume fraction, material, characteristic length, and shape of the inclusion phase and conductivity of the pore-filling electrolyte.

ii. The low-frequency effective conductivity of a geomaterial containing as low as 5% volume fraction of disseminated conductive inclusions was -30% to +100% more than the host conductivity for the operating frequencies in the range of 100 Hz to 100 kHz.

iii. The high-frequency effective relative permittivity of a geomaterial containing as low as 5% volume fraction of disseminated conductive inclusions was +90% to -10% more than the host relative permittivity for the operating frequencies in the range of 100 kHz to 10 MHz.

iv. Geomaterials containing sheet-like inclusions exhibited large frequency dispersion of the effective conductivity in the operating frequency range of galvanic resistivity logging tools. These geomaterials generally exhibited exceedingly large galvanic resistivity measurements compared to the true formation resistivity.

v. EM induction and EM propagation logging measurements were less sensitive to the variations in properties of sheet-like inclusions and highly sensitive to the variations in properties of rod-like and spherical inclusions.

vi. Galvanic resistivity measurements were less sensitive to the variations in properties of rod-like and spherical inclusions and highly sensitive to the variations in properties of sheet-like inclusions.

vii. EM propagation measurements at frequencies close to and higher than 100 MHz were not susceptible to the effects of PPIP phenomena, and could be analyzed using a consistent the effective medium formulations.

viii. The PPIP phenomena generally led to large alteration of EM measurements, highly dispersive complex-valued conductivity response, and high sensitivity of EM measurements to the properties of inclusions and conductivity of pore-filling electrolyte.

7.3 RECOMMENDATIONS FOR FUTURE WORK

The following is a list of recommendations that could advance the research topics documented in this dissertation:

i. The WCEMIT tool operated at seven discrete frequencies. The critical frequency associated with the frequency dispersion phenomena cannot be accurately measured when performing discrete frequency measurements. I recommend re-designing the transmitter resonance circuit to allow a continuous frequency

excitation of the transmitter coils in the EM induction frequency range. In that case, a new method will be required for calibrating all the nine transmitter-receiver coupling responses for the continuous frequency sweep.

ii. The WCEMIT tool operated in the frequency range of 10 kHz to 300 kHz. The transmitter coils should be re-designed to allow a broader frequency range of operation to accommodate the typical frequency of operation of subsurface galvanic resistivity and EM propagation tools. In doing so, whole core measurements using this improved apparatus can be correlated with the subsurface galvanic resistivity and EM propagation tool measurements.

iii. A new apparatus that is designed similar to the WCEMIT but of smaller dimensions needs to be developed to inductively measure the EM response of core plugs.

iv. The FE model generated accurate predictions of the WCEMIT response to dipping, isotropic whole cores oriented at any azimuth angle. However, the FE model requires close to one hour to calculate the response of one transmitter-receiver coupling. Faster 3D finite-element EM forward model should be developed to perform reliable inversion of the WCEMIT measurements.

v. SA model and FE model should be improved to predict the effects of variation in magnetic permeability of whole core samples. The presence of certain mineral inclusions leads to effective magnetic permeability of geomaterials to be more than 1.

vi. A laboratory or a numerical method is required to ascertain the range of dielectric permittivity and dielectric loss factor of the whole core samples that can be reliably simulated using the two EM forward models.

vii. Existing whole core handling procedure requires the whole cores to be slabbed at the core laboratories before conducting any laboratory measurements. This prevented me from obtaining full-diameter as-received whole core samples for petrophysical investigation based on the WCEMIT. Semi-analytic and finite-element EM forward models of the WCEMIT response to slabbed whole core samples should be developed to facilitate WCEMIT-based core analysis in absence of full-diameter whole core.

viii. Most of the laboratories lack methods to clean and re-saturate whole core samples. Also, there is no method to ensure multi-phase fluid injection in a whole core to saturate a whole core sample at different water saturations. New laboratory methods need to be developed to overcome these limitations to extend the WCEMIT applications to the estimation of water saturation exponent.

ix. Capabilities to perform WCEMIT measurements on whole core samples at reservoir pressure and temperature needs to be developed.

x. Applications of the WCEMIT and the effective medium formulation developed in Section 3.3.5 should be tested on actual whole core samples from vuggy carbonate formations to understand the accuracy of prediction of host conductivity in the presence of conductive/non-conductive vugs.

xi. Core-well log integration methods should be developed for layered and thinly-laminated formations to improve the accuracy of estimates of sand resistivity and sand fraction in such subsurface formations. To that end, the WCEMIT could enable high resolution measurements on whole core samples for determining the representative shale resistivity, identify cemented streaks, and quantify sand fraction.

xii. Controlled WCEMIT measurements should be performed on synthetic whole core samples made of various materials of known dielectric dispersion parameters. In doing so, the frequency dispersion of R- and X-signal responses of the WCEMIT to those synthetic samples can be related to the dielectric dispersion parameters of the materials of those synthetic samples. Similarly, controlled WCEMIT measurements should be performed on synthetic whole core samples made of various materials of known dielectric permittivity and dielectric loss factor. In doing so, the frequency dispersion of R- and X-signal responses of the WCEMIT to those synthetic samples can be related to the dielectric permittivity and dielectric loss factor of the materials of those synthetic samples

xiii. WCEMIT measurements should be performed on whole core samples from mature shale gas formations that contain graphitic precursors due to the over-maturation of the kerogen. In doing so, I can develop a better understanding of the relation between kerogen maturity, electrical properties of graphitic precursors, and EM induction multi-frequency response. Subsequently, a new resistivity interpretation technique for subsurface EM induction measurements in mature shale gas formations can be developed to assess the maturity of the formation and to correct the alterations in estimation of conductivity and permittivity due to the presence of conductive graphitic precursors.

xiv. Extensive study is required to describe and quantify the effects of salinity on the WCEMIT response to brine-saturated conductive-mineral-bearing whole core samples.

xv. Extensive study is required to describe and quantify the effects of material of the inclusion phase on the WCEMIT response to brine-saturated conductive-mineral-bearing whole core samples.

xvi. An inversion scheme should be coupled with the PPIP-SCAIP model to perform joint-interpretation of subsurface galvanic resistivity, EM induction, and EM propagation tool measurements.

xvii. PPIP-SCAIP model needs to be improved to account for the (a) randomly oriented conductive mineral inclusions, (b) redox-active host-inclusion interfaces, (c) ellipsoidal conductive mineral inclusions, clay particles, silica grains, and clay-sized grains, (d) high volume fraction of conductive mineral inclusions, and (e) multi-phase fluid distribution.

xviii. PPIP-SCAIP model should be improved to account for the (a) mutual EM interactions between conductive mineral inclusions, clay particles, silica grains, and clay-sized grains and (b) reduction in surface area of host-inclusion interfaces due to the contact of neighboring grains.

xix. PPIP-SCAIP model should be improved to account for the (a) high concentration of charge carriers in the pore-filling electrolyte, (b) percolation length of the pore structure, (c) percolation length of the inclusion phase, (d) presence of more than two charge carriers in the pore-filling electrolyte, (e) variation in EM field strength with the distance from source, and (f) presence of time varying magnetic field in the formation.

xx. PPIP-SCAIP model should be coupled with Maxwell-Wagner polarization model, orientation polarization model, and concentration polarization model.

7.4 RECOMMENDATIONS FOR BEST PRACTICES

The following is a list of recommendations that needs to be adopted as best practices:

i. Interpretation of subsurface galvanic resistivity, EM induction, and EM propagation measurements in conductive-mineral-bearing and clay-rich formations should always account for effects of interfacial polarization of conductive minerals, clay particles, and clay-sized grains.

ii. Petrophysical interpretation methodology in formations susceptible to large interfacial polarization effects should implement joint interpretation of subsurface galvanic resistivity, EM induction, and EM propagation measurements.

iii. Existing resistivity and dielectric interpretation methods in conductive-mineral-bearing and clay-rich formations should first estimate effective electrical properties using the tool model, then PPIP-SCAIP-type mechanistic model should be used to process the estimated effective electrical properties, and finally Archie-type water saturation equations applied to obtain water saturation in the formation.

iv. Commercial laboratory apparatus capable of electrical measurements on whole core samples should be used routinely during for purposes of improved core-well log integration. Whole core logging of whole core samples from turbiditic and other thinly-laminated formations should be performed for purposes of identifying cemented streaks, obtaining electrical properties of representative shale, and accurate assessment of sand fraction.

v. Inversion of WCEMIT-type measurements on non-dipping whole cores to obtain effective electrical properties should be based on the semi-analytic EM forward model instead of finite-element EM forward model.

Appendix A: Sheet-like inclusion in an electrolytic host

An infinite sheet of finite thickness, equal to 2*a*, exhibits dipolarizability along the thickness of the sheet, while dipolarizability is negligible along its length and width. Such an inclusion identifies a lamination or thin bed. In order to compute the dipolarizability of the representative volume (Figure 5.3) comprising an infinite sheet-like inclusion in an electrolytic host, equation 17 in Chapter 5 is expressed in Cartesian coordinates as

$$\frac{\partial^2 d_j}{\partial x^2} = \gamma_j^2 d_j, \tag{A1}$$

where *x* is the perpendicular distance from the plane of symmetry of the sheet that divides the sheet into two volumes of equal thickness, and *j* denotes the phase, such that *i* identifies inclusion and *h* identifies host. A general solution (Morse and Feshbach, 1953) to the above differential equation is

$$d_j(x) = \sum_{m=1}^{\infty} [C_{m,j} \mathrm{e}^{n\gamma_j x} + D_{m,j} \mathrm{e}^{-n\gamma_j x}], \tag{A2}$$

where *m* is an integer and $C_{m,j}$ and $D_{m,j}$ are unknown complex-valued coefficients of the general solution of equation A1. To simplify the analytical derivation of our model, I assume *m*=1. Also, by implementing the condition that $d_j(x)$ should be finite at *r*=0 and *r*= ∞, I obtain two independent particular solutions of $d_j(x)$ for the host, subscript *h*, and inclusion, subscript *i*, phases that can be expressed as

$$d_i(x) = 2C_i \sinh(\gamma_i x), \tag{A3}$$

and

$$d_h(x) = D_h \mathrm{e}^{-\gamma_h x}, \tag{A4}$$

where C_i and D_h are unknown complex-valued coefficients of the particular solution in the inclusion phase and host medium, respectively, obtained from equation A2.

Assuming a separable solution for $\vartheta_\mathrm{j}(\mathrm{x})$, equation 19 can now be expressed in Cartesian coordinates as

$$\Delta\vartheta_j = \frac{\partial^2 \vartheta_j}{\partial x^2} = 0. \tag{A5}$$

A general solution of the above differential equation can be expressed, using m=0 for the standing wave solution, as

$$\vartheta_j(x) = A_{0,j}x + B_{0,j}, \tag{A6}$$

where $A_{0,j}$ and $B_{0,j}$ are unknown complex-valued coefficients of the general solution of the differential equation A5. Now, equation A6 can be rewritten using equation 20 as

$$\varphi_j(x) = A_{0,j}x + B_{0,j} - \frac{\mathrm{q}d_j(x)}{\gamma_j^2 \varepsilon_j}. \tag{A7}$$

The standing wave representation of equation A7 for the inclusion phase, using equation A3, is

$$\varphi_i(x) = A_i x - \frac{2\mathrm{q}C_i \sinh(\gamma_i x)}{\gamma_i^2 \varepsilon_i}, \tag{A8}$$

where A_i is an unknown complex-valued coefficient of the particular solution in the inclusion phase obtained from equation A7. Similarly, the standing wave representation of equation A7 for the host medium, using equation A4, is

$$\varphi_h(x) = B_h - \frac{\mathrm{q}D_h \mathrm{e}^{-\gamma_h x}}{\gamma_h^2 \varepsilon_h}, \tag{A9}$$

where B_h is an unknown complex-valued coefficient of the particular solution in the host obtained from equation A7.

Using boundary condition (a), equations A9 and A8 can be equated on the surface of the sheet at $x=a$. I obtain the following equation:

$$-E_0 a + B_h + E_h D_h = A_i a + F_i C_i, \tag{A10}$$

where E_0 is the amplitude of the externally applied electric field,

$$E_h = -\frac{\mathrm{q}\mathrm{e}^{-\gamma_h a}}{\gamma_h^2 \varepsilon_h},$$

and

$$F_i = -\frac{2\mathrm{q}\sinh(\gamma_i a)}{\gamma_i^2 \varepsilon_i}.$$

The equation obtained using boundary condition (b) at the surface of the sheet can be abbreviated as

$$\varepsilon_h(-E_0 + G_h D_h) = \varepsilon_i(A_i + H_i C_i), \tag{A11}$$

where

$$G_h = \frac{\mathrm{q}\mathrm{e}^{-\gamma_h a}}{\gamma_h \varepsilon_h},$$

and

$$H_i = -\frac{2\mathrm{q}\cosh(\gamma_i a)}{\gamma_i \varepsilon_i}.$$

The equation obtained using boundary condition (c) at the outer surface of the sheet in the host medium can be abbreviated as

$$D_h = -\frac{\sigma_h E_0}{\mathrm{i}\omega G_h \varepsilon_h}. \tag{A12}$$

On the other hand, the equation obtained using boundary condition (c) at the inner surface of the sheet in the inclusion medium can be abbreviated as

$$A_i = \mathrm{i}\omega H_i C_i \frac{\varepsilon_i}{\sigma_i}. \tag{A13}$$

When solving equations A10, A11, A12, and A13, I obtain the dipolarizability of the representative volume comprising a sheet-like inclusion in an electrolytic host as

$$f(\omega) = \frac{B_h}{E_0 a} = \left(1 - \frac{K_h}{K_i}\right) + \frac{\mathrm{i}}{\omega a}\left[\frac{K_h}{K_i}\frac{\sigma_i}{\varepsilon_i}\frac{F_i}{H_i} - \frac{\sigma_h}{\varepsilon_h}\frac{E_h}{G_h}\right]. \tag{A14}$$

Appendix B: Rod-like inclusion in an electrolytic host

A long rod of radius equal to *a*, such that its length $\gg a$, exhibits dipolarizability only in the radial direction, while dipolarizability is negligible in the axial direction. Such an inclusion identifies a pore-filling mineralization. In order to compute the dipolarizability of the representative volume (Figure 5.2) comprising a rod-like inclusion in an electrolytic host, equation 17 in Chapter 5 can be expressed in cylindrical coordinates, assuming axial symmetry and a separable solution for $d_j(r,\theta) = R_j(r)T_j(\theta)$, as

$$\frac{r}{R_j}\frac{\partial R_j}{\partial r} + \frac{r^2}{R_j}\frac{\partial^2 R_j}{\partial r^2} - \gamma_j^2 r^2 + \frac{1}{T_j}\frac{\partial^2 T_j}{\partial \theta^2} = 0, \tag{B1}$$

and

$$\frac{\partial^2 T_j}{\partial \theta^2} = -m^2 T_j, \tag{B2}$$

where *m* is an integer for standing wave solution (Morse and Feshbach, 1953), and *j* denotes the phase such that *i* identifies inclusion and *h* identifies host. A standing wave solution (Weisstein, 2015c) to the above differential equation is

$$T_j = \sum_{m=1}^{\infty} A_{m,j}\, cos(m\theta) + B_{m,j}\, sin(m\theta), \tag{B3}$$

where $A_{m,j}$ and $B_{m,j}$ are unknown complex-valued coefficients of the general solution of the differential equation B2. Using equation B2 in equation B1, I obtain

$$\frac{\partial^2 R_j}{\partial r^2} + \frac{1}{r}\frac{\partial R_j}{\partial r} - (\frac{m^2}{r^2} + \gamma_j^2)R_j = 0. \tag{B4}$$

A standing wave solution (Weisstein, 2015c) to the differential equation B4 is

$$R_j = \sum_{m=1}^{\infty} C_{m,j}\mathrm{I}_m(r\gamma_j) + D_{m,j}\mathrm{K}_m(r\gamma_j), \tag{B5}$$

where I_m and K_m are associated modified Bessel function of the first and second kind (Weisstein, 2015c), respectively, of *m*-th order and $C_{m,j}$ and $D_{m,j}$ are unknown complex-valued coefficients of the general solution of the differential equation B4. To simplify the analytical derivation of our model, I assume *m*=1 and $B_{m,j} = 0$, which reduces equations B5 and B3 to

$$R_j = C_j\mathrm{I}_1\left(r\gamma_j\right) + D_j\mathrm{K}_1\left(r\gamma_j\right), \tag{B6}$$

and

$$T_j = A_j\cos(\theta), \tag{B7}$$

respectively, where C_j, D_j, and A_j and are unknown complex-valued coefficients of the particular solution obtained from equations B3 and B5. Now, the general representation of $d_j(r,\theta)$ can be written, by combining equations B6 and B7, as

$$d_j(r,\theta) = [C_j\mathrm{I}_1(r\gamma_j) + D_j\mathrm{K}_1(r\gamma_j)]\cos(\theta). \tag{B8}$$

Using the condition that $d_j(r,\theta)$ should be finite at *r*=0 and *r*=∞, I obtain two independent particular solutions of $d_j(x)$ for the host, subscript *h*, and inclusion, subscript *i*, phases that can be represented as

$$d_i(r,\theta) = C_i\mathrm{I}_1(r\gamma_i)\cos(\theta), \tag{B9}$$

and

$$d_h(r,\theta) = D_h\mathrm{K}_1(r\gamma_h)\cos(\theta), \tag{B10}$$

where C_i and D_h are unknown complex-valued coefficients of the particular solution in the inclusion phase and host medium, respectively, obtained from equation B8.

Assuming a long rod and a separable solution for $\vartheta_j(r,\theta,z)$, equation 19 can be expressed in cylindrical coordinates as

$$\Delta\vartheta_j = \frac{1}{r}\frac{\partial}{\partial r}\left(r\frac{\partial\vartheta_j}{\partial r}\right) + \frac{1}{r^2}\frac{\partial^2\vartheta_j}{\partial\theta^2} + \frac{\partial^2\vartheta_j}{\partial z^2} = 0. \tag{B11}$$

Assuming axial symmetry, a general solution (Hogg, 2001) to the above partial differential equation can be expressed as

$$\vartheta_j(r,\theta) = A_{0,j} + B_{0,j}\ln(r) + \sum_{n=1}^{\infty}\left[A_{n,j}r^n + B_{n,j}r^{-n}\right]\left[E_{n,j}\cos(n\theta) + F_{n,j}\sin(n\theta)\right], \tag{B12}$$

where n is an integer and $A_{n,j}$, $B_{n,j}$, $E_{n,j}$, and $F_{n,j}$ are unknown complex-valued coefficients of the general solution of the partial differential equation B11. For analytical modeling purposes of our model, I assume n=1, $F_{n,j} = 0$, $A_{0,j} = 0$, and $B_{0,j} = 0$ to obtain an alternate representation of equation B12 as

$$\vartheta_j(r,\theta) = \left[A_{1,j}r^1 + B_{1,j}r^{-1}\right]\cos(\theta), \tag{B13}$$

which can be rewritten using equation 20 as

$$\varphi_j(r,\theta) = \left[A_{1,j}r + B_{1,j}r^{-1}\right]\cos(\theta) - \frac{\mathrm{q}d_j(r,\theta)}{\gamma_j^2\varepsilon_j}. \tag{B14}$$

A standing-wave representation of equation B14 for the inclusion phase, using equation B9, is

$$\varphi_i(r,\theta) = A_i r\cos(\theta) - \frac{\mathrm{q}C_i\mathrm{I}_1(r\gamma_i)\cos(\theta)}{\gamma_i^2\varepsilon_i}, \tag{B15}$$

where A_i is unknown complex-valued coefficient of the particular solution in the inclusion phase obtained from equation B14. A standing-wave representation of equation B14 for the host phase, using equation B10, is

$$\varphi_h(r,\theta) = [-E_0 r + B_h r^{-1}]\cos(\theta) - \frac{\mathrm{q}D_h \mathrm{K}_1(r\gamma_h)\cos(\theta)}{\gamma_h^2 \varepsilon_h}, \tag{B16}$$

where B_h is an unknown complex-valued coefficient of the particular solution in the host obtained from equation B14 and E_0 is the amplitude of the externally applied electric field.

Using boundary condition (a), equations B16 and B15 can be equated on the surface of the long rod of radius equal to *a*. The resulting equation can be abbreviated as

$$-E_0 a + \frac{B_h}{a} + E_h D_h = A_i a + F_i C_i, \tag{B17}$$

where

$$E_h = -\frac{\mathrm{q}\mathrm{K}_1(a\gamma_h)}{\gamma_h^2 \varepsilon_h},$$

and

$$F_i = -\frac{\mathrm{q}\mathrm{I}_1(a\gamma_i)}{\gamma_i^2 \varepsilon_i}.$$

The equation obtained using boundary condition (b) at the surface of the long rod can be abbreviated as

$$\varepsilon_h\left(E_0 + \frac{B_h}{a^2} + G_h D_h\right) = \varepsilon_i(A_i + H_i C_i), \tag{B18}$$

where

$$G_h = -\frac{\mathrm{q}}{\gamma_h \varepsilon_h}\left[-\mathrm{K}_0(a\gamma_h) - \frac{\mathrm{K}_1(a\gamma_h)}{\gamma_h a}\right],$$

and

$$H_i = -\frac{\mathrm{q}}{\gamma_i \varepsilon_i}\left[\mathrm{I}_0(a\gamma_i) - \frac{\mathrm{I}_1(a\gamma_i)}{\gamma_i a}\right].$$

On the other hand, the equation obtained using boundary condition (c) at the outer surface of the long rod in the host medium can be abbreviated as

$$B_h = -a^2\left(E_0 + \mathrm{i}\omega G_h D_h \frac{\varepsilon_h}{\sigma_h}\right). \tag{B19}$$

The equation obtained using equation boundary condition (c) at the inner surface of the rod in the inclusion medium can be abbreviated as

$$A_i = \mathrm{i}\omega H_i C_i \frac{\varepsilon_i}{\sigma_i}. \tag{B20}$$

When solving equations B17, B18, B19, and B20, I obtain the dipolarizability of the representative volume comprising a rod-like inclusion in an electrolytic host as

$$f(\omega) = \frac{B_h}{E_0 a^2} = -1 + \frac{2\mathrm{i}\omega}{\left[\frac{1}{a}\frac{K_h}{K_i}\frac{\sigma_i}{\varepsilon_i}\frac{F_i}{H_i} - \frac{1}{a}\frac{\sigma_h}{\varepsilon_h}\frac{E_h}{G_h} + \mathrm{i}\omega\left(\frac{K_h}{K_i} + 1\right)\right]}. \tag{B21}$$

Appendix C: Spherical inclusion in an electrolytic host

A sphere of radius equal to *a* exhibits dipolarizability in the radial direction. Such an inclusion identifies a grain or vug. In order to compute the dipolarizability of the representative volume (Figure 5.2) comprising a spherical inclusion in an electrolytic host, equation 17 in Chapter 5 can be expressed in spherical coordinates, assuming azimuthal symmetry, axial symmetry, and a separable solution (Young, 2009) for $d_j(r,\theta) = R_j(r)T_j(\theta)$ as

$$\frac{1}{R_j}\frac{\partial}{\partial r}\left(r^2\frac{\partial R_j}{\partial r}\right) - \gamma_j^2 r^2 + \frac{1}{T_j\sin(\theta)}\frac{\partial}{\partial\theta}\left(\frac{\sin(\theta)\,\partial T_j}{\partial\theta}\right) = 0, \tag{C1}$$

and

$$\frac{1}{\sin(\theta)}\frac{\partial}{\partial\theta}\left(\frac{\sin(\theta)\,\partial T_j}{\partial\theta}\right) = -n(n+1)T_j, \tag{C2}$$

where *n* is an integer for the standing wave solution, and *j* denotes the phase such that *i* identifies inclusion and *h* identifies host. A standing-wave solution (Young, 2009) to the above differential equation is

$$T_j = \sum_{n=1}^{\infty} A_{n,j}\mathrm{P}_n^0(\cos(\theta)) + B_{n,j}\,\mathrm{Q}_n^0(\cos(\theta)), \tag{C3}$$

where P_n^0 and Q_n^0 are associated Legendre functions of the first and second kind (Weisstein, 2015a), respectively, of *n*-th order and $A_{n,j}$ and $B_{n,j}$ are unknown complex-valued coefficients of the general solution of the partial differential equation C2. Using equation C2 in equation C1, I obtain

$$\frac{\partial}{\partial r}\left(r^2\frac{\partial R_j}{\partial r}\right) - \left[\gamma_j^2 r^2 + n(n+1)\right]R_j = 0. \qquad (C4)$$

A standing-wave solution to the above differential equation is

$$R_j = \sum_{n=1}^{\infty} C_{n,j}\mathrm{i}_n(r\gamma_j) + D_{n,j}\mathrm{k}_n(r\gamma_j), \qquad (C5)$$

where n is an integer for the standing-wave solution (Young, 2009), i_n and k_n are the modified spherical Bessel function of the first and second kind (Weisstein, 2015b), respectively, of n-th order and $C_{n,j}$ and $D_{n,j}$ are unknown complex-valued coefficients of the general solution of the partial differential equation C4; i_n and k_n can be expressed in terms of modified Bessel function of the first and second kind, respectively, as

$$i_n(r\gamma_j) = \sqrt{\frac{\pi}{2r\gamma_j}}\mathrm{I}_{n+\frac{1}{2}}(r\gamma_j),$$

and

$$k_n(r\gamma_j) = \sqrt{\frac{2}{\pi r\gamma_j}}\mathrm{K}_{n+\frac{1}{2}}(r\gamma_j),$$

where $\mathrm{I}_{n+\frac{1}{2}}$ and $\mathrm{K}_{n+\frac{1}{2}}$ are the modified Bessel function of the first and second kind, respectively, of n-th order. To simplify the analytical derivation of our model, I reduce the series to a single term and use n=1 and $B_{n,j} = 0$ by taking into account the following symmetries of the charge density: (1) axial symmetry, (2) anti-symmetry with respect to θ, and (3) dipolar nature of the externally applied field. This reduces equations C5 and C3 to

$$R_j = [C_j \sqrt{\frac{\pi}{2r\gamma_j}} I_{\frac{3}{2}}(r\gamma_j) + D_j \sqrt{\frac{2}{\pi r\gamma_j}} K_{\frac{3}{2}}(r\gamma_j)], \quad \text{(C6)}$$

and

$$T_j = A_j \cos(\theta), \quad \text{(C7)}$$

respectively, where C_j, D_j, and A_j and are unknown complex-valued coefficients of the particular solution obtained from equations C3 and C5. The general representation of $d_j(r,\theta)$ can now be written, by combining equations C6 and C7, as

$$d_j(r,\theta) = [C_j i_1(ir\gamma_j) + D_j k_1(ir\gamma_j)] \cos(\theta). \quad \text{(C8)}$$

Using the condition that $d_j(r,\theta)$ should be finite at r=0 and r=∞, I obtain two independent particular solutions of $d_j(x)$ for the host, subscript h, and inclusion, subscript i, phases that can be represented as

$$d_i(r,\theta) = B_i \mathrm{i}_1(r\gamma_i) \cos(\theta),$$

or

$$d_i(r,\theta) = B_i [\frac{\cosh(r\gamma_i)}{r\gamma_i} - \frac{\sinh(r\gamma_i)}{r\gamma_i}] \cos(\theta), \quad \text{(C9)}$$

and

$$d_h(r,\theta) = B_h \mathrm{k}_1(r\gamma_h) \cos(\theta),$$

or

$$d_h(r,\theta) = B_h [\mathrm{e}^{-r\gamma_h} \left(\frac{1}{r\gamma_h} + \frac{1}{(r\gamma_h)^2}\right)] \cos(\theta), \quad \text{(C10)}$$

where B_i and B_h are unknown complex-valued coefficients of the particular solution in the inclusion phase and host medium, respectively, obtained from equation C8.

Assuming azimuthal symmetry and a separable solution for $\vartheta_j(r,\theta,\varphi) = R_{\epsilon j}(r)T_{\epsilon j}(\theta)$, equation 19 can be expressed in spherical coordinates as

$$\Delta\vartheta_j = \frac{1}{R_{\epsilon j}}\frac{\partial}{\partial r}\left(r^2\frac{\partial R_{\epsilon j}}{\partial r}\right) + \frac{1}{T_{\epsilon j}\sin(\theta)}\frac{\partial}{\partial\theta}\left(\frac{\sin(\theta)\,\partial T_{\epsilon j}}{\partial\theta}\right) = 0. \quad \text{(C11)}$$

Assuming axial symmetry, a general solution (Hogg, 2001) to the above partial differential equation can be expressed as

$$\vartheta_j(r,\theta) = \sum_{n=0}^{\infty}\left[A_{n,j}r^n + B_{n,j}r^{-(n+1)}\right]\left[E_{n,j}\,\mathrm{P}_n^0(\cos(n\theta)) + F_{n,j}\mathrm{Q}_n^0(\sin(n\theta))\right], \quad \text{(C12)}$$

where n is an integer and $A_{n,j}$, $B_{n,j}$, $E_{n,j}$, and $F_{n,j}$ are unknown complex-valued coefficients of the general solution of the partial differential equation C11. For analytical modeling purposes for our model, I assume n=1, $F_{n,j} = 0$, $A_{0,j} = 0$, and $C_{0,j} = 0$, as these terms do not satisfy the polar angle dependence of the model, to obtain an alternate representation of equation C12 as

$$\vartheta_j(r,\theta) = \left[A_{1,j}r^1 + C_{1,j}r^{-2}\right]\cos(\theta),$$

which can be rewritten using equation 20 as

$$\varphi_j(r,\theta) = \left[A_{1,j}r + C_{1,j}r^{-2}\right]\cos(\theta) - \frac{\mathrm{q}d_j(r,\theta)}{\gamma_j^2\varepsilon_j}. \quad \text{(C13)}$$

A standing-wave representation of equation C13 for the inclusion phase, using C9, is

$$\varphi_i(r,\theta) = A_i r\cos(\theta) - \frac{\mathrm{q}B_i}{\gamma_i^2\varepsilon_i}\left[\frac{\cosh(r\gamma_i)}{r\gamma_i} - \frac{\sinh(r\gamma_i)}{r\gamma_i}\right]\cos(\theta), \quad \text{(C14)}$$

where A_i is unknown complex-valued coefficient of the particular solution in the inclusion phase obtained from equation C13. A standing-wave representation of equation C13 for the host phase, using C10, is

$$\varphi_h(r,\theta) = [-E_0 r + C_h r^{-2}]\cos(\theta) - \frac{\mathrm{q}B_h}{\gamma_h^2 \varepsilon_h}\left[\mathrm{e}^{-r\gamma_h}\left(\frac{1}{r\gamma_h} + \frac{1}{(r\gamma_h)^2}\right)\right]\cos(\theta), \qquad \text{(C15)}$$

where C_h is unknown complex-valued coefficient of the particular solution in the host obtained from equation C13 and E_0 is the amplitude of the externally applied electric field.

Using boundary condition (a), equations C14 and C15 can be equated on the surface of the sphere of radius equal to *a*. The resulting equation can be abbreviated as

$$-E_0 a + \frac{C_h}{a^2} - E_h B_h = A_i a - F_i B_i, \qquad \text{(C16)}$$

where

$$E_h = \frac{\mathrm{q}}{\gamma_h^2 \varepsilon_h}\left[\mathrm{e}^{-a\gamma_h}\left(\frac{1}{a\gamma_h} + \frac{1}{(a\gamma_h)^2}\right)\right],$$

and

$$F_i = \frac{\mathrm{q}}{\gamma_i^2 \varepsilon_i}\left[\frac{\cosh(a\gamma_i)}{a\gamma_i} - \frac{\sinh(a\gamma_i)}{a\gamma_i}\right].$$

The equation obtained using boundary condition (b) at the surface of the sphere can be abbreviated as

$$\varepsilon_h\left(-E_0 - \frac{2C_h}{a^3} + G_h B_h\right) = \varepsilon_i(A_i + H_i B_i), \qquad \text{(C17)}$$

where

$$G_h = \frac{\mathrm{q}}{\gamma_h \varepsilon_h}\mathrm{e}^{-a\gamma_h}\left[\frac{1}{a\gamma_h} + \frac{2}{(a\gamma_h)^2} + \frac{2}{(a\gamma_h)^3}\right],$$

and

$$H_i = \frac{q}{\gamma_i \varepsilon_i}\left[\frac{2\cosh(a\gamma_i)}{(a\gamma_i)^2} - \frac{\sinh(a\gamma_i)}{a\gamma_i} - \frac{2\sinh(a\gamma_i)}{(a\gamma_i)^3}\right].$$

Similarly, the equation obtained using boundary condition (c) at the outer surface of the sphere in the host medium can be abbreviated as

$$C_h = -a^3\left(\frac{E_0}{2} + \frac{\mathrm{i}\omega G_h B_h}{2\sigma_h}\right). \tag{C18}$$

On the other hand, the equation obtained using boundary condition (c) at the inner surface of the sphere in the inclusion medium can be abbreviated as

$$A_i = \frac{\mathrm{i}\omega H_i B_i}{\sigma_i}. \tag{C19}$$

When solving equations C16, C17, C18, and C19, I obtain the dipolarizability of the representative volume comprising a spherical inclusion in an electrolytic host as

$$\frac{C_h}{E_0 a^3} = -\frac{1}{2} + \frac{3}{2}\frac{\mathrm{i}\omega}{\left[\frac{2}{a}\frac{\sigma_h}{\varepsilon_h}\frac{E_h}{G_h} - \frac{2}{a}\frac{K_h}{K_i}\frac{\sigma_i}{\varepsilon_i}\frac{F_i}{H_i} + \mathrm{i}\omega\left(\frac{2K_h}{K_i} + 1\right)\right]}. \tag{C20}$$

Symbols and Nomenclature

i	=	$\sqrt{-1}$
T	=	Absolute temperature (K)
ε_0	=	Absolute permittivity (F/m)
E_0	=	Amplitude of externally applied electric field (V/m)
ω	=	Angular frequency of externally applied electric field (rad/s)
λ	=	Anisotropy ratio
Σ	=	Apparent complex conductivity (S/m)
m	=	Archie's porosity exponent
P_m^0	=	Associated Legendre function of first kind of m-th order
Q_m^0	=	Associated Legendre function of first kind of m-th order
β	=	Azimuth angle (°)
$\mathrm{k_B}$	=	Boltzmann's constant (J/K)
C	=	Chalcopyrite
a	=	Characteristic length of inclusion phase (m)
N	=	Charge-carrier density (charge-carriers/m^3)
Z	=	Charge number of charge carrier
K	=	Complex electrical conductivity (S/m)
$\boldsymbol{\Sigma}$	=	Complex electrical conductivity tensor (S/m)
E	=	Complex representation of externally applied electric field (V/m)
I	=	Current (A)
λ_D	=	Debye screening length (m)
L	=	Depolarization factor of inclusion phase
ε	=	Dielectric permittivity (F/m)

d = Difference of variation in positive charge-carrier density and that in negative charge-carrier density (charge-carriers/m^3)

D = Diffusion coefficient of charge carriers (m^2/s)

θ = Dip angle (°)

f = Dipolarizability or dipole coefficient of an inclusion

x = Distance between two objects (m)

r = Distance along normal to interface (m)

q = Elementary charge (C)

σ = Electrical conductivity (S/m)

I = Electrical current (A)

μ = Electrical mobility ($m^2/(V.s)$)

$\boldsymbol{e}$ = Electric field (V/m)

φ = Electric potential (V)

EM = Electromagnetic

EMI = Electromagnetic Induction

e = Euler's number

FE = Finite element

G = Geometrical factor of a transmitter-receiver coupling ($m.\Omega/s$)

∇ = Gradient operator

HF = High Frequency

X = Imaginary part of the apparent complex conductivity

v = Induced voltage (V)

Δ = Laplace operator

α	=	Lichtenecker-Rother's geometrical arrangement factor
LF	=	Low Frequency
$\boldsymbol{b}$	=	Magnetic field (T)
μ	=	Magnetic permeability (H/m)
Cl	=	Mixture containing dispersed clays
G	=	Mixture containing graphite
P	=	Mixture containing pyrite
SCl	=	Mixture containing sand and dispersed clays
SP	=	Mixture containing sand and pyrite
I_m	=	Modified Bessel function of first kind of *m*-th order
K_m	=	Modified Bessel function of second kind of *m*-th order
i_m	=	Modified spherical Bessel function of first kind of *m*-th order
k_m	=	Modified spherical Bessel function of second kind of *m*-th order
P	=	Net charge (C)
PP	=	Perfectly polarized
PPIP	=	Perfectly polarized interfacial polarization
Θ	=	Phase angle (°)
a'	=	Radius of transmitter and receiver coils (m)
ε_r	=	Relative dielectric permittivity
R	=	Real part of the apparent complex conductivity
SA	=	Semi analytic
n	=	Shape factor of inclusion phase
δ	=	Skin depth (m)
Σ_s	=	Surface conductance (S)

SCAIP	=	Surface-conductance-assisted interfacial polarization
s	=	Sum of variation in positive charge-carrier density and that in negative charge-carrier density (charge-carriers/m^3)
t	=	Time (s)
Z	=	Transimpedance of a transmitter-receiver coupling (V/A)
TR	=	Transmitter-receiver
c	=	Variation in charge-carrier density (charge-carriers/m^3)
ϕ	=	Volume fraction (v/v)
k	=	Wavenumber (m^{-1})

Subscripts

app	=	Apparent
0	=	At time equal to 0 seconds
B	=	Bucking
c	=	Conductivity
eff	=	Effective
p	=	Permittivity
f	=	Free
hor	=	Horizontal
h	=	Host medium
i	=	Inclusion phase
g	=	Indices for orthogonal coils in the transmitter coil system
k	=	Indices for orthogonal coils in the receiver coil system
r	=	Relative

R	=	Receiver
s	=	static
tot	=	Total
T	=	Transmitter
t	=	True
gk	=	Transmitter-receiver coupling
j	=	Type of medium/phase, either host (h) or inclusion (i)
$\hat{n}$	=	Unit vector
vert	=	Vertical
w	=	Water

Superscripts

-	=	Negatively charged carrier
+	=	Positively charged carrier
*	=	Complex-valued

References

Abdel Aal, G. Z., E. A. Atekwana, and A. Revil, 2014, Geophysical signatures of disseminated iron minerals: A proxy for understanding subsurface biophysicochemical processes: Journal of Geophysical Research – Biogeosciences, **119**(9), 1831-1849.

Achour, M. E., M. E. Malhi, J. L. Miane, F. Carmona, and F. Lahjomri, 1999, Microwave properties of carbon black-epoxy resin composites and their simulation by means of mixture laws: Journal of Applied Polymer Science, **73**, 969-973.

Al Duba, 1983, Electrical conductivity of Colorado oil shale to 900 °C: Fuel, **62**(8), 966-972.

Al Duhailan, M. A. and S. Cumella, 2014, Niobrara maturity goes up, resistivity goes down; what's going on?: Presented at the Unconventional Resources Technology Conference.

Allan, A. M., T. Vanorio, and J. E. Dahl, 2013, Thermal maturation-induced variation of P-wave anisotropy and dry resistivity of organic-rich shale: Presented at the Annual Meeting, SEG.

Altman, R., B. Anderson, J. Rasmus, and M. G. Lüling, 2008, Dielectric effects and resistivity dispersion on induction and propagation-resistivity logs in complex volcanic lithologies: A case study: Presented at the 49th Annual Logging Symposium, SPWLA.

Anderson, B. I., T. D. Barber, and T. M. Habashy, 2002, Interpretation and inversion of fully triaxial induction data – a sensitivity study: Presented at the 43rd Annual Logging Symposium, SPWLA.

Anderson, B., T. Barber, and M. Lüling, 2006, Observations of large dielectric effects on induction logs, or can source rocks be detected with induction measurements: Presented at the 47th Annual Logging Symposium, SPWLA.

Anderson, B., T.D. Barber, M. Lüling, J. Rasmus, P.N. Sen, J.R. Tabanou, and M. Haugland, 2007, Observations of large dielectric effects on LWD propagation-resistivity logs: Presented at the 48th Annual Logging Symposium, SPWLA.

Anderson, B., T. Barber, M. Lüling, P. Sen, R. Taherian, and J. Klein, 2008, Identifying potential gas-producing shales from large dielectric permittivities measured by induction quadrature signals: Presented at the 49th Annual Logging Symposium, SPWLA.

Arroyo F. J., F. Carrique, T. Bellini, and A. V. Delgado, 1999, Dielectric dispersion of colloidal suspensions in the presence of Stern Layer conductance – Particle size effects: Journal of Colloid and Interface Science, **210**(1), 194-199.

Asami, K., E. Gheorghiu, and T. Yonezawa, 1999, Real-time monitoring of yeast cell division by dielectric spectroscopy: Biophysical Journal, **76**, 3345-3348.

Barber, T., 1987, Spatial frequency method and apparatus for investigating earth conductivity with high vertical resolution by induction techniques: U. S. Patent 4,837,517.

Beltramo, P. J. and E. M. Furst, 2012, Dielectric spectroscopy of bidisperse colloidal suspensions: Journal of Colloid and Interface Science, **380**(1), 34-41.

Bergosh, J. L., T. R. Marks, and A. F. Mitkus, 1985, New core analysis techniques for naturally fractured reservoirs: Presented at the California Regional Meeting, SPE.

Buseck, P. R. and O. Beyssac, 2014, From organic matter to graphite – Graphitization: Elements, **10**(6), 421-426.

Chen, H. and Z. Heidari, 2014, Pore-scale evaluation of dielectric measurements in formations with complex pore and grain structures: Presented at the 55th Annual Logging Symposium, SPWLA.

Chu, K. T. and M. Z. Bazant, 2006, Nonlinear electrochemical relaxation around conductors: Physical Review E, **74**(1), 011501.

Clavier, C., A. Heim, and C. Scala, 1976, Effect of pyrite on resistivity and other logging measurements: Presented at the 17th Annual Logging Symposium, SPWLA.

Clennell, M. B., M. Josh, L. Esteban, C. D. Piane, S. Schmid, M. Verrall, and B. McMullan, 2010, The influence of pyrite on rock electrical properties – A case study from NW Australian gas reservoirs: Presented at the 51st Annual Logging Symposium, SPWLA.

Corley, B., A. Garcia, H. M. Maurer, M. B. Rabinovich, Z. Zhou, P. DuBois, and N. Shaw, 2010, Study of unusual responses from multiple resistivity tools in the Bossier formation of the Haynesville shale play: Presented at the Annual Technical Conference and Exhibition, SPE.

Cosenza, P., A. Ghorbani, C. Camerlynck, F. Rejiba, R. Guérin, and A. Tabbagh, 2009, Effective medium theories for modeling the relationships between electromagnetic properties and hydrological variables in geomaterials: Near Surface Geophysics, **7**(5), 563-578.

de Kuijper, A. and J. A. de Waal, 2007, An effective-medium saturation model for carbonate rock: Presented at the Middle East Regional Symposium. SPWLA.

Delgado, A. V., F. J. Arroyo, F. González-Caballero, V.N. Shilov, and Y.B. Borkovskaya, 1998, The effect of the concentration of dispersed particles on the mechanisms of low-frequency dielectric dispersion (LFDD) in colloidal suspensions: Colloids and Surfaces A: Physicochemical and Engineering Aspects, **140**(1), 139-149.

Dias, C. A., 2000, Developments in a model to describe low-frequency electrical polarization of rocks: Geophysics, **65**(2), 437-451.

Doll, H. G., 1949, Introduction to induction logging and application to logging of wells drilled with oil base mud: Journal of Petroleum Technology, **1**(6), 148-162.

Dukhin, S. S., V. N. Shilov, and J. J. Bikerman, 1974, Dielectric phenomena and double layer in disperse systems and polyelectrolytes: Journal of The Electrochemical Society, **121**(4), 154C.

Ehrenberg, S. N., 2007, Whole core versus plugs – scale dependence of porosity and permeability measurements in platform carbonates: AAPG Bulletin, **91**(6), 835-846.

Franklin Miller Inc., 2015, Material bulk densities, https://www.franklinmiller.com/latest-news/material-bulk-densities/, accessed 11 July 2015.

Gander, W., and W. Gautschi, 2000, Adaptive quadrature – revisited: BIT Numerical Mathematics, **40**(1), 84-101.

Garcia-Martin, J., J. Gomez-Gil, and E. Vazquez-Sanchez, 2011, Non-destructive techniques based on eddy current testing: Sensors, **11**(3), 2525-2565.

Garrouch, A. A., 1998, Implications of resistivity dispersion on LWD log interpretations: Presented at the SPWLA 39th Annual Logging Symposium.

Ghorbani, A., C. Camerlynck, N. Florsch, P. Cosenza, and A. Revil, 2007, Bayesian inference of the Cole-Cole parameters from time- and frequency-domain induced polarization: Geophysical Prospecting, **55**(4), 589-605.

Gianzero, S., 1999, The paradox of anisotropy revisited: The Log Analyst, **40**(6), 485-491.

Giordano, S., 2003, Effective medium theory for dispersions of dielectric ellipsoids: Journal of Electrostatics, **58**(1), 59-76.

Gray, T. and J. C. Rasmus, 1988, A laboratory study of oomoldic rock substantiating a conductivity-dielectric interpretation technique and the non-interdependence of the Archie petrophysical parameter: Presented at the 29th Annual Logging Symposium, SPWLA.

Grosse, C. and K. R. Foster, 1987, Permittivity of a suspension of charged spherical particles in electrolyte solution: Journal of Physical Chemistry, **91**(11), 3073-3076.

Grosse, C., 1988, Permittivity of a suspension of charged spherical particles in electrolyte solution, Part 2 – Influence of the surface conductivity and asymmetry of the electrolyte on the low- and high-frequency relaxations: The Journal of Physical Chemistry, **92**(13), 3905-3910.

Grosse, C., 1989, Permittivity of a suspension of charged cylindrical particles in electrolyte solution: The Journal of Physical Chemistry, **93**(15), 5865-5869.

Grosse, C. and R. Barchini, 1992, The influence of diffusion on the dielectric properties of suspensions of conductive spherical particles in an electrolyte: Journal of Physics D, **25**(3), 508-515.

Grote, M. J., 1998, Nonreflecting boundary conditions for electromagnetic scattering: Research Report No. 98-09, Seminar für Angewandte Mathematik.

Gurin, G., K. Titov, Y. Ilyin, and A. Tarasov, 2015, Induced polarization of disseminated electronically conductive minerals: a semi-empirical model: Geophysics Journal International, **200**, 1555-1565.

Han, M., J. Cuadros, C. A. P. Suarez, E. Decoster, O. Faivre, L. Mosse, and N. Seleznev, 2012, Continuous estimate of cation exchange capacity from log data – a new approach based on dielectric dispersion analysis: Presented at the 53rd Annual Logging Symposium, SPWLA.

Hanai, T., N. Koizumi, and R. Gotoh, 1959, Dielectric properties of emulsions: Kolloid-Zeitschrift, **167**(1), 41-43.

Hanai, T., K. Asami, and N. Koizumi, 1979, Dielectric theory of concentrated suspensions of shell-spheres in particular reference to the analysis of biological cell suspensions: Bulletin of the Institute of Chemical Research, Kyoto University, **57**, 297-305.

Hizem, M., H. Budan, B. Deville, O. Faivre, L. Mosse, and M. Simon, 2008, Dielectric dispersion – A new wireline petrophysical measurement: Presented at the Annual Technical Conference and Exhibition, SPE.

Hogg,A.J., 2001, Separable solutions to Laplace's equation, http://www.maths.bris.ac.uk/~maajh/fluids/handout3.pdf, accessed 11 June 2015.

Homan, D., J. W. Gibson, J. Jalfin, H. Wang, C. Dupius, and G. N. Minerbo, 2009, Method of and apparatus for measuring tensor resistivity: Provisional Patent Appl. CA2646843 A1.

Honarpour, M. M., N. F. Djabbarah, and K. Sampath, 2003, Whole core analysis – experience and challenges: Presented at the 13th Middle East Oil Show and Conference, SPE.

Jackson, C. and T. Hagiwara, 1998, A new simultaneous anisotropy and dielectric correction algorithm for LWD resistivity measurements: Presented at the 39th Annual Logging Symposium, SPWLA.

Jackson, P. D., M. A. Lovell, J. Roberts, P. Schultheiss, D. Gunn, R. Flint, A. Wood, and R. Holmes, 2006, Rapid non-contacting resistivity logging of core: Presented at the 45th Annual Logging Symposium, SPWLA.

Jackson, P. D., J. F. Williams, L. Ma, A. Camps, C. Rochelle, and A. E. Mildowski, 2008, An investigation of the exponent in Archie's equation: Presented at the 49th Annual Logging Symposium, SPWLA.

Jiangqing, Z., Z. Ding, L. Xuewen, C. Ruihua, and Y. Chunsheng, 1994, Laboratory measurement and applications of anisotropy parameters of rock: Presented at the SPWLA 35th Annual Logging Symposium.

Josh, M., L. Esteban, C. Delle Piane, J. Sarout, D. N. Dewhurst, and M. B. Clennell, 2012, Laboratory characterization of shale properties: Journal of Petroleum Science and Engineering, **88**, 107-124.

Josh, M., 2014, Dielectric Permittivity – A Petrophysical Parameter for Shales: Petrophysics, **55**(04), 319-332.

Josh, M. and B. Clennell, 2015, Broadband electrical properties of clays and shales – Comparative investigations of remolded and preserved samples: Geophysics, **80**, D129-D143.

Jougnot, D., A. Ghorbani, A. Revil, P. Leroy, and P. Cosenza, 2010, Spectral induced polarization of partially saturated clay-rocks: a mechanistic approach: Geophysical Journal International, **180**, 210-224.

Keelan, D. K., 1982, Core analysis for aid in reservoir description: Journal of Petroleum Technology, **34**(11), 2483-2491.

Ken, A. and M. Stewart, 1999, Surface production operations – Design of gas-handling systems and facilities, Vol. 2, Gulf Professional Publishing.

Kennedy, M. W., S. Akhtar, J. A. Bakken, and R. E., Aune, 2011, Analytical and experimental validation of electromagnetic simulations using COMSOL re-

inductance, induction heating, and magnetic fields: Presented at the COMSOL Users Conference.

Kennedy, W. D. and D. C. Herrick, 2004, Conductivity anisotropy in shale-free sandstone: Petrophysics, **45**(1), 38-58.

Kethireddy, N., H. Chen, and Z. Heidari, 2014, Quantifying the effect of kerogen on resistivity measurements in organic-rich mudrocks: Petrophysics, **55**(2), 136-146.

Khair, A. S. and T. M. Squires, 2008, Fundamental aspects of concentration polarization arising from nonuniform electrokinetic transport: Physics of Fluids, **20**, 087102.

Kickhofel, J. L., A. Mohamide, J. Jalfin, J. Gibson, P. Thomas, G. Minerbo, and D. M. Homan, 2010, Inductive conductivity tensor measurement for flowline or material samples: Review of Scientific Instruments, **81**(7), 075102.

Kilic, D. S., 2014, Tilted test loop calibration system: Provisional Patent Appl. US20140156211 A1.

Klein, J. D. and W. R. Sill, 1982, Electrical properties of artificial clay-bearing sandstone: Geophysics, **47**(11), 1593-1605.

Klein, J. D., 1996, Saturation effects on electrical anisotropy: The Log Analyst, **37**(1), 47-49.

Klein, J. D., P. R. Martin, and D. Allen, The petrophysics of electrically anisotropic reservoirs: The Log Analyst, **38**(3), 25-36.

Kriegshäuser, B., O. Fanini, S. Forgang, G. Itskovich, M. Rabinovich, L. Tabarovsky, L. Yu, M. Epov, and J. van-der-Horst, 2000, A new multi-component induction logging tool to resolve anisotropic formations: Presented at the 41st Annual Logging Symposium, SPWLA.

Laswell, P. M., 2006, Core analysis for electrical properties: Petrophysics, **47**(3), 191-213.

Laughrey, C. D., T. E. Ruble, H. Lemmens, J. Kostelnik, A. R. Butcher, G. Walker, and W. Knowles, 2011, AV black shale diagenesis – insights from integrated high-definition analyses of post-mature Marcellus formation rocks, Northeastern Pennsylvania: Presented at the Annual Convention and Exhibition, AAPG.

Le, F., Z. Zhou, H. Maurer, and M. Rabinovich, 2011, 3-D study of resistivity tool responses in formations with vertical fractures or horizontal transverse isotropy: Presented at the 52nd Annual Logging Symposium, SPWLA.

Leao, T. P., E. Perfect, and J. S. Tyner, 2015, Evaluation of Lichtenecker's mixing model for predicting effective permittivity of soils at 50 MHz: Transactions of the ASABE, **58**(1), 83-91.

Lee, S., 2010, Development of approach to estimate volume fraction of multiphase material using dielectrics: Ph.D. dissertation, Texas A&M University.

Leroy, P. and A. Revil, 2004, A triple layer model of the surface electrochemical properties of clay minerals: Journal of Colloid and Interface Science, **270**(2), 371-380.

Lesmes, D. P. and F. D. Morgan, 2001, Dielectric spectroscopy of sedimentary rocks: Journal of Geophysical Research, **106**(B7), 13329-13346.

Loftness, R. L., 1952, The dielectric losses of various filled phenolic resins: Ph.D. dissertation, ETH Zurich.

Lüling, M. G., L. Pettinicchio, R. A. Rosthal, and F. Shray, 2005, Dielectric effects on resistivity anisotropy in laminates: Presented at the 46th Annual Logging Symposium, SPWLA.

Luo, Y. and G. Zhang, 1998, Theory and application of spectral induced polarization: Society of Exploration Geophysicists.

Mahan, M. K., J. D. Redman, and D. W. Strangway, 1986, Complex resistivity of synthetic sulphide bearing rocks: Geophysical Prospecting, **34**(5), 743-768.

Misra, S., C. Torres-Verdín, and K. Sepehrnoori, 2013, Environmental and transport effects on core measurements of water saturation, salinity, and wettability: Presented at the Annual Technical Conference and Exhibition, SPE.

Misra, S., C. Torres-Verdín, D. Homan, and J. Rasmus, 2015a, Complex electrical conductivity of mudrocks and source-rock formations containing disseminated pyrite: Presented at the Unconventional Resources Technology Conference, SPE-AAPG-SEG.

Misra, S., C. Torres-Verdín, D. Homan, G. Minerbo, and J. Rasmus, 2015b, Laboratory investigation of petrophysical applications of multi-frequency inductive-complex conductivity tensor measurements: Presented at the 56th Annual Logging Symposium, SPWLA.

Misra, S., C. Torres-Verdín, A. Revil, D. Homan, and J. Rasmus, 2015c, Interfacial polarization of disseminated conductive minerals in absence of redox-active species, Part 1 – Mechanistic model and validation: Intended for publication in Geophysics Journal.

Misra, S., C. Torres-Verdín, A. Revil, D. Homan, and J. Rasmus, 2015d, Interfacial polarization of disseminated conductive minerals in absence of redox-active species, Part 2 – Effective electrical conductivity and dielectric permittivity: Intended for publication in Geophysics Journal.

Mitchell, W. K., 1997, Method and system for skin effect correction in a multiple transmit frequency induction logging system: U. S. Patent 5,698,982.

Mohamed, S. S. E. D., M. Dernaika, I. Al Hosani, L. Hannon, S. Skjaeveland, and M. Z. Kalam, 2010, Whole core versus plugs: integrating log and core data to decrease uncertainty in petrophysical interpretation and STOIP calculations: Presented at the Abu Dhabi International Petroleum Exhibition and Conference, SPE.

Moran, J. H. and K. S. Kunz, 1962, Basic theory of induction logging and application to study of two-coil sondes: Geophysics, **27**(6), 829-858.

Morse, P. M. and H. Feshbach, 1953, Methods of Theoretical Physics, Part I: Mc Graw-Hill.

Olhoeft, G.R. and D. E. Capron, 1994, Petrophysical causes of electromagnetic dispersion: Presented at the Fifth International Conference on Ground Penetrating Radar.

Olusola, B. K., G. Yu, and R. Aguilera, 2013, The use of electromagnetic mixing rules for petrophysical evaluation of dual- and triple-porosity reservoirs: Presented at the Canadian Unconventional Resources Conference, SPE.

Passey, Q. R., Bohacs, K., Esch, W. L., Klimentidis, R., and Sinha, S., 2010, From oil-prone source rock to gas-producing shale reservoir - geologic and petrophysical characterization of unconventional shale gas reservoirs: Presented at the International Oil & Gas Conference and Exhibition, CPS/SPE.

Pelton, W. H., S. H. Ward, P. G. Hallof, W. R. Sill, and P. H. Nelson, 1978, Mineral discrimination and removal of inductive coupling with multifrequency IP: Geophysics, **43**(3), 588-609.

Perez-Rosales, C., A. Mercado-Diaz, J. Cruz-Hernandez, and R. Islas-Juarez, 2002, Electrical resistivity of vuggy fractured media: Presented at the International Petroleum Conference and Exhibition, SPE.

Placencia-Gómez, E. and L. D. Slater, 2014, Electrochemical spectral induced polarization modeling of artificial sulfide-sand mixtures: Geophysics, **79**(6), EN91-EN106.

Pridmore, D. F. and R. T. Shuey, 1976, The electrical resistivity of galena, pyrite, and chalcopyrite: American Mineralogist, **61**, 248-259.

Rasmus, J. C., and W. E. Kenyon, 1985, An improved petrophysical evaluation of oomoldic Lansing-Kansas City formations utilizing conductivity and dielectric log measurements: Presented at the 26th Annual Logging Symposium, SPWLA.

Revil, A. and M. Skold, 2011, Salinity dependence of spectral induced polarization in sands and sandstones: Geophysical Journal International, **187**, 813-824.

Revil, A., 2012, Spectral induced polarization of shaly sands: Influence of the electrical double layer: Water Resources Research, **48**(2), W02517.

Revil, A., 2013, Effective conductivity and permittivity of unsaturated porous material in the frequency range 1 mHz – 1 Ghz: Water Resources Research, **49**(1), 306-327.

Revil, A., W. F. Woodruff, C. Torres-Verdín, and M. Prasad, 2013, Complex conductivity tensor of anisotropic hydrocarbon-bearing shales and mudrocks, Geophysics, 78(6), D403-D418.

Revil, A., N. Florsch, and D. Mao, 2015a, The complex conductivity response of porous media with metallic particles. 1. A theory for disseminated semi-conductors: in press, Geophysics.

Revil A., G.Z. Abdel Aal, E.A. Atekwana, D. Mao, and N. Florsch, 2015b, The complex conductivity response of porous media with metallic particles. 2. Comparison with a broad database of experimental data: in press, Geophysics.

Romero-Sarmiento, M. F., J. N. Rouzaud, S. Bernard, D. Deldicque, M. Thomas, and R. Littke, 2014, Evolution of Barnett Shale organic carbon structure and nanostructure with increasing maturation: Organic Geochemistry, **71**, 7-16.

Rosthal, R., T. Barber, S. Bonner, K. Chen, S. Davydcheva, G. Hazen, D. Homan, C. Kibbe, R. Schlein, L. Villegas, H. Wang, and F. Zhou, 2003, Field test results of an experimental fully-triaxial induction tool: Presented at the 44th Annual Logging Symposium, SPWLA.

RP40, 1960, Recommended practice for core analysis procedure: A. P. I.

Sabouroux, P. and D. Ba, 2011, Epsimu, a tool for dielectric properties measurement of porous media: Application in wet granular materials characterization: Progress in Electromagnetic Research B, **29**, 191-207.

Santandrea, L. and Y. Le Bihan, 2010, Using COMSOL-multiphysics in an eddy current non-destructive testing context: Presented at the COMSOL Conference.

Scharfetter, H., W. Ninaus, B. Puswald, G. I. Petrova, D. Kovachev, and H. Hutten, 1999, Inductively coupled wideband transceiver for bioimpedance spectroscopy (IBIS): Electrical Bioimpedance Methods, 873, 322-334.

Schmuck, M. and M. Z. Bazant, 2012, Homogenization of the Poisson-Nernst-Planck equations for ion transport in charged porous media, arXiv: 1202.1916v2, preprint available http://arxiv.org/abs/1202.1916.

Schoen, J. H., R. A. Mollison, and D. T. Georgi, 1999, Macroscopic electrical anisotropy of laminated reservoirs – a tensor resistivity saturation model: Presented at the Annual Technical Conference and Exhibition, SPE.

Schwan, H. P., G. Schwarz, J. Maczuk, and H. Pauly, 1962, On the low-frequency dielectric dispersion of colloidal particles in electrolyte solution: The Journal of Physical Chemistry, **66**(12), 2626-2635.

Schwartz, R. C., S. R. Evett, M. G. Pelletier, J. M. Bell, 2009, Complex permittivity model for time domain reflectometry soil water content sensing - I. Theory: Soil Science Society of America Journal, **73**(3), 886-897.

Schwarz, G., 1962, A theory of the low-frequency dielectric dispersion of colloidal particles in electrolyte solution: The Journal of Physical Chemistry, **66**(12), 2636-2642.

Seleznev, N., A. Boyd, T. Habashy, and S. M. Luthi, 2004, Dielectric mixing laws for fully and partially saturated carbonate rocks: Presented at the 45th Annual Logging Symposium, SPWLA.

Sen, P., 1980, The dielectric and conductivity response of sedimentary rocks: Presented at the Annual Technical Conference and Exhibition, SPE.

Shilov, V. N., A. V. Delgado, F. Gonzalez-Caballero, and C. Grosse, 2001, Thin double layer theory of the wide frequency range dielectric dispersion of suspensions of non-conducting spherical particles including surface conductivity of the stagnant layer: Colloids and Surfaces A, **192**, 253- 265.

Shilov, V. N. and Y. B. Borkovskaya, 2010, Theory of broadband dispersion of permittivity of biological cell suspensions: Colloid Journal, **72**(5), 686-695.

Sihvola, A., 2007, Dielectric polarization and particle shape effects: Journal of Nanomaterials, **2007**, 45090, doi:10.1155/2007/45090.

Spötl, C., D. W. Houseknecht, and R. C. Jaques, 1998, Kerogen maturation and incipient graphitization of hydrocarbon source rocks in the Arkoma Basin, Oklahoma and

Arkansas – a combined petrographic and Raman spectrometric study: Organic Geochemistry, **28**, 535-542, ISSN 0146-6380.

Sprunt, E. S., R. E. Maute, and C. L. Rackers, 1990, An interpretation of the SCA electrical resistivity study: The Log Analyst, **31**(02), 76-88.

Stillman, D. E., R. E. Grimm, and S. E. Dec, 2010, Low-frequency electrical properties of ice-silicate mixtures: Journal of Physical Chemistry, **114**(18), 6065-6073.

Stratton, J. A., 1941, reissued 2007, Electromagnetic Theory: IEEE Press Series on Electromagnetic Wave Theory, J. Wiley & Sons, Inc.

Swarco, 2004, version number: GHS 1.0, Reflective Glass Beads Megalux Beads, Safety Data Sheet.

Tarasov, A. and K. Titov, 2013, On the use of the Cole-Cole equations in spectral induced polarization: Geophysical Journal International, 195(1), 352-356.

Tirado, M. and C. Grosse, 2006, Dependence of the broad frequency dielectric spectra of colloidal polystyrene particle suspensions on the difference between the counterion and co-ion diffusion coefficients: Journal of Colloid and Interface Science, **298**(2), 973-981.

Toumelin, E., 2006, Pore-scale petrophysical models for the simulation and combined interpretation of nuclear magnetic resonance and wide-band electromagnetic measurements of saturated rocks: Ph.D. Dissertation, The University of Texas at Austin.

Toumelin, E., C. Torres-Verdín, and N. Bona, 2008, Improving petrophysical interpretation with wide-band electromagnetic measurements: SPE Journal, **13**, no. 2, 205-215.

Ubani, C. E., Y. B. Abedoye, and A. B. Oriji, 2012, Advances in coring and core analysis for reservoir formation evaluation: Petroleum & Coal, **54** (1), 42-51.

Vinegar, H. J. and M. H. Waxman, 1984, Induced polarization of shaly sands – the effect of clay counterion type: The Log Analyst, **25**(6), 11-21.

Volkmann, J. and N. Kiltzsch, 2010, Frequency-dependent electric properties of microscale rock models for frequencies from one milihertz to ten kilohertz: Vadose Zone Journal, **9**(4), 858-870.

Wait, J. R., 1986, Extensions to the phenomenological theory of induced polarization: IEEE Transactions on Geoscience and Remote Sensing, **24**(3), 409-414.

Wakamatsu, H., 1997, A dielectric spectrometer for liquid using the electromagnetic induction method: Hewlett Packard Journal, **48**, 37-44.

Walters, C. C., C. E. Kliewer, D. N. Awwiller, M. D. Rudnicki, Q. R. Passey, and M. W. Lin, 2014, Influence of turbostatic carbon nanostructures on electrical conductivity in shales: International Journal of Coal Geology, **122**, 105-109.

Wang, H., T. Barber, R. Rosthal, J. Tabanou, B. Anderson, and T. Habashy, 2003, Fast and rigorous inversion of triaxial induction logging data to determine formation resistivity anisotropy, bed boundary position, relative dip, and azimuth angles: Presented at the Annual Meeting, SEG.

Wang, H. and A. Poppitt, 2013, The broadband electromagnetic dispersion logging data in a gas shale formation – A case study: Presented at the 54th Annual Logging Symposium, SPWLA.

Waxman, M. H. and L. J. M. Smits, 1968, Electrical conductivities in oil-bearing shaly sand: Society of Petroleum Engineers Journal, **8**(2), 107-122.

Weisstein, E. W., 2015a, Legendre Polynomial, http://mathworld.wolfram.com/LegendrePolynomial.html, accessed 11 June 2015.

Weisstein, E. W., 2015b, Bessel Function, http://mathworld.wolfram.com/BesselFunction.html, accessed 11 June 2015.

Weisstein, E. W., 2015c, Helmholtz Differential Equation: Polar Coordinates, http://mathworld.wolfram.com/HelmholtzDifferentialEquationPolarCoordinates.html, accessed 11 June 2015.

Weisstein, E. W., 2015d, Modified Bessel Function of the First Kind, http://mathworld.wolfram.com/ModifiedBesselFunctionoftheFirstKind.html, accessed 11 June 2015.

Witkowsky, J. M., J. E. Galford, J. A. Quirein, and J. A. Truax, 2012, Predicting pyrite and total organic carbon from well logs for enhanced shale reservoir interpretation: Presented at the Eastern Regional Meeting, SPE.

Won, I. J. and D. A. Keiswetter, 1998, Electromagnetic induction spectroscopy: Presented at the Conference on Detection and Remediation Technologies for Mines and Minelike Targets, SPIE.

Wong, J., 1979, An electrochemical model of the induced-polarization phenomenon in disseminated sulfide ores: Geophysics, **44**(7), 1245-1265.

Wu, J., M. Wisler, and W. H. Meyer, 1997, Measurement of dip angle and horizontal and vertical resistivities using multiple frequency propagation resistivity tools: Presented at the 38th Annual Logging Symposium, SPWLA.

Wu, P., H. Wang, G. Minerbo, D. Homan, T. Barber, and M. Frey, 2007, Borehole effects and correction in OBM with dip and anisotropy for triaxial induction tools: Presented at the Annual Technical Conference and Exhibition, SPE.

Wu, P., T. Barber, G. L. Wang, C. Johnson, D. Heliot, R. Hayden, A. Kumar, W. Xu, H. Wang, S. Clinch, and C. L. Schmidt, 2013, Fracture characterization using triaxial induction tools: Presented at the 54th Annual Logging Symposium, SPWLA.

Yan, L., K. Xiang, P. Li, X. Liu, and Z. Wang, 2014, Study on the induced polarization model in the exploration for shale gas in southern china: Presented at the Annual Meeting, SEG.

Young, P., 2009, Helmholz's and Laplace's Equations in Spherical Polar Coordinates, http://physics.ucsc.edu/~peter/116C/helm_sp.pdf, accessed 11 June 2015.

Yu, G., W. Hu, Z. He, K. Xiang, H. Hu, L. He, and P. Li, 2014, Complex resistivity characteristics of high TOC marine shale core samples and its applications: Presented at the Annual Meeting, SEG.

Yu, L., O. N. Fanini, B. F. Kreigshauser, J. M. V. Koelman, and J. van Popta, 2001, Enhanced evaluation of low-resistivity reservoirs using multi-component induction log data: Petrophysics, **42**(6), 611-623.

Zakri, T., J. P. Laurent, and M. Vauclin, 1998, Theoretical evidence for 'Lichtenecker's mixture formulae' based on the effective medium theory: Journal of Physics D: Applied Physics, **31**(13), 1589-1594.

Zhdanov, M. S., A. B. Cheryauka, and E. Peksen, 2003, Sharp boundary inversion of tensor induction logging data: Presented at the 44th Annual Logging Symposium, SPWLA.

Zhdanov, M. S., 2008, Generalized effective-medium theory of induced polarization: Geophysics, **73**(5), F197-F211.

Zheng, Q. and G. W. Wei, 2011, Poisson–Boltzmann–Nernst–Planck model: Journal of Chemical Physics, **134**(19), 194101, doi: 10.1063/1.3581031.